SCUOLA DI DOTTORATO
UNIVERSITÀ DEGLI STUDI DI MILANO-BICOCCA

Department of Medicine and Surgery

PhD curriculum in

TRANSLATIONAL AND MOLECULAR MEDICINE (DIMET)
XXXVIII cycle

Metabolic Control of Chromatin Accessibility Reverses Age Related Dysfunction in Human Hematopoietic Stem and Progenitor Cells

Farina Giacomo

896454

Supervisor: Serafini Marta

Co-supervisor: Di Micco Raffaella

Coordinator: Serafini Marta

ACADEMIC YEAR 2024/2025

ABSTRACT:
Aging impairs the function of human hematopoietic stem and progenitor cells (HSPCs) through coordinated changes in metabolism and chromatin. We examined whether a metabolic pathway centered on succinate and α-ketoglutarate (αKG) influences chromatin accessibility, energy dependence, and stem cell health in human HSPCs. We characterized young (18–25 years) and aged (> 70 years) human bone marrow (BM) $CD34^+$ cells. Flow cytometry showed a shift toward early progenitors with age, but overall CFU output, especially erythroid colonies, declined. Single-cell differentiation assays (MEM) on purified $CD45RA^-CD38^-CD34^+CD133^+CD90^+$ HSCs confirmed reduced clonogenic efficiency and decreased bi-lineage potential in aged cells. Alkaline comet assays showed increased DNA damage in CD34+ cells with age. RNA-seq (hallmark analysis) revealed enrichment in p53/DNA damage, inflammatory responses (TNFα/IL-6/IL-2/IFNγ), Myc, and metabolic pathways (glycolysis, hypoxia, OXPHOS) in aged HSPCs. ATAC-seq showed globally increased chromatin accessibility, including at TSSs linked to these pathways. Although some chromatin-modifier transcripts differed (SMYD3 decreased, KAT6B decreased, PRDM5 increased), pathway analyses did not fully explain the widespread accessibility gains. Untargeted LC-MS displayed broad metabolite accumulation in aged HSPCs, with notably lower succinate levels, suggesting a succinate/αKG control point for chromatin regulation. To manipulate this axis, we applied short ex vivo treatments (≤72 h). Dose–response testing (1–8 mM) showed that succinate (4 mM) increased CFU numbers, while αKG (4 mM) decreased them without affecting viability or immunophenotype. Western blots supported reciprocal chromatin effects: succinate increased H3K27me3 and decreased H3K27ac, while αKG had the opposite effect. In ATAC-seq, succinate reduced accessibility in aged HSPCs, whereas αKG increased accessibility in young HSPCs. Across sources (mPB, BM), succinate consistently enhanced clonogenicity. In contrast, αKG impaired it in young cells and had little detrimental effect in aged cells. MEM assays mirrored bulk results at the stem-enriched level: clonogenic efficiency and bi-lineage output were modulated by the metabolic treatment. Short treatments also affected in vivo performance. In NSG xenografts, young DMSO controls outperformed aged controls in peripheral blood by weeks 9–12. Succinate pre-treatment restored aged PB engraftment to youthful levels, while αKG decreased young PB engraftment. Lineage composition differences at early time points merged by week 12. BM and spleen engraftment showed minor differences between groups, consistent with the constraints of human hematopoiesis. Mechanistically, SCENITH showed that succinate shifted energy reliance toward glycolysis in bulk $CD34^+$ and primitive $CD34^+CD133^+CD90^+$ cells, resembling youthful dependence; αKG caused an opposite shift in young cells. Succinate increased HIF-2α protein, while αKG decreased it. Pharmacological blockade of HIF-2α (PT2399) partially reduced succinate's benefits on clonogenicity and DNA damage, indicating both HIF-2α–dependent and independent effects linked to dioxygenase cofactors connecting metabolism to chromatin. Overall, these findings support a model in which succinate/αKG tuning regulates chromatin accessibility and energy status in human HSPCs, reducing DNA damage, boosting clonogenic potential, and improving early peripheral blood engraftment after brief ex vivo exposure.

Table of Contents

1. Hematopoietic Stem and Progenitor Cells

1.1 Hematopoiesis and HSC Hierarchy

Hematopoiesis is a lifelong process that produces all circulating blood cells and sustains immune function, oxygen transport, and blood clotting from a relatively small pool of stem cells. At the top of this system are hematopoietic stem cells (HSCs), which, by definition, combine self-renewal, the ability to reproduce themselves over decades, with multipotency, the capacity to develop into all mature blood cells.[1] For much of the twentieth century, this process was depicted as a neatly tiered pyramid, where HSCs produced multipotent progenitors that then gave rise to oligopotent intermediates and, ultimately, to unipotent cells.[2]

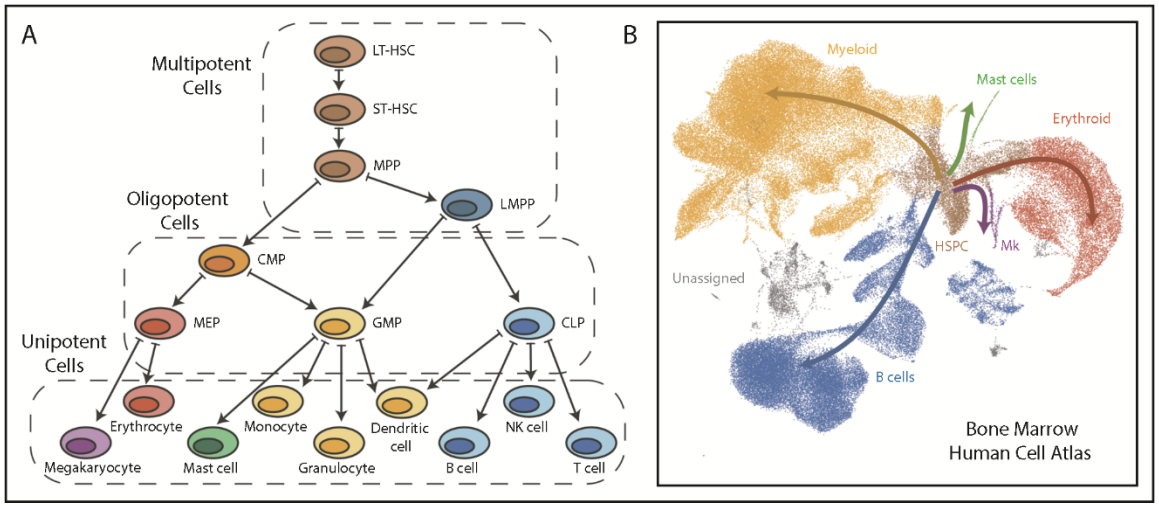

Figure 1. Schematic representation of the bone marrow niche.
(A) Stylized "tree" of the hematopoietic system. Dashed boxes group three potency tiers: multipotent cells at the top, bi/oligopotent intermediates, and unipotent terminal lineages at the bottom. (B) UMAP projection of single-cell transcriptomes from bone marrow mononuclear cells. Arrows show main differentiation trajectories inferred from canonical marker expression. Gray indicates cells without a confident identity assignment. (B) UMAP projection of single-cell transcriptomes from bone marrow mononuclear cells. Arrows show main differentiation trajectories inferred from canonical marker expression. Gray indicates cells without a confident identity assignment. [Adapted from PMID: 30728144]

That classical diagram illustrated the overall direction of differentiation but masked the dynamism and continuity now evident when hematopoiesis is examined at the single-cell level. Modern studies show that lineage priming begins surprisingly early, even among phenotypic HSCs, and that fate decisions occur along a continuum of transcriptional and chromatin states rather than through a few distinct ones.[4,5] In this view, early trajectories diverge toward megakaryocyte–erythroid output on one side and toward a lympho-myeloid spectrum on the other, with platelet and erythroid options detectable close to the stem cell state and myelomonocytic and lymphoid options branching with graded probabilities.[2,6] Experimental work with prospective isolation has been crucial in constructing this map. In humans, enriching HSCs and progenitors within the CD34+ compartment is followed by more refined separation using CD38, CD90 (Thy-1), and CD45RA to distinguish long-term HSCs from multipotent and lymphoid-primed cells. While these immunophenotypes are not perfect indicators of function, clonal assays often show heterogeneity within each gate; they provide consistent reference points across labs and clinical protocols.[1,7] Single-cell RNA and chromatin accessibility profiling enhance this framework by measuring how lineage-related programs gradually strengthen along trajectories, how quiescent stem cells exhibit low levels of future fate signatures, and how small pools of long-lived clones can dominate steady-state production for long periods.[4,5,6,8] Overall, current evidence supports a synthesis: hematopoiesis follows a

hierarchical pattern in terms of fate restriction and timing, but functions as a fluid landscape where cell-intrinsic variability, randomness, and microenvironmental cues all influence downstream decisions.[2] This blended model is more than just a conceptual update; it changes how we define, isolate, and test human stem and progenitor cells, providing a baseline for understanding age-related changes.

1.2 HSPCs Maintenance and Regulation

Hematopoietic stem and progenitor cells (HSPCs) do not function alone: their behavior results from ongoing interactions with the bone marrow niche.[9] This microenvironment is a complex, multicellular, perivascular ecosystem that integrates biochemical, mechanical, and temporal signals to maintain quiescence, enable rapid activation during stress, and preserve the long-term stem cell pool.

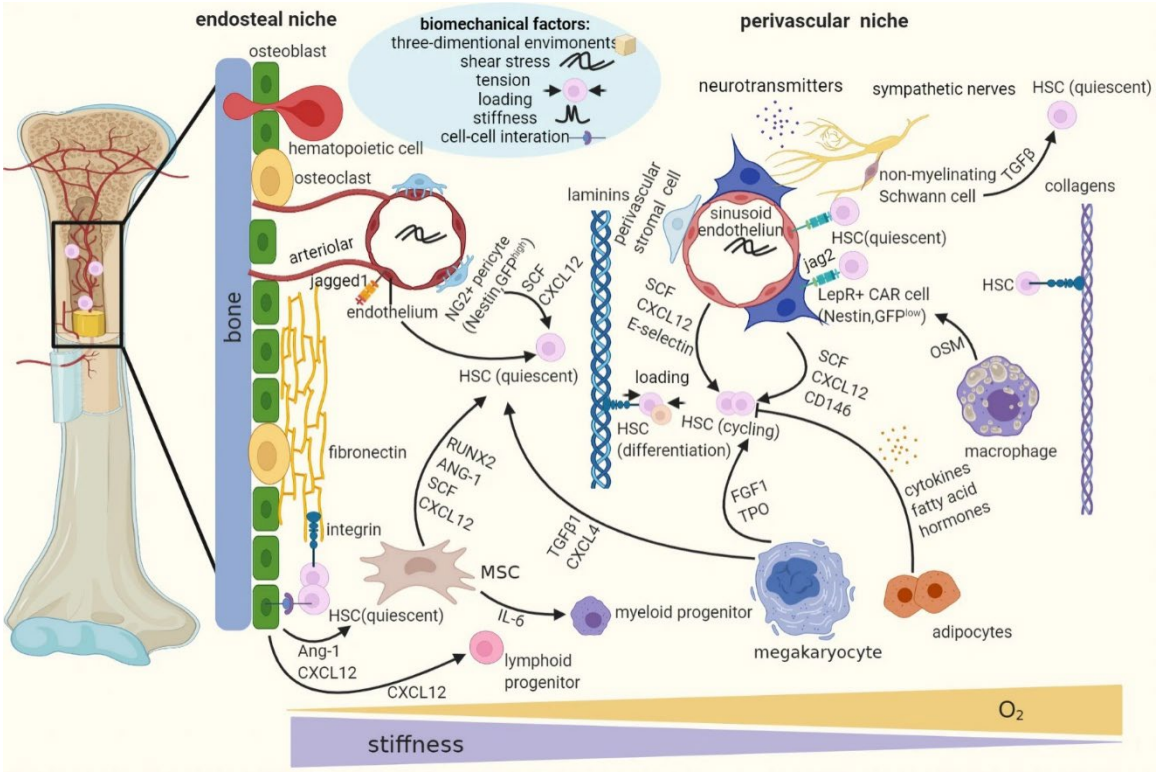

Figure 2. Biomechanical cues as master regulators of hematopoietic stem cell fate
Adult HSCs exist in specific three-dimensional microenvironments: an endosteal niche near the trabecular bone and perivascular niches around arterioles and sinusoids. The endosteal niche is typically associated with deep quiescence, while perivascular regions, supported by vascular and stromal cells, favor cell-cycle entry, proliferation, and lineage commitment. Notably, quiescent HSCs are often found along small endosteal arterioles, whereas the most primitive long-term HSCs are maintained close to sinusoidal vessels. In vivo, biochemical, biophysical, and biomechanical signals interact to regulate these states. (PMID: 34232331)

Perivascular mesenchymal stromal cells, arteriolar and sinusoidal endothelial cells, osteolineage cells, megakaryocytes, macrophages, and sympathetic nerve fibers form overlapping microdomains that provide various, partly redundant support functions. Quiescence and self-renewal are promoted by cytokine-receptor axes such as thrombopoietin-MPL and stem cell factor-KIT, endothelial-derived angiocrine signals including Notch ligands, and cell-to-cell and cell-matrix adhesion that stabilize residence near vessels.[10,11,12,13] Spatial heterogeneity is functionally important: arteriolar regions tend to be relatively hypoxic and promote deep quiescence, whereas sinusoidal areas are better suited for activation, trafficking, and interactions with circulating cues.[14,15,16] Negative regulation is equally essential. Megakaryocytes can suppress HSC proliferation through paracrine mediators, including CXCL4

and TGF-β.[17,18] Meanwhile, stromal CXCL12 acts as a retention cue that, along with macrophage-mediated regulation, anchors HSPCs within protective niches.[19,20,21] Conversely, circadian rhythms of mobilization are influenced by sympathetic activity and granulocyte maturation and clearance, indicating a temporal control mechanism within the niche.[22,23,24] The niche can rapidly remodel during infection, bleeding, or cytotoxic injury: changes include alterations in endothelial barrier function, stromal composition, and transient expansion of progenitor pools to restore homeostasis.[24] As the organism ages, this ecosystem shifts: sympathetic innervation decreases, adipocytes accumulate, vascular and stromal cells adopt a pro-inflammatory state, and signals favor myeloid output and faster activation at the expense of long-term function.[25,26,27,28] Culture conditions reflect many of these effects. Factors like oxygen levels, nutrients, extracellular matrix stiffness, and cytokines influence whether HSPCs proliferate, differentiate, or remain quiescent and self-renew.[29,30] Small changes in these variables can alter transplantation outcomes, such as engraftment potential and lineage output.[31] Recognizing HSPCs maintenance as a distributed property, arising from local cell populations, vascular structure, innervation, mechanics, and timing, helps explain variability in experiments and guides strategies that target both the niche and stem cells directly.[28] It also emphasizes a key message for clinical practice: successfully manipulating HSPCs for mobilization, gene therapy, or transplantation depends on maintaining the signals and spatial organization that keep stem cells resilient and responsive.

2. Molecular Mechanisms of HSPCs Aging

2.1 Functional decline of HSPCs in mice/humans upon aging

Aging gradually reduces HSPCs performance through both internal and external mechanisms, which together decrease regenerative capacity and change lineage output.[32]
Functionally, old HSCs are less effective at homing, engrafting, and maintaining long-term hematopoiesis after stress; serial transplantation shows a progressive loss of self-renewal even when aged cells are placed into a youthful microenvironment, indicating that damage accumulates within the stem cell compartment itself. [33,34]

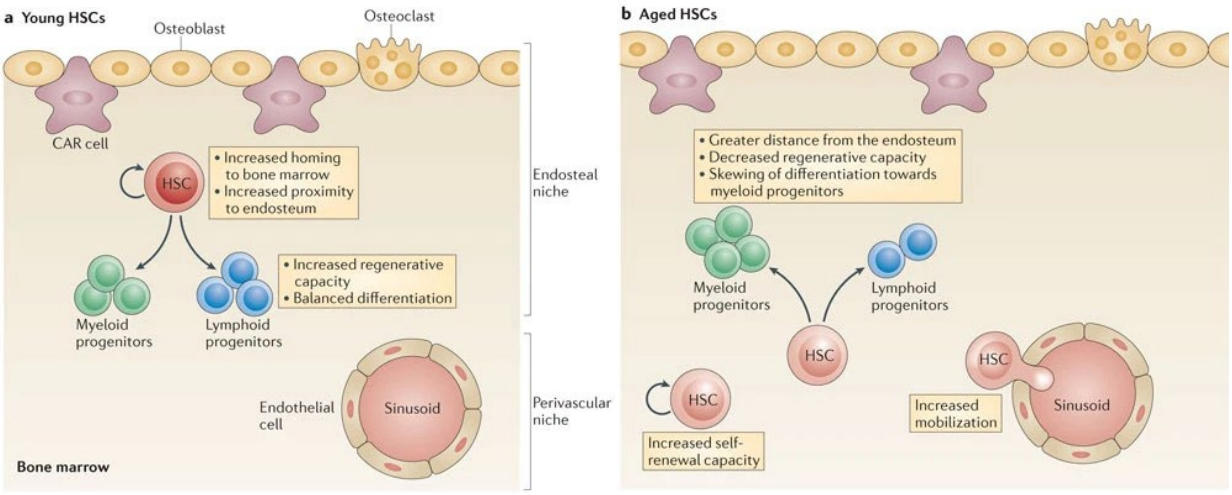

Figure 3. Phenotypical and functional changes in HSCs upon ageing
(A) Young HSCs. After homing to the bone marrow, young hematopoietic stem cells localize near the endosteum. They exhibit high self-renewal and regenerative capacity, with a balanced output toward both lymphoid and myeloid progenitors. (B) Aged HSCs. With age, the phenotypic HSC pool in the bone marrow expands, likely reflecting increased self-renewal, yet individual cells show reduced regenerative potential compared with young HSCs. Post-transplant, aged HSCs preferentially occupy niches away from the endosteum, indicating selection for different microenvironments. They are also home to the bone marrow, which is less efficiently mobilized (about twofold reduction) but can be

mobilized in higher numbers after cytokine stimulation. A key feature is myeloid-biased differentiation, producing more myeloid and fewer lymphoid progenitors than young HSCs. (Adapted from PMID: 23584423)

Meanwhile, aged bone marrow often contains more phenotypic HSCs than young marrow, a paradox explained by single-cell assays showing a higher proportion of functionally compromised or lineage-biased cells and a smaller fraction of truly long-term, multipotent stem cells.[36,32,37]
Clinically, these characteristics result in delayed immune recovery after chemotherapy and transplantation, higher susceptibility to cytopenias and infections, and increased prevalence of clonal hematopoiesis.[38,39]

2.2 Transcriptional and Epigenetic Changes in Aged HSPCs

Comparing profiles of young and old HSCs in mice consistently reveals heightened stress-responsive and inflammatory modules, particularly interferon signaling and NF-κB-linked networks, along with reduced lymphoid priming and quiescence-related programs.[32,40] These changes provide a mechanistic link between decreased lymphopoiesis, increased myeloid bias, and slower recovery after stress.[41] Single-cell studies reveal greater variability: with age, the stem cell compartment becomes less diverse, including clones that shift to highly reactive transcriptional states alongside others that maintain youthful features.[42,43] Another consistent finding is a looser link between cell-cycle control and long-term stemness. In aged HSCs, some cells stay quiescent but respond slowly to activation signals. In contrast, others enter the cycle more easily but incur long-term fitness costs, suggesting that checkpoint regulation and damage surveillance have been adjusted.[43] Beyond pathway-level changes, regulatory architecture also shifts: enhancer landscapes and transcription factor networks are remodeled so that lineage-specific factors, especially those regulating myeloid fate, have greater influence in specific aged cell subsets.[44,45] Inflammatory cytokines from the niche further stabilize these states, creating a feedback loop where chronic signaling leaves lasting transcriptional marks that limit HSC plasticity.[46] Aging HSCs show widespread epigenetic changes that record prior stress exposures and restrict future stemness potential.[44,45] DNA methylation patterns drift across the genome, with site-specific hyper- and hypomethylation correlating with shifts in lineage output and self-renewal capacity. [47,48] Chromatin accessibility and histone modification landscapes are reconfigured at enhancers and promoters, altering the responsiveness of key transcriptional networks and often reducing accessibility of elements linked to lymphoid differentiation.[44,45,49] These changes occur through multiple, sometimes overlapping pathways. First, repeated rounds of proliferation and mild replication stress gradually disrupt the epigenome, especially in regions that require precise maintenance of methylation or nucleosome positioning for proper repression.[47] Second, chronic inflammatory and metabolic signals in the aging niche influence the activity of chromatin-modifying enzymes, many of which depend on cofactors and are sensitive to redox state and metabolite levels.[46,50] Third, the hematopoietic system increasingly accumulates somatic mutations in epigenetic regulators like DNMT3A, TET2, and ASXL1, giving mutant clones a competitive edge by favoring altered methylation or chromatin states that promote expansion.[38,39,51,52,53] This results in clonal hematopoiesis, common in older adults and linked to higher risks of myeloid cancers and cardiovascular disease.[38,39] Importantly, epigenetic changes are not just passive signs of aging. Disruptions in enhancer activity and transcription factor binding can influence cell fate decisions and impair balanced regeneration.[44] Conversely, targeted reversal of specific epigenetic lesions can restore aspects of youthful function. Since epigenetic marks are, in principle, reversible, they are promising targets for rejuvenation strategies.[54,49] The main

challenge lies in ensuring specificity: interventions should reset chromatin programs that limit lymphoid potential and self-renewal without causing uncontrolled proliferation or damaging immune defenses.

2.3 Metabolic Changes in Aged HSCs in mice/humans

Metabolic organization is a key feature of stemness. Quiescent HSCs prefer glycolysis, maintain a low mitochondrial membrane potential, and tightly control reactive oxygen species to preserve genome integrity and long-term function.[55,56,57] This state is actively supported by signaling pathways that restrict pyruvate entry into the tricarboxylic acid cycle, limit excessive oxidative phosphorylation, and promote mitophagy and organelle quality control.[58,59]

	Quiescent HSCs	Cycling HSCs
Reconstitution activity	High	Low
ΔΨm	Low	High
ATP production	Low	High
Glycolysis activity	High	High
FAO	High	Low
Purine metabolism	High	Low
Intracellular ROS levels	Low	High
Autophagy/mitophagy	High	Low
Intracellular calcium levels	Low	High
Protein synthesis	Low	High
Lysosomal activity	High	Low

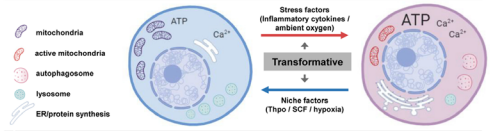

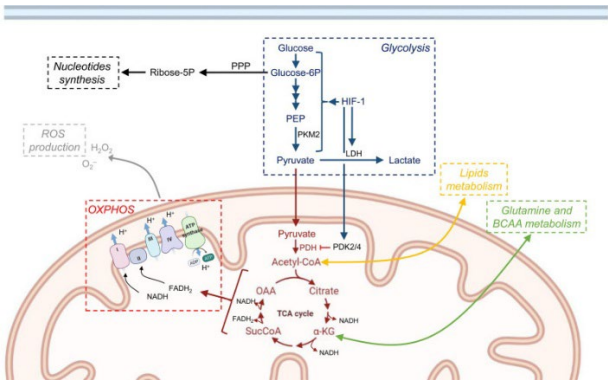

Figure4. Summary of metabolic alteration in HSCs
(A) Schematic representation of the differences between quiescent HSCs and cycling HSCs in different compartments. (PMID: 32693057)
(B) Schematic representation of metabolic contribution to maintenance of HSCs' self-renewal and differentiation (PMID: 35785147).

Nutrient-sensing pathways link these metabolic states to fate decisions. The PI3K–mTOR axis encourages growth and translation, but when it remains active for too long, it reduces stemness; conversely, inhibiting mTOR activity keeps cells in a quiescent state. [62,63] Hypoxia-inducible programs steer cells toward glycolytic metabolism and away from excessive respiration, connecting local oxygen levels to chromatin and transcriptional regulation.[64] Sirtuin-dependent checkpoints and the mitochondrial unfolded protein response regulate redox balance, proteostasis, and chromatin regulation, establishing a direct link between metabolic state and gene expression.[65,66] As organisms age, chronic inflammatory signals and mitochondrial stress alter these set points: oxidative phosphorylation and reactive oxygen species tend to increase at baseline, activation thresholds shift, and lineage output favors myeloid fates.[46,57] The overall result is decreased metabolic flexibility, the ability to switch smoothly between quiescent and activated programs, which in turn limits regenerative potential.[61]

3. Why metabolism and chromatin meet in aging stem cells

Across aging HSPCs, metabolic state and chromatin regulation converge at multiple control points. Quiescent stem cells typically favor glycolysis, maintain low mitochondrial membrane potential, and tightly regulate ROS, which protects genome integrity and long-term function.[55,57,58,59] With age, baseline oxidative phosphorylation and oxidative stress increase, while metabolic flexibility decreases, shifting activation thresholds and lineage output.[46,57,61] These metabolic changes influence the epigenetic machinery, which is sensitive to cofactors and redox state: inflammatory and metabolic signals modify chromatin-modifying enzymes, and micronutrient levels directly influence TET-dependent DNA demethylation in vivo.

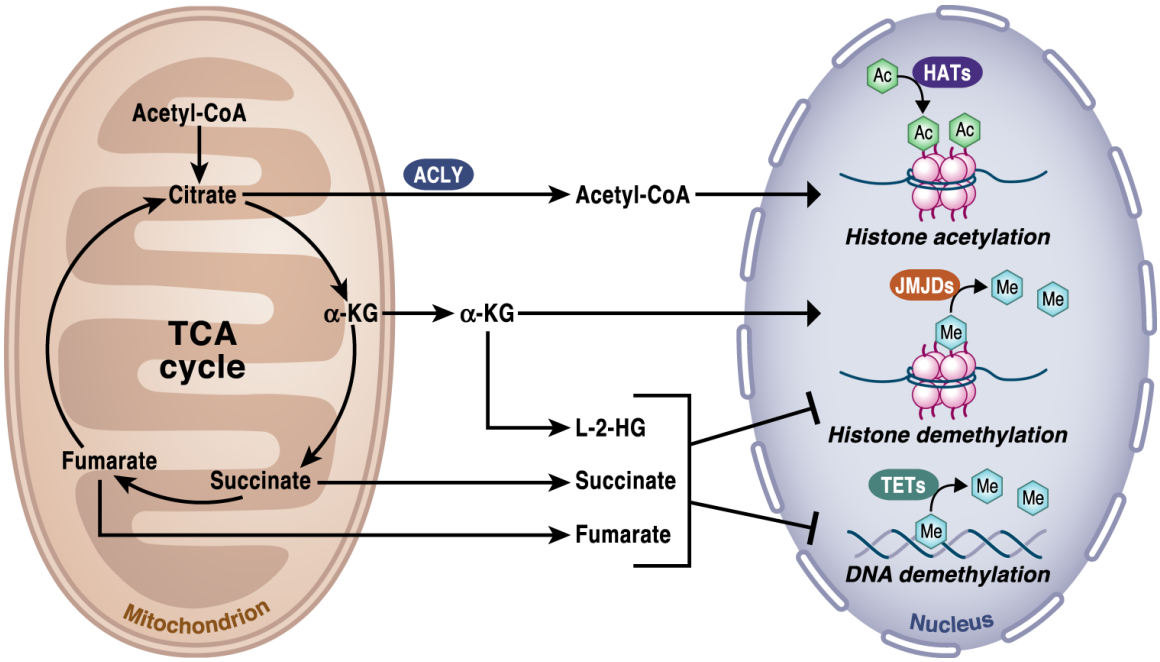

Figure 5. Metabolic regulation of epigenetic markers
The tricarboxylic acid (TCA) cycle produces key metabolites that regulate chromatin modifications and DNA methylation. Histone acetylation by histone acetyltransferases (HATs) relies on cytosolic acetyl-CoA, which is produced by ATP-citrate lyase (ACLY) from citrate exported from mitochondria. α-Ketoglutarate (α-KG) acts as an essential cofactor for 2-oxoglutarate–dependent dioxygenases (2-OGDDs), including JmjC-domain histone demethylases (JMJDs) and TET DNA demethylases. The reaction product, succinate, inhibits 2-OGDDs activity when it accumulates, thereby limiting demethylation. (PMID: 31900386)

This links metabolic inputs to methylation homeostasis and stem-cell.[46,50] Systemically, aging involves regulatory rewiring, remodeling of enhancer landscapes, changes in transcription factor networks, and widespread shifts in chromatin accessibility and DNA methylation that favor myeloid differentiation while reducing lymphoid priming.[47,48,49,44,45] Notably, single-cell atlases identify the strongest age-related accessibility within HSCs themselves, with partial resolution during differentiation. This positions the metabolic–chromatin interface at the top of hematopoietic hierarchies, where small metabolic shifts can durably imprint epigenetic states and, consequently, stem-cell function.[45,44,48,49]

Aim of the project

In my PhD project, we position our work at the intersection of metabolism, chromatin regulation, and hypoxia signaling in human HSPCs. Building on evidence that metabolite availability can influence chromatin accessibility and modify the functionality of aged HSPCs, we aim to determine whether targeted modulation of the metabolic pathway can restore a more functional regulatory state in aged HSPCs and improve stem cell performance. Consistent with this rationale, our results provide initial support for the idea that carefully shifting this metabolic balance can realign accessibility programs and stress responses to promote better function, thus motivating focused mechanistic and translational investigation of this axis. (**Manuscript 3)**

Additional work discussed in which I took part during this PhD:

1. **Molecular and phenotypic blueprint of the hematopoietic compartment reveals proliferation stress as a driver of age-associated human stem cell dysfunctions.**
   In this study, aging of human hematopoiesis is regarded as a quality issue rather than a quantity problem: primitive HSC numbers stay largely stable with age, but their differentiation accuracy and stress resistance decline. By combining population profiling, single-cell transcriptome and chromatin maps, and functional tests, the work connects activation-induced proliferative stress to key aging features, including increased inflammatory and replication-stress activity, DNA damage, and loss of multilineage clonogenic capacity. A targeted xenograft model shows that inducing early proliferation mimics old chromatin states and functional traits, offering a mechanistic link between clinical interventions and long-term graft success. These findings explain why older donors can engraft but often perform worse over time, and we suggest actionable strategies to preserve stemness and improve durable reconstitution in transplantation and gene therapy.
2. **A p38 MAPK-ROS axis fuels proliferation stress and DNA damage during CRISPR-Cas9 gene editing in hematopoietic stem and progenitor cells.**
   This work identifies a mechanistic bottleneck in clinical HSPC gene editing: the ex vivo activation needed for efficient CRISPR–Cas9 HDR triggers a p38 MAPK–driven, mitogenic ROS pathway that speeds up cell-cycle entry, causes proliferation stress, and increases DNA damage across HSPC subsets—ultimately impairing long-term function. By analyzing this pathway, the study demonstrates that controlling culture timing and temporarily inhibiting p38 can reduce stress responses, enrich transcriptionally defined HSCs, and enhance multilineage output and sustained engraftment after transplantation, while also highlighting trade-offs with HDR efficiency. These findings offer a practical framework to separate editing success from stem cell loss, aligning protocol design with the biology of HSC stress pathways and extending earlier connections between ROS–p38 signaling and HSC exhaustion to the specific area of therapeutic genome editing.

Results

Manuscript 1:

Paper accepted on 29/10/2025 on JEM

Molecular and phenotypic blueprint of the hematopoietic compartment reveals proliferation stress as a driver of age-associated human stem cell dysfunctions

Emanuele Lettera[1,2], Luca Basso-Ricci[1], Edoardo Carsana[1], Kety Giannetti[1], Teresa Tavella[1], Luca Seffin[1,2], Giacomo Farina[1,8], Nicolo Gualandi[1], Pamela Quaranta[1,2], Elena Lo Furno[1], Guido Pacini[1], Lucrezia della Volpe[1], Kerstin B. Kaufmann[3], Laura Garcia-Prat[3], Raisa Jofra Hernandez[1], Alex Murison[3], Alicia G. Aguilar-Navarro[4], Stefano Beretta[1], Anastasia Conti[1], Eugenia Flores- Figueroa[4], Marco Ometti[5], Ivan Merelli[1], Alessandro Aiuti[1,2,6], Stephanie Z. Xie[3#], Serena Scala[1#], and Raffaella Di Micco[1,7#§].

[1] San Raffaele Telethon Institute for Gene Therapy (SR-TIGET), IRCCS Ospedale San Raffaele, Milan, 20132 Italy.

[2] Università Vita-Salute San Raffaele, Milan, 20132, Italy

[3]Princess Margaret Cancer Centre, University Health Network, Toronto, Canada

[4]Unidad de Investigación Médica en Enfermedades Oncológicas, Centro Médico Nacional Siglo XXI, Instituto Mexicano del Seguro Social, Mexico City, Mexico

[5]Department of Orthopedic Surgery and Traumatology, IRCCS Ospedale San Raffaele, Milan, 20132 Italy.

[6] Pediatric Immunohematology and Bone Marrow Transplantation Unit, IRCCS San Raffaele Scientific Institute, Milan, 20132 Italy.

[7] University School of Advanced Studies IUSS, 27100 Pavia, Italy.

[8] Università degli Studi di Milano Bicocca, School of Medicine and Surgery, PhD program in Molecular and Translational Medicine (DIMET)

# These authors share senior authorship

§Corresponding author and lead contact: dimicco.raffaella@hsr.it

Abstract

Hematopoietic stem/progenitor cell (HSPC) aging has been associated with myeloid skewing, reduced clonal output, and impaired regenerative capacity, but quantitative immunophenotypic and functional analysis across human aging is lacking. Here, we provide a comprehensive phenotypic, transcriptional, and functional dissection of human hematopoiesis across the lifespan. Although primitive hematopoietic stem cell (HSC) numbers were stable during aging, overall cellularity was reduced, especially for erythroid and lymphoid lineages. Notably, HSPC from aged individuals had similar repopulating frequency of younger counterparts in primary and secondary xenografts; yet aged HSC displayed impaired differentiation capacity, changes in chromatin accessibility, dysregulation of cell cycle, inflammatory signatures, and a reduced capacity to counteract

activation-induced proliferative stress with concomitant accumulation of DNA damage and senescence-like features upon xenotransplantation. This age-associated phenotypic and functional decline was recapitulated by enforcing proliferative stress *in vivo* on cord blood (CB) HSPC. Overall, our work sheds light on dysregulated responses to activation-induced proliferation underlying HSPC aging and establishes CB xenotransplantation-based models as suitable for studying age-associated hematopoietic defects.

Introduction

Age-associated changes in the hematopoietic stem and progenitor cell (HSPC) compartment have been extensively unveiled in mice, where a marked myeloid skewing, impaired lymphoid and erythroid potential, and a decreased clonal output of hematopoietic stem cells (HSC) have been reported upon aging[1–3]. Mechanistically, changes in metabolic pathways, compromised maintenance of genome integrity, and epigenetic dysregulation have been linked to rapid exhaustion of the aging stem cell pool and impaired regeneration properties[4–10]. It has also been proposed that the most primitive HSC are predominantly in a quiescent state and may divide only a few times in the lifetime of a mouse[11,12] to minimize DNA replication-associated mutations, and ultimately stem cell exhaustion. In agreement with this, the proliferative history of HSC has emerged as an important contributor to the dysfunctional output of aged HSC[13–16]. Additionally, upon exposure to mitogenic stimuli, murine aged HSC display elevated levels of DNA replication stress associated with cell cycle defects and chromosome gaps or breaks[16,17]. Moreover, as transplantation itself imposes a strong proliferative stress on repopulating HSC, old murine HSC were shown to display a significant reduction in long-term repopulating potential compared to young HSC as well as decreased homing and engraftment capacity upon transplantation[7,18]. To date, it remains unclear to what degree these phenotypic observations on stem cell pool and lineage outputs in mouse settings as well as the underlying molecular principles are conserved during human hematopoietic aging. The functional decline of the lymphoid compartment, responsible for a defective adaptive immunity in old age, and the increased incidence of myeloproliferative disorders and hematopoietic myeloid malignancies in aged individuals[19–23] led to the common interpretation that, likewise in mice, human HSPC aging is associated with a prominent myeloid skewing[24–26]. Moreover, there is evidence in humans that aging is associated with anemia[27] and clonal hematopoiesis[20] (CH) which may act as additional cofactors in the development of myelodysplasia and hematopoietic malignancies[28,29]. Recent transcriptomic analyses of steady-state circulating HSPC (cHSPC) in the peripheral blood (PB) of healthy adults have revealed age-associated alterations in cHSPC composition. These changes are characterized by a shift toward myeloid-biased differentiation and a modest reduction in transcriptionally defined common lymphoid progenitors. These age-related shifts are further associated with CH and an increased risk of developing myelodysplastic syndromes [30].

However, we and others have shown that bone marrow (BM) and PB HSPC compartments differ in their phenotypic, transcriptomic and functional properties under physiological conditions[31,32]. Thus, it remains of paramount importance to investigate the impact of aging of HSPC residing within the BM niche. A growing body of literature has uncovered the functional and molecular heterogeneity of human HSC throughout life to maintain a constant blood supply under homeostatic steady-state conditions[33–39]. Significant efforts led to the identification of surface markers and gene signatures to unambiguously define the subset of purified HSC responsible for long-term outcomes upon transplantation[35,38,40–43] and subsequent molecular studies performed in the context of aging had a clear focus on this primitive and rare cell subset. For instance, analysis of proliferation rate in highly purified HSC has revealed altered responses of aged cells to mitogenic stimuli potentially contributing to hematopoietic dysfunctions upon transplant[44,45]. However, it is worth noting that in several therapeutic applications for non-malignant and malignant hematological diseases, a sizable fraction of a heterogenous population of progenitors and long-term HSC needs to be harvested, cultured *ex-vivo* with early-acting cytokines and reinfused in patients to maximize engraftment in the early-phases post-transplant. Furthermore, in the transplantation setting, increasing donor age correlates with higher transplant-related mortality and reduced immune reconstitution[46–48] while younger donor transplant results in a better long-term outcome with reduced graft-versus-host- disease and increased disease-free survival[49,50]. Thus, characterizing the cellular and molecular landscape of the mature and HSPC compartment at steady-state and understanding the functional impact of aging on HSPC function during *ex-vivo* activation and upon transplantation has the potential to contribute to improving the application of HSPC-based therapies to the elderly.

Here, we report the results of a comprehensive quantitative characterization of blood cell subpopulations in bone marrow and peripheral blood from a large healthy donor cohort across the human lifetime, providing the first comparative analysis of immunophenotypic proportion *vs.* cellular numbers of BM lineages. We combined advanced genomics and *in vivo* primary and secondary transplantation assays to interrogate the functional contribution of proliferative stress to age-related changes in hematopoietic output and stem cell fitness. Overall, our work provides a blueprint of the HSPC compartment upon aging and establishes

a relevant transplantation-based model of neonatal HSPC for future studies to further untangle the complex molecular programs underlying human hematopoietic aging and aging-associated diseases.

Results

A global reduction in lymphoid output and a steady hematopoietic stem cell content in bone marrow during physiological aging.

To dissect the changes in hematopoietic cell composition during aging we first analyzed 73 BM samples from pediatric (0 to 18 years old, n=9), young adults (18 to 30 years old, n= 13), middle-aged (40 to 60 years old, n= 20), and old (>65 years old, n=31) healthy individuals. As an additional and complementary dataset, we collected 56 PB samples from 12 pediatric, 17 young, 8 middle-aged, and 19 old subjects (Supplemental Data Table S1). All the samples were analyzed by our validated multi-parametric flow cytometry protocol[51] which allows us to unambiguously identify and quantify 25 different hematopoietic subsets, including 10 distinct HSPC subpopulations (See Supplementary Figure 1 for gating strategy). By means of this analysis, we found a significant decrease in bone marrow cellularity and in the frequency of the HSPC compartment during aging (Supplementary Figure 1B and Figure 1A). Myeloid compartment remained stable over aging, since we did not observe any correlations between donors' age and monocytes, immature granulocytes (iPMN), mature granulocytes (PMN) and myeloblasts cell counts, with the only exception of dendritic cells (DC), whose number decreased over time (Figure 1B-D and Supplemental Figure 1C-D). We also found a gradual decrease of lymphocyte progenitor (Pro-lympho, Supplementary Figure 1E) and B cell count during aging, while a dramatic drop of B cell Precursors (PreB) and B cell Progenitors (ProB) was observed as early as 30 years of age (Figure 1E-G). BM-resident NK cells showed a slight reduction over aging, while NKt lymphocytes increased during aged hematopoiesis (Supplementary Figure 1F-G). Similar changes in mature hematopoietic cell composition were also detected in the PB of the analyzed subjects, with marked reduction mainly in the absolute count of B, NK, and T lymphocytes (Supplementary Figure 2A-G). Our analyses also revealed a decline in the number of erythroblasts and pro-erythroblasts with age (Figure 1H and Supplementary Figure 1H), in line with the severe anemia reported in

elderly subjects[27].

We next evaluated the changes occurring within the most undifferentiated hematopoietic compartment and found reduced cell counts of both CD34+ cells as well as of CD34+LIN- cells (defining the HSPC population) (Figure 1I and Supplementary Figure 1I). Of note, the number of primitive HSC and MPP subsets was stable during aging (Figure 1J-K), while a prominent decline was observed in lymphoid- (MLP and PreB/NK), myeloid- (CMP, GMP) and erythroid (EP and MEP) committed progenitors, except for early T progenitors (ETP) and megakaryocyte progenitors (MKp) which remained stable over aging (Figure 1L and Supplementary Figure 2H-N). To evaluate the impact of CH on the observed immunophenotypic changes we sequenced via whole exome sequencing, 8/31 aged BM samples in the old cohort for whom material was available and detected CH-associated mutations in *DNMT3A/KRAS*, *KDM6A* and *ATM* genes in 3/8 donors with a VAF <0.2. Nevertheless, the hematopoietic cell counts of the subjects with CH-mutations were consistent with the counts measured in individuals with no CH (Supplementary Figure 2O-T).

To exclude any potential geographic or collection bias that might account for the observed changes among donors of different age groups, we validated our findings in a North American cohort of 13 donors (age range 21-83y). By comparing HSPC subpopulation frequencies, we found consistent changes in HSPC subsets between the two cohorts of healthy subjects (Supplementary Figure 3A-I). Of note, we observed an increased frequency of primitive subpopulations within the HSPC compartment during aging (Supplementary Figure 3A-B), in line with previous reports[52], while the frequency of long-term HSC (LT-HSC defined as CD34+CD19-CD38-CD45RA- CD90+CD49f+ cells) remained stable across ages (Supplementary Figure 3I).

Altogether, our data indicate that, despite the stable HSC and MPP cell counts, lineage- committed HSPC progenitors and the overall BM cellularity are severely reduced over aging. This latter observation is the result of a sharp reduction of the lymphoid cell production (especially in the B cell compartment), while myeloid cell counts remained steady through aging.

Human HSPC repopulating potential in xenotransplantation assays is comparable across age.

The study of aging in human HSC using *in vivo* functional assays is limited, but the

evidencesuggests that the functional decline of human primitive HSC upon aging is more complex than reported in animal studies[44,45,52–55]. Although we cannot assay the functional activity of human HSC *in vivo* in the bone marrow during steady-state hematopoiesis, transplantation into immunodeficient mice allows us to measure the hematopoietic reconstitution potential across aging under the same genetic microenvironment, thus reducing the variability related to extrinsic factors. We undertook a comprehensive limiting dilution xenotransplantation study to quantitatively measure HSPC engraftment of young (21-32y, n=5), middle-aged (52-57y, n=3), and old (78-83y, n=5) BM CD34+ cells relative to the neonatal CB-derived CD34+ cells using 314 immunodeficient non-obese diabetic (NOD)-severe combined immunodeficiency (SCID)-IL2Rg-/- (NSG) mice (Figure 2A). Three cell doses (60,000, 10,000, and 1,000 cells) were selected based on a prior study to measure CB functional HSC frequency[43]. Human CD45 engraftment levels were measured at 4-, 12-, and 20-weeks post-transplantation and used to calculate the 1/CD34+ repopulating cell frequency in all four sources of human HSPC (Figure 2B-E, Supplemental Data Table S2, Supplementary Figure 3J-K). As expected, CB repopulating cell frequency was superior to BM sources, although this was not statistically significant for middle-aged and old BM HSPC at 12 weeks[56] (Figure 2B, Supplementary Figure 3J). CD34+ repopulating cell frequency kinetics was found to undergo dynamic changes across time with BM sources peaking at 12 weeks and dropping to the lowest frequency at 20 weeks. By contrast, the stem cell frequency for CB was highest at 20 weeks[43] (1/504 CD34+ cells, Figure 2B, Supplementary Figure 3J). Surprisingly, middle-age and old BM HSPC had a significantly higher CD34+ repopulating cell frequency at 12 weeks and showed superior engraftment relative to young BM HSPC at the 60,000 cell dose for all timepoints (Figure 2C-E). Additionally, at 4 weeks human cell grafts contained lower B cells but a higher fraction of myeloid cells in all the mice transplanted with BM-CD34+ cells with respect to CB, independently from the age of the BM donors likely reflecting a distinct proportion of repopulating hematopoietic progenitors in the two cell sources (Supplementary Figure 3L-M). To account for the differences in HSC+MPP frequency in old vs. young HSPC (Figure 1, Supplementary Figures 1-3), we normalized the human content in the BM of transplanted mice for the number of infused HSC+MPP in young, middle-age and old experimental groups (Figure 2F-H). This analysis revealed that while CB engraftment remained overall higher when compared to adult BM sources, young, middle-age and old HSPC were endowed with similar engraftment capacity at all the experimental time

points and across cell doses (Figure 2F-H).

Additionally, to further assess the self-renewal capacity of long-term HSC from old vs. young donors *in vivo,* we performed secondary transplants into immune-deficient mice (Figure 2I). We transplanted CD34+ cells from young (n=3) or old (n=3) donors in 23 NSG mice (each donor into 3-4 mice). At 12 weeks post-transplant, we collected human CD45+ cells from the BM of primary recipients and performed secondary transplants into 23 NSG mice. The BM of secondary recipients was analyzed after 12 weeks, and data normalized on HSC+MPP content in the infused HSPC were reported. Strikingly, we found no differences in the human cell engraftment both in primary and secondary recipients when transplanting young and old HSPC (Figure 2J). Similar lineage output was also observed *in vivo* (Supplementary Figure 3N). However, through comet assay, we measured higher presence of both single- and double-stranded DNA breaks in old vs. young HSPC isolated from secondary transplanted mice, implying that old LT-HSC have reduced capability of counteracting DNA damage imposed by xenotransplantation (Figure 2K-L).

Overall, these data indicate that human aged HSC have a similar *in vivo* long-term repopulating capacity but increased sensitivity to transplantation stress than their young counterparts.

Aged LT-HSC have reduced differentiation potential associated with transcriptomic and chromatin accessibility alterations.

Given the reduced support to human myeloid and erythroid production of NSG mice and the restriction to the B cell lymphoid output in the human graft, we investigated the differentiation capacity of human CD34+ cells as well as sorted LT-HSC from young and old donors in an optimize *in vitro* stroma-free multi-lineage assay, allowing the differentiation toward diverse lymphoid, myeloid, erythroid and megakaryocyte lineages (Figure 3A, Supplementary Figure 4A)[32,57]. Whereas bulk CD34+ cells mainly produced erythroid cells due to the presence of committed progenitors, the hematopoietic output of sorted HSC was more evenly distributing among erythroid, lymphoid and myeloid cells in line with the enrichment for a subset endowed with higher multi-lineage differentiation capacity (Supplementary Figure 4B). Of note, both bulk CD34+ cells and HSC from young and old donors display similar differentiation output in culture (Supplementary Figure 4B). To ultimately dissect the effect of ageing on the differentiation potential of individual LT-HSC, we also performed an *in vitro* differentiation assay on single, individual HSC, stained with CD49f marker for index sorting

analyses. We found that in this setting the differentiation efficiency of both CD49f+ and CD49f- aged HSC was lower with respect to the young counterparts (Figure 3B-C). Moreover, by scoring the differentiation output of the single colonies, we found an overall decrease of Lymphoid-only or Myeloid-lympho clonal outputs in aged HSC, while the proportion of lymphoid-erythroid colonies was increased (Supplementary Figure 4C-D). Additionally, we detected uni-myeloid colonies only in old HSC, albeit at low frequency. The same trends were also observed when dissecting LT-HSC according to the expression of CD49f surface marker (Figure 3D-E). Of note, we measured an increased fraction of clones showing multi-lineage production in young vs. old LT-HSC (6.52% vs. 1.54%), suggesting a reduced differentiation potential of individual aged LT-HSC and an increased primitiveness of young LT-HSC. Along this line, we did not detect any differences in the number of cells produced by old and young LT-HSC clones, except for a trend of higher cellularity in young vs. old multi- lineage LT-HSC clones (Supplementary Figure 4E).

To understand the molecular underpinnings for the distinct differentiation capacity of aged human HSC relative to young HSC, we generated a single-cell RNAseq (scRNAseq) dataset by integrating previously published scRNAseq data from sorted HSPC from young and old donors[31,32,58–60]. To avoid batch- and donor-related effect, data were harmonized after integration (Supplementary Data Table S3). The final dataset encompassed 134,184 HSPC (89,884 from 17 young donors, 44,300 from 7 old donors). Unsupervised clustering partitioned the full dataset in 21 clusters. By comparing cluster transcriptional profiles with published reference datasets[32] and according to the expression of HSPC marker genes, we identified immature (HSC/MPP, cycling- HSC, Myeloid/Lymphoid-CMP, MEP), myeloid (CMP, CMP-GMP; Granulocyte progenitors, GP; Mono-dendritic Progenitors, MDP), lymphoid (clusters MLP, PreB and PreNK), megakaryocytic, erythroid (Immature and mature erythroid progenitors) and basophil/eosinophil/mast (BEM) cell transcriptional clusters (Figure 3F). By analyzing the distribution across clusters of young and old HSPC, we observed that old HSPC were enriched in clusters with HSC/MPP and erythroid progenitor transcriptional commitment, while young HSPC displayed an increased proportion of lymphoid progenitors in line with the immunophenotypic analyses (Figure 3G). To focus on LT- HSC, the HSC/MPP cluster was further partitioned into 4 subclusters and differential expression (DE) analysis among them allowed the identification of LT-HSC, MPP, Myelo/lympho-MPP; Myelo/Ery-MPP (Figure 3H). Of note, the composition of the HSC/MPP cluster was similar between young and

old subject, with a comparable proportion of cells belonging to LT-HSC cluster, in line with the stable frequencies of CD49f+ cells across aging measured through immunophenotypic analyses (Supplementary Figure 3I). DE analyses between young and old HSC/MPP and LT-HSC revealed increased expression of genes associated to activation (*CD69, RGS2*), inflammation (*NR4A1, NR4A2, IL1B*) and response to stress and DNA damage (*TIPIN, DDIT4, HSPB1*) in old HSPC subsets, while young HSC showed higher expression of genes involved into metabolism (*RNASEK, ALDOA*), differentiation (*CEBP*), cell cycle (*EIF4A1*) and self-renewal (*MAFF, AVP*) (Figure 3I). Consistently, LT-HSC from young donors display increased expression of gene modules associated to stemness[61–69] (Figure 3J). Moreover, we found deregulated expression of genes involved in DNA replication stress response, fork stability and replication origin control[70,71] in aged HSPC and LT-HSC, potentially contributing to the observed accumulation of DNA damage in aged cells retrieved upon secondary transplantation (Figure 3K).

To further corroborate these findings, we interrogated the chromatin accessibility landscape of HSPC subpopulations isolated from young and old subjects by ATAC-seq. We found 6 signatures by non-negative matrix factorization (NMF) within 31 HSPC samples, belonging to the distinct HSPC subpopulations (young: 3 donors, 21-28y, n=16; old: 4 donors, 52-79y, n=15; Supplemental Data Table S4, Supplementary Figure 4F). When we assessed the strength of all 6 signatures in young and old CD49f + primitive HSC samples, signature 1 was significantly enriched in old HSC, whilst signature 2 was enriched in young HSC (Supplementary Figure 4G). Transcription factor motif analysis within these two signatures yielded three clusters: shared motifs, motifs enriched in young CD49+ primitive-HSC, and motifs enriched in old CD49+ primitive-HSC (Supplementary Figure 4H and Supplemental Data Table S5 with enrichment data for all motifs identified). Among the shared motifs are well-known HSC regulators including ERG, FLI1, and ETV2[72–74]. Importantly, motifs that are accessible in young CD49+ primitive-HSC are associated with cell cycle regulation (E2F)[75] and hematopoietic lineage decisions (BCL11a and PU.1)[76] (Supplementary Figure 4I). In contrast, inflammation response motifs (NFKB and AP1) were enriched in old CD49+ primitive-HSC (Supplementary Figure 4J), in line with transcriptomic data. Additionally, we found that accessibility of HOXB4 motifs, a factor shown to potently expand HSC[77,78] was enriched in old HSC (Supplementary Figure 4J). Strikingly, genes involved in these pathways were also found differentially expressed in young and old LT-HSC at transcriptomic level

(Supplementary Figure 4K).

Together, our data suggest that despite a similar repopulating capacity in xenotransplantation experiments, aged BM HSC show reduced differentiation proficiency with chromatin and transcriptomic alterations in cell cycle, inflammation, and self-renewal factors compared to younger counterparts, and prompted us to investigate the biological and functional response of aged HSPC to activation and proliferative stimuli.

Human aged HSPC show altered proliferation kinetics and impaired clonogenic efficiency upon *ex-vivo* activation.

We exploited the generated scRNAseq data to infer the cell cycle state of HSPC, HSC/MPP and LT-HSC from young and old donors at steady state (Figure 4A). Specifically, we estimated the cell cycle stage based on the cell-cycle marker genes (see also Methods section). This classification was further refined computing cell-wise module cores based on sets of genes that positively or negatively regulate dormancy (as previously shown in Quaranta et al. [32]), allowing classification of G0-cells within G1-cells showing a highly dormient transcriptomic profile. This analysis revealed that a small fraction (5-10%) of cells within HSPC display transcriptional signature associated to G0 phase, which increases moving from HSPC HSC/MPP LT-HSC, validating our G0 classification. Moreover, old HSPC, HSC/MPP and LT-HSC are more quiescent with respect to their young counterparts (Figure 4A). We next interrogated the responses of young and old HSPC to a cocktail of human recombinant cytokines and growth factors, including Fms-related tyrosine kinase 3 (Flt3), Stem cell factor (SCF), thrombopoietin (TPO) and IL-3, previously reported to promote proliferation of HSPC without inducing major differentiation[79–81] and currently representing the gold-standard for HSPC-based gene therapy and transplantation-based clinical applications[82,83]. Specifically, we stimulated BM CD34$^+$ cells isolated from young (<35 years old, n=6) and old (>60 years old, n=6) subjects and analyzed their transcriptional profiles, proliferation rates, and clonogenic potential (Figure 4B). Global gene expression analyses identified 1269 statistically significant differentially expressed genes (DEGs) (FDR < 0.05) in CD34+ cells from old subjects compared to their younger counterparts after an overnight activation, of which 529 were upregulated and 740 were downregulated, (Supplementary Figure 5A, Supplemental Data Table S6). Gene set enrichment analysis (GSEA) against hallmark gene sets from Reactome Database revealed upregulation of genes associated to Cell cycle (*RAD17, CDK7, BUB3, CENPN*), Inflammation (*IFIT1, IFIT3, IFIT5, STAT2, OAS2,*

ISG15, ISG20, SMAD3, BIRC3, TRIM22, CDC23), Chromatin conformation and Gene expression regulation (*H3-3B, TAF9, HAT1, ELP5, KAT7, SLU7, H2AC6, JUN*), and Protein Translation and localization (*RARS2, EIF4B, WARS1, PEX19, SARS1, TIMM10B, MRPS16*) categories in activated old CD34+ cells with concomitant downregulation of genes belonging to Hematopoiesis (*AVP, PTGIR, OR2V2, ADCY9, GNAZ, GNB2, GRK2, HRH2, GPR176, ASH2L*) and Cellular organization and Transport categories (*SERPINA1, COPB2, ARCN1, SEC23IP, SCFD1, COPB1, CAPZA1*) (Figure 4C and Supplementary Figure 5B). Growth curve analysis showed that aged HSPC displayed a higher proliferation rate, mainly at early time points post-activation. Moreover, in line with the cell cycle state measured in old and young HSPC at steady state in our scRNAseq, old HSPC display reduced ki67+ cells before culture, but higher percentage of proliferating cells post-activation as compared to younger counterparts (Figure 4D-E), suggesting a faster exit from quiescence. To better elucidate whether the earlier activation of old compared to young HSPC can be captured in the subset enriched for the most primitive HSPC, we analyzed cell division kinetics with Cell trace(CT), a fluorescent cytoplasm- binding molecule that allows tracing multiple generations on the basis of dye dilution, on sorted HSC/MPP (defined as LIN-CD34+CD38-CD45RA- cells), and more committed subsets including myeloid, erythroid and megakaryocytes progenitors (defined as LIN+CD34+CD38+CD10-CD7- cells) (Figure 4F). Total CD34+ cells and sorted HSC enriched subsets from both young and old subjects were labelled with CT dye and cultured for 96h to monitor their proliferation rate over time (Figure 4F and Supplementary Figure 5C-D). A higher percentage of total CD34+ cells as well as of HSC/MPP and committed subsets isolated from old donors completed one or more cell divisions at earlier time points in comparison to younger counterparts. These early differences in proliferation rate diminished over time with a similar profile of cell divisions observed at later time-points between young and aged HSPC subsets (Figure 4F). We next evaluated the clonogenic potential of young and aged CD34+ progenitor cells and found that while early upon activation there was a comparable number of colonies, a significant reduction in aged-HSPC derived colonies was observed at later time points (Figure 4G).

Taken together, these data suggest that, after *ex-vivo* activation, aged HSPC showed a faster exit from quiescence resulting in altered proliferation rates, characterized by transcriptional changes in cell cycle-related and inflammatory gene categories that may ultimately contribute to reduced clonogenicity upon prolonged time in culture.

Activated aged HSPC retain differentiation potential but display impaired long-term fitness after *in vivo* transplantation.

To assess the hematopoietic output of pre-activated aged HSPC *in vivo*, we next transplanted at high doses (see Methods) overnight cultured CD34+ cells derived from young (n=4) and old (n=4) donors into immunodeficient NSG mice and compared their human hematopoietic engraftment and blood lineages reconstitution over time (Figure 5A). Upon transplantation, we found no significant differences in the kinetics and the frequency of human CD45+ hematopoietic cells in peripheral blood (Figure 5B). Instead, we observed a reduced human graft in the BM of mice transplanted with CD34+ cells isolated from aged donors at 20 weeks post-transplant (Figure 5B, Supplementary Figure 6A). Of note, mice transplanted with old CD34+ cells showed a statistically significant reduction in both myeloid and B cell output accompanied by a relative increase of T cell content (CD3+) in the peripheral blood at the time of euthanasia (Figure 5C-E). These changes in the lymphoid compartment were also observed in the spleen of the mice transplanted with old CD34+ cells (Figure 5D-E). We also confirmed by quantitative analyses a reduced B cell output both in PB and in BM from mice belonging to the old group accompanied by a reduction of the overall HSPC content at 20 weeks (Supplementary Figure 6B-C). In line with the differences in HSPC composition observed in old compared to young subjects at steady state (Supplementary Figure 3A-I), we found an increased frequency of LIN-CD34+CD38- cells and a reduced lymphoid progenitor contribution in the human HSPC engrafted in the BM of the mice transplanted with old CD34+ cells (Supplementary Figure 6D-E). In contrast, absolute quantification of distinct HSPC subsets in the BM of the two groups of transplanted mice unveiled a reduced amount of primitive but not of more committed HSPC progenitors in the old group (Supplementary Figure 6F). Moreover, CD34+ cells retrieved at the endpoint of mice transplanted with old CD34+ cells showed reduced clonogenic potential with respect to their younger counterparts when rechallenged in colony assays (Figure 5F). Interestingly, gene expression analyses on CD34+ cells isolated at sacrifice from transplanted mice belonging to the old group showed increased levels of cell cycle inhibitor *p21* and several pro-inflammatory cytokines (including *IL6*, *IL8*, *IL1*, *MCP1*, and *TNF*) compared to younger counterparts (Figure 5G-L), together with the accumulation of DNA double-strand breaks (DSB), detected through the phosphorylation of histone H2A.X (H2AX) (Figure 5M). These data suggest that, although pre-activated aged HSPC reconstitute all main blood cell lineages (myeloid, T, and B cells) shortly upon transplantation, they are likely unable to

counteract transplant-related proliferation stress resulting in detrimental cellular responses that impair their functionality in the long-term.

Establishing an *in vivo* model of proliferation stress by low cell dose transplantation.

To study the impact of proliferative stress on hematopoietic reconstitution *in vivo,* we hypothesized that, when transplanted in limited numbers, HSPC may undergo an increased number of cell divisions to repopulate the bone marrow than when transplanted in higher amounts[43]. We therefore transplanted overnight cultured neonatal CB-derived HSPC at different cell doses in sub- lethally irradiated immune-compromised mice and tested their repopulating capacity and blood lineage reconstitution at early (6 weeks) and late (20 weeks) phases after transplantation. We designed three experimental groups: a high-dose group ($5x10^4$ CD34+ cells), an intermediate-dose group ($1x10^4$ CD34+ cells), and a low-dose group ($3x10^3$ CD34+ cells) (Figure 6A). Concomitantly, to validate that low engraftment in transplantation experiments associates with a higher proliferation rate of the infused cells, we combined cell number measurements with a previously established short-timescale dual pulse labelling method[84] that allows us to quantify the number of cells entering S-phase per hour. Specifically, before euthanasia, NSG mice were subjected to an initial intravenous EdU pulse (2 hours) followed by a second intravenous injection of BrdU. By measuring the cells positive for one or both markers we estimated the number of cells in active proliferation at early and late phases after transplantation.

To assess the effect of proliferation stress on the engraftment, we further stratified our transplanted mice according to their engraftment in the bone marrow (Figure 6B; low-engrafted:<10% of hCD45+ cells; middle-engrafted: 10-50% of hCD45+ cells; high-engrafted: >50% of hCD45+ cells). Interestingly, we observed that low-engrafted mice displayed a phenotype of hematopoietic reconstitution like that observed after transplantation of old CD34+ cells in NSG mice. Indeed, we found slightly increased myeloid output at 6 weeks in the PB of low-engrafted mice and reduced B cell production with a tendency of increased T cell output (4 out of 9 mice) in the PB at 20 weeks (Figure 6C). At the same time point, low-engrafted mice showed a significant decrease in the percentage of human HSPC in the BM, with an expansion of more primitive cells (defined as LIN-CD34+CD38-) and a concomitant decrease in the percentage of B lymphoid progenitors (PreB/NK), a phenotype also observed in mice transplanted with old CD34+ cells (Figure 6D-E and Supplementary Figure 7A).

Moreover, the evaluation of EdU and BrdU uptake revealed a statistically significant negative correlation between the percentage of HSPC entering in S phase per hour (defined as EdU-BrdU+ cells)[84] or total proliferating HSPC (EdU-BrdU+, EdU+BrdU+, and EdU+BrdU- cells) and the human graft in the BM at 6 weeks and 20 weeks post-transplantation (Figure 6F-G and Supplementary Figure 7B-C). These data imply that low cell engraftment is associated with increased HSPCs proliferation both at 6- and 20-weeks post transplantation. In addition, we also observed a higher T cell proliferation in low-engrafting mice, suggesting that the increased T cell frequencies observed at 20 weeks was likely due to mature T cell proliferation in the PB rather than *de novo* T cell production (Supplementary Figure 7D).

We reasoned that the increased proliferation rate imposed by low-cell transplantation could lead to premature exhaustion of HSPC, thus recapitulating the defects observed upon activation in transplanted aged HSPC. Strikingly, when plated at the same number, we found a reduced clonogenic capacity of CD34+ cells retrieved at the time of euthanasia (20 weeks post- transplantation) from the BM of low-engrafted mice with respect to middle/high-engrafted mice (Figure 6H). Moreover, CD34+ cells isolated from mice transplanted with low cell doses displayed a significant increase in expression levels of senescence-associated cell cycle inhibitors *p16* and *p21* (Figure 6I-J) as well as in inflammatory genes *IL1-β*, *MCP-1*, and *TNF-α* (Supplementary Figure 7E-G). The proliferative stress imposed by the low-cell dose was associated also with the higher presence of both single- and double-stranded DNA breaks, measured through comet assay[85] (Supplementary Figure 7H-I). On the same line, CD34+ cells isolated from low-engrafting mice showed a statistically significant increased frequency of pRPA-positive cells (Figure 6K), a well- established marker of DNA replicative stress[86] which inversely correlated with the engraftment levels in the bone marrow (Supplementary Figure 7J). Next, we profiled the chromatin state by ATAC-seq of human CD34+ cells retrieved from mice transplanted with the low and high cell input of CB-derived HSPC and we evaluated Differentially Accessible Regions (DARs) belonging to the signature 1 (enriched in old HSC) and 2 (enriched in young HSC) from the ATACseq analyses shown in Supplementary Figure 4. We found an enrichment of DARs belonging mainly to the regions associated with the "Young" signature (3679 versus 1806) in the High-engrafted mice, while the Low-engrafted mice display enrichment of regions associated to the "Old" signature (2697 versus 3167) (Figure 6L). Analyses of shared transcription factor (TF) binding site motifs between High- and Low-engrafted mice revealed differential enrichment of AP-1 and RUNX1 motifs in Low-

engrafted mice, while High-engrafted mice showed enrichment of ETS/PU.1 motifs, consistently with the old and young signature from the ATACseq data on human HSPC subpopulations (Figure 6M). These analyses imply that our low cell input model recapitulates the chromatin state of aged HSPC. Finally, by analyzing the Top-20 unique TF motifs for Low- and High-engrafted mice we found that HSPC from low-engrafted mice display enrichment in TF binding site associated to myeloid/erythroid specification and oxidative stress, while TF binding site motifs from mice transplanted with high cell dose are mainly associated to lymphoid differentiation and HSC self-renewal (Supplementary Figure 7K).

Taken together, these findings indicate that the proliferative burst imposed by low cell transplantation in human HSPC recapitulates age-associated phenotypic, functional and chromatin changes of human hematopoiesis and leads to the activation of detrimental cellular responses characterized by DNA damage accumulation and inflammatory programs, ultimately leading to altered hematopoietic output and premature exhaustion of the HSPC compartment.

Discussion

Here, we provide a comprehensive quantitative characterization of the phenotypic and molecular changes occurring during hematopoietic aging in a cohort of 73 healthy donors, comprising PB and BM collected from pediatric as well as young, middle-aged, and old subjects. By virtue of quantitative measurements of the overall hematopoietic system, we found that human hematopoiesis in the elderly at steady state is characterized by an overall reduction of differentiated cell production, primarily impacting lymphoid and erythroid lineages, accompanied by a generally stable myeloid output with a significant decrease in dendritic cell populations. Thus, we conclude that the reported myeloid skewing observed in previous works[52] may primarily result from a reduction in lymphoid and erythroid lineages, rather than from an actual enhancement in myeloid output, despite having a comparable number of human HSC and MPPs throughout life.

To gain deeper insights into the biological and functional characteristics of individual LT- HSC in young and aged individuals, we employed a dual approach combining scRNA-seq datasets with a functional multilineage differentiation assay. Of note, although LT-HSCs from aged and young donors showed similar behavior when plated as a pool, single-cell plating revealed that LT- HSCs from aged donors exhibited a marked reduction in differentiation

efficiency compared to their younger counterparts. Specifically, aged LT-HSC generated fewer multilineage colonies *in vitro* and showed a pronounced skewing toward erythroid and myeloid outputs, suggesting an age- associated impairment in balanced lineage commitment. These differentiation defects in aged LT- HSC were in line with the transcriptional changes detected through scRNA-seq analysis, including decreased expression of key genes involved in stem cell self-renewal, maintenance of stemness, and balanced myeloid-lymphoid differentiation. These findings point to a progressive erosion of transcriptional programs that sustain multipotency and long-term self-renewal with age. Interestingly, despite their impaired differentiation profile in vitro, aged and young HSPC exhibited comparable repopulating frequencies *in vivo*, indicating that aged LT-HSC, when transplanted as a pool of CD34+ cells, retain the capacity to engraft and contribute to hematopoiesis under transplant conditions. These differential outcomes might result from: i) inherent limitations of current xenotransplantation models for faithfully capturing subtle age-related changes in human HSC differentiation potential, especially towards the myeloid, erythroid and megakaryocyte lineages; ii) a bystander effect of supportive MPP and progenitor cells present in bulk CD34+ cells used to perform *in vivo* experiments studies that might have contributed to the observed hematopoietic reconstitution. Still, our *in vivo* functional studies provide significant and novel insight on the biological properties of aged HSC. Indeed, we observed LT-HSC from aged donors retrieved from recipient animals showed increased levels of DNA damage, aligning with the deregulation of DNA replication stress response and LT-HSC activation genes observed in our scRNA-seq datasets. These data imply that while aged HSPC can still functionally repopulate the host, they may do so under a state of elevated cellular stress and risk for genomic instability. Importantly, although overall human cell chimerism was similar between young and aged transplantation conditions, we cannot exclude the possibility that the clonal architecture of hematopoiesis differs significantly. Specifically, grafts derived from aged LT-HSC may exhibit reduced clonal diversity or increased clonal dominance, as recently demonstrated in human transplantation studies[87], potentially reflecting a diminished pool of truly multipotent stem cells with aging. Future studies using barcoding strategies will provide definitive answers on the clonal output of aged HSPC. Interestingly, although our sample size was limited, the immunophenotypic profiles we observed did not appear to be influenced by the clonal hematopoiesis (CH) mutations identified through exome sequencing. These mutations were infrequent and exhibited low

variant allele frequencies (VAFs), suggesting a minimal impact on the observed cellular phenotypes. Therefore, it is unlikely that CH-related mutations in these or other donors are responsible for driving phenotypic alterations in the aged hematopoietic compartment.

Using a novel inflammation-recovery xenotransplantation model some of us recently discovered an inflammatory memory in LT-HSC (HSC-iM) subset that is equivalent to a subset of HSC found in the bone marrow of old adults[94]. HSC-iM retain transcriptional and epigenetic memory of prior inflammation concordant with signatures associated with T cell memory and inflammatory memory in epithelial stem cells (e.g. AP-1 transcriptional and epigenetic upregulation). Accordingly, many of the top motifs enriched in the chromatin accessibility signature from aged *vs*. young immunophenotypic CD49f+ primitive HSC (AP-1 and NFkB) at steady-state are the same motifs enriched in HSC-iM after recovery from inflammatory challenge[88]. Considering these findings, we hypothesize that repeated stress events in the form of acute infections or inflammatory stimuli across the human lifespan are an "allostatic load" that impacts HSC function[89]. Moreover, this inflammatory memory of aged HSPC may sensitize them to damage, heightening their response to the proliferative stress induced by *ex-vivo* activation and transplantation, as previously reported for skin epithelial cells and akin to trained immunity in HSC[90–95]. Indeed, even if at steady state we observed a slight increase in transcriptionally defined dormant HSCs in the old subjects, when activated, aged HSPC displayed a higher proliferation rate with a more rapid exit from dormancy associated with accumulation of proliferation stress-induced DNA damage, cell cycle inhibitors, inflammatory cytokines, and reduced long-term engraftment, likely due to deregulation of genes involved in DNA replication initiation, fork stability and DNA damage response checkpoint genes, in line with data in murine old HSC[96] . The enhanced ability of aged HSPC, and of sorted HSC/MPP subset, to respond to mitogenic stimuli *ex-vivo* appear in contrast with the recent evidence reporting that individual CD49f$^+$ primitive HSC showed age-associated delayed timing of first division and prolonged G1 phase[44] and likely highlight a differential response to distinct mitogenic stimuli between a pool of progenitors/stem cells compared with highly purified individual primitive cells. Instead, our findings align with literature in murine HSPC reporting increased DNA replication stress in aged HSC during the S phase[16] and with the evidence that DNA damage in LT-HSCs is a uniform consequence of treating mice with a range of stimuli, including viral infections, that provoke HSC cycle entry[97,98].

Notably, the altered aged phenotype observed in mice transplanted with aged CD34+ cells was recapitulated in mice transplanted with a low input of pre-activated neonatal CB cells. Interestingly, chromatin accessibility profiling of HSPC isolated from the low-cell input xenotransplantation model revealed an enrichment of transcription factor binding motifs, including AP-1, that are also prominently found in LT-HSC from aged individuals. This shared epigenetic signature suggests that the proliferative stress imposed on HSPC transplanted at low cell dose may induce a chromatin landscape resembling that of physiologically aged stem cells, potentially reflecting age-associated changes in regulatory networks governing stem cell function and lineage commitment. The increased proliferation rate of HSPC transplanted at low cell doses might be result of different factors. Although there is no selective pressure on human cells driven by host survival in sub- lethally irradiated mice, irradiation still damages the murine niche and generates an inflammatory milieu that may promote uncontrolled proliferation of transplanted human cells—an effect that is more pronounced when the transplanted cell dose is low. An alternative explanation is the limited number of true repopulating cells within the 3,000 $CD34^+$ cells, which may lead to oligoclonal hematopoiesis and premature exhaustion. In line with this, the presence of "bystander cells" in the transplantation setting of higher cell doses may help condition the bone marrow niche to better support human engraftment. From a preclinical perspective, our *in vivo* proliferation-stress model can be also used to test innovative strategies to mitigate stress-induced defects of human hematopoiesis or the reduced HSPC clonality observed in transplanted patients in the long-term[99]. These effects might also be exacerbated in the case of limited HSPC graft size due to patients' intensive pre-treatments or other underlying conditions[83]. Finally, even if most autologous gene therapy treatments occur in pediatric patients or young adults[82,83], applications to cancer and degenerative diseases are predicted to increase in the next decades. In this setting, hematopoietic stress and inflammation could be further amplified upon *ex vivo* culture of autologous stem cells from middle aged to old subjects leading to reduced long-term functionality and altered hematopoietic reconstitution, possibly affecting both the health span and lifespan of treated patients. Altogether, our data show that human hematopoietic aging is associated with overall hematopoietic reduction with impaired functionality and altered proliferation-stress responses acting at the HSC level. Moreover, we provide a powerful in vivo model for studying aging of human HSPC with clinically relevant implications, and overcome the limitations imposed by low

availability of human aged BM samples in the context of pre-clinical research.

Methods

Human hematopoietic samples in the Italian Cohort. We complied with all the ethical regulations for retrieving biological materials from healthy donors. To characterize the hematopoietic compartment over aging we collected BM samples from 9 pediatric (0 to 18 years old), 13 young adults (18 to 40 years old), 20 middle-aged (40 to 60 years old) and 31 aged (>65 years old) healthy individuals as well as PB samples from 12 pediatric (0 to 18 years old), 17 young adults (18 to 30 years old), 8 middle-aged (40 to 60 years old) and 19 aged (>65 years old) healthy subjects. Pediatric BM samples were collected as residual excess material from subjects undergoing BM harvest as donors for transplantation, after parents' signing informed consent. Aged BM samples were collected from subjects who underwent hip replacement surgery at San Raffaele Hospital, Milan, after obtaining written informed consent. BM CD34+ cells from young healthy donors for functional assays were collected at San Raffaele Hospital or purchased from Lonza. For the phenotypic analyses the sample size was determined by the number of individuals for whom excess material was available, after signing informed consent for research protocols approved by the San Raffaele Scientific Institute's Ethics Committee (according to protocol TIGET09). We excluded from our analyses all subjects with compromised immune functions and previous history of cancer or cancer treatments. We also excluded subjects that were positive to HBV, HCV, and HIV infections. We included only subjects that scored as "no frail" upon Edmonton Frailty Scale (EFS)[100] evaluation.

Human hematopoietic samples in the North American Cohort. Human bone marrow mononuclear cells (MNC) were either purchased from Lonza, collected from young healthy volunteers from Toronto with informed consent, or collected from patients undergoing hip replacement surgery at the at the Traumatology and Orthopedics Hospital Lomas Verdes (IMSS), Mexico with verbal consent, as determined by the Institutional Ethical Board. The Mexican samples were confirmed to have no dysplasia of any hematopoietic lineages by histological and complete blood count analysis[101]. Ethical approval was obtained from the Institutional Review Board (R- 2012-785-092). Samples were viably frozen and stored at -150°C. All Toronto hematopoietic samples were collected with informed consent according to the procedures approved by the University Health Network (UHN) Research Ethics Board (REB 01-0573-C). CB samples were obtained from Trillium and Credit Valley Hospital and

William Osler Health Centre, processed as previously described, and stored viably as CD34 enriched HSPC at -150°C[102]. BM samples were thawed and CD34 enrichment from BM samples was performed by positive selection with the CD34 Microbead kit (Miltenyi) with MACS magnet technology (Miltenyi) and stained with the following panel for HSPC immunophenotypic analysis: FITC-anti-CD45RA, PE-anti-CD90, APC-anti-CD10, PE-Cy5-anti-CD49f, BV711-anti-CD19, APC-Cy7-anti-CD34, PE-Cy7-anti-CD38, biotin-anti-CD135, Alexa-Fluor-anti-CD7, V421-anti-CD33, BV650-anti-CD71, streptavidin- Qdot605, and propidium iodide.

Whole Blood Dissection Staining. PB samples and BM aspirate were stained according to the published Whole Blood Dissection (WBD) protocol[51]. In brief, after red-blood cell lysis, the samples were labeled with the following fluorescent antibodies:

- Mouse anti-human CD3-BV605 (Clone: OKT3; Biolegend, 317322), Verified Reactivity: Human; Application: Flow cytometric analysis of antibody surface-stained cells. Dilution: 1:50
- Mouse anti-human CD56-PC5 (Clone: 5.1H11; Biolegend, 362516), Verified Reactivity: Human; Application: Flow cytometric analysis of antibody surface-stained cells. Dilution: 1:50
- Mouse anti-human CD14-BV510 (Clone: M5E2; Biolegend, 301842), Verified Reactivity: Human, Cynomolgus, Rhesus; Application: Flow cytometric analysis of antibody surface- stained cells. Dilution: 1:50
- Mouse anti-human CD33-BB515 (Clone: WM53; BD Biosciences, 564588), Verified Reactivity: Human (QC Testing); Application: Flow cytometry (Routinely Tested). Dilution: 1:50
- Mouse anti-human CD41/CD61-PC7 (Clone: A2A9/6; Biolegend, 359812), Verified Reactivity: Human; Application: Flow cytometric analysis of antibody surface-stained cells. Dilution: 1:50
- Mouse anti-human CD66b-BB515 (Clone: G10F5; BD Biosciences, 564679), Verified Reactivity: Human (QC Testing); Application: Flow cytometry (Routinely Tested). Dilution: 1:50
- Mouse anti-human CD7-BB700 (Clone: M-T701; BD Biosciences, 566488), Verified Reactivity: Human (QC Testing) , Rhesus, Cynomolgus, Baboon (Reported); Application: Flow cytometry (Routinely Tested). Dilution: 1:50

- Mouse anti-human CD45-BUV395 (Clone: HI30; BD Biosciences, 563792), Verified Reactivity: Human (QC Testing); Application: Flow cytometry (Routinely Tested). Dilution: 1:33
- Mouse anti-human CD38-BUV737 (Clone: HB7; BD Biosciences, 612824), Verified Reactivity: Human (QC Testing); Application: Flow cytometry (Routinely Tested). Dilution: 1:33
- Mouse anti-human CD90-APC (Clone: 5E10; BD Biosciences, 559869), Verified Reactivity: Human (QC Testing), Rhesus, Cynomolgus, Baboon, Pig, Dog (Tested in Development); Application: Flow cytometry (Routinely Tested). Dilution: 1:33
- Mouse anti-human CD135-PE (Clone: BV10A4H2; Biolegend, 313306), Verified Reactivity: Human; Application: Flow cytometric analysis of antibody surface-stained cells. Dilution: 1:33
- Mouse anti-human CD11c-BV650 (Clone: B-ly6; BD Biosciences, 563404), Verified Reactivity: Human (QC Testing); Application: Flow cytometry (Routinely Tested). Dilution: 1:20
- Mouse anti-human CD10-BV786 (Clone: HI10a; BD Biosciences, 564960), Verified Reactivity: Human (QC Testing), Rhesus, Cynomolgus, Baboon (Tested in Development); Application: Flow cytometry (Routinely Tested). Dilution: 1:20
- Mouse anti-human CD34-BV421 (Clone: 561; Biolegend, 343610), Verified Reactivity: Human; Application: Flow cytometric analysis of antibody surface-stained cells. Dilution: 1:20
- Mouse anti-human CD45RA-APCH7 (Clone: HI100; Biolegend, 304128), Verified Reactivity: Human; Reported Reactivity: Chimpanzee; Application: Flow cytometric analysis of antibody surface-stained cells. Dilution: 1:20
- Mouse anti-human CD71-BV711 (Clone: M-A712; BD Biosciences, 563767), Verified Reactivity: Human (QC Testing); Application: Flow cytometry (Routinely Tested). Dilution: 1:20
- Mouse anti-human CD19-APCR700 (Clone: SJ25C1; BD Biosciences, 659121), Verified Reactivity: Human; Application: Flow cytometry. Dilution: 1:20

All the antibodies were purchased from Biolegend and BD Biosciences and they are well characterized and validated by providers. Titration assays were performed to assess the

best antibody concentration. After surface marking, the cells were incubated with PI (Biolegend) to stain dead cells. Absolute cell quantification was performed by adding Flowcount beads (BD Biosciences) to samples before WBD procedure. All stained samples were acquired through BD LSR-Fortessa (BD Biosciences) cytofluorimeter after Rainbow beads (Spherotech) calibration. Raw data were collected through DIVA software Version 8.0.2 and analyzed with FlowJo software Version 10.5.3(BD Biosciences). Technically validated results were always included in the analyses, and we did not apply any exclusion criteria for outliers.

Whole Exome Sequencing Analysis for identification of CH-associated mutations.

Somatic variant calling was performed according to the GATK "Best Practice Workflows" to identify somatic variants in each sample. Identified variants were then confirmed using VarDict[103] . Raw read quality was assessed using FastQC (v0.11.9). Raw reads were then trimmed using Trim Galore (v0.6.6) to remove low-quality bases. To eliminate possible mouse contamination, a disambiguation procedure was performed[104] : reads were aligned to both human and mouse reference genomes, and then each one was assigned to the organism with the best mapping (or marked as ambiguous and discarded). Next, human specific reads were aligned against the human genome assembly (GRCh38) using BWA (v0.7.17)[105] . Duplicates were marked using Picard MarkDuplicates (v2.25.6), and GATK (v4.2.0.0) BaseRecalibrator and ApplyBQSR were used to recalibrate base quality scores using dbSNP known sites.[106]

Mutect2 in tumor-only mode was used to call variants in each sample with a minimum tumor LOD of 2. Variants were then filtered using FilterMutectCalls. Only variants passing all default Mutect2 filters or only failing the “clustered_events” filter were retained for further analyses. Variants were additionally filtered by depth, retaining only variants with a minimum of 5 variant reads for SNVs or a minimum of 10 variant reads for indels. Finally, to enrich for true somatic variants, putative germline variants were flagged and removed according to the following criteria: variant alleles with a minor allele frequency (MAF) > 1% in the dbSNP database and with a variant allele frequency (VAF) between 0.4 and 0.6 or greater than 0.9[106]

To obtain a high-confidence list of mutations, variants were also independently called using VarDict with a minimum variant allele frequency of 0.01, minimum base quality score of 25 and a minimum of 2 supporting reads[103]. Variants were filtered by retaining only those with

a minimum of 5 variant reads for SNVs, a minimum of 10 variant reads for indels, a minimum base quality score of 30, a minimum mapping quality score of 40 and a maximum strand bias Fisher p-value of 0.0001. To identify a high-confidence set of somatic variants, only variants independently identified by both Mutect2 and VarDict were retained.

The high-confidence set of somatic variants in the cohort was then explored using a gene panel containing 97 genes related to clonal hematopoiesis retrieved from Jakobsen et al.[107]. Somatic variants in clonal hematopoiesis genes were explored using an OncoPrint reporting the type (SNV, insertion, or deletion) as well as the identity of genes harboring a mutation, with the relative percentage in the cohort under study. OncoPrint were generated using the ComplexHeatmap R package[108].

Limiting dilution xenotransplantation study of uncultured human BM HSPC across aging. All animal experiments were done in accordance with institutional guidelines approved by the University Health Network Animal care committee. Aged match female NSG mice (NOD.Cg *Prkdc*scid*Il2rg*tm1Wjl /SzJ; Jackson Laboratory) 10-12 weeks of age were sublethally irradiated with 225 rads 1 day before intrafemoral injection. CB CD34-enriched cells and BM samples were thawed, and CD34 enrichment from BM samples was performed by positive selection with the CD34 Microbead kit (Miltenyi) with MACS magnet technology (Miltenyi) the morning of xenotransplantation. A limiting dilution assay (LDA) to quantitatively measure CD34 repopulating frequency across aging (CB, young BM (21-32y, n=5), middle-age BM (52-57y, n=3), and old BM (78-83y, n=5) in 314 NSG mice was designed based on a prior study to measure CB functional HSC frequency in NSG[43]. CD34-enriched samples were injected into the right femur of mice at three cell doses (60,000 cells, 10,000 cells, and 1,000 cells). Flow cytometry analysis was conducted on an aliquot of each sample to quantify the number of CD34+ cells injected using the following panel: PE-anti-CD19, APC-anti-CD34, PECy7-anti-CD38, FITC-anti-CD45RA and propidium iodide. Each sample was distributed across the indicated cell doses for transplant (n=3- 11 mice/cell dose) based on available sample material (see Supplemental Data Table 1). Human engraftment in the bones of mice were assessed at 4, 12, and 20 weeks post-transplantation as previously described by flow cytometry analysis on a BD Celesta with the following antibodies: PE-Cy5-anti-CD45, V500-anti-CD45, PE-anti-GlyA, PE-anti-CD19, BV786-anti-CD33, APC-anti-CD34, FITC-anti-CD71, APC-Cy7-anti-CD41, and BV605-anti-CD56 and a viability dye[43,102] (sytox blue, ThermoFisher). Mice were considered engrafted if CD45+ cells were >0.05%.

CD34 repopulating frequency was estimated using ELDA software[109] (http://bioinf.wehi.edu.au/software/elda/).

In vitro multi-lineage differentiation assay. For differentiation assays, 500 Lin-CD34+ cells (bulk), 500 HSC (Lin-CD34+CD38-CD90+CD45RA- cells) or single HSC (Lin-CD34+CD38-CD90+CD45RA- cells, also stained for CD49f to perform index sorting analyses) were sorted from young (n=3) or old (n=3) subjects and seeded on non-tissue culture treated flat bottom plates (Thermo Scientific) pre-coated with StemSpan Differentiation Coating Material(Stem Cell Technologies), according to manufacturer's specifications. Cells were cultured in SFEM II medium(Stem Cell Technologies) supplemented with hSCF(100 ng/ml), hFLT3(10 ng/ml), hIL- 7(100 ng/ml), hIL-2(10 ng/ml) (Novartis), hTPO(75 ng/ml), hIL-6(40 ng/ml), hIL-3(10 ng/ml), hIL- 11(50 ng/ml), hEPO(0.1 U/ml) (Peprotech), hIL-4(10 ng/ml) (Miltenyi Biotec), hLDL(4 ug/ml) (Stem Cell technologies). Medium change was performed every 3-4 days. After 3 weeks of culture, cells were harvested and labeled with the following anti-human conjugated antibodies: anti- CD235a, anti-CD1a, anti-CD5, anti-CD19, anti-CD42b, CD33, anti- CD7, anti-CD71, anti- CD11c (BD Bioscience) and anti-CD41, anti-CD10, anti-CD15, anti-CD3, anti-CD56, anti-CD34 (Biolegend). The stained samples were acquired through BD FACS Symphony A5 (BD Biosciences) cytofluorimeter after Rainbow bead (Spherotech) calibration. Raw FACS data were collected through DIVA software (BD Biosciences) and subsequently analyzed with FlowJo software Version 10.5.3 and the graphical output was generated through Prism v10.0.0 (GraphPad). The threshold for positive wells was determined based on negative controls. For annotate the potential of LT-HSC, each single cell output was scored as uni-, bi- and multi-lineage based on the most abundant differentiation output toward lymphoid, myeloid, erythroid and megakaryocyte lineages. Uni-lineage clones were defined when >75% of produced cells belonged to only one lineage, while bi-lineage clones were characterized by two major differentiation outputs (each more than 20%) accounting for >70% of total cell output. Cells with detectable output toward all the 4 lineages were defined as Multi-lineage, while cells with heterogeneous output, not falling in the other three categories, were defined as mixed clones.

Generation of scRNAseq atlas and analysis. We combined publicly available scRNA-seq dataset profiling BM-derived HSPC collected from young (16-30 yrs) or elderly (>60 yrs)

human healthy donors, namely: Ainciburu et al. (GSE180298), Li et al. (GSE189161), Mende et al. (GSE190067), Quaranta et al. (GSE253485), Setty et al. (ENA-ERP120467). Such combined dataset profiles the transcriptomes of 134,184 cells across 13,748 genes, upon the removal of donors with < 100 sequenced cells and sequenced cells with < 500 or >5000 detected genes. We set up a standardized analysis using Seurat R package v.4.1.1[110,111], and harmony R package v.0.1. The expression level of each gene was then scaled (ScaleData) by its overall library size (nCount_RNA) and the scaled gene expression matrix was then fed as an input to compute the principal components (RunPCA) restricting the analysis to the top-1000 most variable genes (NormalizeData & FindVariableFeatures). The first 67 PCs were then used to perform data integration with Harmony (RunHarmony) accounting for both dataset and donor batch effects. The resulting harmonized PCs were then used to compute the harmonized UMAP embeddings (RunUMAP) and to define a neighboring cell-graph (FindNeighbors). Such graph was then used to perform cell clustering (FindClusters) at different resolutions (0.1 to 1 by 0.1) through the Louvain algorithm. Module scores (AddModuleScore) were computed based on a set of celltype-specific markers derived from previous publications. Such modules combined with the results of between clusters differential gene expression analyses were used to associate each inferred cell cluster (res = 0.5) to a cell-type label. Finally, we performed sub-clustering (FindSubCluster, res = 0.2) on the most primitive HSPC set (namely, HSC) and identified subsets of cells showing long-term HSC, MPP or lineage-primed profiles. To infer the cell cycle, a continuous measure was derived by the CellCycleScoring R function based on the “regev_lab_cell_cycle_human.rds” cell-cycle marker genes. This classification was further refined computing cell-wise module scores based on sets of genes that positively or negatively regulate dormancy, allowing classification of G0-cells within G1-cells showing a highly dormient transcriptomic profile. Differential gene expression (DGE) analysis between two groups of cells was performed (FindMarkers) through a Wilcoxon Mann-Whitney test. The nominal p-values were adjusted to account for the multiple hypotheses testing issue through the Benjamini-Hochberg procedure and the difference in expression levels of each gene or gene set was deemed as significant whenever the adjusted p-value was smaller or equal than 0.05.

ATAC-Seq library preparations and analyses. From human HSPC subpopulations: Library preparation for ATAC-Seq was performed on 1000-2000 cells with Nextera DNA Sample

Preparation kit (Illumina), according to previously reported protocol[112]. 4 ATAC-seq libraries were sequenced per lane in HiSeq 2500 System (Illumina) to generate paired-end 50-bp reads. Raw sequencing reads were aligned to the hg38 genome build using BWA[113]. All duplicate reads, and reads mapped to mitochondria, chrY, an ENCODE blacklisted region or an unspecified contig were removed (ENCODE Project Consortium, 2012). The set of samples (n=31 subfractions, n=3 young donors (21-28y), n=4 mid/old donors (52-79y)) that passed quality control and used for downstream analysis is in Supplemental Table 3. The catalog of all peaks called in any population was produced by merging all called peaks which overlapped by at least one base pair using bedtools and divided into 500bp windows. The MACS bdgcmp function[114] was used to compute the fold enrichment over background for all populations, and the bedtools map function was used to identify the maximum fold enrichment observed at each window covering a peak in the catalog in each population. Maximum fold enrichment at each site in the catalog was quantile normalized between samples, we define this as the ATAC-Seq signal for further analyses. The NMF package[115] was used to perform non-negative matrix factorization on the quantile normalized fold enrichment at each peak in the catalog (using the brunet method with default parameters) for between 3 and 10 signatures. 6 signatures was selected as optimal. or each signature, sites were ranked according to the strength of each signature, and the top 5% of sites identified as being the sites for each signature. Homer[116] was used to identify uniquely enriched motifs within the top 5% of sites for each signature, using default parameters. Contiguous genomic windows were merged and the catalog of all called peaks was used as a background. Sites enriched in the top 5% of sites of both signatures were removed prior to computing enrichment.

From xenotransplantation model of proliferative stress: A total of 1 × 10^5 cells from purified human CD34+ from murine bone marrow samples were lysed with digitonin (Promega; cat. #G944A) and tagmented with an engineered Tn5 transposase (Illumina; cat. #15027865) at 37°C for 30 minutes, following a protocol optimized for blood cells. Tagmented DNA was purified and amplified with 10 cycles of PCR. Before the sequencing, fragments with a 1 to 5 kbp size range were removed by magnetic separation with AMPure XP beads (Beckman Coulter; cat. #A63881).

For the downstream analyses, reads were trimmed with Trim Galore, aligned with BWA-MEM (release 0.7.17-r1188), to the human genome (GRCh38 primary assembly). Mus

musculus (GRCm39) and Bos taurus (GCF_002263795.3) genomes were used for sequential disambiguation[104] to remove potential contaminant reads from FBS and host DNA of the in-vivo experiment. Bam files were filtered for mitochondrial, Y chromosome and PCR duplicated reads with Picard (2.25.0-0). Blacklisted regions were filtered using as reference ENCODE blacklist (hg38 v2). Soft-clipped reads were filtered out with gatk when the ratio of clipped over the total bases exceeded 0.25. Finally, only properly paired reads, with non-secondary alignment and mapping quality of at least 15 and length > 45 bp were retained. To quantify open chromatin regions, bedtools multibamcov (with parameters -q 10) was used against the Rank6 signatures regions unique of old and young conditions, generated from the previous experiment. Differential accessibility was computed with DESeq2, filtering regions with less then 10 counts, and testing for the contrast High vs Low dose (FDR 0.05). The analysis of known motif enriched in DARs was conducted with Homer software[117] (parameters -size 200 -mask).

Total RNA-seq library preparation and analysis. Whole transcriptomic analysis was performed on a pool of BM CD34+ cells derived from three young and old donors. All conditions were performed in triplicate. Total RNA was isolated after an overnight in liquid culture using miRNeasy Micro Kit (QIAGEN), and DNase treatment was performed using RNase-free DNase Set (QIAGEN), according to the manufacturer's instructions. Total RNA was used for library preparation with NEBNext Ultra-low input II Directional RNA Library Prep Kit (Illumina) and sequenced on an Illumina HiSeq with 2x150 bp sequencing configuration (Illumina).

RNA-seq analysis. High quality reads, obtained after reads quality inspection and adapter trimming with Trim Galore (https://www.bioinformatics.babraham.ac.uk/projects/trim_galore/) were aligned to the human reference genome (GENCODE GRCh38 primary assembly) with STAR release 2.7.6a. Gene expression quantification was obtained with featureCounts v2.0.1, using the GENCODE annotation (version v35 primary assembly). Raw counts were normalized by library size, and the differential expression (DE) analysis was performed with the DESeq2 package, testing for the contrast OLD vs. YOUNG. Finally, Benjamini-Hochberg adjusted *P* values were used to retain significant differentially expressed genes (FDR < 0.05). For the Gene Set Enrichment Analysis (GSEA)[118] genes were ranked by Log-Fold Change and analyzed with the *gsePathway* function from clusterProfiler, considering the Reactome

database, retaining gene categories with FDR < 0.05. All figures were plotted with ggplot2 in R.

Colony forming unit assay. CFU assay was performed at the indicated time points plating 800 cells in methylcellulose-based medium (MethoCult H4434, StemCell Technologies) supplemented with penicillin and streptomycin. Two weeks after plating, colonies were counted in blind and identified as myeloid and erythroid colonies according to morphological criteria.

***In vitro* growth curve of young and old CD34+ cells.** Human CD34+ cells were seeded at the concentration of $5*10^5$ CD34+ cells/ml in serum-free StemSpan medium (StemCell Technologies) supplemented with penicillin, streptomycin, glutamine and human early-acting cytokines (SCF 300 ng/ml, Flt3-L 300 ng/ml, TPO 100 ng/ml, and IL-3 60 ng/ml; all purchased from Peprotech). All cultures were kept at 37°C in a 5% CO_2 water jacket incubator (Thermo Scientific) and cell count was assessed every 24h hours.

Ki67 staining and flow cytometry analysis. Cells were washed and fixed using BD Cytofix buffer (Cat. #554655), washed and permeabilized with BD Perm 2 (Cat. # 347692), washed and stained with FITC-conjugated Ki67 antibody (BD Biosciences, 556026). The cells were then analysed on a BD LSR-Fortessa cytometer (BD Biosciences).

Cell Trace Proliferation Assay. Bulk HSPC or FACS-sorted HSPC subsets from young and aged healthy donors were washed and incubated with CellTrace Violet (ThermoFisher, C34557) 5 mM for 20 minutes at 37°, protected from light. Cell sorting was performed using FACS Aria Fusion (BD Biosciences). After incubation, cells were washed and resuspended in a fresh pre-warmed complete culture medium and cultured in serum-free StemSpan medium (StemCell Technologies) supplemented with penicillin, streptomycin, glutamine and hSCF 300 ng/ml, hFlt3-L 300 ng/ml, hTPO 100 ng/ml, and hIL-3 60 ng/ml (all purchased from Peprotech). Cells were collected every 24h to measure the cell divisions through flow cytometry. Cells were acquired to BD LSRFortessa Cytometer (BD Biosciences).

Gene expression analysis. For gene expression analyses, total RNA was extracted using either miRNeasy Micro Kit (QIAGEN) or RNeasy Plus Micro Kit (QIAGEN), according to the manufacturer's instructions and DNase treatment was performed using RNase-free DNase Set (QIAGEN). cDNA was synthetized with iScript cDNA Synthesis Kit (Bio-Rad). For selected analyses, cDNA was then pre-amplified using TaqMan PreAmp Master Mix (ThermoFisher) and used for q-PCR in a Viia7 Real-time PCR thermal cycler using both Fast

SYBR Green Master Mix (ThermoFisher), after standard curve method optimization to reach the 100% primer efficiency for each couple of primers listed in Supplementary Data Table S7. The relative expression of each target gene was first normalized to *GUSB* or β*2M* housekeeping genes expression and then represented as 2^-ΔCt relative to the indicated control conditions.

Immunofluorescence analysis. Multi-test slides (10 well, MP Biomedicals) were treated for 20' with Poly-L-lysine solution (Sigma-Aldrich) at 1mg/ml concentration. After two washes with DPBS solution, approximately 0.5/1x10^5 cells were seeded on covers for 20' and fixed with 4% paraformaldehyde (Santa Cruz Biotechnology) for other 20'. Cells were then permeabilized with 0.2% Triton X100. After blocking with 0.5% BSA and 0.2% fish gelatin in DPBS, cells were probed with the indicated primary antibodies. After primary antibodies incubation (Anti-phospho RPA (Ser33) Antibody, Merck) cells were washed three times with DPBS and incubate with Alexa 488-, 568- and/or 647-labeled secondary antibodies (Invitrogen). Nuclear DNA was stained with DAPI (Sigma-Aldrich) and covers were mounted with Aqua-Poly/Mount solution (Polysciences. Inc.) on glass slides (Bio-Optica). Fluorescent images were acquired using Leica SP2 and Leica SP5 Confocal microscopes. Where indicated, quantification of DNA damage response nuclear foci in immunofluorescence images was conducted using ImageJ64 (version 1.47).

Transplantation experiments of activated human HSPC across aging and for the *in vivo* model of proliferation stress. Mouse studies were conducted according to protocols approved by the San Raffaele Scientific Institute and the Italian Ministry of Health (IACUC, #872). NOD.Cg- Prkdc^{scid} IL2rγ^{tm1Wjl}/SzJ (NSG) mice were purchased from The Jackson Laboratory (cat. #005557 Jackson Laboratories, Bar Harbor, ME). All animals were maintained in the SPF animal facility at IRCCS Ospedale San Raffaele. The handling of the animals was performed by trained personnel, with the aim of minimizing the degree of stress and suffering and the period of constraint.

For transplantation, 2.5x10^5 BM-CD34+ cells isolated from young and old healthy donors or different doses of CB-CD34+ (50x10^3; 10x10^3; 3x10^3) were injected intravenously into 8-weeks old female sub-lethally irradiated NSG mice (150-180 cGy). Mice were monitored three times a week by weight assessment and general appearance, taking into consideration motility, fur conditions, kyphosis, and other signs of disease. Human CD45+ cell engraftment and blood lineages reconstitution were monitored by serial collection of

blood from the mouse tail and at time of sacrifice BM, spleen and distal organs were harvested. Human cell engraftment in murine organs was assessed by applying WBD protocol (see "Whole Blood Dissection Staining" section). Before WBD procedure, cells were incubated with a mouse FcR blocking reagent (BD Biosciences, dilution 1:100).

BrdU and EdU *in vivo* administration and staining procedure. For cell proliferation analysis, EdU and BrdU double labelling was used as previously described[84]. Both nucleotide analogues are incorporated during DNA synthesis and, when combined, allow to analyse cell cycle kinetics. Pulse-chase timings were previously optimized[84] to achieve consistent *in vivo* incorporation of EdU and BrdU, and later detection in the cell population of interest. EdU (1 mg/mouse, Component A, Click-iT EdU Alexa Fluor 647, ThermoFisher, C10635) and BrdU (2 mg/mouse, Sigma-Aldrich, B5002-100MG) were subsequently administrated via tail vein injections (2h apart); 30 min after BrDU injection, mice were culled, and BM cells were isolated to perform human cell staining. The staining procedure was performed as follows:

- Surface staining of BM cells with labeled with the following fluorescent antibodies:
- Mouse anti-human CD45-BUV395 (Clone: HI30; BD Biosciences, 563792), Verified Reactivity: Human (QC Testing); Application: Flow cytometry (Routinely Tested). Dilution: 1:33
- Mouse anti-human CD3-BV605 (Clone: OKT3; Biolegend, 317322), Verified Reactivity: Human; Application: Flow cytometric analysis of antibody surface-stained cells. Dilution: 1:50
- Mouse anti-human CD56-PC5 (Clone: 5.1H11; Biolegend, 362516), Verified Reactivity: Human; Application: Flow cytometric analysis of antibody surface-stained cells. Dilution: 1:50
- Mouse anti-human CD14-PE (Clone: M5E2; Biolegend, 301806), Verified Reactivity: Human, Cynomolgus, Rhesus; Application: Flow cytometric analysis of antibody surface- stained cells. Dilution: 1:50
- Mouse anti-human CD34-BV421 (Clone: 561; Biolegend, 343610), Verified Reactivity: Human; Application: Flow cytometric analysis of antibody surface-stained cells. Dilution: 1:20
- Mouse anti-human CD15-APCfire750 (Clone: W6D3; Biolegend, 323041), Verified Reactivity: Human; Application: Flow cytometric analysis of antibody surface-

stained cells. 1:50

- Mouse anti-human CD19-APCR700 (Clone: SJ25C1; BD Biosciences, 659121), Verified Reactivity: Human; Application: Flow cytometry. Dilution: 1:20
- Mouse anti-human CD38-BV510 (Clone: HB-7; Biolegend, 356612), Verified Reactivity: Human (QC Testing); Application: Flow cytometry (Routinely Tested). Dilution: 1:40
- Mouse anti-human CD11c-BV650 (Clone: B-ly6; BD Biosciences, 563404), Verified Reactivity: Human (QC Testing); Application: Flow cytometry (Routinely Tested). Dilution: 1:20
- Fixation and permeabilization followed by EdU staining (Click-iT EdU Alexa Fluor 647, ThermoFisher, C10635) according to manufactures' instructions.
- Permeabilization using Cytoperm Buffer PLUS (BD Biosciences) 10 mins on ice followed by permeabilization through CytoFix/CytoPerm kit solution (BD Biosciences) 5 mins at room temperature
- DNAse treatment (Qiagen) for 1 hour at 37°C
- Staining with anti-BrDU-Alexa488 antibody, Clone: 3D4, Biolegend, 364105, Application: Intracellular Flow cytometry (Routinely Tested). Dilution: 1:50.

Samples were acquired at BD LSR-Fortessa (BD Biosciences) at 400 event/sec rate.

Neutral and Alkaline Comet Assays. Purified HSPC from CD34+ cells isolated from mice transplanted with distinct doses of CD34+ cells at 20 weeks were suspended at 1 x 10^5 cells/ml in ice cold 1X DPBS and mixed with molten Comet LMAgarose (Trevigen, MD) at a ratio of 1:10 (v/v) and immediately pipetted onto CometSlides (Trevigen, MD) and placed at +4°C. Once solidified, the slides were immersed in pre-chilled Lysis Solution (Trevigen, MD) overnight at +4°C. For *Neutral comet assay,* after lysis, slides were immersed in Neutral Electrophoresis Buffer pH 8 (50 mM Tris, 150 mM Sodium Acetate) for 1 hour at +4°C and then electrophoresed in Neutral Electrophoresis Buffer pH 8 (100 mM Tris, 300 mM Sodium Acetate) at 300 mA for 40 min. Slides were gently immersed in DNA Precipitation Solution (375 mM Ammonium Acetate in Ethanol 95%) for 30 minutes at RT and fixed in 70% ethanol for 30 min. For *Alkaline comet assay*, after lysis, slides were immersed in freshly prepared Alkaline Unwinding Solution pH > 13 (300 mM NaOH, 1mM EDTA) for 1 hour at +4°C and then electrophoresed in Alkaline Electrophoresis Solution pH > 13 (300 mM NaOH, 1mM EDTA) at 300 mA for 20 min. Slides were washed twice in ddH2O and fixed in 70% ethanol for 5 min. Comets were stained with SYBR Safe (Invitrogen) for 30 min at RT. All steps were

conducted in the dark to prevent additional DNA damage. Comets were analysed using a Nikon Eclipse E600 microscope and a Nikon-DS-RI2 camera. At least 80 nuclei for each individual donor were analysed with CASP software to determine "Olive Tail Moments" of individual nuclei.

Statistical analyses. Statistical test and *p* values were specified in each figure legend or in within figure graphs. To assess the correlation between two variables the Spearman index was calculated and a regression line (with 95% confidence intervals) was estimated after assessing the normality of residuals as appropriate. Non-parametric tests were used for comparing two or more groups when continuous variables were considered. The analyses were performed using Prism v9.1.0 software (GraphPad). For the longitudinal analyses of growth curve of cultured cells, a linear mixed-effects (LME) model has been applied. To better capture growth dynamics, group indicator (young *vs.* old) and time variable (a categorical variable taking 5 values, from 0 to 96 hours) were entered in the model as main effects as well as in interaction. To account for donor-specific heterogeneity, a random effect was specified on donors' ID, thus leading to estimate random intercept models. This modelling approach properly accounts for the dependency among observations arising from measuring the same unit more than once and over time. Logarithmic transformation of the outcome variable was considered to satisfy underlying model assumptions. Analyses were performed using R statistical software (version 4.0.4). Significance level was set at 0.05. LME were estimated using the *nlme* package and post-hoc comparisons, to compare groups at a fixed time point, have been performed using *emmeans* package.

Acknowledgments

This work was supported by Fondazione Telethon (TIGET Core Grant B2, A.A TGT21016, A.A and S.S.), the Italian Ministero della Salute (GR-2019-12369499, S.S.) and Else Kröner-Fresenius- Stiftung (EKFS) prize (A.A.). Research in Di Micco's lab is supported by a My First AIRC Grant MFAG 2019–PI ID.23321, by Telethon (TIGET Core grant E5 and TGT21018), by a Career Development Award from Human Frontier Science Program, by the Interstellar Initiative on Healthy Longevity from the New York Academy of Sciences and the Japan Agency for Medical Research and Development, by the ASH Global Research Award, by the New York Stem Cell Foundation,the European Research Council (Consolidator grant 101003186, ReviveSTEM), the X- PAND Pathfinder European Commission grant (G.A.

101070950), and European Union – NextGenerationEU (National Recovery and Resilience Plan, Investment, Project Age-It - Ageing Well in an Ageing Society, Project ID PE000015, CUP D43C22003100007. A.C. is an early career scientist in the European Hematology Association and the American Society of Hematology Translational Research Training in Hematology (EHA and ASH TRTH). T.T. is enrolled in the EHA-EMBL/EBI computational biology training in hematology. S.Z.X. is supported by funds from the Princess Margaret Cancer Foundation. We thank F. Ciceri, ME Bernardo and all medical and nursing staff at Raffaele Scientific Institute and the San Raffaele Stem Cell Programme; we thank C. Villa and S. Di Terlizzi of the Flow Cytometry Resource, Advanced Cytometry Technical Applications Laboratory (FRACTAL) at Ospedale San Raffaele for cell sorting and technical help with instrumentation; we thank C. Brombin of University Center for Statistics in the Biomedical Science (CUSSB) for LME statistical models. E.L. L.S. L.d.V and P.Q. conducted this study as partial fulfilment of their Ph.D. in Molecular Medicine, Cellular and Molecular Physiopathology Program, San Raffaele University, Milan, Italy. G.F. conducted this study as partial fulfilment of his Ph.D. in Molecular Medicine at University of Milano-Bicocca, DIMET, Milan, Italy. R.D.M. is a New York Stem Cell Foundation Robertson Investigator.

Author contributions

E.L. and SS performed phenotypic characterization, *in vitro* and *in vivo* assays, collected and interpreted the data, and wrote the manuscript; L.B.-R. performed phenotypic characterization and isolation of HSPC subpopulations, performed *in vitro* and *in vivo* assays and analyzed the data; E.C. performed *in vivo* experiments; T.T. performed analyses of RNAseq and ATACseq dataset generated by G.F and A.C. L.S. performed *in vitro* differentiation assay; N.G. performed CH analyses; L.G.P., K.B.K., and S.Z.X performed phenotypic characterization and isolation of HSPC subpopulations, quantitative xenotransplantation, and collected data. A.M. performed analyses of the ATAC-seq dataset generated by L.G.P; P.Q, K.G. and R.J.H. performed *in vivo* assays; G.P generated the scRNAseq atlas and performed the analyses; L.d.V. performed immunofluorescence analyses on *in vivo* experiments; E.L.F. performed Comet assay and analyses; P.C, M.O., A.G.A.N., E.F.F. provided human BM samples from aged donors; S.B and I.M. supervised RNAseq analyses; A.A supervised the research activities and provided funds; S.Z.X., S.S. and R.D.M interpreted data, supervised team members and contributed to writing-review

and editing of the manuscript. R.D.M conceived the study and secured funding.

Disclosure of Conflicts of Interest

All the authors declare no competing interests.

Data and Code availability

The RNA sequencing data generated and discussed in this study have been deposited in NCBI's Gene Expression Omnibus (Edgar *et al.*, 2002) and are accessible through GEO Series accession number GSE243327 (link: https://www.ncbi.nlm.nih.gov/geo/query/acc.cgi?acc=GSE243327 reviewer token = **shaheumsxrapvyd**). The code used to process and to generate the images of RNAseq data in this manuscript is available at: http://www.bioinfotiget.it/gitlab/custom/LetteraScala_Ageing/bulk_RNAseq.

The ATAC-seq data generated and discussed in this study are available at the following GEO Series accession number GSE243641 (link: https://urldefense.com/v3/ https://www.ncbi.nlm.nih.gov/geo/query/acc.cgi?acc=GSE243641_;!! CjcC7IQ!Ofaxoq7RYR6R8NkioMNy6R6AhC8Iz68-17IqPK2Sb1o4cuUi9ey-4N0XLLXPuYVoEim7ONoI9tWjKnwNDtgRJ8y1pmFuqQ$ reviewer token = **sfczyyqmfhwhduf**).

REFERENCES

1. Sudo, K., Ema, H., Morita, Y., and Nakauchi, H. (2000). Age-associated characteristics of murine hematopoietic stem cells [In Process Citation]. J Exp Med *192*.
2. de Haan, G., and Lazare, S.S. (2018). Aging of hematopoietic stem cells. Blood *131*, 479– 487. https://doi.org/10.1182/blood-2017-06-746412.
3. Morrison, S.J., Wandycz, A.M., Akashi, K., Globerson, A., and Weissman, I.L. (1996). The aging of hematopoietic stem cells. Nat Med *2*, 1011–1016. https://doi.org/10.1038/nm0996- 1011.
4. Young, K., Eudy, E., Bell, R., Loberg, M.A., Stearns, T., Sharma, D., Velten, L., Haas, S., Filippi, M.-D., and Trowbridge, J.J. (2021). Decline in IGF1 in the bone marrow microenvironment initiates hematopoietic stem cell aging. Cell Stem Cell *28*, 1473-1482.e7. https://doi.org/10.1016/j.stem.2021.03.017.
5. Oh, J., Lee, Y.D., and Wagers, A.J. (2014). Stem cell aging: mechanisms, regulators and therapeutic opportunities. Nat Med *20*, 870–880. https://doi.org/10.1038/nm.3651.
6. Sun, D., Luo, M., Jeong, M., Rodriguez, B., Xia, Z., Hannah, R., Wang, H., Le, T., Faull, K.F., Chen, R., et al. (2014). Epigenomic profiling of young and aged HSCs reveals concerted changes during aging that reinforce self-renewal. Cell Stem

Cell *14*, 673–688. https://doi.org/10.1016/j.stem.2014.03.002.

7. Rossi, D.J., Bryder, D., Zahn, J.M., Ahlenius, H., Sonu, R., Wagers, A.J., and Weissman, I.L. (2005). Cell intrinsic alterations underlie hematopoietic stem cell aging. Proc Natl Acad Sci U S A *102*, 9194–9199. https://doi.org/10.1073/pnas.0503280102.
8. Beerman, I., Seita, J., Inlay, M.A., Weissman, I.L., and Rossi, D.J. (2014). Quiescent hematopoietic stem cells accumulate DNA damage during aging that is repaired upon entry into cell cycle. Cell Stem Cell *15*, 37–50. https://doi.org/10.1016/j.stem.2014.04.016.
9. Luchsinger, L.L., de Almeida, M.J., Corrigan, D.J., Mumau, M., and Snoeck, H.-W. (2016). Mitofusin 2 maintains haematopoietic stem cells with extensive lymphoid potential. Nature *529*, 528–531. https://doi.org/10.1038/nature16500.
10. Simsek, T., Kocabas, F., Zheng, J., Deberardinis, R.J., Mahmoud, A.I., Olson, E.N., Schneider, J.W., Zhang, C.C., and Sadek, H.A. (2010). The distinct metabolic profile of hematopoietic stem cells reflects their location in a hypoxic niche. Cell Stem Cell *7*, 380– 390. https://doi.org/10.1016/j.stem.2010.07.011.
11. Morita, Y., Ema, H., and Nakauchi, H. (2010). Heterogeneity and hierarchy within the most primitive hematopoietic stem cell compartment. J Exp Med *207*, 1173–1182. https://doi.org/10.1084/jem.20091318.
12. Bernitz, J.M., Kim, H.S., MacArthur, B., Sieburg, H., and Moore, K. (2016). Hematopoietic Stem Cells Count and Remember Self-Renewal Divisions. Cell *167*, 1296-1309.e10. https://doi.org/10.1016/j.cell.2016.10.022.
13. Kirschner, K., Chandra, T., Kiselev, V., Flores-Santa Cruz, D., Macaulay, I.C., Park, H.J., Li, J., Kent, D.G., Kumar, R., Pask, D.C., et al. (2017). Proliferation Drives Aging-Related Functional Decline in a Subpopulation of the Hematopoietic Stem Cell Compartment.
14. Cell Rep *19*, 1503–1511. https://doi.org/10.1016/j.celrep.2017.04.074.
15. Walter, D., Lier, A., Geiselhart, A., Thalheimer, F.B., Huntscha, S., Sobotta, M.C., Moehrle, B., Brocks, D., Bayindir, I., Kaschutnig, P., et al. (2015). Exit from dormancy provokes DNA-damage-induced attrition in haematopoietic stem cells. Nature *520*, 549–552. https://doi.org/10.1038/nature14131.
16. Beerman, I., Bock, C., Garrison, B.S., Smith, Z.D., Gu, H., Meissner, A., and Rossi, D.J. (2013). Proliferation-dependent alterations of the DNA methylation landscape underlie hematopoietic stem cell aging. Cell Stem Cell *12*, 413–425. https://doi.org/10.1016/j.stem.2013.01.017.
17. Flach, J., Bakker, S.T., Mohrin, M., Conroy, P.C., Pietras, E.M., Reynaud, D., Alvarez, S., Diolaiti, M.E., Ugarte, F., Forsberg, E.C., et al. (2014). Replication stress is a potent driver of functional decline in ageing haematopoietic stem cells. Nature *512*, 198–202. https://doi.org/10.1038/nature13619.
18. Wang, M., Brandt, L.T.L., Wang, X., Russell, H., Mitchell, E., Kamimae-Lanning, A.N., Brown, J.M., Dingler, F.A., Garaycoechea, J.I., Isobe, T., et al. (2023). Genotoxic aldehyde stress prematurely ages hematopoietic stem cells in a p53-driven manner. Mol Cell *83*, 2417- 2433.e7. https://doi.org/10.1016/j.molcel.2023.05.035.
19. Liang, Y., Van Zant, G., and Szilvassy, S.J. (2005). Effects of aging on the homing and engraftment of murine hematopoietic stem and progenitor cells. Blood *106*, 1479–1487. https://doi.org/10.1182/blood-2004-11-4282.
20. von Bonin, M., Jambor, H.K., Teipel, R., Stölzel, F., Thiede, C., Damm, F., Kroschinsky, F., Schetelig, J., Chavakis, T., and Bornhäuser, M. (2021). Clonal

hematopoiesis and its emerging effects on cellular therapies. Leukemia *35*, 2752–2758. https://doi.org/10.1038/s41375-021-01337-8.

21. Jaiswal, S., and Ebert, B.L. (2019). Clonal hematopoiesis in human aging and disease. Science (1979) *366*. https://doi.org/10.1126/science.aan4673.
22. Signer, R.A.J., Montecino-Rodriguez, E., Witte, O.N., McLaughlin, J., and Dorshkind, K. (2007). Age-related defects in B lymphopoiesis underlie the myeloid dominance of adult leukemia. Blood *110*, 1831–1839. https://doi.org/10.1182/blood-2007-01-069401.
23. Vas, V., Wandhoff, C., Dörr, K., Niebel, A., and Geiger, H. (2012). Contribution of an Aged Microenvironment to Aging-Associated Myeloproliferative Disease. PLoS One *7*, e31523. https://doi.org/10.1371/journal.pone.0031523.
24. Henry, C.J., Marusyk, A., Zaberezhnyy, V., Adane, B., and DeGregori, J. (2010). Declining
lymphoid progenitor fitness promotes aging-associated leukemogenesis. Proceedings of the National Academy of Sciences *107*, 21713–21718. https://doi.org/10.1073/pnas.1005486107.
25. Chung, S.S., and Park, C.Y. (2017). Aging, hematopoiesis, and the myelodysplastic syndromes. Blood Adv *1*, 2572–2578. https://doi.org/10.1182/bloodadvances.2017009852.
26. van Galen, P., Kreso, A., Wienholds, E., Laurenti, E., Eppert, K., Lechman, E.R., Mbong, N., Hermans, K., Dobson, S., April, C., et al. (2014). Reduced lymphoid lineage priming promotes human hematopoietic stem cell expansion. Cell Stem Cell *14*, 94–106. https://doi.org/10.1016/j.stem.2013.11.021.
27. Pang, W.W., Schrier, S.L., and Weissman, I.L. (2017). Age-associated changes in human hematopoietic stem cells. Semin Hematol *54*, 39–42. https://doi.org/10.1053/j.seminhematol.2016.10.004.
28. Stauder, R., Valent, P., and Theurl, I. (2018). Anemia at older age: etiologies, clinical implications, and management. Blood *131*, 505–514. https://doi.org/10.1182/blood-2017-07- 746446.
29. Shlush, L.I. (2018). Age-related clonal hematopoiesis. Blood *131*, 496–504. https://doi.org/10.1182/blood-2017-07-746453.
30. Avagyan, S., and Zon, L.I. (2023). Clonal hematopoiesis and inflammation – the perpetual cycle. Trends Cell Biol *33*, 695–707. https://doi.org/10.1016/j.tcb.2022.12.001.
31. Furer, N., Rappoport, N., Milman, O., Tavor, S., Lifshitz, A., Bercovich, A., Ben-Kiki, O., Danin, A., Kedmi, M., Shipony, Z., et al. (2025). A reference model of circulating hematopoietic stem cells across the lifespan with applications to diagnostics. Nat Med. https://doi.org/10.1038/s41591-025-03716-5.
32. Mende, N., Bastos, H.P., Santoro, A., Mahbubani, K.T., Ciaurro, V., Calderbank, E.F., Londono, M.Q., Sham, K., Mantica, G., Morishima, T., et al. (2022). Unique molecular and functional features of extramedullary hematopoietic stem and progenitor cell reservoirs in humans. Blood *139*, 3387–3401. https://doi.org/10.1182/blood.2021013450.
33. Quaranta, P., Basso-Ricci, L., Jofra Hernandez, R., Pacini, G., Naldini, M.M., Barcella, M., Seffin, L., Pais, G., Spinozzi, G., Benedicenti, F., et al. (2024). Circulating hematopoietic
stem/progenitor cell subsets contribute to human hematopoietic homeostasis. Blood *143*, 1937–1952.

34. Belluschi, S., Calderbank, E.F., Ciaurro, V., Pijuan-Sala, B., Santoro, A., Mende, N., Diamanti, E., Sham, K.Y.C., Wang, X., Lau, W.W.Y., et al. (2018). Myelo-lymphoid lineage restriction occurs in the human haematopoietic stem cell compartment before lymphoid- primed multipotent progenitors. Nat Commun *9*, 4100. https://doi.org/10.1038/s41467-018- 06442-4.
35. Zhang, Y.W., Mess, J., Aizarani, N., Mishra, P., Johnson, C., Romero-Mulero, M.C., Rettkowski, J., Schönberger, K., Obier, N., Jäcklein, K., et al. (2022). Hyaluronic acid- GPRC5C signalling promotes dormancy in haematopoietic stem cells. Nat Cell Biol *24*, 1038–1048. https://doi.org/10.1038/s41556-022-00931-x.
36. García-Prat, L., Kaufmann, K.B., Schneiter, F., Voisin, V., Murison, A., Chen, J., Chan- Seng-Yue, M., Gan, O.I., McLeod, J.L., Smith, S.A., et al. (2021). TFEB-mediated endolysosomal activity controls human hematopoietic stem cell fate. Cell Stem Cell *28*, 1838-1850.e10. https://doi.org/10.1016/j.stem.2021.07.003.
37. Milyavsky, M., Gan, O.I., Trottier, M., Komosa, M., Tabach, O., Notta, F., Lechman, E., Hermans, K.G., Eppert, K., Konovalova, Z., et al. (2010). A distinctive DNA damage response in human hematopoietic stem cells reveals an apoptosis-independent role for p53 in self-renewal. Cell Stem Cell *7*, 186–197. https://doi.org/10.1016/j.stem.2010.05.016.
38. Laurenti, E., and Göttgens, B. (2018). From haematopoietic stem cells to complex differentiation landscapes. Nature *553*, 418–426. https://doi.org/10.1038/nature25022.
39. Takayama, N., Murison, A., Takayanagi, S.-I., Arlidge, C., Zhou, S., Garcia-Prat, L., Chan- Seng-Yue, M., Zandi, S., Gan, O.I., Boutzen, H., et al. (2021). The Transition from Quiescent to Activated States in Human Hematopoietic Stem Cells Is Governed by Dynamic 3D Genome Reorganization. Cell Stem Cell *28*, 488-501.e10. https://doi.org/10.1016/j.stem.2020.11.001.
40. Kaufmann, K.B., Zeng, A.G.X., Coyaud, E., Garcia-Prat, L., Papalexi, E., Murison, A., Laurent, E.M.N., Chan-Seng-Yue, M., Gan, O.I., Pan, K., et al. (2021). A latent subset of human hematopoietic stem cells resists regenerative stress to preserve stemness. Nat Immunol *22*, 723–734. https://doi.org/10.1038/s41590-021-00925-1.
41. Xie, S.Z., Kaufmann, K.B., Wang, W., Chan-Seng-Yue, M., Gan, O.I., Laurenti, E., Garcia- Prat, L., Takayanagi, S.-I., Ng, S.W.K., Xu, C., et al. (2021). Sphingosine-1-phosphate receptor 3 potentiates inflammatory programs in normal and leukemia stem cells to promote differentiation. Blood Cancer Discov *2*, 32–53. https://doi.org/10.1158/2643-3230.BCD-20- 0155.
42. Notta, F., Zandi, S., Takayama, N., Dobson, S., Gan, O.I., Wilson, G., Kaufmann, K.B., McLeod, J., Laurenti, E., Dunant, C.F., et al. (2016). Distinct routes of lineage development reshape the human blood hierarchy across ontogeny. Science *351*, aab2116. https://doi.org/10.1126/science.aab2116.
43. Notta, F., Doulatov, S., Laurenti, E., Poeppl, A., Jurisica, I., and Dick, J.E. (2011). Isolation of single human hematopoietic stem cells capable of long-term multilineage engraftment. Science *333*, 218–221. https://doi.org/10.1126/science.1201219.
44. Laurenti, E., Frelin, C., Xie, S., Ferrari, R., Dunant, C.F., Zandi, S., Neumann, A., Plumb, I., Doulatov, S., Chen, J., et al. (2015). CDK6 levels regulate quiescence exit in human hematopoietic stem cells. Cell Stem Cell *16*, 302–313.

https://doi.org/10.1016/j.stem.2015.01.017.

45. Hammond, C.A., Wu, S.W., Wang, F., MacAldaz, M.E., and Eaves, C.J. (2023). Aging alters the cell cycle control and mitogenic signaling responses of human hematopoietic stem cells. Blood *141*, 1990–2002. https://doi.org/10.1182/blood.2022017174.
46. Amoah, A., Keller, A., Emini, R., Hoenicka, M., Liebold, A., Vollmer, A., Eiwen, K., Soller, K., Sakk, V., Zheng, Y., et al. (2022). Aging of human hematopoietic stem cells is linked to changes in Cdc42 activity. Haematologica *107*, 393–402. https://doi.org/10.3324/haematol.2020.269670.
47. Jiang, P., Cai, Y., Zhou, X., Yang, J., Tong, Y., Huang, C., Qiu, H., Zhou, K., Xu, X., Zhang, Y., et al. (2023). Immune reconstitution and survival of patients after allogeneic hematopoietic stem cell transplantation from older donors. Clin Transplant *37*. https://doi.org/10.1111/ctr.14844.
48. Duda, K., Wieczorkiewicz-Kabut, A., Koclęga, A., Zielińska, P., Woźniczka, K., Krzemień, H., Armatys, A., and Helbig, G. (2023). Allogeneic hematopoietic stem cell transplantation remains a feasible approach for elderly with acute myeloid leukemia: a 10-year experience. Ann Hematol *102*, 1907–1914. https://doi.org/10.1007/s00277-023-05226-1.
49. Mehta, R.S., Marin, D., Alousi, A., Kanakry, C.G., Champlin, R.E., Rezvani, K., Shpall, E.J., Page, K., Gadalla, S.M., Weisdorf, D., et al. (2023). Haploidentical vs matched unrelated donors for patients with ALL: donor age matters more than donor type. Blood Adv *7*, 1594– 1603. https://doi.org/10.1182/bloodadvances.2022009240.
50. Artz, A.S. (2012). From Biology to Clinical Practice: Aging and Hematopoietic Cell Transplantation. Biology of Blood and Marrow Transplantation *18*, S40–S45. https://doi.org/10.1016/j.bbmt.2011.11.003.
51. Kollman, C., Howe, C.W.S., Anasetti, C., Antin, J.H., Davies, S.M., Filipovich, A.H., Hegland, J., Kamani, N., Kernan, N.A., King, R., et al. (2001). Donor characteristics as risk factors in recipients after transplantation of bone marrow from unrelated donors: the effect of donor age. Blood *98*, 2043–2051. https://doi.org/10.1182/blood.V98.7.2043.
52. Basso-Ricci, L., Scala, S., Milani, R., Migliavacca, M., Rovelli, A., Bernardo, M.E., Ciceri, F., Aiuti, A., and Biasco, L. (2017). Multiparametric Whole Blood Dissection: A one-shot comprehensive picture of the human hematopoietic system. Cytometry Part A *91*, 952–965. https://doi.org/10.1002/cyto.a.23148.
53. Pang, W.W., Price, E.A., Sahoo, D., Beerman, I., Maloney, W.J., Rossi, D.J., Schrier, S.L., and Weissman, I.L. (2011). Human bone marrow hematopoietic stem cells are increased in frequency and myeloid-biased with age. Proc Natl Acad Sci U S A *108*, 20012–20017. https://doi.org/10.1073/pnas.1116110108.
54. Rundberg Nilsson, A., Soneji, S., Adolfsson, S., Bryder, D., and Pronk, C.J. (2016). Human and Murine Hematopoietic Stem Cell Aging Is Associated with Functional Impairments and Intrinsic Megakaryocytic/Erythroid Bias. PLoS One *11*, e0158369. https://doi.org/10.1371/journal.pone.0158369.
55. Zhang, L., Mack, R., Breslin, P., and Zhang, J. (2020). Molecular and cellular mechanisms of aging in hematopoietic stem cells and their niches. J Hematol Oncol *13*, 157. https://doi.org/10.1186/s13045-020-00994-z.
56. Kuranda, K., Vargaftig, J., de la Rochere, P., Dosquet, C., Charron, D., Bardin, F., Tonnelle, C., Bonnet, D., and Goodhardt, M. (2011). Age-related changes in human hematopoietic stem/progenitor cells. Aging Cell *10*, 542–546.

https://doi.org/10.1111/j.1474- 9726.2011.00675.x.

57. Wang, J.C., Doedens, M., and Dick, J.E. (1997). Primitive human hematopoietic cells are enriched in cord blood compared with adult bone marrow or mobilized peripheral blood as measured by the quantitative in vivo SCID-repopulating cell assay. Blood *89*, 3919–3924.
58. Scala, S., Ferrua, F., Basso-Ricci, L., Dionisio, F., Omrani, M., Quaranta, P., Hernandez, R.J., Del Core, L., Benedicenti, F., Monti, I., et al. (2023). Hematopoietic reconstitution dynamics of mobilized- and bonemarrow-derived human hematopoietic stem cells after gene therapy. Nat Commun *14*, 1–18. https://doi.org/10.1038/s41467-023-38448-y.
59. Li, H., Côté, P., Kuoch, M., Ezike, J., Frenis, K., Afanassiev, A., Greenstreet, L., Tanaka- Yano, M., Tarantino, G., Zhang, S., et al. (2025). The dynamics of hematopoiesis over the human lifespan. Nat Methods *22*, 422–434. https://doi.org/10.1038/s41592-024-02495-0.
60. Setty, M., Kiseliovas, V., Levine, J., Gayoso, A., Mazutis, L., and Pe'er, D. (2019). Characterization of cell fate probabilities in single-cell data with Palantir. Nat Biotechnol *37*, 1237–1237. https://doi.org/10.1038/s41587-019-0282-0.
61. Ainciburu, M., Ezponda, T., Berastegui, N., Alfonso-Pierola, A., Vilas-Zornoza, A., San Martin-Uriz, P., Alignani, D., Lamo-Espinosa, J., San-Julian, M., Jiménez-Solas, T., et al. (2023). Uncovering perturbations in human hematopoiesis associated with healthy aging and myeloid malignancies at single-cell resolution. Elife *12*. https://doi.org/10.7554/eLife.79363.
62. Kaufmann, K.B., Zeng, A.G.X., Coyaud, E., Garcia-Prat, L., Papalexi, E., Murison, A., Laurent, E.M.N., Chan-Seng-Yue, M., Gan, O.I., Pan, K., et al. (2021). A latent subset of human hematopoietic stem cells resists regenerative stress to preserve stemness. Nat Immunol *22*, 723–734. https://doi.org/10.1038/s41590-021-00925-1.
63. Zhang, Y.W., Mess, J., Aizarani, N., Mishra, P., Johnson, C., Romero-Mulero, M.C., Rettkowski, J., Schönberger, K., Obier, N., Jäcklein, K., et al. (2022). Hyaluronic acid– GPRC5C signalling promotes dormancy in haematopoietic stem cells. Nat Cell Biol *24*, 1038–1048. https://doi.org/10.1038/s41556-022-00931-x.
64. Komic, H., Schmachtel, T., Simoes, C., Külp, M., Yu, W., Jolly, A., Nilsson, M.S., Gonzalez, C., Prosper, F., Bonig, H., et al. (2025). Continuous map of early hematopoietic stem cell differentiation across human lifetime. Nature Communications *16*. https://doi.org/10.1038/s41467-025-57096-y.
65. Belluschi, S., Calderbank, E.F., Ciaurro, V., Pijuan-Sala, B., Santoro, A., Mende, N., Diamanti, E., Sham, K.Y.C., Wang, X., Lau, W.W.Y., et al. (2018). Myelo-lymphoid lineage restriction occurs in the human haematopoietic stem cell compartment before lymphoid- primed multipotent progenitors. Nat Commun *9*. https://doi.org/10.1038/s41467-018-06442- 4.
66. Laurenti, E., Frelin, C., Xie, S., Ferrari, R., Dunant, C.F., Zandi, S., Neumann, A., Plumb, I., Doulatov, S., Chen, J., et al. (2015). CDK6 levels regulate quiescence exit in human hematopoietic stem cells. Cell Stem Cell *16*, 302–313. https://doi.org/10.1016/j.stem.2015.01.017.
67. Zeng, A.G.X., Nagree, M.S., Jakobsen, N.A., Shah, S., Murison, A., Cheong, J.-G., Turkalj, S., Lim, I.N.X., Jin, L., Araújo, J., et al. (2023). Identification of a human hematopoietic stem cell subset that retains memory of inflammatory stress.

Preprint at bioRxiv, https://doi.org/10.1101/2023.09.11.557271 https://doi.org/10.1101/2023.09.11.557271.

68. Johnson, C.S., Williams, M., Sham, K., Belluschi, S., Ma, W., Wang, X., Lau, W.W.Y., Kaufmann, K.B., Krivdova, G., Calderbank, E.F., et al. Adaptation to ex vivo culture reduces human hematopoietic stem cell activity independently of the cell cycle.
69. Schönberger, K., Obier, N., Romero-Mulero, M.C., Cauchy, P., Mess, J., Pavlovich, P. V., Zhang, Y.W., Mitterer, M., Rettkowski, J., Lalioti, M.E., et al. (2022). Multilayer omics analysis reveals a non-classical retinoic acid signaling axis that regulates hematopoietic stem cell identity. Cell Stem Cell *29*, 131-148.e10. https://doi.org/10.1016/j.stem.2021.10.002.
70. García-Prat, L., Kaufmann, K.B., Schneiter, F., Voisin, V., Murison, A., Chen, J., Chan- Seng-Yue, M., Gan, O.I., McLeod, J.L., Smith, S.A., et al. (2021). TFEB-mediated endolysosomal activity controls human hematopoietic stem cell fate. Cell Stem Cell *28*, 1838-1850.e10. https://doi.org/10.1016/j.stem.2021.07.003.
71. Jacobs, K., Doerdelmann, C., Krietsch, J., González-Acosta, D., Mathis, N., Kushinsky, S., Guarino, E., Gómez-Escolar, C., Martinez, D., Schmid, J.A., et al. (2022). Stress-triggered hematopoietic stem cell proliferation relies on PrimPol-mediated repriming. Mol Cell *82*, 4176-4188.e8. https://doi.org/10.1016/j.molcel.2022.09.009.
72. della Volpe, L., Midena, F., Vacca, R., Tavella, T., Alessandrini, L., Farina, G., Brandas, C., Lo Furno, E., Giannetti, K., Carsana, E., et al. (2024). A p38 MAPK-ROS axis fuels proliferation stress and DNA damage during CRISPR-Cas9 gene editing in hematopoietic stem and progenitors cells
73. Xu, C.-X., Lee, T.-J., Sakurai, N., Krchma, K., Liu, F., Li, D., Wang, T., and Choi, K. (2017). ETV2/ER71 regulates hematopoietic regeneration by promoting hematopoietic stem cell proliferation. J Exp Med *214*, 1643–1653. https://doi.org/10.1084/jem.20160923.
74. Pimanda, J.E., Ottersbach, K., Knezevic, K., Kinston, S., Chan, W.Y.I., Wilson, N.K., Landry, J.-R., Wood, A.D., Kolb-Kokocinski, A., Green, A.R., et al. (2007). Gata2, Fli1, and Scl form a recursively wired gene-regulatory circuit during early hematopoietic development. Proc Natl Acad Sci U S A *104*, 17692–17697. https://doi.org/10.1073/pnas.0707045104.
75. Kruse, E.A., Loughran, S.J., Baldwin, T.M., Josefsson, E.C., Ellis, S., Watson, D.K., Nurden, P., Metcalf, D., Hilton, D.J., Alexander, W.S., et al. (2009). Dual requirement for the ETS transcription factors Fli-1 and Erg in hematopoietic stem cells and the megakaryocyte lineage. Proc Natl Acad Sci U S A *106*, 13814–13819. https://doi.org/10.1073/pnas.0906556106.
76. Iaquinta, P.J., and Lees, J.A. Life and death decisions by the E2F transcription factors.
77. Luc, S., Huang, J., McEldoon, J.L., Somuncular, E., Li, D., Rhodes, C., Mamoor, S., Hou, S., Xu, J., and Orkin, S.H. (2016). Bcl11a Deficiency Leads to Hematopoietic Stem Cell Defects with an Aging-like Phenotype. Cell Rep *16*, 3181–3194. https://doi.org/10.1016/j.celrep.2016.08.064.
78. Amsellem, S., Pflumio, F., Bardinet, D., Izac, B., Charneau, P., Romeo, P.-H., Dubart-Kupperschmitt, A., and Fichelson, S. (2003). Ex vivo expansion of human hematopoietic stem cells by direct delivery of the HOXB4 homeoprotein. Nat Med *9*, 1423–1427. https://doi.org/10.1038/nm953.
79. Sauvageau, G., Thorsteinsdottir, U., Eaves, C.J., Lawrence, H.J., Largman, C., Lansdorp, P.M., and Humphries, R.K. (1995). Overexpression of HOXB4 in

hematopoietic cells causes the selective expansion of more primitive populations in vitro and in vivo. Genes Dev *9*, 1753–1765. https://doi.org/10.1101/gad.9.14.1753.

80. Miller, C.L., and Eaves, C.J. (1997). Expansion in vitro of adult murine hematopoietic stem cells with transplantable lympho-myeloid reconstituting ability. Proc Natl Acad Sci U S A *94*, 13648–13653. https://doi.org/10.1073/pnas.94.25.13648.
81. Conneally, E., Cashman, J., Petzer, A., and Eaves, C. (1997). Expansion *in vitro* of transplantable human cord blood stem cells demonstrated using a quantitative assay of their lympho-myeloid repopulating activity in nonobese diabetic– *scid/scid* mice. Proceedings of the National Academy of Sciences *94*, 9836–9841. https://doi.org/10.1073/pnas.94.18.9836.
82. Bhatia, M., Bonnet, D., Kapp, U., Wang, J.C., Murdoch, B., and Dick, J.E. (1997). Quantitative analysis reveals expansion of human hematopoietic repopulating cells after short-term ex vivo culture. J Exp Med *186*, 619–624. https://doi.org/10.1084/jem.186.4.619.
83. Ferrari, G., Thrasher, A.J., and Aiuti, A. (2021). Gene therapy using haematopoietic stem and progenitor cells. Nat Rev Genet *22*, 216–234. https://doi.org/10.1038/s41576-020-00298-5.
84. Ferrari, S., Valeri, E., Conti, A., Scala, S., Aprile, A., Di Micco, R., Kajaste-Rudnitski, A., Montini, E., Ferrari, G., Aiuti, A., et al. (2023). Genetic engineering meets hematopoietic stem cell biology for next-generation gene therapy. Cell Stem Cell *30*, 549–570. https://doi.org/10.1016/j.stem.2023.04.014.
85. Akinduro, O., Weber, T.S., Ang, H., Haltalli, M.L.R., Ruivo, N., Duarte, D., Rashidi, N.M., Hawkins, E.D., Duffy, K.R., and Lo Celso, C. (2018). Proliferation dynamics of acute myeloid leukaemia and haematopoietic progenitors competing for bone marrow space. Nat Commun *9*, 519. https://doi.org/10.1038/s41467-017-02376-5.
86. Olive, P.L., and Banáth, J.P. (2006). The comet assay: a method to measure DNA damage in individual cells. Nat Protoc *1*, 23–29. https://doi.org/10.1038/nprot.2006.5.
87. Ciccia, A., and Elledge, S.J. (2010). The DNA damage response: making it safe to play with knives. Mol Cell *40*, 179–204. https://doi.org/10.1016/j.molcel.2010.09.019.
88. Spencer Chapman, M., Wilk, C.M., Boettcher, S., Mitchell, E., Dawson, K., Williams, N., Müller, J., Kovtonyuk, L., Jung, H., Caiado, F., et al. (2024). Clonal dynamics after allogeneic haematopoietic cell transplantation. Nature *635*, 926–934. https://doi.org/10.1038/s41586-024-08128-y.
89. Zeng, A.G.X., Nagree, M.S., Jakobsen, N.A., Shah, S., Murison, A., Cheong, J.-G., Lim, I., Jin, L., Aguilar-Navarro, A.G., Araujo, J., et al. (2023). A hematopoietic stem cell subset that retains memory of prior inflammatory stress accumulates in aging and clonal hematopoiesis. bioRxiv, 2023.09.11.557271. https://doi.org/10.1101/2023.09.11.557271.
90. McEwen, B.S. (2003). Interacting mediators of allostasis and allostatic load: towards an understanding of resilience in aging. Metabolism *52*, 10–16. https://doi.org/10.1016/S0026- 0495(03)00295-6.
91. Cirovic, B., de Bree, L.C.J., Groh, L., Blok, B.A., Chan, J., van der Velden, W.J.F.M., Bremmers, M.E.J., van Crevel, R., Händler, K., Picelli, S., et al. (2020). BCG Vaccination in Humans Elicits Trained Immunity via the Hematopoietic Progenitor Compartment. Cell Host Microbe *28*, 322-334.e5.

https://doi.org/10.1016/j.chom.2020.05.014.

92. de Laval, B., Maurizio, J., Kandalla, P.K., Brisou, G., Simonnet, L., Huber, C., Gimenez, G., Matcovitch-Natan, O., Reinhardt, S., David, E., et al. (2020). C/EBPβ-Dependent Epigenetic Memory Induces Trained Immunity in Hematopoietic Stem Cells. Cell Stem Cell *26*, 657- 674.e8. https://doi.org/10.1016/j.stem.2020.01.017.
93. Kaufmann, E., Sanz, J., Dunn, J.L., Khan, N., Mendonça, L.E., Pacis, A., Tzelepis, F., Pernet, E., Dumaine, A., Grenier, J.-C., et al. (2018). BCG Educates Hematopoietic Stem Cells to Generate Protective Innate Immunity against Tuberculosis. Cell *172*, 176-190.e19. https://doi.org/10.1016/j.cell.2017.12.031.
94. Naik, S., and Fuchs, E. (2022). Inflammatory memory and tissue adaptation in sickness and in health. Nature *607*, 249–255. https://doi.org/10.1038/s41586-022-04919-3.
95. Bogeska, R., Mikecin, A.-M., Kaschutnig, P., Fawaz, M., Büchler-Schäff, M., Le, D., Ganuza, M., Vollmer, A., Paffenholz, S. V, Asada, N., et al. (2022). Inflammatory exposure drives long-lived impairment of hematopoietic stem cell self-renewal activity and accelerated aging. Cell Stem Cell *29*, 1273-1284.e8. https://doi.org/10.1016/j.stem.2022.06.012.
96. Naik, S., Larsen, S.B., Gomez, N.C., Alaverdyan, K., Sendoel, A., Yuan, S., Polak, L., Kulukian, A., Chai, S., and Fuchs, E. (2017). Inflammatory memory sensitizes skin epithelial stem cells to tissue damage. Nature *550*, 475–480. https://doi.org/10.1038/nature24271.
97. Flach, J., Bakker, S.T., Mohrin, M., Conroy, P.C., Pietras, E.M., Reynaud, D., Alvarez, S., Diolaiti, M.E., Ugarte, F., Forsberg, E.C., et al. (2014). Replication stress is a potent driver of functional decline in ageing haematopoietic stem cells. https://doi.org/10.1038/nature13619.
98. Jacobs, K., Doerdelmann, C., Krietsch, J., González-Acosta, D., Mathis, N., Kushinsky, S., Guarino, E., Gómez-Escolar, C., Martinez, D., Schmid, J.A., et al. (2022). Stress-triggered hematopoietic stem cell proliferation relies on PrimPol-mediated repriming. Mol Cell *82*, 4176-4188.e8. https://doi.org/10.1016/j.molcel.2022.09.009.
99. Walter, D., Lier, A., Geiselhart, A., Thalheimer, F.B., Huntscha, S., Sobotta, M.C., Moehrle, B., Brocks, D., Bayindir, I., Kaschutnig, P., et al. (2015). Exit from dormancy provokes DNA-damage-induced attrition in haematopoietic stem cells. Nature *520*, 549–552. https://doi.org/10.1038/nature14131.
100. Lahav, M., Uziel, O., Kestenbaum, M., Fraser, A., Shapiro, H., Radnay, J., Szyper-Kravitz, M., Avihai, S., Hardan, I., Shem-Tov, N., et al. (2005). Nonmyeloablative Conditioning Does Not Prevent Telomere Shortening after Allogeneic Stem Cell Transplantation. Transplantation *80*, 969–976. https://doi.org/10.1097/01.TP.0000173649.99261.DF.
101. Perna, S., Francis, M.D., Bologna, C., Moncaglieri, F., Riva, A., Morazzoni, P., Allegrini, P., Isu, A., Vigo, B., Guerriero, F., et al. (2017). Performance of Edmonton Frail Scale on frailty assessment: its association with multi-dimensional geriatric conditions assessed with specific screening tools. BMC Geriatr *17*, 2. https://doi.org/10.1186/s12877-016-0382-3.
102. Aguilar-Navarro, A.G., Meza-León, B., Gratzinger, D., Juárez-Aguilar, F.G., Chang, Q., Ornatsky, O., Tsui, H., Esquivel-Gómez, R., Hernández-Ramírez, A., Xie, S.Z., et al. (2020). Human Aging Alters the Spatial Organization between CD34+ Hematopoietic Cells and Adipocytes in Bone Marrow. Stem Cell Reports *15*, 317–325.

https://doi.org/10.1016/j.stemcr.2020.06.011.

103. Xie, S.Z., Garcia-Prat, L., Voisin, V., Ferrari, R., Gan, O.I., Wagenblast, E., Kaufmann, K.B., Zeng, A.G.X., Takayanagi, S., Patel, I., et al. (2019). Sphingolipid Modulation Activates Proteostasis Programs to Govern Human Hematopoietic Stem Cell Self-Renewal. Cell Stem Cell *25*, 639-653.e7. https://doi.org/10.1016/j.stem.2019.09.008.
104. Lai, Z., Markovets, A., Ahdesmaki, M., Chapman, B., Hofmann, O., McEwen, R., Johnson, J., Dougherty, B., Barrett, J.C., and Dry, J.R. (2016). VarDict: a novel and versatile variant caller for next-generation sequencing in cancer research. Nucleic Acids Res *44*, e108. https://doi.org/10.1093/nar/gkw227.
105. Ahdesmäki, M.J., Gray, S.R., Johnson, J.H., and Lai, Z. (2016). Disambiguate: An open- source application for disambiguating two species in next generation sequencing data from grafted samples. F1000Res *5*, 2741. https://doi.org/10.12688/f1000research.10082.1.
106. Li, H., and Durbin, R. (2009). Fast and accurate short read alignment with Burrows-Wheeler transform. Bioinformatics *25*, 1754–1760. https://doi.org/10.1093/bioinformatics/btp324.
107. Smigielski, E.M., Sirotkin, K., Ward, M., and Sherry, S.T. (2000). dbSNP: a database of single nucleotide polymorphisms. Nucleic Acids Res *28*, 352–355. https://doi.org/10.1093/nar/28.1.352.
108. Jakobsen, N.A., Turkalj, S., Zeng, A.G.X., Stoilova, B., Metzner, M., Rahmig, S., Nagree, M.S., Shah, S., Moore, R., Usukhbayar, B., et al. (2024). Selective advantage of mutant stem cells in human clonal hematopoiesis is associated with attenuated response to inflammation and aging. Cell Stem Cell *31*, 1127-1144.e17. https://doi.org/10.1016/j.stem.2024.05.010.
109. Gu, Z., Eils, R., and Schlesner, M. (2016). Complex heatmaps reveal patterns and correlations in multidimensional genomic data. Bioinformatics *32*, 2847–2849. https://doi.org/10.1093/bioinformatics/btw313.
110. Hu, Y., and Smyth, G.K. (2009). ELDA: extreme limiting dilution analysis for comparing depleted and enriched populations in stem cell and other assays. J Immunol Methods *347*, 70–78. https://doi.org/10.1016/j.jim.2009.06.008.
111. Butler, A., Hoffman, P., Smibert, P., Papalexi, E., and Satija, R. (2018). Integrating single- cell transcriptomic data across different conditions, technologies, and species. Nat Biotechnol *36*, 411–420. https://doi.org/10.1038/nbt.4096.
112. Stuart, T., Butler, A., Hoffman, P., Hafemeister, C., Papalexi, E., Mauck, W.M., Hao, Y., Stoeckius, M., Smibert, P., and Satija, R. (2019). Comprehensive Integration of Single-Cell Data. Cell *177*, 1888-1902.e21. https://doi.org/10.1016/j.cell.2019.05.031.
113. Buenrostro, J.D., Giresi, P.G., Zaba, L.C., Chang, H.Y., and Greenleaf, W.J. (2013). Transposition of native chromatin for fast and sensitive epigenomic profiling of open chromatin, DNA-binding proteins and nucleosome position. Nat Methods *10*, 1213–1218. https://doi.org/10.1038/nmeth.2688.
114. Li, H., and Durbin, R. (2009). Fast and accurate short read alignment with Burrows-Wheeler transform. Bioinformatics *25*, 1754–1760. https://doi.org/10.1093/bioinformatics/btp324.
115. Zhang, Y., Liu, T., Meyer, C.A., Eeckhoute, J., Johnson, D.S., Bernstein, B.E., Nusbaum, C., Myers, R.M., Brown, M., Li, W., et al. (2008). Model-based Analysis of

ChIP-Seq (MACS). Genome Biol *9*, R137. https://doi.org/10.1186/gb-2008-9-9-r137.

116. Gaujoux, R., and Seoighe, C. (2010). A flexible R package for nonnegative matrix factorization. BMC Bioinformatics *11*, 367. https://doi.org/10.1186/1471-2105-11-367.

117. Heinz, S., Benner, C., Spann, N., Bertolino, E., Lin, Y.C., Laslo, P., Cheng, J.X., Murre, C., Singh, H., and Glass, C.K. (2010). Simple Combinations of Lineage-Determining

Transcription Factors Prime cis-Regulatory Elements Required for Macrophage and B Cell Identities. Mol Cell *38*, 576–589. https://doi.org/10.1016/j.molcel.2010.05.004.

118. Heinz, S., Benner, C., Spann, N., Bertolino, E., Lin, Y.C., Laslo, P., Cheng, J.X., Murre, C., Singh, H., and Glass, C.K. (2010). Simple combinations of lineage-determining transcription factors prime cis-regulatory elements required for macrophage and B cell identities. Mol Cell *38*, 576–589. https://doi.org/10.1016/j.molcel.2010.05.004.

119. Subramanian, A., Tamayo, P., Mootha, V.K., Mukherjee, S., Ebert, B.L., Gillette, M.A., Paulovich, A., Pomeroy, S.L., Golub, T.R., Lander, E.S., et al. (2005). Gene set enrichment analysis: A knowledge-based approach for interpreting genome-wide expression profiles. Proceedings of the National Academy of Sciences *102*, 15545–15550. https://doi.org/10.1073/pnas.0506580102

Figure Legends

Figure 1

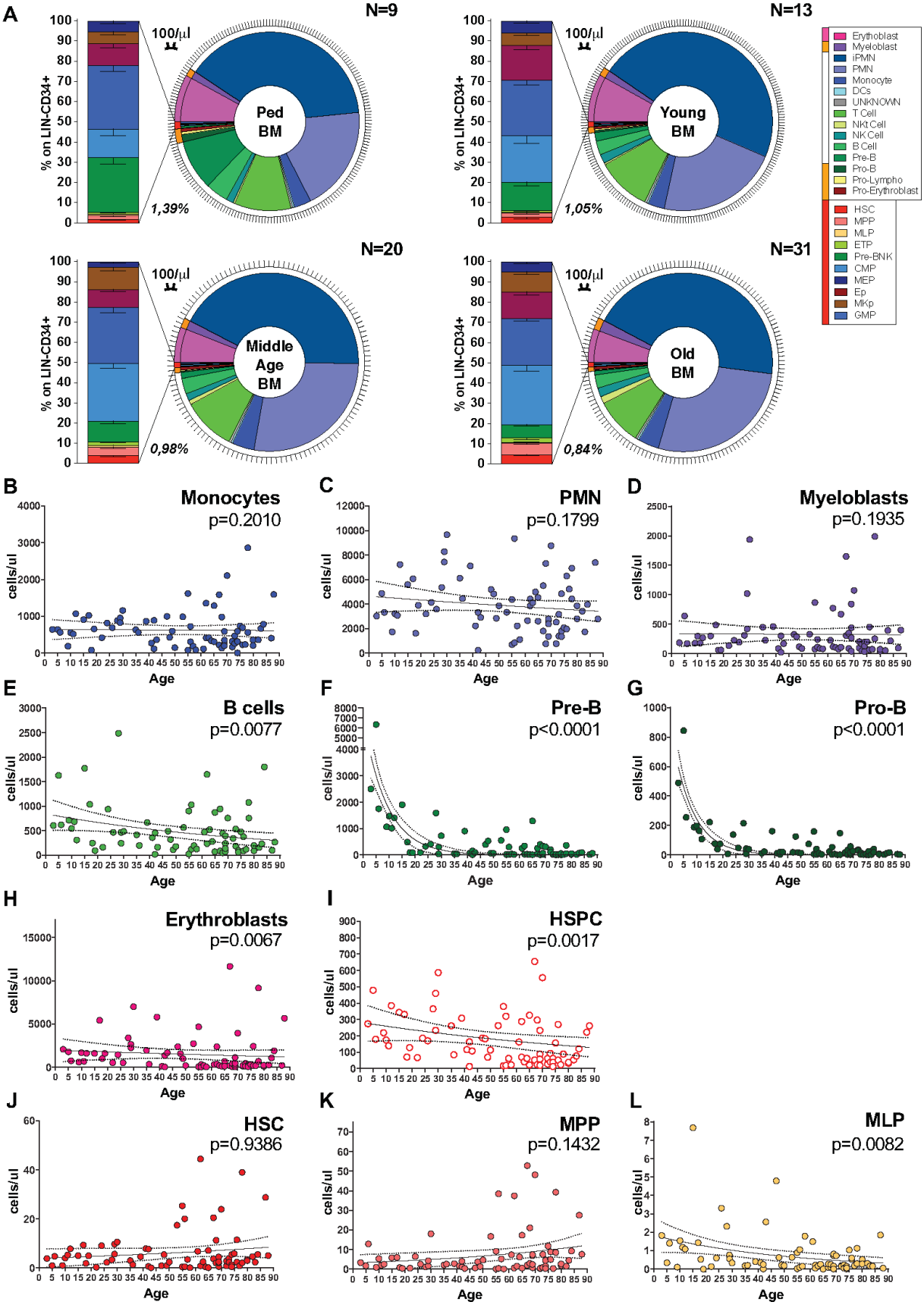

Figure 1. Bone marrow composition of healthy subjects over aging. A. (from top left to bottom right) Hematopoietic composition of BM samples from pediatric (< 18 years old, n=9), young adult (18-40 years old; n=13), middle age (40-65 years old; n=20) and old (>65 years old; n=31) healthy subjects. Pie charts show the distribution of 25 hematopoietic subsets within the CD45+ gate. Black outer ticks indicate absolute count (1000 cells/µl). Percentages indicate the frequency of the HSPC population (CD34+ LIN-) on total CD45+ cells. The stacked bar graphs indicate the frequency of HSPC subpopulations on LIN-CD34+ cells. **B-L.** Correlation analysis of the absolute counts of each cell subtype (expressed as cells/µL) in the BM with the age of 73 subjects analyzed. HSC, hematopoietic stem cells; MPP, multi-potent progenitors; MLP, multi-lymphoid progenitors; PMN, polymorphonucleated cells. Statistical test for correlation: Spearman r.

Figure 2

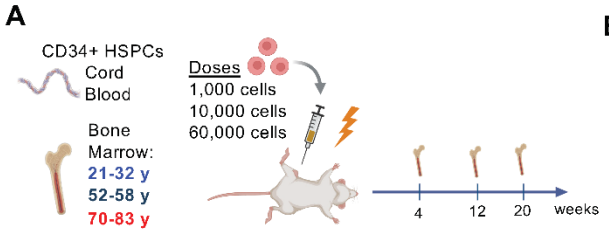

B

CD34+ source	1/ (CD34+ repopulating cell frequency)		
	4 weeks (# mice)	12 weeks (# mice)	20 weeks (# mice)
Cord Blood	**1647** (22)	**1694** (24)	**504** (17)
Y (21-32)	**11944** (27)	**10052** (28)	**36280** (18)
M (52-57y)	**4487** (29)	**1208** (30)	**14537** (13)
O (78-83 y)	**5574** (38)	**1097** (33)	**12247** (35)
	116 mice	115 mice	83 mice

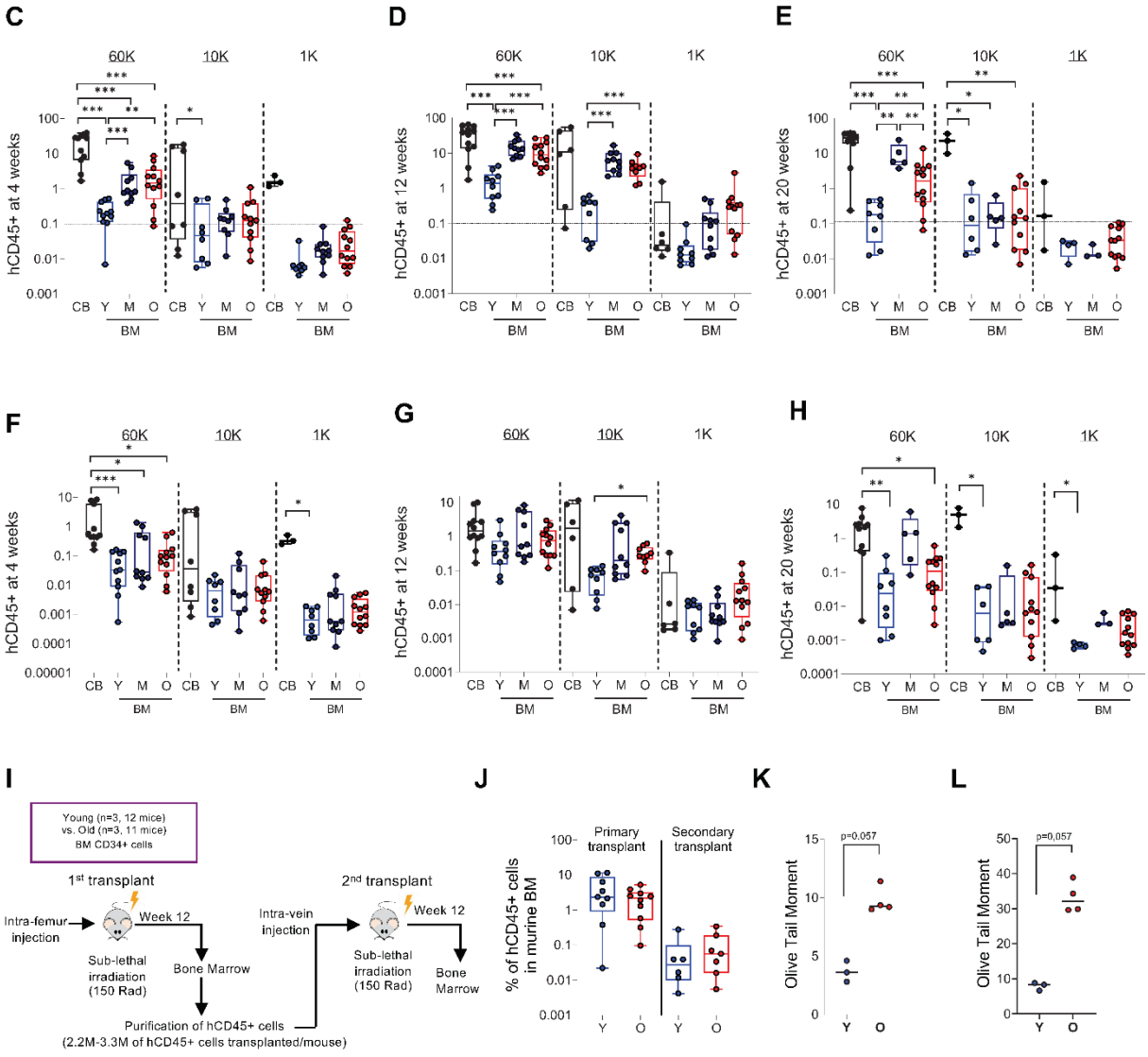

Figure 2. Limiting dilution xenotransplantation assays of uncultured HSPC show a

higher frequency of repopulating cells in aged HSPC compared to young HSPC. A. Experimental scheme using 3 cell doses in a xenotransplantation time course experiment where human CD45^{+} engraftment and lineage in the bone marrow of NSG mice were assessed at 4, 12, and 20 weeks for the indicated human HSPC cell sources. **B.** The CD34+ repopulating cell frequency for 4, 12 and 20 weeks for CB and BM samples from indicated age groups. **C-E.** Box plots showing human CD45+ cell frequencies in the murine BM in mice transplanted with 60K, 10K and 1K HSPC for CB and BM samples at 4 **(C)**, 12 **(D)**, and 20 **(E)** weeks. **F-H.** Box plots showing human CD45+ cell frequencies in the murine BM in mice transplanted with 60K, 10K and 1K HSPC for CB and BM samples at 4 **(F)**, 12 **(G)**, and 20 **(H)** weeks normalized on the HSC+MPP content of the infused cells. **I.** Experimental scheme for secondary transplant. CD34+ cells isolated from 3 young and 3 old donors were intrafemorally transplanted in 23 primary recipients (each donor into 3-4 mice). At 12 weeks post-transplant, human CD45+ cells from the BM of primary mice were collected and transplanted into 23 secondary recipients. The murine BM of the secondary recipients was analyzed at 12 weeks. Transplanted mice with engraftment below 0.05% in the murine BM were considered not engrafted and excluded from the graphical representation **J**. Box plots showing human CD45+ cell frequencies in the murine BM in primary and secondary recipients at 12 weeks, normalized on the content of HSC+MPP infused. **K-L.** Olive Tail Moment average values of neutral (**K**) or alkaline (**L**) comet experiments conducted in CD34+ isolated at 12 weeks after secondary transplantation of CD34+ cells from young and old donors (CD34+ isolated from the mice transplanted with the same donor were pooled) Statistical test for multiple comparisons: Kruskal- Wallis test with Dunn's correction for multiple comparisons; Mann-Whitney test.

Figure 3

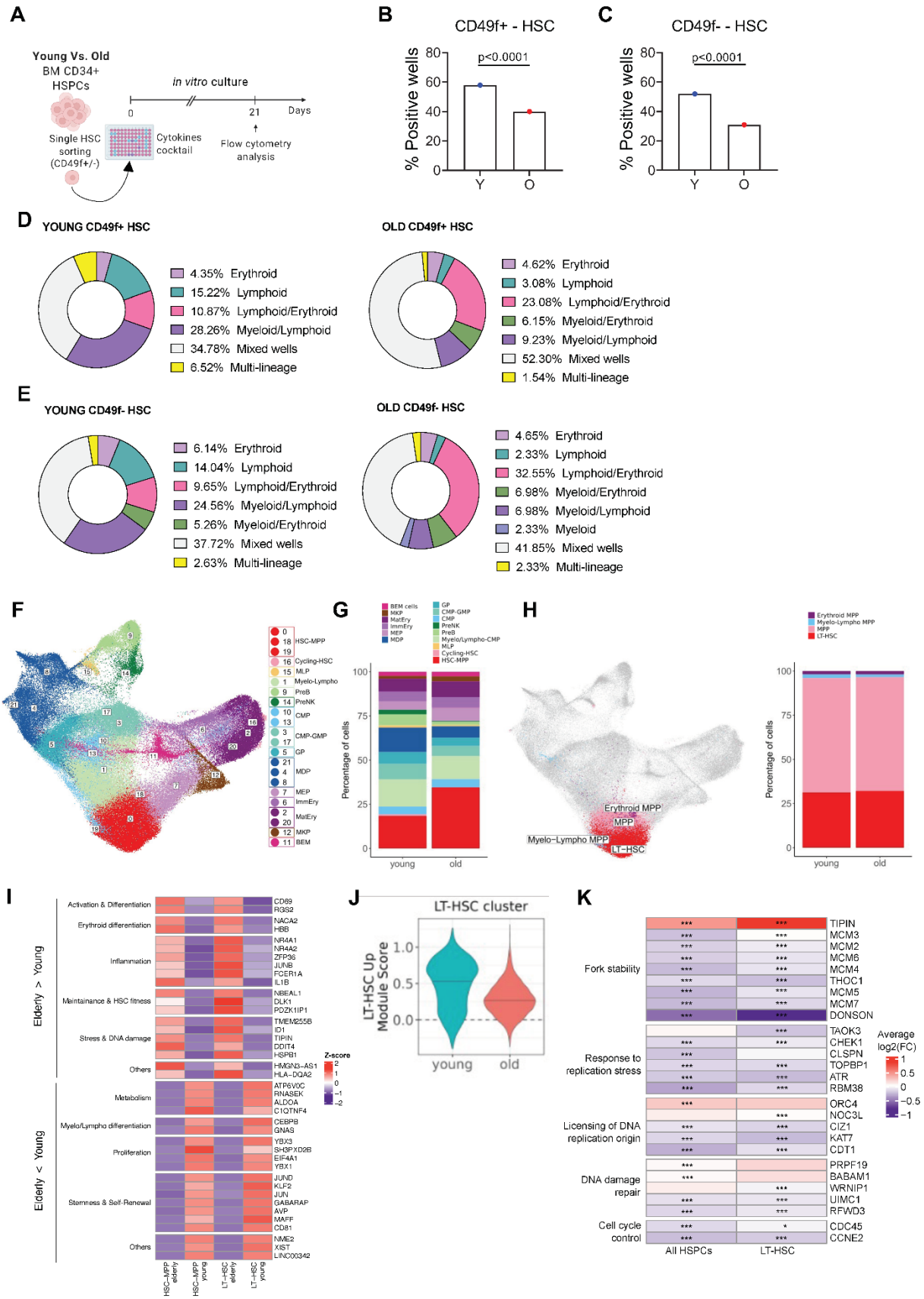
A
Young Vs. Old
BM CD34+
HSPCs
in vitro culture
0
21
Days
Single HSC
sorting
(CD49f+/-)
Cytokines
cocktail
Flow cytometry
analysis
B
CD49f+ - HSC
p<0.0001
% Positive wells
Y
O
C
CD49f- - HSC
p<0.0001
% Positive wells
Y
O
D
YOUNG CD49f+ HSC
4.35% Erythroid
15.22% Lymphoid
10.87% Lymphoid/Erythroid
28.26% Myeloid/Lymphoid
34.78% Mixed wells
6.52% Multi-lineage
OLD CD49f+ HSC
4.62% Erythroid
3.08% Lymphoid
23.08% Lymphoid/Erythroid
6.15% Myeloid/Erythroid
9.23% Myeloid/Lymphoid
52.30% Mixed wells
1.54% Multi-lineage
E
YOUNG CD49f- HSC
6.14% Erythroid
14.04% Lymphoid
9.65% Lymphoid/Erythroid
24.56% Myeloid/Lymphoid
5.26% Myeloid/Erythroid
37.72% Mixed wells
2.63% Multi-lineage
OLD CD49f- HSC
4.65% Erythroid
2.33% Lymphoid
32.55% Lymphoid/Erythroid
6.98% Myeloid/Erythroid
6.98% Myeloid/Lymphoid
2.33% Myeloid
41.85% Mixed wells
2.33% Multi-lineage
F
HSC-MPP
Cycling-HSC
MLP
Myelo-Lympho
PreB
PreNK
CMP
CMP-GMP
GP
MDP
MEP
ImmEry
MatEry
MKP
BEM
G
Percentage of cells
young
old
H
Erythroid MPP
MPP
Myelo-Lympho MPP
LT-HSC
Percentage of cells
young
old
I
Elderly > Young
Elderly < Young
Activation & Differentiation
Erythroid differentiation
Inflammation
Maintainance & HSC fitness
Stress & DNA damage
Others
Metabolism
Myelo/Lympho differentiation
Proliferation
Stemness & Self-Renewal
Others
Z-score
HSC-MPP elderly
HSC-MPP young
LT-HSC elderly
LT-HSC young
J
LT-HSC cluster
LT-HSC Up Module Score
young
old
K
Fork stability
Response to replication stress
Licensing of DNA replication origin
DNA damage repair
Cell cycle control
TIPIN
MCM3
MCM2
MCM6
MCM4
THOC1
MCM5
MCM7
DONSON
TAOK3
CHEK1
CLSPN
TOPBP1
ATR
RBM38
ORC4
NOC3L
CIZ1
KAT7
CDT1
PRPF19
BABAM1
WRNIP1
UIMC1
RFWD3
CDC45
CCNE2
Average log2(FC)
All HSPCs
LT-HSC

Figure 3. Single cell functional and transcriptomic analyses of aged LT-HSC. A. Experimental scheme for *in vitro* multi-lineage differentiation assay on single CD49f+/- HSC (100 cells/donor for a total of 600 cells) from young (n=3) and old (n=3) donors. **B-C**. Differentiation efficiency of single CD49f+ HSC (B) and CD49f- HSC (C) from young and old donors. Pearson's Chi-squared test with Yates' continuity correction was used to measure statistical significance of the observed differences. **D-E**. Pie charts representing the lineage scores of young and old CD49f+ HSC (D) and CD49f- HSC (E), based on the most abundant differentiation outputs toward lymphoid, myeloid, erythroid and megakaryocyte lineages detected at the end of the single-cell in vitro differentiation assay. Cells showing differentiation toward all the 4 lineages were scored as “multi-lineage”. **F.** UMAP embedding showing 21 seurat clusters identified after unsupervised clustering. The legend on the right shows the annotation of the single clusters. **G**. Stacked bar graph showing the distribution of the transcriptional annotated clusters in young and old HSPC. **H** On the left, UMAP embedding showing 4 annotated seurat subclusters identified after unsupervised clustering of cluster 0. On the right, stacked bar graph showing the distribution of the 4 transcriptional subclusters in young and old HSC. **I.** Heatmap showing the top-20 differentially upregulated and down-regulated genes between young and old HSC-MPP or LT-HSC. **J**. Expression of LT-HSC module score on young and old LT-HSC. The module score was computed based on a set of marker genes associated to LT-HSC properties derived from previous publications. **K.** Heatmap showing average log2FC of genes related to DNA replication stress between young and old HSPC or LT-HSC. Genes found statistically significant in at least one of the two cell populations with log2FC < -0.1 and > 0.1 were shown.

Figure 4

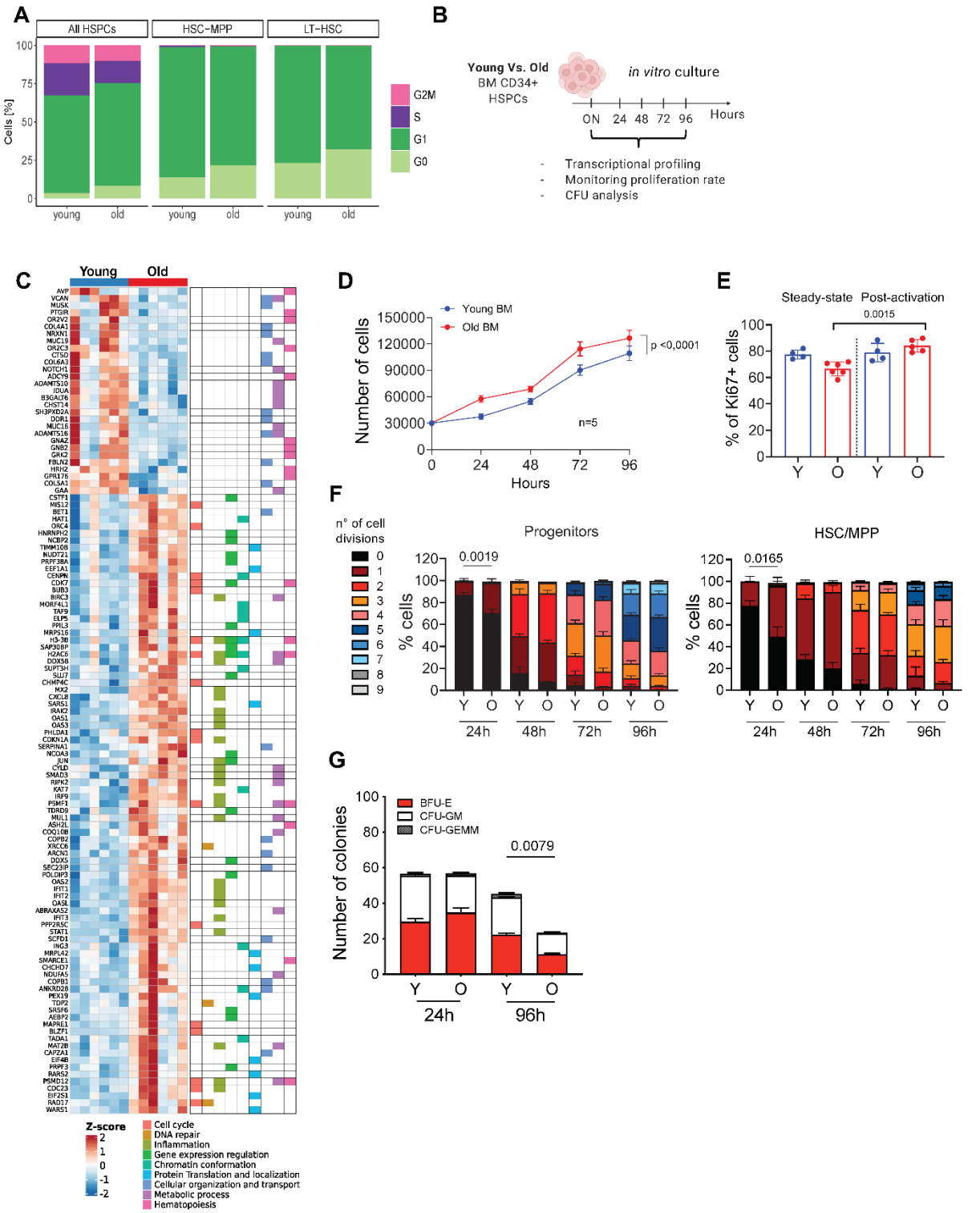
A
All HSPCs
HSC-MPP
LT-HSC
Cells [%]
young
old
G2M
S
G1
G0
B
Young Vs. Old
BM CD34+
HSPCs
in vitro culture
ON 24 48 72 96
Hours
- Transcriptional profiling
- Monitoring proliferation rate
- CFU analysis
C
Young
Old
Z-score
Cell cycle
DNA repair
Inflammation
Gene expression regulation
Chromatin conformation
Protein Translation and localization
Cellular organization and transport
Metabolic process
Hematopoiesis
D
Young BM
Old BM
Number of cells
p <0,0001
n=5
Hours
E
Steady-state
Post-activation
0.0015
% of Ki67+ cells
Y
O
F
n° of cell divisions
Progenitors
HSC/MPP
0.0019
0.0165
% cells
24h
48h
72h
96h
G
BFU-E
CFU-GM
CFU-GEMM
0.0079
Number of colonies
24h
96h

Figure 4. *In vitro* functional characterization of human aged HSPC. A. Histograms representing the percentage of cells in G0, G1, S, and G2M cell cycle phases for total HSPC, HSC-MPP and LT- HSC in old and young donors from scRNAseq dataset. **B.** Experimental scheme for *in vitro* proliferation assay. 3x10^5 BM-derived CD34+ cells from young and old individuals were cultured in the presence of the human recombinant cytokines and analyzed at the indicated time points for transcriptome, proliferation rate and clonogenic potential. **C.** Graph showing, on the left, a heatmap with DEGs between young (n=6) and old (n=6) CD34+ cells upon overnight activation in culture and, on the right, the Reactome categories associated with the distinct genes. **D.** Growth curve showing the proliferation of both BM-derived young (n=5) and old (n=5) CD34+ cells. Data are shown as mean SD. **E.** Fold change of Ki67+ cells relative to overnight activated condition of young (n=4) and aged (n=5) BM-derived CD34+ cells at 24h after culture. Data are shown as mean SD. **F**. Stacked bar graphs showing the frequencies of cells that completed one or more cell division over time in culture in young and old Progenitor (**left**) and HSC/MPP (**right**) subsets. **G.** Number of erythroid (BFU-E), myeloid (CFU-GEM) and mixed (CFU-GEMM) colonies generated starting from 800 alive BM-derived CD34+ cells of young (n=5) and old(n=5) donors upon activation in culture. Colonies were counted 14 days after plating in CFU-C assay. Data are shown as mean SEM. Statistical test for growth curves: Linear mixed-effects (LME) model. Statistical test for group comparison: Mann-Whitney test.

Figure 5

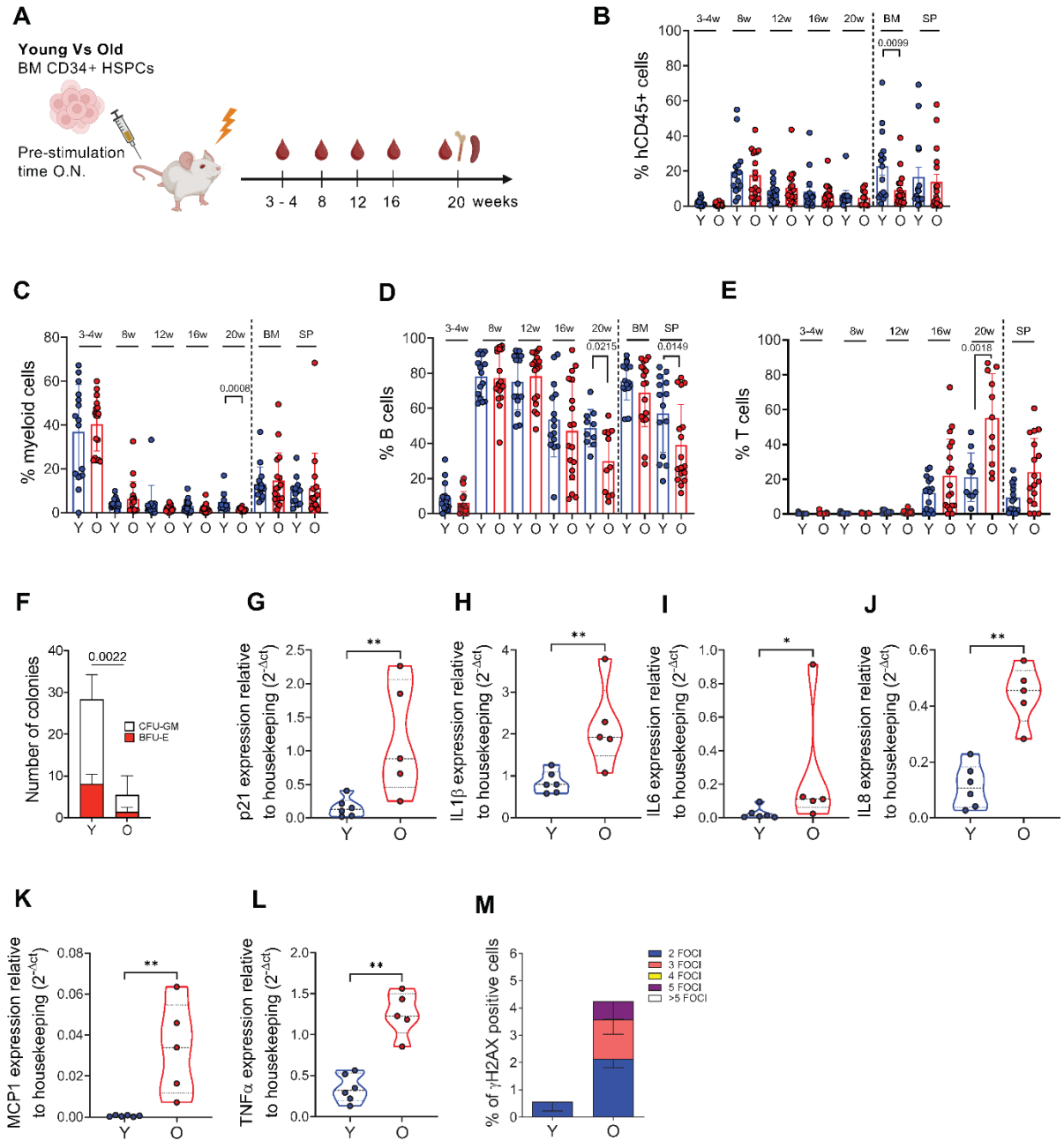
A
Young Vs Old
BM CD34+ HSPCs
Pre-stimulation
time O.N.
3 - 4
8
12
16
20 weeks
B
% hCD45+ cells
3-4w
8w
12w
16w
20w
BM
SP
0.0099
C
% myeloid cells
0.0008
D
% B cells
0.0215
0.0149
E
% T cells
0.0018
F
Number of colonies
0.0022
CFU-GM
BFU-E
G
p21 expression relative to housekeeping (2-Δct)
H
IL1β expression relative to housekeeping (2-Δct)
I
IL6 expression relative to housekeeping (2-Δct)
J
IL8 expression relative to housekeeping (2-Δct)
K
MCP1 expression relative to housekeeping (2-Δct)
L
TNFα expression relative to housekeeping (2-Δct)
M
% of γH2AX positive cells
2 FOCI
3 FOCI
4 FOCI
5 FOCI
>5 FOCI
Y
O

Figure 5. *In vivo* functional characterization of pre-activated human aged HSPC. A. Experimental scheme for xenotransplantation experiment where human CD34⁺ cells from young (n=4) and old donors (n=4) were pre-cultured overnight prior transplantation into NSG mice (n=3 mice for each donor). **B.** Percentage of human engrafted cells (CD45+ cells) in PB overtime as well as in BM and Spleen (SP) at euthanasia in mice transplanted with young or aged HSPC. **C-E.** Percentage of human myeloid cells (CD13+ cells; (C)), B cells (CD19+ cells, (D)) and T cells (CD3+ cells, (E)) in PB overtime as well as BM and SP at 20 weeks in mice transplanted with young or old HSPC. **F.** Number of colonies generated starting from the same amount of CD34+ cells isolated from transplanted mice at 20 weeks. **G-L.** Relative mRNA expression of cell cycle inhibitor *p21* and inflammatory genes *IL1□, IL6, IL8, MCP1* and *TNF□*in human CD34+ cells isolated from BM of mice transplanted with young and aged HSPC (20 weeks). Gene expression was measured by quantitative Real-Time PCR and represented as 2^-ΔCt relative to housekeeping. **M.** Frequencies of cells showing nuclear □H2AX foci in human CD34+ cells isolated from BM of mice transplanted with young and old HSPC at 20 weeks. Statistical test: Mann-Whitney test.

Figure 6

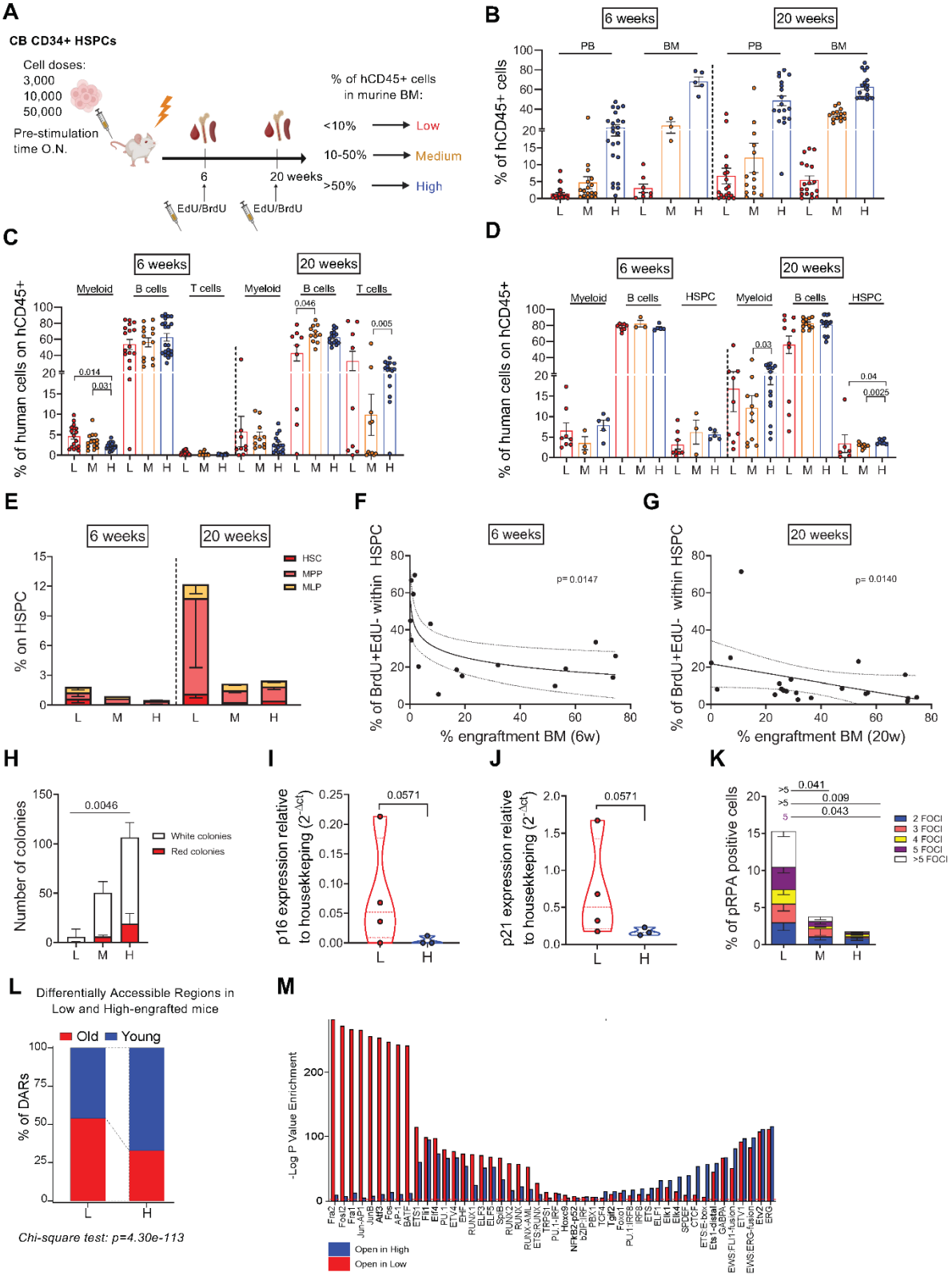
A
CB CD34+ HSPCs
Cell doses:
3,000
10,000
50,000
Pre-stimulation time O.N.
6
20 weeks
EdU/BrdU
EdU/BrdU
% of hCD45+ cells in murine BM:
<10% Low
10-50% Medium
>50% High
B
6 weeks
20 weeks
PB
BM
PB
BM
% of hCD45+ cells
C
6 weeks
20 weeks
Myeloid
B cells
T cells
% of human cells on hCD45+
D
6 weeks
20 weeks
Myeloid
B cells
HSPC
% of human cells on hCD45+
E
6 weeks
20 weeks
HSC
MPP
MLP
% on HSPC
F
6 weeks
p= 0.0147
% of BrdU+EdU- within HSPC
% engraftment BM (6w)
G
20 weeks
p= 0.0140
% of BrdU+EdU- within HSPC
% engraftment BM (20w)
H
Number of colonies
0.0046
White colonies
Red colonies
I
p16 expression relative to housekkeping (2-Δct)
0.0571
J
p21 expression relative to housekkeping (2-Δct)
0.0571
K
% of pRPA positive cells
0.041
0.009
0.043
2 FOCI
3 FOCI
4 FOCI
5 FOCI
>5 FOCI
L
Differentially Accessible Regions in Low and High-engrafted mice
Old
Young
% of DARs
Chi-square test: p=4.30e-113
M
-Log P Value Enrichment
Open in High
Open in Low

Figure 6. *In vivo* modeling of proliferation stress. A. Schematic representation of the *in vivo* transplantation setting. Three groups of mice are transplanted with different doses of CB-derived CD34+ cells. After evaluation of human cell content in the murine BM at euthanasia, mice were divided into 3 distinct categories according to the level of engraftment: Low-engrafted (L, <10% hCD45+ cells), Middle-engrafted (M, 10-50% of hCD45+ cells) and High-engrafted (H, >50% hCD45+ cells). Mice with engraftment below 0.05% in the murine bone marrow were considered not engrafted and excluded from the graphical representation. **B.** Percentage of human engrafted cells (CD45+ cells) in PB and BM of transplanted mice at both 6 and 20 weeks after transplantation**. C.** Percentage of human myeloid cells (CD33+CD66b+ cells), B cells (CD19+ cells), and T cells (CD3+ cells) in PB of transplanted mice at both 6 and 20 weeks after transplantation. **D.** Percentage of human myeloid cells (CD33+CD66b+ cells), B cells (CD19+ cells), and HSPC (CD34+ cells) in BM of transplanted mice at both 6 and 20 weeks after transplantation. **E.** Percentage of primitive HSPC subsets within BM HSPC compartment in transplanted mice at both 6 and 20 weeks after transplantation. **F-G.** Correlation between the percentage of HSPC that entered S phase per hour (BrdU+EdU-) with human engraftment in murine BM at 6 and 20 weeks after transplantation. **H.** Number of colonies generated starting from the same amount of CD34+ cells isolated from transplanted mice at 20 weeks. **I-J.** Relative mRNA expression of cell cycle inhibitors *p16* and *p21* in human CD34+ cells isolated from low or high- engrafted mice (20 weeks). **K.** Frequencies of cells showing nuclear pRPA foci in human CD34+ cells isolated from BM of transplanted mice (20 weeks). Only statistically significant p-values were reported. **L.** Differentially Accessible Regions detected in human CD34+ isolated from mice transplanted with the low and high cell input of CB-derived HSPC from ATACseq analyses, annotated with unique old and young ATAC signatures on sorted primitive HSPC (as defined in Supplementary Figure 4E-G). **M.** List of shared motifs associated to transcription binding sites enriched in high-engrafted (blue) and low-engrafted (red) mice. Red dashed line indicates adjusted p-value < 0.05.
Statistical test for multiple comparisons: Kruskal-Wallis test with Dunn's correction for multiple comparisons; Mann-Whitney test. Statistical test for association of DARs to young and old signature: Chi-square test.

Manuscript 2:

Cell Reports
Medicine

Article

A p38 MAPK-ROS axis fuels proliferation stress and DNA damage during CRISPR-Cas9 gene editing in hematopoietic stem and progenitor cells

Graphical abstract

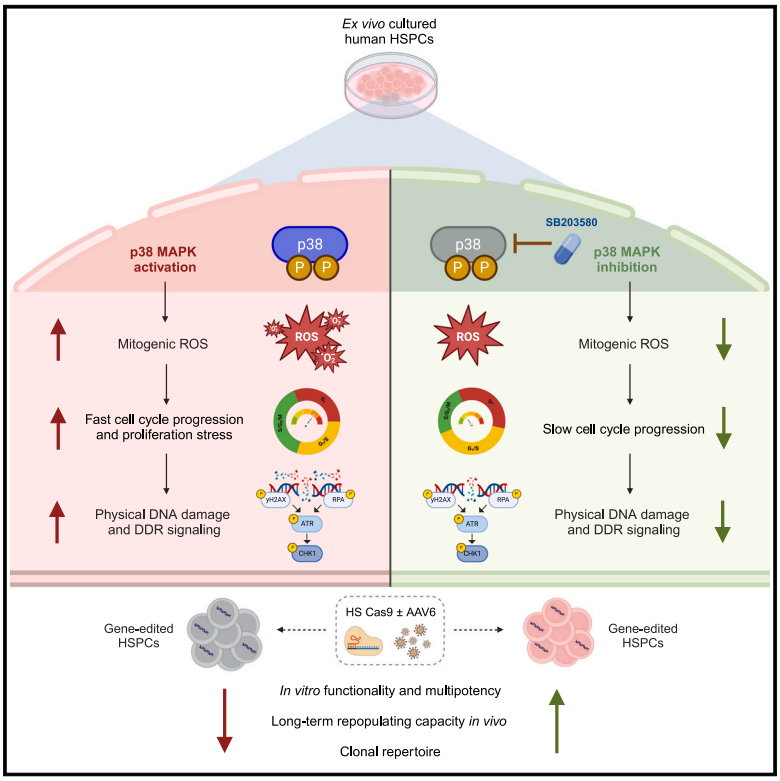

Highlights

- Shortening HSPC pre-stimulation reduces DDR-mediated responses to gene editing
- p38 MAPK-ROS induce fast cell-cycle progression fueling DNA damage and DDR signaling
- Preventing p38 activity mitigates proliferative stress and improves HSC fitness
- p38 inhibition enhances polyclonal and long-term reconstitution of edited HSPCs

Authors

Lucrezia della Volpe, Federico Midena, Roberta Vacca, ..., Anna Villa, Luigi Naldini, Raffaella Di Micco

Correspondence

dimicco.raffaella@hsr.it

In brief

Although detrimental, *ex vivo* activation of hematopoietic stem cells is required for gene editing strategies. Here, della Volpe et al. uncover a p38 MAPK-dependent molecular axis causing functional decline of gene-edited cells. Temporary p38 inhibition enhances the fitness of engineered cells for more effective and safer clinical applications.

della Volpe et al., 2024, Cell Reports Medicine *5*, 101823
November 19, 2024
https://doi.org/10.1016/j.xcrm.2024.101823

CellPress

Cell Reports Medicine

CellPress
OPEN ACCESS

Article

A p38 MAPK-ROS axis fuels proliferation stress and DNA damage during CRISPR-Cas9 gene editing in hematopoietic stem and progenitor cells

Lucrezia della Volpe,[1,2,7] Federico Midena,[1,2,7] Roberta Vacca,[1,2,7] Teresa Tavella,[1] Laura Alessandrini,[1,2] Giacomo Farina,[1,3] Chiara Brandas,[1] Elena Lo Furno,[1] Kety Giannetti,[1] Edoardo Carsana,[1] Matteo M. Naldini,[1,2] Matteo Barcella,[1] Samuele Ferrari,[1] Stefano Beretta,[1] Antonella Santoro,[1] Simona Porcellini,[1] Angelica Varesi,[1] Diego Gilioli,[1,2] Anastasia Conti,[1] Ivan Merelli,[4] Bernhard Gentner,[1,5] Anna Villa,[1,4] Luigi Naldini,[1,2] and Raffaella Di Micco[1,6,8,9,*]

[1]San Raffaele Telethon Institute for Gene Therapy (SR-Tiget), IRCCS San Raffaele Scientific Institute, 20132 Milan, Italy
[2]Vita-Salute San Raffaele University, 20132 Milan, Italy
[3]University of Milan-Bicocca, 20126 Milan, Italy
[4]National Research Council, Institute for Biomedical Technologies, 20054 Segrate, Italy
[5]Ludwig Institute for Cancer Research and Department of Oncology, University of Lausanne (UNIL) and Lausanne University Hospital (CHUV), 1066 Lausanne, Switzerland
[6]University School of Advanced Studies IUSS, 27100 Pavia, Italy
[7]These authors contributed equally
[8]X (formerly Twitter): @DiMiccoLab
[9]Lead contact
*Correspondence: dimicco.raffaella@hsr.it
https://doi.org/10.1016/j.xcrm.2024.101823

SUMMARY

Ex vivo activation is a prerequisite to reaching adequate levels of gene editing by homology-directed repair (HDR) for hematopoietic stem and progenitor cell (HSPC)-based clinical applications. Here, we show that shortening culture time mitigates the p53-mediated DNA damage response to CRISPR-Cas9-induced DNA double-strand breaks, enhancing the reconstitution capacity of edited HSPCs. However, this results in lower HDR efficiency, rendering *ex vivo* culture necessary yet detrimental. Mechanistically, *ex vivo* activation triggers a multi-step process initiated by p38 mitogen-activated protein kinase (MAPK) phosphorylation, which generates mitogenic reactive oxygen species (ROS), promoting fast cell-cycle progression and subsequent proliferation-induced DNA damage. Thus, p38 inhibition before gene editing delays G1/S transition and expands transcriptionally defined HSCs, ultimately endowing edited cells with superior multi-lineage differentiation, persistence throughout serial transplantation, enhanced polyclonal repertoire, and better-preserved genome integrity. Our data identify proliferative stress as a driver of HSPC dysfunction with fundamental implications for designing more effective and safer gene correction strategies for clinical applications.

INTRODUCTION

Ex vivo hematopoietic stem and progenitor cell (HSPC)-based gene therapies (GTs) represent a revolutionary class of ''living medicines'' for treating various monogenic diseases, including immunodeficiencies, hereditary anemias, and metabolic disorders.[1,2] GT is a multi-step process encompassing the harvest of HSPCs, *ex vivo* culture, exposure to engineering reagents, and reinfusion into patients to ensure a life-long supply of corrected hematopoietic progeny. Specifically, functional genes can be inserted by gene transfer (through randomly integrating γRetroviral or Lentiviral vectors) or precisely restored by gene editing (GE) with programmable nucleases such as CRISPR-Cas9.[2–4] Nuclease-induced double-strand breaks (DSBs) can be sealed by the error-prone non-homologous end joining (NHEJ) pathway disrupting a faulty gene or repaired by the high-fidelity homology-directed repair (HDR)[5] occurring during the S and G2 phase of the cell cycle.[6] Currently, HDR remains the only option for long-range correction of disease-causing mutations by inserting a functional cDNA cassette, often delivered with an adenoviral-associated viral vector (AAV6). As HDR engagement in long-term repopulating hematopoietic stem cells (HSCs) requires cell-cycle activation,[7,8] current protocols consist of 48–72 h of pre-stimulation with a previously optimized combination of cytokines and stem-preserving factors to force exit from quiescence and ensure a sizable fraction of corrected primitive cells.[8–12]

We recently discovered that GE culminates into a p53-mediated DNA damage response (DDR) activation, leading to cell differentiation, loss of engraftment, and reduced graft clonality,[11–13] although whether these responses might be exacerbated by prolonged *ex vivo* culture remains to be established.

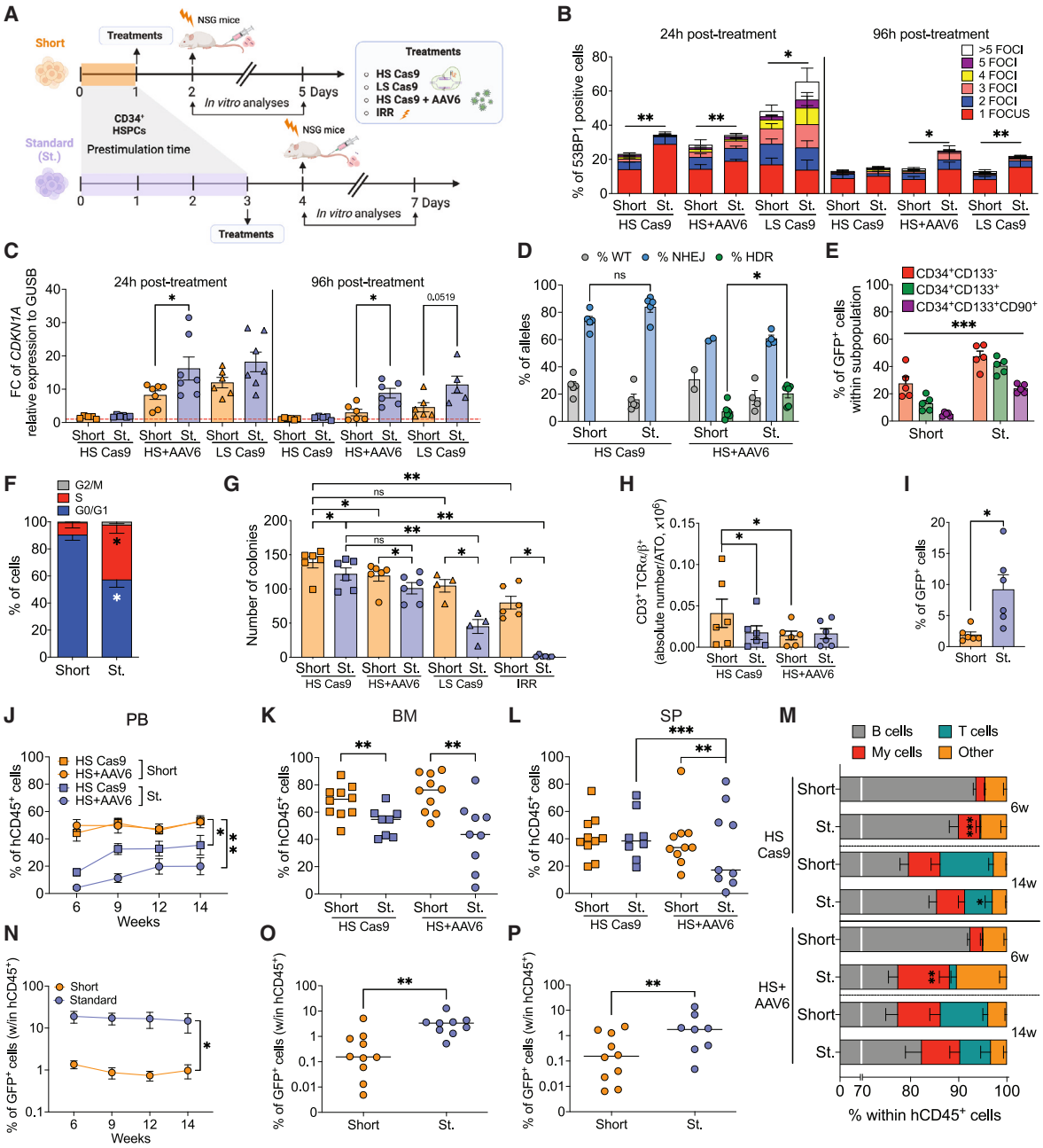

Figure 1. *Ex vivo* activation is a prerequisite for efficient HDR-based correction, although it heightens DDR activation and affects GE HSPC repopulation capacity

(A) Experimental workflow for short and standard protocols in human CB-derived HSPCs. Indicated treatments were performed at day 1 (short) or day 3 (standard) post-thawing, while *in vitro* analyses were conducted at 24 or 96 h post-treatments (corresponding to day 2 or 4, and day 5 or 7, respectively).

(B) 53BP1 foci distribution (24 h: n = 6,8,5,8,6,8; 96 h: n = 6, 6, 6, 4, 6, 7). Mann-Whitney test.

(C) Relative expression of *CDKN1A* (24 h: n = 5, 6, 7, 7, 6, 7; 96 h: n = 6, 5, 6, 6, 6, 5). For each time point, fold change was calculated relatively to HSPCs treated with an RNP loaded with a gRNA with no specificity against the human genome. Mann-Whitney test.

(D) Percentage of wild-type and HDR- or NHEJ-edited alleles measured 96 h post-editing (HS: n = 5; HS+AAV6: n = 2, 2, 6, 4, 4, 6). Wilcoxon test.

(E) Percentage of GFP$^+$ cells within HSPC subpopulations (CD34$^+$CD133$^-$, CD34$^+$CD133$^+$, and CD34$^+$CD133$^+$CD90$^+$ cells) at 96 h post-treatments (n = 5). Kruskal-Wallis test.

(F) Percentage of HSPCs in indicated cell-cycle phases measured at day 1 (short: n = 5) and day 3 (standard: n = 4). Mann-Whitney test.

(G) Number of colonies generated by HSPCs plated at 96 h post-treatment (HS Cas9: n = 6; HS+AAV6: n = 6; LS Cas9: n = 4; IRR: n = 6). Wilcoxon test for intra-treatment comparisons or Mann-Whitney test for inter-treatment measurements.

(H) Absolute number of CD3$^+$TCRα/β^+ cells in ATO seeded with HSPCs after the indicated treatment (n = 6). Wilcoxon test.

(legend continued on next page)

Previous studies reported that similar detrimental consequences may be due to the accumulation of reactive oxygen species (ROS) and activation of the p38 mitogen-activated protein kinase (MAPK) resulting in differentiation and loss of HSC self-renewal,[14–16] which could be counteracted by p38 inhibition,[17,18] leading to the assumption that ROS may directly act as pro-differentiating molecules on HSPCs.

Here, we identified a molecular axis where p38 MAPK-induced ROS act primarily as mitogenic molecules that alter HSPC cell-cycle dynamics, ultimately converging in proliferation-associated DNA damage accumulation and DDR activation. Importantly, p38 MAPK inhibition before GE mitigates culture stress by slowing down cell-cycle kinetics, preserving transcriptionally defined primitive HSCs, and enhancing the clonal output of edited HSPCs in the long term.

RESULTS

Ex vivo culture increases DDR burden and affects the functionality of genetically engineered human HSPCs

To study the contribution of *ex vivo* culture on HSPC response to nuclease-induced DSBs and viral vectors employed for long-range GE, we investigated the impact of DDR activation and DNA repair mechanisms in human HSPCs ($CD34^+$ cells) after an overnight recovery post-thawing ("short" protocol) or upon three days of pre-stimulation ("standard or St." protocol) (Figure 1A). HSPCs were nucleofected with Cas9 ribonucleoprotein complexes (RNPs) pre-assembled with guide RNA (gRNA)[19] previously reported to have no detectable off-targets (high specificity [HS Cas9], targeting the *AAVS1* safe harbor),[11,12] or more relaxed accuracy (low specificity Cas9 [LS Cas9], targeting *IL2RG*).[12] We also included cells treated with HS Cas9 in the presence of an AAV6 template for HDR integration of a GFP-expressing cassette (defined HS+AAV6) and low-dose irradiation (IRR) as a heightened load of DSBs and elevated DDR burden control (Figure 1A).

To investigate how *ex vivo* culture impacts HSPC proficiency to repair individual or multiple DSBs and activate p53-mediated DDR, we compared the accumulation and resolution of 53BP1 nuclear foci and *CDKN1A* (p21) levels across treatments. In line with our previous findings,[12] we reported an increased DDR burden when cells experienced the combination of HS and AAV6 or multiple DSBs by LS Cas9. Importantly, we observed a higher number of 53BP1 foci *per* cell and p21 levels in HSPCs edited with the standard protocol, reflecting higher vulnerability and protracted DDR activation, albeit changes in apoptosis were negligible (Figures 1B, 1C, S1A, and S1B). As persistency of DSBs during cell divisions may trigger genome instability phenomena, we analyzed the presence of micronuclei (MNs)-positive cells[20] and found a significant increase in MN-carrying cells across conditions after standard protocol, particularly in HS+AAV6 and LS Cas9 treatments (Figure S1C). Similarly, when we further increased the DNA damage load by IRR, the standard protocol displayed more DNA damage, reduced DNA repair proficiency, and higher p53-mediated DDR activation over time (Figures S1D and S1E).

We next evaluated on-target repair proficiency by NHEJ and HDR in HSPCs treated with the two clinically relevant conditions (HS Cas9 for gene disruption or HS+AAV6 for gene correction strategies). We found that, while NHEJ levels were comparable in all conditions, HDR efficiency was consistently lower across subsets in the short protocol (Figures 1D and 1E; see the gating strategy in Figure S1F), according to a reduced fraction of cells that progressed into the S phase of the cell cycle (Figure 1F).

For all conditions tested, we evaluated the clonogenic capacity and found that, according to the extent of DDR activation, short protocol-treated HSPCs showed an overall improved functionality (Figure 1G), especially for the myeloid output (Figure S1G). Moreover, we assessed the capacity of HSPCs edited with HS Cas9 and HS+AAV6 to differentiate along the lymphoid lineage in an innovative artificial thymic organoid (ATO) platform.[21] Thus, we reported increased output of $CD3^+TCR\alpha/\beta^+$ cells for HS Cas9 HSPCs of the short protocol and a reduction of $CD3^+TCR\alpha/\beta^+$ cells for HS+AAV6 conditions irrespective of the protocol employed (Figure 1H). Moreover, T cell-progenitor subsets were similar across all conditions, albeit with a modest reduction in early T cell precursors (ETPs) and pro-T cells (Pro-T) for the HS+AAV6 treatment of the standard protocol (Figures S1H). Nevertheless, the frequency of GFP-expressing cells (a surrogate for HDR-mediated gene correction) was reduced in the short protocol (Figure 1I).

Finally, we transplanted GE HSPCs into immunodeficient non-obese diabetic (NOD)-severe combined immunodeficiency (SCID)-$IL2Rg^{-/-}$ (NSG) mice. Thus, we found a significant reduction in the percentage of human $CD45^+$ ($hCD45^+$) engrafted cells in the standard protocol in the peripheral blood (PB), bone marrow (BM), and spleen (SP) (Figures 1J–1L). Analyzing the differentiation output in the PB (Figure S1I), we found an early expansion of myeloid cells and decreased T cells at the last time point in standard protocol conditions (Figure 1M). Conversely, BM and SP graft compositions were comparable within treatments (Figures S1J and S1K). Nonetheless, the percentage of GFP^+ cells was lower in the short protocol editing group (Figures 1N–1P).

Altogether, our results indicate that a longer pre-stimulation heightened the DDR burden and ultimately affected gene-edited HSPC functionality. While minimizing culture time would be favorable for NHEJ-mediated gene disruption, the short protocol is not suitable for HDR-gene correction as it reduced the fraction

(I) Percentage of GFP^+ cells measured by flow cytometry in ATO seeded with HS+AAV6-edited HSPCs ($n = 6$). Wilcoxon test.
(J–L) Percentage of human $CD45^+$ cells in the (J) PB, (K) BM, and (L) SP of mice transplanted with HSPCs edited as indicated ($n = 10, 8, 10, 9$). Mann-Whitney test (calculated at the last time point for PB).
(M) Percentage of B cells, T cells, myeloid, and other cells within the human graft (PB) ($n = 10, 8, 10, 9$). Mann-Whitney test for short vs. standard comparisons.
(N–P) Percentage of GFP^+ cells (within $hCD45^+$) measured in the (N) PB, (O) BM, and (P) SP of mice transplanted with HS+AAV6 HSPCs ($n = 10, 9$). Mann-Whitney test (calculated at the last time point for PB). Mean ± SEM and, unless otherwise specified, lines indicate median values. ns > 0.05; $^*p < 0.05$; $^{**}p < 0.01$; $^{***}p < 0.001$.

of HDR-edited cells, prompting us to investigate HSPC responses to *ex vivo* culture.

HSPC *ex vivo* cell-cycle progression is controlled by the p38 MAPK-ROS axis

As exposure to cytokines and growth factors has been associated with the stress-responsive p38 MAPK,[22–25] we evaluated its activation in HSPCs and found that phospho-p38 MAPK (p-p38) increased upon time in culture across subsets (Figures 2A, S2A, and S2B). Thus, we tested SB203580, a highly specific ATP-competitive inhibitor of p38 MAPK[26] (p38i), treating HSPCs during the first two days of culture (Figure 2B). According to its mechanism of action, p38i suppressed the phosphorylation of MAPKAPK2 (MK2) without impacting HSPC viability (Figures S2C and S2D). Measuring cytosolic ROS and mitochondrial superoxides, we found that HSPCs progressively accumulate oxidative stress, dampened to levels comparable to uncultured HSPCs by p38i administration (Figures 2C, 2D, and S2E). Moreover, mitochondrial respiration analyses revealed lower basal oxygen consumption rate (OCR) and spare respiratory capacity (SRC) upon p38i treatment (Figures 2E, 2F, and S2F). Conversely, measurement of extracellular acidification rate (ECAR) showed slight but consistent higher glycolysis and glycolytic capacity (GC) (Figures 2G, 2H, and S2G), likely implying a metabolic switch toward glycolysis.

As ROS can act as proliferative cues,[27] we reasoned that the primary trigger for adverse HSPC responses to culture may be the sudden onset of p38/ROS-mediated proliferation in otherwise quiescent cells. Thus, we measured the number of cell divisions over seven days of culture across HSPC subsets in vehicle- or p38i-treated cells and employed palbociclib (CDK4/6 inhibitor) as cell-cycle slowdown control. We found that HSPCs performed slightly fewer rounds of cell divisions upon p38i treatment (on average, each cell divided 0.36 times less than control) (Figures 2I and S2H). This effect resulted in an evident reduction in cumulative proliferation, measured by live imaging on bulk HSPCs and, most importantly, on the more HSC-enriched subpopulation (Figures 2J and 2K). To quantitatively assess the duration of cell-cycle phases in single HSPCs, we employed a lentiviral vector encoding for the fluorescent ubiquitination-based cell-cycle indicator 2a system (Fucci2a),[28] which allows discriminating between G1, G1/S transition, and S/G2/M. Comparative analysis revealed a significantly higher median duration of G1/S transition and a slightly longer G1 phase upon p38i (G1/S: 9.05 vs. 5.5 h; G1: 8.75 vs. 6.5 h, respectively); instead, the duration of the HDR-permissive S/G2/M was comparable between conditions (Figure 2L).

To confirm that ROS acts as mitogenic signals in our setting, we employed the ROS scavenger N-acetyl cysteine (NAC). Indeed, NAC supplementation during the first two days of *ex vivo* culture transiently reduced oxidative stress (Figure S2I) and slowed down HSPC proliferation by prolonging all cell-cycle phases (Figures 2M, 2N, and S2J). Nevertheless, NAC treatment did not counteract p38 MAPK activation (Figure S2K). Similarly, additional antioxidants, including resveratrol and tempol, and their combinations with NAC showed a transient ROS reduction (Figure S2L), leading to decreased HSPC proliferation (Figure S2M). However, ROS scavenging was not sufficient to reduce p38 MAPK phosphorylation (Figure S2N), implying that ROS are produced downstream of p38 MAPK activation, as confirmed by similar results obtained by maintaining HSPCs in low-oxygen conditions (hypoxia) (Figure S2O–S2Q).

Our findings highlight that HSPC *ex vivo* culture involves p38 MAPK activation, which controls mitogenic ROS that mediate rapid cell-cycle progression. Notably, p38 inhibition reduces ROS levels and prolongs the G1/S transition duration, slowing down HSPC proliferation alongside mitochondrial respiration and promoting a minor metabolic switch toward glycolysis, a feature associated with slow cycling and more dormant HSCs.[29,30]

p38 MAPK-mediated proliferation stress leads to DNA damage accumulation

Consistent with ROS capacity to oxidize DNA bases, we reported a cumulative 8-oxo-2′-deoxyguanosine (8-oxo-dG) induction, counteracted by p38 inhibition (Figure 3A). Next, we investigated physical single-strand breaks (SSBs) and DSBs accumulation using the alkaline comet assay and found increased DNA damage upon culture, which was mitigated by p38i administration (Figure 3B). Because murine HSCs accumulate DNA damage upon exiting quiescence,[31] we asked whether p38 MAPK-dependent DNA damage would be caused by proliferative stress. Of note, both transient CDK4/6i-mediated cell-cycle inhibition and NAC decreased physical DNA breaks according to the extent of proliferation slowdown, confirming the link between *ex vivo* proliferation and DNA damage accumulation (Figure 3C). We also found increased levels of phosphorylated histone variant H2AX (γH2AX) and phosphorylated replication protein A (pRPA) upon culture, which were rescued by p38 inhibition (Figures 3D, 3E, and S3A). Consistently, p38i alleviated the activation of the apical DNA replication stress kinase ataxia telangiectasia and Rad3-related protein (ATR) (phospho-ATR, Ser428) and its downstream target CHK1 (phospho-CHK1, Ser345) (Figure 3F). Finally, we also reported a slight but persistent increase in the proportion of phenotypically defined primitive HSPCs ($CD34^+133^+90^+$ cells) in the p38i condition (Figure 3G).

Altogether, our data highlight a multi-step process with a precise sequence of events involving p38 MAPK phosphorylation, generation of mitogenic ROS, and alteration of cell-cycle dynamics, leading to consequent proliferation stress and activation of the DDR cascade. Importantly, p38 MAPK inhibition limits the activation of this molecular axis, better preserving primitive HSPCs.

Ex vivo p38 inhibitor administration ameliorates the functionality of gene-edited HSPCs

We reasoned that by decreasing proliferation-associated endogenous DNA damage, p38 inhibition would also mitigate GE-induced detrimental responses and better preserve the long-term functionality of genetically engineered HSPCs. Thus, we cultured HSPCs in the presence of p38i and nucleofected with the HS Cas9 alone or in combination with the GFP-expressing AAV6 (HS+AAV6) required for HDR-mediated GE (Figure 4A). p38i did not affect cell viability nor NHEJ and HDR efficiency across progenitors (Figures S4A–S4C) but preserved the fraction of $CD34^+133^+90^+$ cells and increased HDR-mediated correction

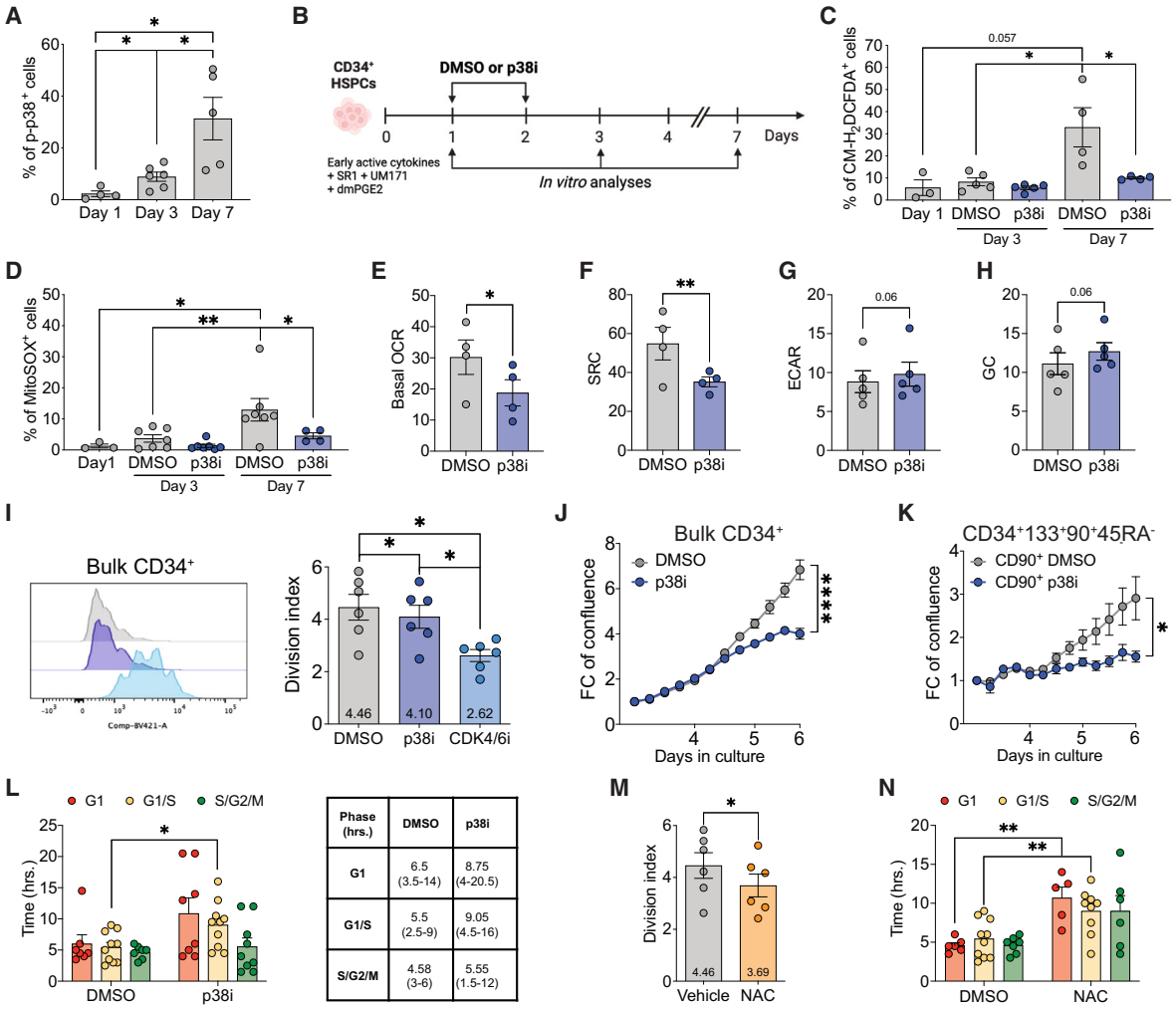

Phase (hrs.)	DMSO	p38i
G1	6.5 (3.5-14)	8.75 (4-20.5)
G1/S	5.5 (2.5-9)	9.05 (4.5-16)
S/G2/M	4.58 (3-6)	5.55 (1.5-12)

Figure 2. p38 MAPK activation mediates excessive proliferation through mitogenic ROS

(A) Quantification of phospho-p38 by flow cytometry analysis in *ex vivo* cultured HSPCs (n = 4, 6, 5). Mann-Whitney test.

(B) Experimental workflow indicating *in vitro* treatments with DMSO (vehicle) or 4 μM p38i at day 1 and 2 post-thawing of human CB-derived HSPCs. *In vitro* analyses were conducted on days 1, 3, and 7 post-thawing.

(C and D) Quantification of (C) cytosolic ROS detected by CM-H_2DCFDA and of (D) mitochondrial superoxides measured by MitoSOX (C: n = 3, 5, 5, 4, 4; D: n = 3, 7, 7, 7, 4). Mann-Whitney test.

(E and F) Quantification of (E) basal oxygen consumption rate (OCR) or (F) spare respiratory capacity (SRC) after 7 days of culture (n = 4). Mann-Whitney test.

(G and H) Quantification of (G) extracellular acidification rate (ECAR) or (H) glycolytic capacity (GC) after 7 days of culture (n = 5). Wilcoxon test.

(I) Representative plot of CellTrace dilution and division index of $CD34^+$ cells measured at day 7 (n = 6). Wilcoxon test.

(J and K) Cellular confluence of (J) bulk $CD34^+$ or (K) $CD34^+CD133^+CD90^+CD45RA^-$ HSPCs reported as fold change (FC) to the first time point (n = 3). Mann-Whitney test.

(L) Duration (hours) of cell-cycle phases measured in single HSPCs expressing the Fucci2a reporter. Live imaging started on day 2 after p38 inhibitor treatment; each dot represents individual cells. Mann-Whitney test.

(M) Division index of HSPCs measured at day 7 (n = 6). As a control, the DMSO condition from (I) is reported. Wilcoxon test.

(N) Duration (hours) of cell-cycle phases measured in single HSPCs expressing the Fucci2a reporter. Live imaging started on day 2 after NAC treatment; each dot represents individual cells. As a control, the DMSO condition from (L) is reported. Mann-Whitney test. Mean ± SEM. *p < 0.05; **p < 0.01; ****p < 0.0001.

in this primitive subset (Figures 4B, 4C, and S4D). Moreover, p38 inhibition diminished oxidative stress and reduced DNA damage accumulation and ATR/CHK1 activation (Figures 4D–4G), ameliorating GE genotoxicity risk by decreasing MN-bearing HSPCs (Figure 4H). Of note, p38i-treated conditions gave rise to a higher colony number, mostly due to increased mixed-colony output, the progeny of more primitive and multi-potent HSPCs (Figures 4I and 4J). This result was confirmed by secondary colony-forming unit cell (CFU-C) assay, as p38i enhanced the clonogenic output upon serial replating (Figure 4K).

We next assessed the impact of p38 MAPK activity on an adult HSPC source, such as mobilized peripheral blood (mPB). After testing different doses (data not shown), we selected a slightly higher optimal concentration, not affecting cell vitality (Figure S4E),

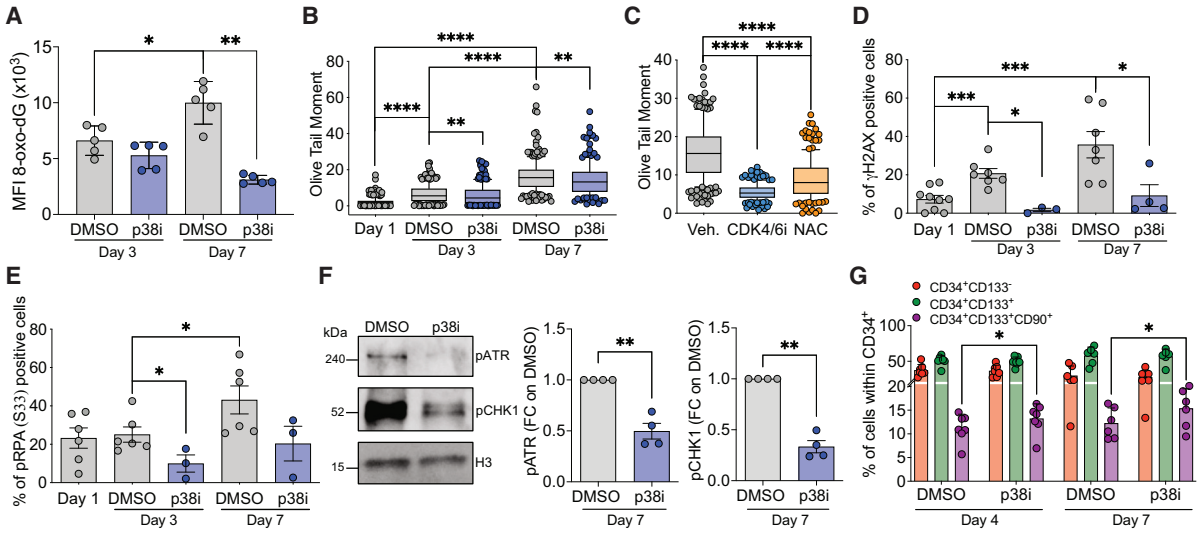

Figure 3. p38 MAPK/ROS triggers proliferation stress and heightens DNA damage

(A) Quantification of 8-oxo-2′-deoxyguanosine by flow cytometry (n = 5). Mann-Whitney test.

(B) Quantification of SSBs and DSBs by comet assay; each point represents a single cell from 3 independent experiments (up to 250 cells were analyzed). Mann-Whitney test. Whiskers represent 10–90 percentile.

(C) Quantification of SSBs and DSBs by comet assay at day 7 of culture; each point represents a single cell from 3 independent experiments (up to 250 cells were analyzed). Mann-Whitney test. Whiskers represent 10–90 percentile.

(D and E) Percentage of (D) γH2AX- or (E) pRPA-positive HSPCs (γH2AX: n = 9, 7, 3, 7, 4; pRPA = n = 6, 6, 3, 6, 3). Mann-Whitney test.

(F) Western blot analysis of pATR (left) and pCHK1 (right) at day 7 (n = 4). Histone H3 was used as a loading control, and fold change relative to control is reported. One-sample t test.

(G) Percentage of HSPC subpopulations ($CD34^+CD133^-$, $CD34^+CD133^+$, and $CD34^+CD133^+CD90^+$ cells) (n = 7). Wilcoxon test. Unless otherwise specified, mean ± SEM. *p < 0.05; **p < 0.01; ***p < 0.001; ****p < 0.0001.

due to increased p38 MAPK activation in mPB $CD34^+$ cells compared to CB (Figure S4F). Nevertheless, p38i treatment in mPB-derived HSPCs did not compromise HDR efficiency and increased the number of mixed colonies (Figures S4G and S4H).

The amelioration of HSPC functionality was specific to p38 signaling blockage, as inhibition of other MAPK, such as c-Jun N-terminal kinase (JNK) and extracellular signal-regulated kinase (ERK),[32,33] slightly promoted cell death, ultimately impairing HSPC *in vitro* clonogenicity (Figures S4I and S4J). Additionally, we also tested whether NAC or low-oxygen conditions could mimic p38i in the GE context. Interestingly, NAC had no impact on ROS accumulation upon GE, which was instead reduced in hypoxia (Figure S4K). Moreover, both conditions showed only a minor effect on HSPC clonogenic potential, slightly decreasing cell viability and lowering HDR correction, especially in the more primitive subset (Figures S4L–S4N), likely due to a more pronounced proliferation slowdown compared to p38 inhibition (Figures 2I, 2M, and S2P).

Overall, p38 inhibition improves gene-corrected HSPC functionality by mitigating proliferation-induced DNA damage that, in addition to GE tools exposure, makes HSPCs exceed a threshold of tolerable DDR and prematurely exhaust.

Single-cell transcriptomics reveals replication stress mitigation and stemness maintenance by p38 inhibition across HSPC subsets

To elucidate p38i-mediated responses across HSPC subsets, we performed droplet-based single-cell RNA sequencing (scRNA-seq). For a more reliable HSC characterization, we enhanced their representation by sorting the HSC-enriched fraction ($CD34^+CD133^+CD90^+CD45RA^-$) and mixed them with the bulk population upon hashtag marking, allowing a comprehensive view of cell composition across not edited, HS Cas9, and HS+AAV6 conditions after vehicle or p38i administration. Moreover, HDR-edited HSPCs were further sorted according to GFP expression (Figure 5A). Through the expression of previously reported marker genes,[35–42] we annotated 15 cell clusters and further validated by computing the module scores of HSC and cell lineage signature from the literature (Figures 5B, S5A, and S5B). Comparison of cluster composition across not edited and HS Cas9 conditions did not reveal major differences upon p38i, while HS+AAV6 samples showed a modest expansion of megakaryocytes-erythroid progenitor (MEP), eosinophil baso-mast progenitor (EBMP)/Baso/Mast, and megakaryocyte erythroid mast cell and basophil progenitor (MEMBP), more evident in the GFP^+ population (Figure 5C; Data S1A). Extrapolating the HSC-sorted fraction, we found an enrichment of cells belonging to the HSC/multi-potent progenitor (MPP) subset, which was slightly more represented upon p38i treatment, especially in the GFP^+ fraction. The same trend was observed for MEP, while MPP was reduced in not edited and GFP^+ cells (Figure 5D; Data S1B). Of note, the higher representation of the HSC/MPP in the GFP^- condition likely reflects their limited propensity to engage HDR.

Gene set enrichment analysis (GSEA) showed significant downregulation of DNA replication, cell cycle, and G2M

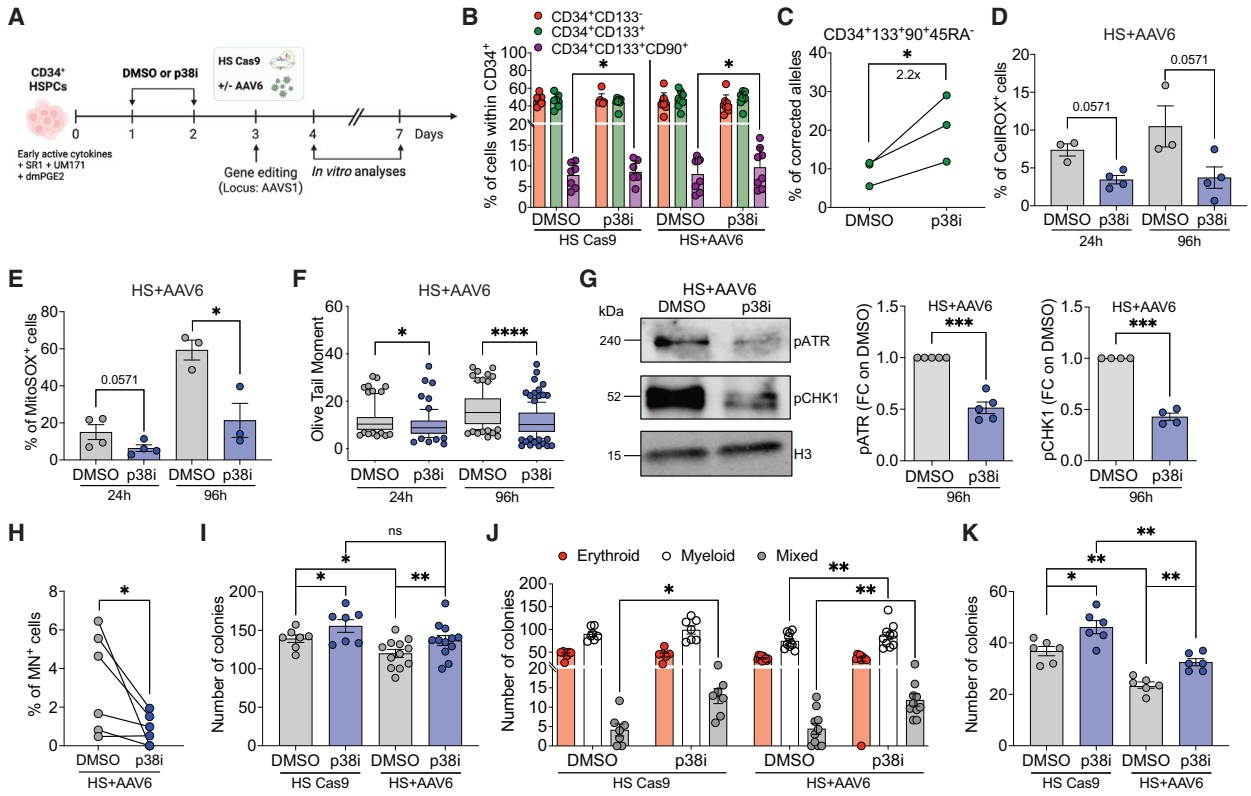

Figure 4. The functionality of gene-edited HSPCs is enhanced by p38 inhibitor treatment

(A) Experimental workflow indicating *in vitro* treatments with vehicle (DMSO) or p38i at day 1 and 2 post-thawing of human CB- or mPB-derived HSPCs. Cells were GE at day 3 by nucleofection of HS Cas9 in the presence or not of AAV6. *In vitro* analyses were conducted on days 4 and 7 (24 and 96 h post-editing, respectively).

(B) Percentage of HSPC subpopulations ($CD34^+CD133^-$, $CD34^+CD133^+$, and $CD34^+CD133^+CD90^+$ cells) at 96 h post-nucleofection (HS Cas9: n = 7, 7, 7; HS+AAV6: n = 8, 8, 8). Wilcoxon test.

(C) Percentage of HDR-corrected alleles at 96 h post-editing in CB-sorted $CD34^+CD133^+CD90^+CD45RA^-$ (n = 3). Mann-Whitney test.

(D and E) Quantification of (D) cytosolic ROS detected by CellROX and of (E) mitochondrial superoxides measured by MitoSOX in HS+AAV6 CB-derived HSPCs (D: n = 3, 4, 3, 4; E: n = 4, 4, 3, 3). Mann-Whitney test.

(F) Quantification of SSBs and DSBs by comet assay in HS+AAV6 CB-derived HSPCs; each point represents a single cell from 2 independent experiments (up to 165 cells were analyzed). Mann-Whitney test. Whiskers represent 10–90 percentile.

(G) Western blot analysis of pATR (left) and pCHK1 (right) at 96 h post-nucleofection in HS+AAV6-edited HSPCs (pATR: n = 5; pCHK1: n = 4). Histone H3 was used as a loading control, and fold change relative to control is reported. One-sample t test.

(H) Percentage of micronuclei-positive HSPCs at 96 h post-editing (HS+AAV6: n = 6). Wilcoxon test.

(I) Number of colonies generated by CB-derived HSPCs plated in methylcellulose 24 h post-treatments (HS Cas9: n = 7; HS+AAV6: n = 12). Wilcoxon test for intra-treatment comparisons or Mann-Whitney test for inter-treatment measurements were performed.

(J) Number of erythroid, myeloid, and mixed colonies from (I). Wilcoxon test.

(K) Number of colonies generated after secondary replating in methylcellulose (n = 6). Mann-Whitney test. Mean ± SEM. ns > 0.05; *p < 0.05; **p < 0.01; ***p < 0.001; ****p < 0.0001.

checkpoint upon p38i, particularly in the HSC/MPP. Instead, hypoxia genes were upregulated across most clusters (Figure 5E), suggesting that p38i may confer a more physiological metabolic phenotype. Similarly, p38i upregulated the PI3K-AKT-mTOR pathway, important to sustain the maintenance of long-term HSCs,[43,44] specifically in the HS+AAV6 condition. Of note, gene lists of G1/S transition and cell-cycle regulation analyses confirmed and extended our molecular data on HSPC proliferation kinetics to GE cells (Figure 5E; Data S1C). Interestingly, RNA processing and translation showed a different behavior among conditions with upregulation in not edited and HS Cas9-treated cells and an opposite orientation in HS+AAV6 GFP^- and GFP^+ samples, likely reflecting a distinctive response to p38i in cells exposed to the AAV6 vector (Figure 5E). Cell-cycle inferences revealed a marked S phase representation in not edited cells, even for the HSC/MPP cluster, which was reduced in HS Cas9 and HS/AAV6 conditions. Consistently, p38i enriched G1 representation in all conditions across most clusters, including the HSC/MPP cluster (Figures 5F and S5C; Data S1D and S1E).

Furthermore, we assessed possible changes in HSC/MPP replication dynamics and found downregulation of replication

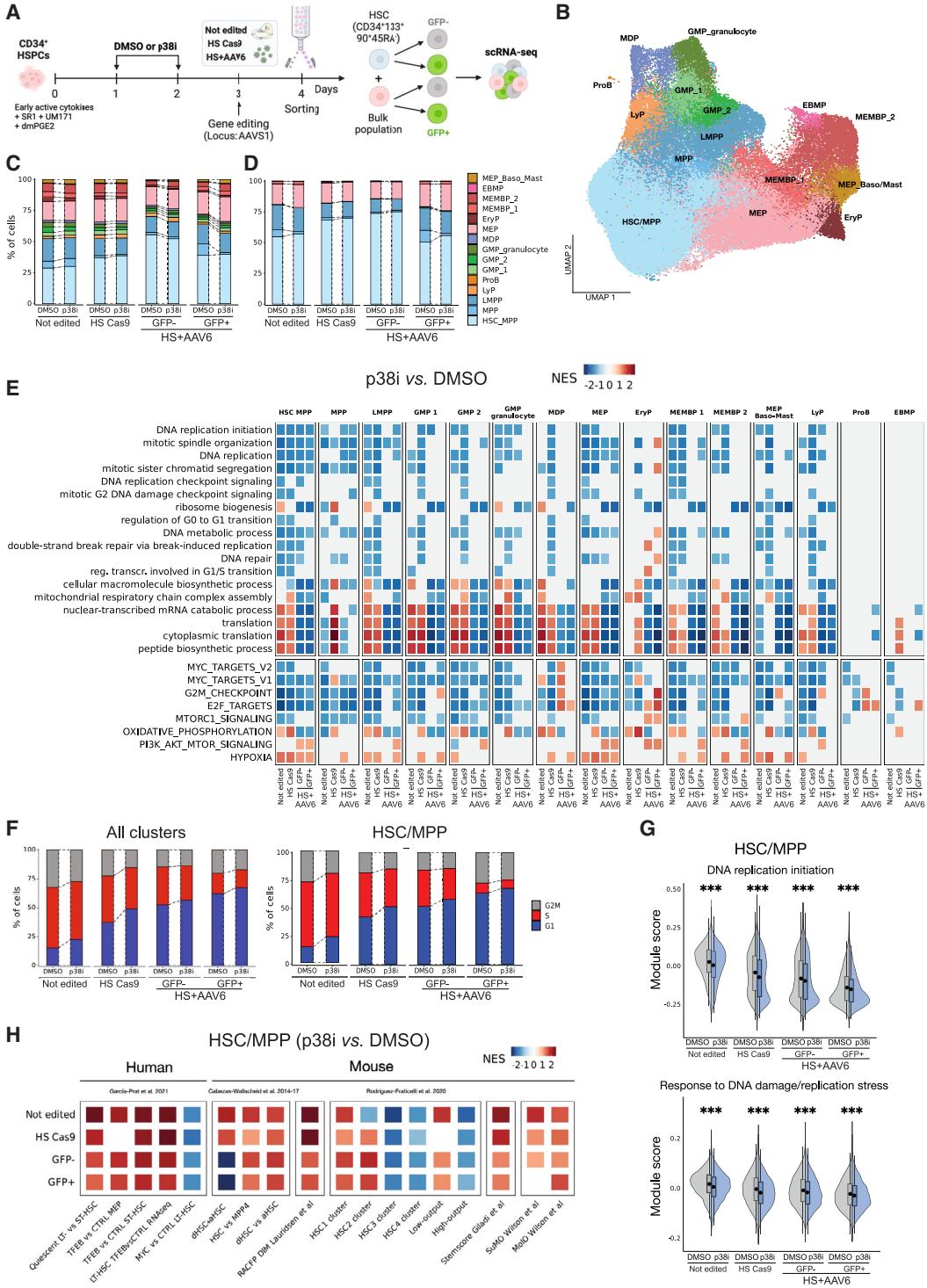

Figure 5. Single-cell transcriptomic analysis reveals replication stress mitigation and stemness maintenance by p38 inhibition across conditions

(A) Schematic representation of the single-cell RNA transcriptomic analysis experimental workflow: at day 1 and 2 post-thawing human CB-derived HSPCs were treated with vehicle (DMSO) or p38i. At day 3, cells were nucleofected with HS Cas9 in the presence or not of AAV6. A not edited control was included. At day 4 (24 h post-editing), HSPCs were sorted and collected for subsequent analyses.

(B) Uniform manifold approximation and projection (UMAP) of annotated populations with cells belonging to all conditions.

(C and D) Barplots showing the distribution of (C) all the cells retrieved and (D) $CD34^{+}CD133^{+}CD90^{+}CD45RA^{-}$ assigned to each subpopulation.

(legend continued on next page)

initiation and response to DNA damage and replication stress programs[34] upon p38i, further supporting that proliferation slowdown mitigates culture-triggered DNA damage (Figure 5G). We also found modest downregulation of genes involved in DNA replication fork restart (*WRN, DNA2*) and repriming (*PRIMPOL*, *BLM*), likely resulting in reduced discontinuous DNA synthesis and single-stranded DNA gap accumulation. Similarly, we found in not edited and HS Cas9 p38i-treated cells reduced expression of genes involved in fork reversal, which were conversely upregulated in the HS+AAV6 condition, suggesting that HSPCs may be more prone to activate this DNA repair pathway in response to viral sensing (Figure S5D). Lastly, p38 inhibition increased HSC/MPP cells harboring molecular signatures of self-renewal, dormancy, metabolic fitness, and higher repopulating capacity[29,45–49] (Figure 5H).

Collectively, these data link p38 MAPK-mediated DNA replication control with reduced fitness in unmanipulated and genetically engineered HSCs, as putatively identified in our single-cell analysis, that could be mitigated by p38 inhibition.

Multi-lineage differentiation of primitive HDR-corrected HSCs is enhanced by p38 inhibition

To simultaneously address the impact of culture and genetic engineering on HSC lineage specification, we fluorescence-activated cell sorting (FACS) sorted the HSC-enriched fraction post-thawing, post-culture, and GE (Figures 6A and S6A) and characterized the differentiation potential along the myeloid (My), lymphoid (Ly), megakaryocytes (Meg), and erythroid (Ery) lineages[50] (Figure S6B). First, we reported that culture *per se* increases the fraction of cells incapable of differentiating and uni-lineage colonies at the expense of multi-lineage potential. This effect was further exacerbated by GE, especially in the fraction of cells that had undergone HDR (GFP^+) compared to cells that did not integrate the GFP cassette (GFP^-), although they had likely experienced AAV6 exposure and repaired nuclease-induced DSB by NHEJ (Figure 6B). Accordingly, also the cellularity of colonies was reduced upon culture and in response to GE in the fraction of HDR-corrected cells (Figure 6C). Next, we assessed how p38 MAPK inhibition impacts HSC multi-potency (Figure 6A). While p38i did not rescue the impact of GE on HSC clonogenic capacity (Figure S6C), both not edited and HS+AAV6 p38i-treated cells generated more multi-lineage colonies (Figure 6D). By analyzing the composition of uni-lineage and multi-lineage colonies (Figure S6D), we reported fewer My-only and Ery-only colonies upon p38i (Figure S6E). Instead, among multi-lineage colonies, p38 inhibition expanded My/Ery and My/Ery/Meg colonies in not edited (NE) conditions, and My/Meg, Ery/Meg, My/Ery/Meg, My/natural killer (NK)/Ery, and even of the rarest NK/Ery/Meg, My/NK/Meg, and My/NK/Ery/Meg colonies in GE HSCs (Figure 6E).

We next evaluated HSC multi-potency specifically in HDR-edited cells and found that despite there being no differences in the clonogenic efficiency (Figure S6F), we detected a higher percentage of multi-lineage colonies from both GFP^- and GFP^+ HSCs when pre-treated with p38i (Figures 6F and S6G). Indeed, we observed fewer My-only and Ery-only colonies (Figure S6H), while the composition of some multi-lineage colonies was sample specific and treatment independent: in particular, NK/Meg and My/NK/Ery colonies derived only from GFP^+ HSCs, which also showed an expansion of My/NK colonies compared to GFP^-. Among treatment-driven changes, p38i expanded My/Meg, Ery/Meg, My/Ery/Meg, and other tri- and quadri-lineage colonies in GFP^- and/or GFP^+ HSCs (Figure 6G).

Altogether, these data indicate that *ex vivo* culture and GE affect HSC differentiation at the single-cell level that can be rescued by p38 inhibition, ameliorating multi-lineage differentiation and enhancing erythroid and megakaryocyte stem-proximal outputs.

p38 MAPK inhibition improves gene-edited HSPC repopulating capacity and clonal output long-term post-transplantation

To test the impact of p38 inhibition before GE on reconstitution capacity, we transplanted HSPCs nucleofected with the HS Cas9 or HS+AAV6 upon treatment into NSG mice. After 15 weeks, $CD34^+$ HSPCs were purified from the mice and re-challenged in clonogenic assay or injected into secondary recipients (Figure 7A). By measuring human chimerism in PB, BM, and SP, we found that while the engraftment of the HS Cas9 groups was similar, likely due to saturation of the host, the engraftment of p38i-treated HS+AAV6 HSPCs was significantly higher than that of control (Figures 7B, 7C, and S7A). In addition, we found an early reduction of myeloid cells in HS+AAV6 and more T cells at the last time point in HS Cas9 of the p38i condition (Figure S7B). While similar results were reported in the SP, BM graft compositions were comparable between treatments (Figure S7C and S7D). Additionally, the percentage of GFP-expressing cells was similar across organs and conditions (Figures 7D, 7E, and S7E). Nonetheless, p38i increased the overall yield of gene-corrected cells due to the higher engraftment. Upon $CD34^+$ cell retrieval from the BM of the mice, we reported a higher colony output in the p38i-treated conditions (Figures 7F and 7G).

Because we recently demonstrated that GE affects the clonal repertoire of edited HSPCs,[11] we asked whether p38 inhibition could impact the number of reconstituting edited clones. Indeed, we reported improved clonal diversity in both p38i conditions when measuring NHEJ-induced insertion or deletion (indel) diversity (Figure 7H). To determine HDR-clonal output, we used an AAV6 carrying a "barcode" sequence (BAR)[11] and found enhanced polyclonal reconstitution of HDR-edited clones upon p38 inhibition (Figure 7I). Moreover, inter-mouse BAR sharing

(E) Enriched terms obtained performing GSEA of intra-condition comparisons of p38i vs. vehicle. Rows report terms enriched in at least one of the comparisons (columns) (false discovery rate < 0.1) from the gene ontology (GO), biological processes (BP), and the hallmark signatures (MSigDB). Colors indicate negative/positive normalized enrichment score (NES).

(F) Percentage of cell-cycle distribution across all the cell subpopulations (left) or the HSC cluster (right).

(G) Module score of DNA replication initiation and response to DNA damage/replication stress signatures as in Jacobs et al.[34] Wilcoxon test (***$p < 0.001$).

(H) GSEA analysis of intra-condition comparisons of p38i vs. vehicle of HSPC-related categories retrieved from the literature (see STAR Methods).

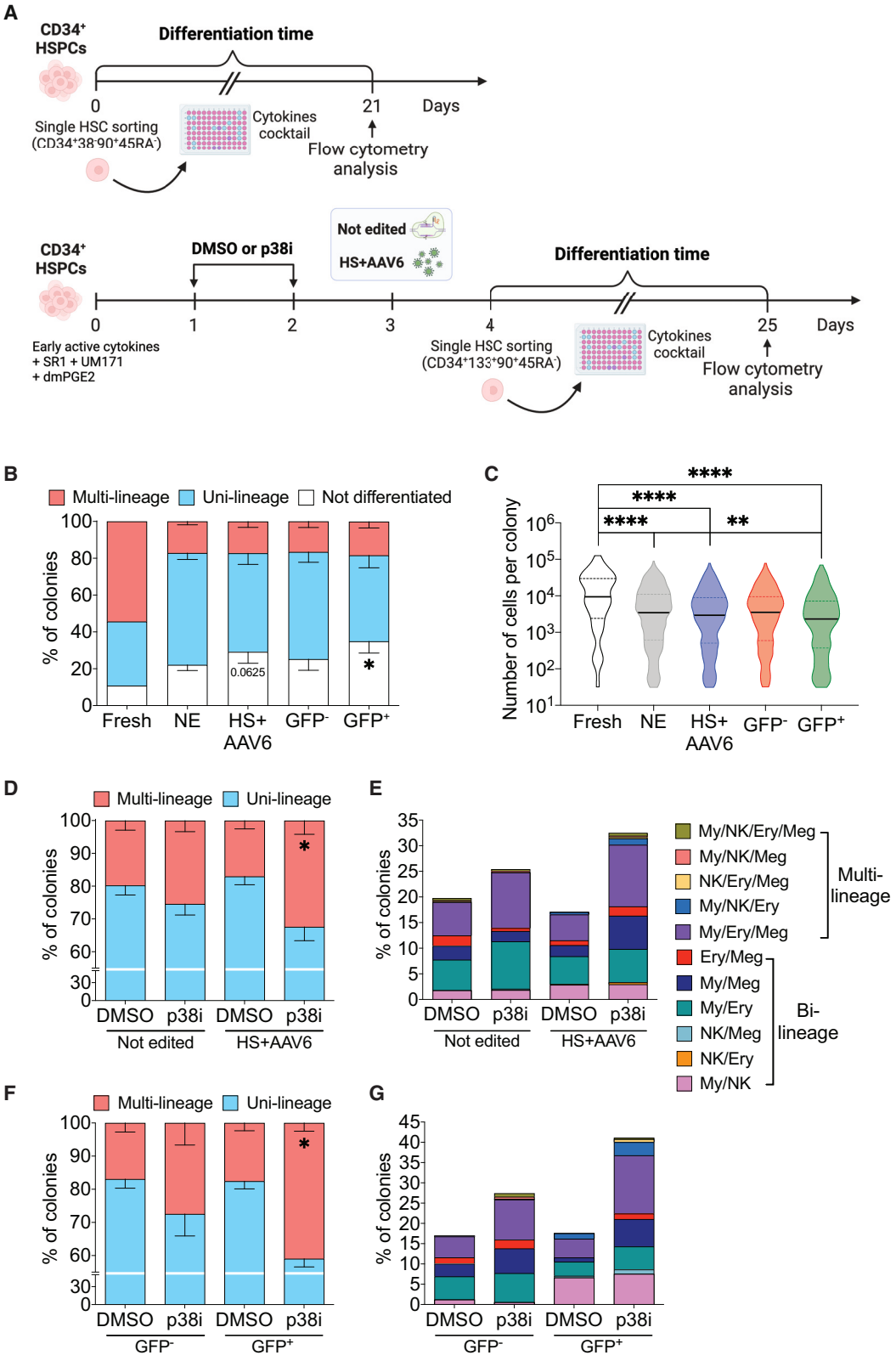

(legend on next page)

revealed few pre-infusion duplications of HDR-edited HSPCs that maintained repopulation potential upon transplantation[11] (Figure S7F).

These findings were recapitulated by transplanting in NSG mice mPB-derived CD34$^+$ cells (HS+AAV6). Indeed, p38i increased human engraftment without compromising the percentage of HDR-corrected cells in PB and BM (Figures S7G–S7J) and enhanced the clonogenic potential with mixed-colony expansion from BM-derived CD34$^+$ cells (Figures S7K and S7L).

Finally, to specifically test the repopulating capacity of long-term HSCs, we injected BM-derived CD34$^+$ cells into secondary recipients (Figure 7J). Thus, we reported higher human chimerism in the p38i group in PB and SP (Figures 7K and S7M), while similar engraftment was found in the BM (Figure 7L). Strikingly, only the p38i group retained a sizable fraction of HDR-edited cells (Figures 7M, 7N, and S7N). In addition, when analyzing the impact of p38i on graft composition, we found that the p38i-treated group showed fewer myeloid cells at early and late time points post-transplant and more T cells at the endpoint (Figures 7O, S7O, and S7P).

Overall, our data indicate that p38i treatment prior to GE improves polyclonal reconstitution of HDR-edited HSCs and better preserves their long-term repopulating capacity through serial transplantation.

DISCUSSION

HSPC *ex vivo* culture is required for HDR engagement in long-range gene correction for clinical applications. Here, we reported that *ex vivo* culture contributes to GE HSC functional impairment and investigated the mechanism behind such dysfunction. Through a side-by-side comparison between a short (overnight activation) and a standard protocol (three days of pre-stimulation), we found that the p53-mediated DDR activation, triggered by concomitant exposure to CRISPR-Cas9-induced DSBs and AAV6 vectors,[12] was higher and more prolonged in HSPCs subjected to the standard protocol, resulting in decreased colony number and impaired repopulating capacity, with higher myeloid skewing and lower T cell differentiation, resembling the output of aged HSCs.[51–53] While these effects were mitigated in the short protocol, HDR efficiency was drastically lower and insufficient to guarantee an optimal representation of gene-corrected cells upon transplant. For these reasons, shortening pre-stimulation time should be envisioned specifically for gene disruption by NHEJ.

To identify dysfunction determinants during *ex vivo* culture, we uncovered a molecular axis that links p38 MAPK activation, ROS, and proliferation stress to loss of multi-potency and reduced repopulating capacity of genetically engineered HSPCs. Distinctively from previous works,[14,15,18,54] we showed that p38 MAPK triggers ROS that are primarily mitogenic and fuel faster proliferation, as demonstrated by the alteration of cell-cycle dynamics upon antioxidant administration and low-oxygen conditions. Consequently, excessive proliferation mediates the accumulation of DNA damage with markers of DNA replication stress, including activation of the ATR-CHK1 DDR axis. Even if we cannot completely rule out p38 MAPK involvement in other aspects of culture adaptation,[55] our study shows that longer G1 phase and G1/S transition are associated with reduced DNA damage and DDR levels after *ex vivo* culture, likely by limiting replication forks stalling as suggested in murine embryonic stem cells.[56] While most efforts in the GE field have focused on promoting cell-cycle progression and/or favoring HDR,[7,11] our work highlights that faster proliferation may initiate premature exhaustion of engineered HSPCs. Similarly, slowing cell-cycle progression should be considered in *ex vivo* expansion protocols,[44,57,58] which are particularly relevant for genetic diseases with limited BM harvest or HSPC mobilization.[59]

Although we detected a similar percentage of GFP$^+$ cells in primary recipients, only the p38i group retained a sizable fraction of long-term HDR-corrected HSCs in secondary transplantation. Deep sequencing revealed a more polyclonal graft in edited HSPCs upon p38i treatment in clones that underwent NHEJ and HDR. This gain in the clonal repertoire is particularly relevant for clinical translation as an oligoclonal graft might delay hematopoietic recovery after conditioning, restricting the presence of corrected HSPCs in the long term and favoring the emergence of clonal hematopoiesis, possibly affecting the overall safety of the procedure.[11] Moreover, both shortening time in culture and p38i treatment diminished the percentage of MNs-positive HSPCs, and although their fate upon the replicative stress imposed by transplantation remains unknown, our data suggest that p38i will likely endow engineered HSPCs with improved safety profile.

In conclusion, our study sheds light on the mechanisms contributing to the functional impairment of genetically engineered HSPCs by providing molecular details on how human HSPCs cope with endogenous stress during *ex vivo* culture. Our data uncover the p38 MAPK-ROS axis as a key regulator of cell-cycle progression and heightened DNA damage in engineered HSPCs and highlights a strategy based on temporary inhibition of p38 MAPK prior to genetic manipulation to endow edited HSCs with superior long-term and polyclonal repopulating capacity for wider and safer GT applications.

Figure 6. *In vitro* multi-potency of GE HSCs is enhanced by p38 MAPK inhibition

(A) Experimental workflow of the single-cell differentiation assay. CB-derived HSPCs were FACS-sorted and seeded as single cells in a cytokine-enriched medium immediately after thawing (fresh), or at day 4 for not edited and HS+AVV6 conditions. Colonies were harvested and analyzed after 25 days of culture.
(B) Percentage of not differentiated, uni-lineage, and multi-lineage colonies. HS+AAV6 condition was subsequently analyzed as GFP$^-$ and GFP$^+$ colonies. >100 colonies for fresh condition and >1,000 colonies for all the other conditions from 4 independent experiments were analyzed. Mann-Whitney test.
(C) Distribution of the number of cells composing individual colonies analyzed in (B). Mann-Whitney test.
(D) Percentage of uni-lineage and multi-lineage colonies. >1,000 colonies analyzed from 4 independent experiments. Mann-Whitney test.
(E) Percentage of colonies with the indicated composition derived from multi-lineage colonies in (D).
(F) Percentage of uni-lineage and multi-lineage colonies derived from HS+AAV6 in (D). Mann-Whitney test.
(G) Percentage of colonies with the indicated composition derived from multi-lineage colonies in (F). Mean ± SEM. *$p < 0.05$; **$p < 0.01$; ****$p < 0.0001$.

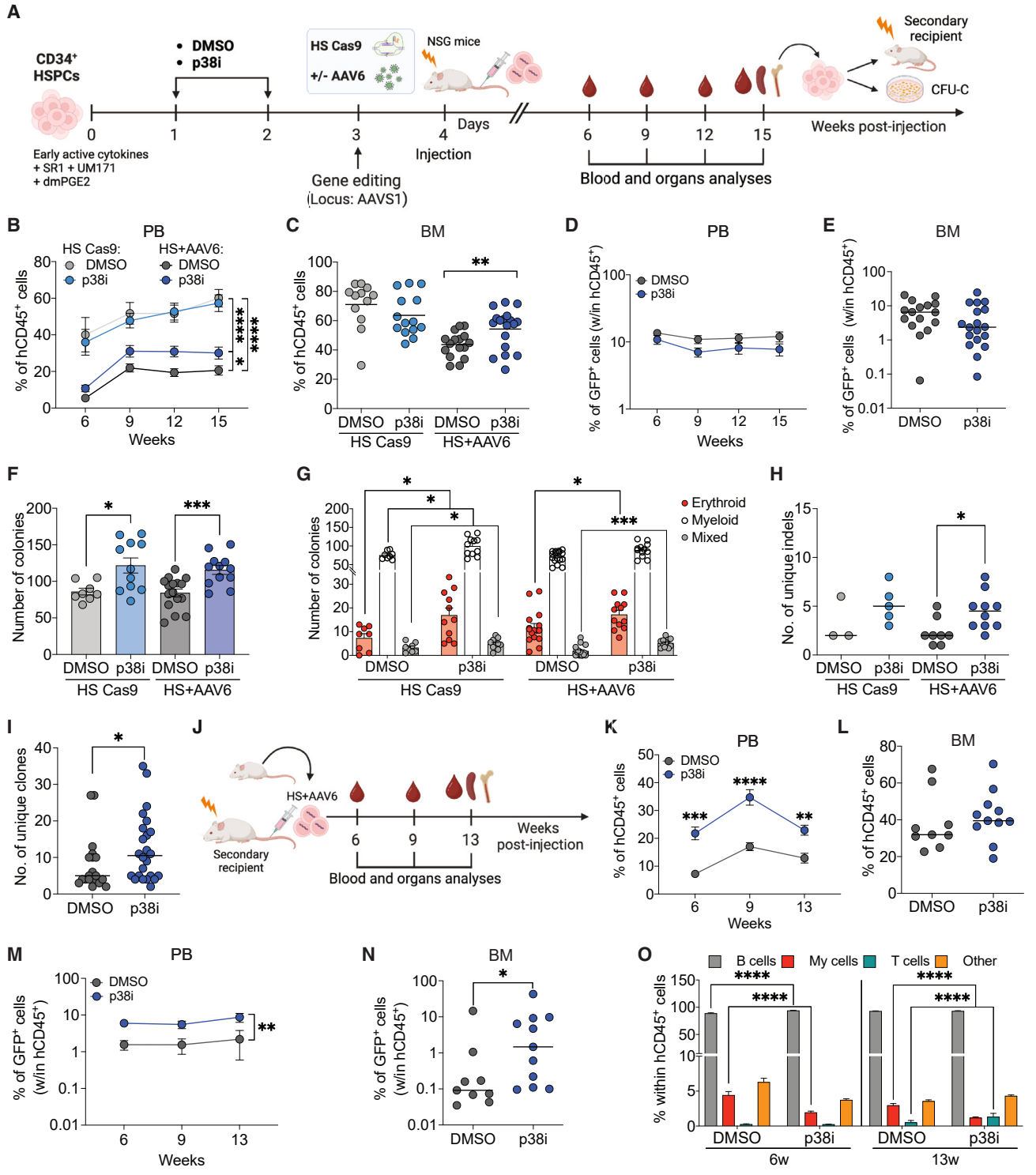

Figure 7. Repopulating capacity and clonal repertoire of GE HSPCs are ameliorated by p38 inhibitor administration

(A) Experimental workflow showing the time of *in vitro* treatments, GE, and *in vivo* injection of human CB- or mPB-derived HSPCs into NSG mice, followed by blood and organ analyses.

(B and C) Percentage of human CD45$^+$ cells in the (B) PB and (C) BM of NSG mice transplanted with CB-derived HSPCs edited as indicated (n = 12, 14, 16, 18). Mann-Whitney test (calculated at the last time point for PB).

(D and E) Percentage of GFP$^+$ cells (within hCD45$^+$ cells) in the (D) PB and (E) BM of mice from (B and C) (n = 16, 18). Mann-Whitney test.

(legend continued on next page)

Limitations of the study

Our study utilized HSPCs from healthy donors, which may not fully reflect the behavior of patient-derived cells. To gain more clinically relevant insights, similar experiments should be conducted on HSPCs from patients with disease-specific backgrounds. Although we observed improved engraftment, clonal output, and persistence of HDR-edited HSCs in xenotransplant models, clinical trials are needed to confirm the therapeutic benefits of p38 inhibition in GE approaches. Finally, while we consistently observed reduced DNA damage and MN accumulation in HSPCs edited in the presence of p38 inhibitor, further investigation into potential genotoxic effects is required before clinical application.

RESOURCE AVAILABILITY

Lead contact

The lead contact for this work is Raffaella Di Micco (dimicco.raffaella@hsr.it).

Materials availability

This study did not generate new reagents.

Data and code availability

- scRNA-seq data have been deposited in the NCBI's Gene Expression Omnibus (GEO: GSE238189) and are publicly available.
- The code used for the analysis is available at the following GitLab repository: http://www.bioinfotiget.it/gitlab/custom/dellavolpe_geneediting/dellavolpe_scrna-seq.
- Any additional raw data and information required to reanalyze the data reported in this paper are available from the lead contact upon request.

ACKNOWLEDGMENTS

We thank A. Jacob for technical help with BAR-seq library preparation, R. De Marco for micronuclei quantification, the FRACTAL and ALEMBIC facilities at San Raffaele Hospital, and the biostatisticians at Centro Universitario di Statistica per le Scienze Biomediche (CUSSB) for advice on statistical analyses. L.d.V., R.V., F.M., and D.G. conducted this study partially fulfilling their Ph.D. in Molecular Medicine, Vita-Salute San Raffaele University, Milan, Italy. G.F. conducted this study partially fulfilling his Ph.D. in Translational and Molecular Medicine – DIMET University of Milano Bicocca. L.d.V. was funded by Assegno di Ricerca Fronzaroli. A.C. is an early career scientist in the EHA and ASH TRTH. T.T. is enrolled in the EHA-EMBL/EBI computational biology training in hematology. A.S. is funded by EMBO long-term postdoctoral fellowship (awarded ALTF-245-2022). Work in the R.D.M., L.N., and B.G. lab was supported by a Horizon Europe 2020 Program X-PAND grant (G.A. 101070950). The R.D.M. laboratory was supported by a Career Development award from the Human Frontier Science Program, the New York Stem Cell Foundation, a My First AIRC grant (MFAG 2019–PI ID.23321), the European Research Council (consolidator grant 101003186, ReviveSTEM), and Fondazione Telethon (SR-Tiget Core Grant, Tele21-E5). R.D.M. is a New York Stem Cell Foundation Robertson Investigator.

AUTHOR CONTRIBUTIONS

L.d.V., F.M., and R.V. planned and performed experiments and analyzed and interpreted the data; L.A. contributed to various *in vitro* experiments; T.T. and M.B. performed bioinformatics analysis and interpreted computational data; S.B. performed clonal tracking analyses; I.M. coordinated the bioinformatics analysis; M.M.N. and B.G. provided intellectual input for scRNA-seq experimental design and analysis; C.B. and S.P. performed ATO experiments; G.F. performed seahorse experiments; E.L.F. performed WB experiments; S.F. and A. Varesi helped with library preparations for clonal tracking analysis. A. Villa supervised C.B. and S.P. and critically discussed the manuscript; S.F. and L.N. supervised A. Varesi and critically discussed the manuscript; A.S. helped with single-cell differentiation experiments; D.G., A.C., K.G., and E.C. provided technical help for animal experiments; K.G. helped with molecular assays and provided intellectual input and critical discussion. R.D.M. designed, coordinated, and interpreted the data, secured funding, and supervised the research. L.d.V., F.M., and R.D.M. wrote the manuscript with input from all the authors.

DECLARATION OF INTERESTS

R.D.M., L.d.V., F.M., A.C., L.N., and S.F. are inventors of patents on applications of gene editing in HSPCs owned and managed by the San Raffaele Scientific Institute and the Telethon Foundation. L.N. is a founder and quota holder of GeneSpire.

STAR★METHODS

Detailed methods are provided in the online version of this paper and include the following:

- KEY RESOURCES TABLE
- EXPERIMENTAL MODEL AND STUDY PARTICIPANT DETAILS
  - Mice
  - Primary cell cultures
- METHOD DETAILS
  - *In vitro* treatments
  - Gene editing
  - Colony-forming unit cell assay
  - Artificial thymic organoid (ATO) system
  - Single-cell differentiation assay
  - CD34$^+$ HSPC xenotransplantation studies in NSG mice
  - NHEJ analysis
  - Digital droplet PCR (ddPCR)
  - Quantitative PCR (qPCR)
  - Flow cytometry
  - Immunofluorescence analysis
  - Comet assay
  - Seahorse metabolic flux analysis
  - Western blot
  - EdU incorporation and detection for flow cytometry
  - Live imaging analysis of confluency
  - Cell trace violet
  - Cell cycle analyses with the Fucci2a system
  - BAR- and indels-based clonal tracking libraries

(F) Number of colonies formed by BM-derived CD34$^+$ cells purified from mice in (C) (HS Cas9: n = 8, 11; HS + AAV6: n = 16, 12). Mann-Whitney test.
(G) Number of erythroid, myeloid, and mixed colonies from samples in (F). Mann-Whitney test.
(H) Number of unique indels in human BM-derived cells (HS Cas9: n = 3, 5; HS+AAV6: n = 8, 10). Median values are reported. Mann-Whitney test.
(I) Number of unique BARs in HS+AAV6 human BM-derived cells (n = 19, 24). Median values are reported. Mann-Whitney test.
(J) Schematic representation of the secondary transplantation: BM-derived CD34$^+$ cells recovered from primary mice were injected into secondary recipients. Hematopoietic organs were analyzed at the endpoint (13 weeks).
(K and L) Percentage of hCD45$^+$ cells in the (K) PB and (L) BM of secondary-transplanted mice (n = 9, 11). Mann-Whitney test.
(M and N) Percentage of GFP$^+$ cells (within hCD45$^+$ cells) in the (M) PB and (N) BM of mice in (K and L) (n = 9, 11). Mann-Whitney tests.
(O) Percentage of B cells, T cells, myeloid, and other cells within hCD45$^+$ cells in the PB of mice in (K) (n = 9, 11). Mann-Whitney test. Mean ± SEM and, unless otherwise specified, lines indicate median values. *p < 0.05; **p < 0.01; ***p < 0.001; ****p < 0.0001.

- BAR-seq analysis
- Indels-based clonal tracking analysis
- Single-cell RNA-sequencing and analysis

- QUANTIFICATION AND STATISTICAL ANALYSIS

SUPPLEMENTAL INFORMATION

Supplemental information can be found online at https://doi.org/10.1016/j.xcrm.2024.101823.

Received: March 22, 2024
Revised: August 26, 2024
Accepted: October 18, 2024
Published: November 12, 2024

REFERENCES

1. Naldini, L., Cicalese, M.P., Bernardo, M.E., Gentner, B., Gabaldo, M., Ferrari, G., and Aiuti, A. (2022). The EHA Research Roadmap: Hematopoietic Stem Cell Gene Therapy. HemaSphere *6*, E671.
2. Ferrari, S., Valeri, E., Conti, A., Scala, S., Aprile, A., Di Micco, R., Kajaste-Rudnitski, A., Montini, E., Ferrari, G., Aiuti, A., and Naldini, L. (2023). Genetic engineering meets hematopoietic stem cell biology for next-generation gene therapy. Cell Stem Cell *30*, 549–570.
3. Doudna, J.A., and Charpentier, E. (2014). The new frontier of genome engineering with CRISPR-Cas9. Science *346*, 1258096.
4. Porteus, M.H. (2019). A New Class of Medicines through DNA Editing. N. Engl. J. Med. *380*, 947–959.
5. Scully, R., Panday, A., Elango, R., and Willis, N.A. (2019). DNA double-strand break repair-pathway choice in somatic mammalian cells. Nat. Rev. Mol. Cell Biol. *20*, 698–714.
6. Symington, L.S. (2014). End resection at double-strand breaks: Mechanism and regulation. Cold Spring Harb. Perspect. Biol. *6*, a016436.
7. Lomova, A., Clark, D.N., Campo-Fernandez, B., Flores-Bjurström, C., Kaufman, M.L., Fitz-Gibbon, S., Wang, X., Miyahira, E.Y., Brown, D., DeWitt, M.A., et al. (2019). Improving Gene Editing Outcomes in Human Hematopoietic Stem and Progenitor Cells by Temporal Control of DNA Repair. Stem Cell. *37*, 284–294.
8. Genovese, P., Schiroli, G., Escobar, G., Tomaso, T.D., Firrito, C., Calabria, A., Moi, D., Mazzieri, R., Bonini, C., Holmes, M.C., et al. (2014). Targeted genome editing in human repopulating haematopoietic stem cells. Nature *510*, 235–240.
9. Rai, R., Romito, M., Rivers, E., Turchiano, G., Blattner, G., Vetharoy, W., Ladon, D., Andrieux, G., Zhang, F., Zinicola, M., et al. (2020). Targeted gene correction of human hematopoietic stem cells for the treatment of Wiskott - Aldrich Syndrome. Nat. Commun. *11*, 4034.
10. De Ravin, S.S., Brault, J., Meis, R.J., Liu, S., Li, L., Pavel-Dinu, M., Lazzarotto, C.R., Liu, T., Koontz, S.M., Choi, U., et al. (2021). Enhanced homology-directed repair for highly efficient gene editing in hematopoietic stem/progenitor cells. Blood *137*, 2598–2608.
11. Ferrari, S., Jacob, A., Beretta, S., Unali, G., Albano, L., Vavassori, V., Cittaro, D., Lazarevic, D., Brombin, C., Cugnata, F., et al. (2020). Efficient gene editing of human long-term hematopoietic stem cells validated by clonal tracking. Nat. Biotechnol. *38*, 1298–1308.
12. Schiroli, G., Conti, A., Ferrari, S., Della Volpe, L., Jacob, A., Albano, L., Beretta, S., Calabria, A., Vavassori, V., Gasparini, P., et al. (2019). Precise Gene Editing Preserves Hematopoietic Stem Cell Function following Transient p53-Mediated DNA Damage Response. Cell Stem Cell *24*, 551–565.e8.
13. Conti, A., and Di Micco, R. (2018). p53 activation: A checkpoint for precision genome editing? Genome Med. *10*, 66.
14. Jang, Y.Y., and Sharkis, S.J. (2007). A low level of reactive oxygen species selects for primitive hematopoietic stem cells that may reside in the low-oxygenic niche. Blood *110*, 3056–3063.
15. Tesio, M., Tang, Y., Müdder, K., Saini, M., von Paleske, L., Macintyre, E., Pasparakis, M., Waisman, A., and Trumpp, A. (2015). Hematopoietic stem cell quiescence and function are controlled by the CYLD-TRAF2-p38MAPK pathway. J. Exp. Med. *212*, 525–538.
16. Henry, E., Souissi-Sahraoui, I., Deynoux, M., Lefèvre, A., Barroca, V., Campalans, A., Ménard, V., Calvo, J., Pflumio, F., and Arcangeli, M.L. (2020). Human hematopoietic stem/progenitor cells display reactive oxygen species-dependent long-term hematopoietic defects after exposure to low doses of ionizing radiations. Haematologica *105*, 2044–2055.
17. Zou, J., Zou, P., Wang, J., Li, L., Wang, Y., Zhou, D., and Liu, L. (2012). Inhibition of p38 MAPK activity promotes ex vivo expansion of human cord blood hematopoietic stem cells. Ann. Hematol. *91*, 813–823.
18. Li, X., Ma, X., Chen, Y., Peng, D., Wang, H., Chen, S., Xiao, Y., Li, L., Zhou, H., Cheng, F., et al. (2020). Coinhibition of activated p38 MAPKα and mTORC1 potentiates stemness maintenance of HSCs from SR1-expanded human cord blood $CD34^+$ cells via inhibition of senescence. Stem Cells Transl. Med. *9*, 1604–1616.
19. Hendel, A., Bak, R.O., Clark, J.T., Kennedy, A.B., Ryan, D.E., Roy, S., Steinfeld, I., Lunstad, B.D., Kaiser, R.J., Wilkens, A.B., et al. (2015). Chemically modified guide RNAs enhance CRISPR-Cas genome editing in human primary cells. Nat. Biotechnol. *33*, 985–989.
20. Leibowitz, M.L., Papathanasiou, S., Doerfler, P.A., Blaine, L.J., Sun, L., Yao, Y., Zhang, C.Z., Weiss, M.J., and Pellman, D. (2021). Chromothripsis as an on-target consequence of CRISPR–Cas9 genome editing. Nat. Genet. *53*, 895–905.
21. Castiello, M.C., Brandas, C., Ferrari, S., Porcellini, S., Sacchetti, N., Canarutto, D., Draghici, E., Merelli, I., Barcella, M., Pelosi, G., et al. (2024). Exonic knockout and knockin gene editing in hematopoietic stem and progenitor cells rescues RAG1 immunodeficiency. Sci. Transl. Med. *16*, eadh8162.
22. Desterke, C., Bilhou-Nabéra, C., Guerton, B., Martinaud, C., Tonetti, C., Clay, D., Guglielmelli, P., Vannucchi, A., Bordessoule, D., Hasselbalch, H., et al. (2011). FLT3-mediated p38-MAPK activation participates in the control of megakaryopoiesis in primary myelofibrosis. Cancer Res. *71*, 2901–2915.
23. Ezumi, Y., Nishida, E., Uchiyama, T., and Takayama, H. (1999). Thrombopoietin potentiates agonist-stimulated activation of p38 mitogen-activated protein kinase in human platelets. Biochem. Biophys. Res. Commun. *261*, 58–63.
24. Nishikai-Yan Shen, T., Kanazawa, S., Kado, M., Okada, K., Luo, L., Hayashi, A., Mizuno, H., and Tanaka, R. (2017). Interleukin-6 stimulates Akt and p38 MAPK phosphorylation and fibroblast migration in non-diabetic but not diabetic mice. PLoS One *12*, e0178232.
25. Sundström, M., Alfredsson, J., Olsson, N., and Nilsson, G. (2001). Stem cell factor-induced migration of mast cells requires p38 mitogen-activated protein kinase activity. Exp. Cell Res. *267*, 144–151.
26. Cuenda, A., Rouse, J., Doza, Y.N., Meier, R., Cohen, P., Gallagher, T.F., Young, P.R., and Lee, J.C. (1995). SB 203580 is a specific inhibitor of a MAP kinase homologue which is stimulated by cellular stresses and interleukin-1. FEBS Lett. *364*, 229–233.
27. Ogrunc, M., Di Micco, R., Liontos, M., Bombardelli, L., Mione, M., Fumagalli, M., Gorgoulis, V.G., and d'Adda di Fagagna, F. (2014). Oncogene-induced reactive oxygen species fuel hyperproliferation and DNA damage response activation. Cell Death Differ. *21*, 998–1012.
28. Pineda, G., Lennon, K.M., Delos Santos, N.P., Lambert-Fliszar, F., Riso, G.L., Lazzari, E., Marra, M.A., Morris, S., Sakaue-Sawano, A., Miyawaki, A., and Jamieson, C.H.M. (2016). Tracking of Normal and Malignant Progenitor Cell Cycle Transit in a Defined Niche. Sci. Rep. *6*, 23885.
29. García-Prat, L., Kaufmann, K.B., Schneiter, F., Voisin, V., Murison, A., Chen, J., Chan-Seng-Yue, M., Gan, O.I., McLeod, J.L., Smith, S.A., et al. (2021). TFEB-mediated endolysosomal activity controls human hematopoietic stem cell fate. Cell Stem Cell *28*, 1838–1850.e10.

30. Liang, R., Arif, T., Kalmykova, S., Kasianov, A., Lin, M., Menon, V., Qiu, J., Bernitz, J.M., Moore, K., Lin, F., et al. (2020). Restraining Lysosomal Activity Preserves Hematopoietic Stem Cell Quiescence and Potency. Cell Stem Cell *26*, 359–376.e7.

31. Walter, D., Lier, A., Geiselhart, A., Thalheimer, F.B., Huntscha, S., Sobotta, M.C., Moehrle, B., Brocks, D., Bayindir, I., Kaschutnig, P., et al. (2015). Exit from dormancy provokes DNA-damage-induced attrition in haematopoietic stem cells. Nature *520*, 549–552.

32. Wei, Z., and Liu, H.T. (2002). MAPK signal pathways in the regulation of cell proliferation in mammalian cells. Cell Res. *12*, 9–18.

33. Cicenas, J., Zalyte, E., Bairoch, A., and Gaudet, P. (2018). Kinases and Cancer. Cancers *10*, 63.

34. Jacobs, K., Doerdelmann, C., Krietsch, J., González-Acosta, D., Mathis, N., Kushinsky, S., Guarino, E., Gómez-Escolar, C., Martinez, D., Schmid, J.A., et al. (2022). Stress-triggered hematopoietic stem cell proliferation relies on PrimPol-mediated repriming. Mol. Cell *82*, 4176–4188.e8.

35. Doulatov, S., Vo, L.T., Chou, S.S., Kim, P.G., Arora, N., Li, H., Hadland, B.K., Bernstein, I.D., Collins, J.J., Zon, L.I., and Daley, G.Q. (2013). Induction of multipotential hematopoietic progenitors from human pluripotent stem cells via respecification of lineage-restricted precursors. Cell Stem Cell *13*, 459–470.

36. Clien, L., Kostadima, M., Martens, J.H.A., Canu, G., Garcia, S.P., Turro, E., Downes, K., Macaulay, I.C., Bielczyk-Maczynska, E., Coe, S., et al. (2014). Transcriptional diversity during lineage commitment of human blood progenitors. Science *345*, 1251033.

37. Fares, I., Chagraoui, J., Lehnertz, B., MacRae, T., Mayotte, N., Tomellini, E., Aubert, L., Roux, P.P., and Sauvageau, G. (2017). EPCR expression marks UM171-expanded CD34+ cord blood stem cells. Blood *129*, 3344–3351.

38. Velten, L., Haas, S.F., Raffel, S., Blaszkiewicz, S., Islam, S., Hennig, B.P., Hirche, C., Lutz, C., Buss, E.C., Nowak, D., et al. (2017). Human haematopoietic stem cell lineage commitment is a continuous process. Nat. Cell Biol. *19*, 271–281.

39. Popescu, D.M., Botting, R.A., Stephenson, E., Green, K., Webb, S., Jardine, L., Calderbank, E.F., Polanski, K., Goh, I., Efremova, M., et al. (2019). Decoding human fetal liver haematopoiesis. Nature *574*, 365–371.

40. Drissen, R., Buza-Vidas, N., Woll, P., Thongjuea, S., Gambardella, A., Giustacchini, A., Mancini, E., Zriwil, A., Lutteropp, M., Grover, A., et al. (2016). Distinct myeloid progenitor-differentiation pathways identified through single-cell RNA sequencing. Nat. Immunol. *17*, 666–676.

41. Psaila, B., Wang, G., Rodriguez-Meira, A., Li, R., Heuston, E.F., Murphy, L., Yee, D., Hitchcock, I.S., Sousos, N., O'Sullivan, J., et al. (2020). Single-Cell Analyses Reveal Megakaryocyte-Biased Hematopoiesis in Myelofibrosis and Identify Mutant Clone-Specific Targets. Mol. Cell *78*, 477–492.e8.

42. Mende, N., Bastos, H.P., Santoro, A., Mahbubani, K.T., Ciaurro, V., Calderbank, E.F., Quiroga Londoño, M., Sham, K., Mantica, G., Morishima, T., et al. (2022). Unique molecular and functional features of extramedullary hematopoietic stem and progenitor cell reservoirs in humans. Blood *139*, 3387–3401.

43. Lechman, E.R., Gentner, B., van Galen, P., Giustacchini, A., Saini, M., Boccalatte, F.E., Hiramatsu, H., Restuccia, U., Bachi, A., Voisin, V., et al. (2012). Attenuation of miR-126 activity expands HSC in vivo without exhaustion. Cell Stem Cell *11*, 799–811.

44. Sakurai, M., Ishitsuka, K., Ito, R., Wilkinson, A.C., Kimura, T., Mizutani, E., Nishikii, H., Sudo, K., Becker, H.J., Takemoto, H., et al. (2023). Chemically defined cytokine-free expansion of human haematopoietic stem cells. Nature *615*, 127–133.

45. Cabezas-Wallscheid, N., Klimmeck, D., Hansson, J., Lipka, D.B., Reyes, A., Wang, Q., Weichenhan, D., Lier, A., von Paleske, L., Renders, S., et al. (2014). Identification of regulatory networks in HSCs and their immediate progeny via integrated proteome, transcriptome, and DNA methylome analysis. Cell Stem Cell *15*, 507–522.

46. Lauridsen, F.K.B., Jensen, T.L., Rapin, N., Aslan, D., Wilhelmson, A.S., Pundhir, S., Rehn, M., Paul, F., Giladi, A., Hasemann, M.S., et al. (2018). Differences in Cell Cycle Status Underlie Transcriptional Heterogeneity in the HSC Compartment. Cell Rep. *24*, 766–780.

47. Rodriguez-Fraticelli, A.E., Weinreb, C., Wang, S.W., Migueles, R.P., Jankovic, M., Usart, M., Klein, A.M., Lowell, S., and Camargo, F.D. (2020). Single-cell lineage tracing unveils a role for TCF15 in haematopoiesis. Nature *583*, 585–589.

48. Giladi, A., Paul, F., Herzog, Y., Lubling, Y., Weiner, A., Yofe, I., Jaitin, D., Cabezas-Wallscheid, N., Dress, R., Ginhoux, F., et al. (2018). Single-cell characterization of haematopoietic progenitors and their trajectories in homeostasis and perturbed haematopoiesis. Nat. Cell Biol. *20*, 836–846.

49. Wilson, A., Laurenti, E., Oser, G., van der Wath, R.C., Blanco-Bose, W., Jaworski, M., Offner, S., Dunant, C.F., Eshkind, L., Bockamp, E., et al. (2008). Hematopoietic Stem Cells Reversibly Switch from Dormancy to Self-Renewal during Homeostasis and Repair. Cell *135*, 1118–1129.

50. Belluschi, S., Calderbank, E.F., Ciaurro, V., Pijuan-Sala, B., Santoro, A., Mende, N., Diamanti, E., Sham, K.Y.C., Wang, X., Lau, W.W.Y., et al. (2018). Myelo-lymphoid lineage restriction occurs in the human haematopoietic stem cell compartment before lymphoid-primed multipotent progenitors. Nat. Commun. *9*, 4100.

51. Matteini, F., Mulaw, M.A., and Florian, M.C. (2021). Aging of the Hematopoietic Stem Cell Niche: New Tools to Answer an Old Question. Front. Immunol. *12*, 738204.

52. Hammond, C.A., Wu, S.W., Wang, F., MacAldaz, M.E., and Eaves, C.J. (2023). Aging alters the cell cycle control and mitogenic signaling responses of human hematopoietic stem cells. Blood *141*, 1990–2002.

53. Lettera, E., Scala, S., Basso-Ricci, L., Tavella, T., Volpe, L.d., Furno, E.L., Kaufmann, K.B., Garcia-Prat, L., Quaranta, P., Hernandez, R.J., et al. (2023). Molecular and phenotypic blueprint of the hematopoietic compartment reveals proliferation stress as a driver of age-associated human stem cell dysfunctions. bioRxiv. https://doi.org/10.1101/2023.09.15.557553.

54. Ito, K., Hirao, A., Arai, F., Takubo, K., Matsuoka, S., Miyamoto, K., Ohmura, M., Naka, K., Hosokawa, K., Ikeda, Y., and Suda, T. (2006). Reactive oxygen species act through p38 MAPK to limit the lifespan of hematopoietic stem cells. Nat. Med. *12*, 446–451.

55. Johnson, C.S., Williams, M., Sham, K., Belluschi, S., Ma, W., Wang, X., Lau, W.W.Y., Kaufmann, K.B., Krivdova, G., Calderbank, E.F., et al. (2024). Adaptation to ex vivo culture reduces human hematopoietic stem cell activity independently of the cell cycle. Blood *144*, 729–741.

56. Ahuja, A.K., Jodkowska, K., Teloni, F., Bizard, A.H., Zellweger, R., Herrador, R., Ortega, S., Hickson, I.D., Altmeyer, M., Mendez, J., and Lopes, M. (2016). A short G1 phase imposes constitutive replication stress and fork remodelling in mouse embryonic stem cells. Nat. Commun. *7*, 10660.

57. Calvanese, V., Nguyen, A.T., Bolan, T.J., Vavilina, A., Su, T., Lee, L.K., Wang, Y., Lay, F.D., Magnusson, M., Crooks, G.M., et al. (2019). MLLT3 governs human haematopoietic stem-cell self-renewal and engraftment. Nature *576*, 281–286.

58. Zonari, E., Desantis, G., Petrillo, C., Boccalatte, F.E., Lidonnici, M.R., Kajaste-Rudnitski, A., Aiuti, A., Ferrari, G., Naldini, L., and Gentner, B. (2017). Efficient Ex Vivo Engineering and Expansion of Highly Purified Human Hematopoietic Stem and Progenitor Cell Populations for Gene Therapy. Stem Cell Rep. *8*, 977–990.

59. Capo, V., Penna, S., Merelli, I., Barcella, M., Scala, S., Basso-Ricci, L., Draghici, E., Palagano, E., Zonari, E., Desantis, G., et al. (2021). Expanded circulating hematopoietic stem/progenitor cells as novel cell source for the treatment of TCIRG1 osteopetrosis. Haematologica *106*, 74–86.

60. Schiroli, G., Ferrari, S., Conway, A., Jacob, A., Capo, V., Albano, L., Plati, T., Castiello, M.C., Sanvito, F., Gennery, A.R., et al. (2017). Preclinical modeling highlights the therapeutic potential of hematopoietic stem cell gene editing for correction of SCID-X1. Sci. Transl. Med. *9*, eaan0820.

61. Strobel, B., Miller, F.D., Rist, W., and Lamla, T. (2015). Comparative Analysis of Cesium Chloride- and Iodixanol-Based Purification of Recombinant

Adeno-Associated Viral Vectors for Preclinical Applications. Hum. Gene Ther. Methods *26*, 147–157.

62. Gnani, D., Crippa, S., Della Volpe, L., Rossella, V., Conti, A., Lettera, E., Rivis, S., Ometti, M., Fraschini, G., Bernardo, M.E., and Di Micco, R. (2019). An early-senescence state in aged mesenchymal stromal cells contributes to hematopoietic stem and progenitor cell clonogenic impairment through the activation of a pro-inflammatory program. Aging Cell *18*, e12933.
63. Clement, K., Rees, H., Canver, M.C., Gehrke, J.M., Farouni, R., Hsu, J.Y., Cole, M.A., Liu, D.R., Joung, J.K., Bauer, D.E., and Pinello, L. (2019). CRISPResso2 provides accurate and rapid genome editing sequence analysis. Nat. Biotechnol. *37*, 224–226.
64. Nestorowa, S., Hamey, F.K., Pijuan Sala, B., Diamanti, E., Shepherd, M., Laurenti, E., Wilson, N.K., Kent, D.G., and Göttgens, B. (2016). A single-cell resolution map of mouse hematopoietic stem and progenitor cell differentiation. Blood *128*, e20–e31.
65. Korsunsky, I., Millard, N., Fan, J., Slowikowski, K., Zhang, F., Wei, K., Baglaenko, Y., Brenner, M., Loh, P.R., and Raychaudhuri, S. (2019). Fast, sensitive and accurate integration of single-cell data with Harmony. Nat. Methods *16*, 1289–1296.
66. McInnes, L., Healy, J., Saul, N., and Großberger, L. (2018). UMAP: Uniform Manifold Approximation and Projection. J. Open Source Softw. *3*, 861.
67. Wang, G., Wen, W.X., Mead, A.J., Roy, A., Psaila, B., and Thongjuea, S. (2022). Processing single-cell RNA-seq datasets using SingCellaR. STAR Protoc. *3*, 101266.
68. Subramanian, A., Tamayo, P., Mootha, V.K., Mukherjee, S., Ebert, B.L., Gillette, M.A., Paulovich, A., Pomeroy, S.L., Golub, T.R., Lander, E.S., and Mesirov, J.P. (2005). Gene set enrichment analysis: a knowledge-based approach for interpreting genome-wide expression profiles. Proc. Natl. Acad. Sci. USA *102*, 15545–15550.
69. Tirosh, I., Izar, B., Prakadan, S.M., Wadsworth, M.H., 2nd, Treacy, D., Trombetta, J.J., Rotem, A., Rodman, C., Lian, C., Murphy, G., et al. (2016). Dissecting the multicellular ecosystem of metastatic melanoma by single-cell RNA-seq. Science *352*, 189–196.
70. Wilson, N.K., Schoenfelder, S., Hannah, R., Sánchez Castillo, M., Schütte, J., Ladopoulos, V., Mitchelmore, J., Goode, D.K., Calero-Nieto, F.J., Moignard, V., et al. (2016). Integrated genome-scale analysis of the transcriptional regulatory landscape in a blood stem/progenitor cell model. Blood *127*, e12–e23.

STAR★METHODS

KEY RESOURCES TABLE

REAGENT or RESOURCE	SOURCE	IDENTIFIER
Antibodies		
Anti-human CD133/1 PE-Vio 770 (Clone AC133)	Miltenyi Biotec	Cat#130-113-110; RRID: AB_2725939
Anti-human CD34 PE (Clone AC136)	Miltenyi Biotec	Cat#130-113-179; RRID: AB_2726006
Anti-human CD90 APC (Clone 5E10)	BD Biosciences	Cat#559869; RRID: AB_398677
Anti-human CD45 APC-eFluor 780 (Clone HI30)	Invitrogen	Cat#47-0459-42; RRID: AB_1944368
Anti-human CD19 PE (Clone SJ25C1)	BD Biosciences	Cat#345789; RRID: AB_2868815
Anti-human CD13 BV421 (Clone WM15)	BD Biosciences	Cat#562596; RRID: AB_2737672
Anti-human CD3 APC (Clone UCHT1)	BD Biosciences	Cat#555335; RRID: AB_398591
Anti-human CD33 PE-Cy7 (Clone P67.6)	BD Biosciences	Cat#333952; RRID: AB_2713932
Anti-human CD8 PE-Cy7 (Clone RPA-T8)	BD Biosciences	Cat#557746; RRID: AB_396852
Anti-human CD38 PerCP-Cy5.5 (Clone HB-7)	BioLegend	Cat#356614; RRID: AB_2562183
Anti-human CD34 PE-Cy7 (Clone 8G12)	BD Biosciences	Cat#348811; RRID: AB_2868855
Anti-human CD33 BV421 (Clone WM53)	BD Biosciences	Cat#562854; RRID: AB_2737405
Anti-human CD11 b PE (Clone M1/70)	BioLegend	Cat#101207; RRID: AB_312790
Anti-human CD41 PE-Cy5 (Clone HIP8)	BioLegend	Cat#303708; RRID: AB_314378
Anti-human CD45 PE-Cy7 (Clone HI30)	BioLegend	Cat#304016; RRID: AB_314404
Anti-human CD235a (GlyA) APC (Clone GA-R2 (HIR2))	BD Biosciences	Cat#551336; RRID: AB_398499
Anti-human CD14 APC-Cy7 (Clone M5E2)	BioLegend	Cat#301820; RRID: AB_493695
Anti-human CD56 Pacific Blue (Clone MEM-188)	BioLegend	Cat#304629; RRID: AB_2282499
Anti-human CD45Ra Alexa Fluor 700 (Clone HI100)	BioLegend	Cat#304120; RRID: AB_493763
Anti-human CD15 BV510 (Clone W6D3)	BioLegend	Cat#323028; RRID: AB_2563400
Anti-human CD3 PE (Clone OKT3)	BioLegend	Cat#317308; RRID: AB_571913
Anti-human CD19 BV510 (Clone HIB19)	BioLegend	Cat#302242; RRID: AB_2561668
Anti-human CD71 BV421 (Clone CY1G4)	Biolegend	Cat#334122; RRID: AB_2734337
Anti-human CD61 PE-Cy7 (Clone VI-PL2)	Biolegend	Cat#336416; RRID: AB_2566692
Anti-human CD56 PE (Clone AF12-7H3)	Miltenyi Biotec	Cat#130-113-312; RRID: AB_2726090
Anti-human CD45 PerCP-Cy5.5 (Clone 2D1)	Biolegend	Cat#368504; RRID: AB_2566352
Anti-human CD1a APC (Clone HI149)	Biolegend	Cat#300110; RRID: AB_314024
Anti-human CD7 APC-Vio 770 (Clone CD7-6B7)	Miltenyi Biotec	Cat#130-117-677; RRID: AB_2733142
Anti-human CD5 PE-Vio 770 (Clone UCHT2)	Miltenyi Biotec	Cat#130-119-943; RRID: AB_2751939
Anti-human CD34 VioBlue (Clone AC136)	Miltenyi Biotec	Cat#130-095-393; RRID: AB_10827793
Anti-human CD8a APC-H7 (Clone HIT8a)	BD Biosciences	Cat#560179; RRID: AB_1645481
Anti-human TCRα/β PerCP-Cy5.5 (Clone IP26)	Biolegend	Cat#306724; RRID: AB_2563002
Anti-human CD3 APC (Clone REA613)	Miltenyi Biotec	Cat#130-113-135; RRID: AB_2725963
Anti-human CD4 PE-Vio 770 (Clone REA623)	Miltenyi Biotec	Cat#130-113-227; RRID: AB_2726038
Anti-human CD45 Vio Blue (Clone REA747)	Miltenyi Biotec	Cat#130-110-637; RRID: AB_2658243
Anti-human p38-MAPK pThr180/pTyr182	Cell Signaling	Cat#9211; RRID: AB_331641
Anti-8-oxo-2′deoxyguanosine	Trevigen	Cat#4354-MC-050; RRID: AB_1857195
Anti-human FCR Blocking	Miltenyi Biotec	Cat#130059901; RRID: AB_2892112
Purified Rat anti-mouse CD16/CD32 (Clone 2.4G2)	BD Biosciences	Cat#553141; RRID: AB_394656
Donkey anti-mouse IgG (H + L) Secondary Antibody, Alexa Fluor 647	Thermo Fisher Scientific	Cat#A-31571; RRID: AB_162542

(*Continued on next page*)

Continued

REAGENT or RESOURCE	SOURCE	IDENTIFIER
Donkey anti-mouse IgG (H + L) Secondary Antibody, Alexa Fluor 488	Thermo Fisher Scientific	Cat#A-21202; RRID: AB_141607
Donkey anti-rabbit IgG (H + L) Secondary Antibody, Alexa Fluor 568	Thermo Fisher Scientific	Cat#A-10042; RRID: AB_2534017
Mouse anti-human Phospho-Histone H2A.X (Ser139) (Clone JBW301)	Merck Millipore	Cat#05–636; RRID: AB_309864
Rabbit anti-human 53BP1	Bethyl Laboratories	Cat#A300-272A; RRID: AB_185520
Rabbit anti-human phospho-RPA32 (S33)	Bethyl Laboratories	Cat#A300-246A; RRID: AB_2180847
Rabbit anti-human phospho-ATR (Ser428)	Cell Signaling	Cat#2853; RRID: AB_2290281
Rabbit anti-human phospho-CHK1 (Ser345) (Clone 133D3)	Cell Signaling	Cat#2348; RRID: AB_331212
Rabbit anti-human phospho-MAPKAPK-2 (Thr334) (Clone 27B7)	Cell Signaling	Cat#3007; RRID: AB_490936
Rabbit anti-human MAPKAPK-2 (Clone D1E11)	Cell Signaling	Cat#12155; RRID: AB_2797831
Rabbit anti-human phospho-CHK2 (Thr68) (Clone C13C1)	Cell Signaling	Cat#2197; RRID: AB_2080501
Rabbit anti-human Histone H3	Abcam	Cat#ab1791; RRID: AB_302613
Goat anti-rabbit IgG (H + L) Secondary Antibody, HRP	Thermo Fisher Scientific	Cat#31460; RRID: AB_228341
Goat anti-mouse IgG (H + L) Secondary Antibody, HRP	Thermo Fisher Scientific	Cat#31430; RRID: AB_228307
Biological samples		
Umbilical cord blood	San Raffaele Hospital	N/A
Mobilized peripheral blood	Mobilized Leukopak (AllCells)	N/A
Chemicals, peptides, and recombinant proteins		
16,16-Dimethyl Prostaglandin E2	Cayman Chemical	Cat#14750
StemSpan SFEM	STEMCELL Technologies	Cat#09650
MethoCult	STEMCELL Technologies	Cat#H4434
Iscove's DMEM, 1X	Corning	Cat#15-016-CVR
RPMI 1640	Corning	Cat#10-040-CM
B27 supplement	ThermoFisher Scientific	Cat#17504044
L-ascorbic acid 2-phosphate sesqui magnesium salt hydrate	Sigma-Aldrich	Cat#A8960
GlutaMAX™ Supplement	ThermoFisher Scientific	Cat#35050061
Recombinant human stem cell factor (SCF)	Peprotech	Cat#300-07
Recombinant human thrombopoietin (TPO)	Peprotech	Cat#300-18
Recombinant human Flt3-Ligand	Peprotech	Cat#300-19
Recombinant human IL6	Peprotech	Cat#200-06
Recombinant human IL7	Peprotech	Cat#200-07
StemRegenin 1 (SR1)	Biovision	Cat#1967
UM171	STEMCell Technologies	Cat#72914
Human IL-3 recombinant protein	Peprotech	Cat#200-03
Human IL-11	Miltenyi Biotec	Cat#130-103-439
Human GM-CSF	Miltenyi Biotec	Cat#130-093-862
Human IL-2	Miltenyi Biotec	Cat#130097743
Human IL-7	Miltenyi Biotec	Cat#130-095-363
Erythropoietin (EPO, Eprex)	Janssen-Cilag	N/A
Human Low-Density Lipoproteins (LDL)	Stem Cell Technologies	Cat#02698
p38 MAPK inhibitor (SB-203580)	Sigma-Aldrich	Cat#559389

(*Continued on next page*)

Continued

REAGENT or RESOURCE	SOURCE	IDENTIFIER
ERK inhibitor (FR180204)	Sigma-Aldrich	Cat#SML0320
JNK inhibitor (SP600125)	Sigma-Aldrich	Cat#S5567
NAC (N-acetyl-L-cysteine)	Sigma-Aldrich	Cat#A9165
Resveratrol (SRT501)	MedChemExpress	Cat#HY-16561
Tempol (4-Hydroxy-TEMPO)	MedChemExpress	Cat#HY-100561
CDK4/6 inhibitor (Palbociclib-PD0332991)	Selleck Chemicals	Cat#S1116
Cas9 enhancing	Integrated DNA Technologies	Cat#1075916
Alt-R CRISPR-Cas9 tracrRNA	Integrated DNA Technologies	Cat#1072534
Alt-R CRISPR-Cas9 crRNA	Integrated DNA Technologies	http://www.idtdna.com/
Alt-R CRISPR-Cas9 Negative Control crRNA #1	Integrated DNA Technologies	Cat#1072544
SpCas9 Nuclease	Aldevron	Cat#9212
7-AAD Viability Staining solution	Biolegend	Cat#420403
Pacific Blue Annexin V	Biolegend	Cat#640918
CM-H2DCFDA	Thermo Fisher	Cat#C6827
CellROX™ Deep Red Reagent	Thermo Fisher	Cat#C10422
MitoSOX™ Red reagent	Thermo Fisher	Cat#M36008
Intracellular Staining Permeabilization Wash Buffer	Biolegend	Cat#421002
CometAssay Lysis Solution	R&D Systems	Cat#4250-050-01
CometAssay LMAgarose	R&D Systems	Cat#4250-050-02
Poly-L-lysine solution	Sigma-Aldrich	Cat#P8920
Paraformaldehyde solution 4% in PBS	Santa Cruz Biotechnology	Cat#SC-281692
DAPI for nucleic acid staining	Sigma-Aldrich	Cat#D9542
Hoechst 3342 Fluorescent Stain	Thermo Fisher	Cat#62249
Pierce™ Protease and Phosphatase Inhibitor Mini Tablets	Thermo Scientific	Cat#A32961
Critical commercial assays		
QIAamp DNA Micro Kit	QIAGEN	Cat#56304
miRNeasy Micro Kit	QIAGEN	Cat#1071023
RNeasy Plus Micro Kit	QIAGEN	Cat#74034
RNase-free DNase Set	QIAGEN	Cat#79254
iScript cDNA Synthesis Kit	Bio-Rad	Cat#170-8891
P3 Primary Cell 4D-Nucleofector X Kit S	Lonza	Cat#V4XP-3032
Fast SYBR Green Master Mix 2X	Thermo Fisher	Cat#4385618
T7 Endonuclease I	New England Biolabs	Cat#M0302L
iScript cDNA Synthesis Kit	Bio-RAD	Cat#170-8891
TaqMan PreAmp Master Mix 2X	Thermo Fisher	Cat#4488593
Click-iT EdU Alexa Fluor 647 Flow cyometry assay kit	Thermo Fisher	Cat#C10635
Chromium single cell 3′ feature barcode library kit	10X Genomics	Cat#PN-1000079
Seahorse XF Cell Mito Stress Test Kit	Agilent Technologies	Cat#103708-100
Seahorse XF Glycolysis Stress Test Kit	Agilent Technologies	Cat#103020-100
CellTrace™ Violet Cell Proliferation Kit	Thermo Scientific	Cat# C34557
Deposited data		
Raw and analyzed single-cell RNA-seq data	This paper	GEO: GSE238189
Experimental models: cell lines		
Human cord blood CD34^{+} Stem/Progenitor cells	Lonza	Cat#2C-101

(*Continued on next page*)

Continued

REAGENT or RESOURCE	SOURCE	IDENTIFIER
DLL4-expressing stromal cell line (MS5-hDLL4)	Department of Pathology and Laboratory Medicine, David Geffen School of Medicine, Univ. of California, Los Angeles (UCLA)	N/A
Experimental models: organisms/strains		
NOD.CG- Prkdc^{scid}Il2rg^{tm1Wjl}/SzJ (NSG) *Mus Musculus*	Charles River Laboratories (IACUC: #1385)	RRID: IMSR_JAX:005557
Oligonucleotides		
See Table S1	This paper	N/A
Recombinant DNA		
AAV6.PGK.GFP (AAVS1 HA)	Schiroli et al.[12]	N/A
AAV6.PGK.GFP.bar (AAVS1 HA)	Ferrari et al.[11]	N/A
pCCLsin.PPT.hEF1A-intron.FUCCI.Wpre	Pineda et al.[28]	N/A
Software and algorithms		
BD FACSDiva software	BD Biosciences	https://www.bdbiosciences.com/en-us/products/software/instrument-software/bd-facsdiva-software
Prism software (v8)	GraphPad Prism	https://www.graphpad.com/
QuantaSoft (v1.7)	Biorad	https://www.bio-rad.com/
ImageJ (v2.9)	NIH	https://imagej.nih.gov/ij/
ImageLab (v6)	Bio-Rad	https://www.bio-rad.com/it-it/product/image-lab-software?ID=KRE6P5E8Z
LAS X Leica Software	Leica Mycrosystems	https://www.leica-microsystems.com/it/prodotti/software-per-microscopi/dettagli/product/leica-las-x-ls/
FlowJo	FlowJo	https://www.flowjo.com/
IncuCyte Software S3 (v2018A)	Sartorius	https://www.sartorius.com/en/products/live-cell-imaging-analysis/live-cell-analysis-software/incucyte-s3-software-v2018a?srsltid=AfmBOooK9off6fcxr8aHGCvb8-zK2PlKqZa7PkGJQB6VTRg7V19t5Wd_
Seahorse Wave software (v2.6)	Agilent Technologies	https://www.agilent.com/en/product/cell-analysis/real-time-cell-metabolic-analysis/xf-software/seahorse-wave-controller-software-2-6-1-740904
Code used for the single-cell RNA-seq	This paper	http://www.bioinfotiget.it/gitlab/custom/dellavolpe_geneediting/dellavolpe_scrna-seq.

EXPERIMENTAL MODEL AND STUDY PARTICIPANT DETAILS

Mice

NOD-SCID-IL2Rg$^{-/-}$ (NSG) mice were purchased from Charles River Laboratories and maintained in specific-pathogen-free (SPF) conditions. Specifically, in order to ensure higher transplantation success, engraftment, and better reproducibility, only female mice (8 weeks of age) were used. The procedures involving animals were designed and performed with the approval of the Animal Care and Use Committee of the San Raffaele Hospital and communicated to the Ministry of Health and local authorities according to Italian law (IACUC #1385).

Primary cell cultures

CD34$^+$ HSPCs were either freshly purified from human CB after obtaining informed consent and upon approval by the San Raffaele Hospital ethical committee (TIGET09) or purchased frozen from Lonza. After thawing, HSPCs were seeded at the concentration of 5 × 10^5 cells/mL in serum-free StemSpan SFEM medium (StemCell Technologies) supplemented with 10μM 16,16-Dimethyl Prostaglandin E2 (added only at thawing) (Cayman), L-glutamine (2mM) and Penicillin-Streptomycin (100 IU/mL penicillin, 100 mg/mL streptomycin), 1μM SR-1 (Biovision), 50nM UM171 (STEMCell Technologies), and human early-acting cytokines (SCF 100 ng/mL, Flt3-L 100 ng/mL, TPO 20 ng/mL, and IL-6 20 ng/mL; Peprotech).

G-CSF or G-CSF + Plerixafor mPB CD34$^+$ HSPCs collected from healthy donors were purified in-house with the CliniMACS CD34 Reagent System (Miltenyi Biotec) from Mobilized Leukopak (AllCells) according to the TIGET-HPCT protocol approved by OSR Ethical Committee and following the manufacturer's instructions. HSPCs were seeded at the concentration of 0.5–1x10^6 cells/mL in serum-free StemSpan SFEM medium supplemented with 10μM 16,16-Dimethyl Prostaglandin E2 (added only at thawing) (Cayman), L-glutamine (2mM) and Penicillin-Streptomycin (100 IU/mL penicillin, 100 mg/mL streptomycin), 1μM SR-1(Biovision), 35nM UM171 (STEMCell Technologies), and human early-acting cytokines (SCF 300 ng/mL, Flt3-L 300 ng/mL, and TPO 100 ng/mL; Peprotech). All cells were cultured in a 20% O_2 and 5% CO_2 humidified atmosphere at 37°C, except for low-oxygen conditions experiments in which cells were cultured in 3% O_2. Male and female donors were randomly allocated to the experimental groups and the sample size is reported in figure legends for each experiment.

Cell lines

The murine stromal cell line (MS5) edited to ectopically express human Notch ligand, delta-like 4 (hDLL4) was used for the ATO platform and was kindly provided by G.M. Crooks, Department of Pathology and Laboratory Medicine, David Geffen School of Medicine, Univ. of California, Los Angeles (UCLA). hDLL4 cells tested negative for mycoplasma contamination. ATO complete medium is composed by RPMI 1640 (Corning), 4% B27 supplement (ThermoFisher Scientific), 30 μM L-ascorbic acid 2-phosphate sesqui magnesium salt hydrate (Sigma-Aldrich) reconstituted in PBS, 0.2% Primocin (InvivoGen), 100x Glutamax (ThermoFisher Scientific), 5 ng/mL Flt3-L and 5 ng/mL IL-7 (Peprotech).

METHOD DETAILS

In vitro treatments

Where indicated, at day 1 and day 2 post-thawing, HSPCs were treated with 4 or 8μM of p38 inhibitor, 4μM ERK, 2μM JNK inhibitors (SB-203580, FR180204, SP600125; Sigma-Aldrich), 2mM NAC (Sigma-Aldrich) 10μM Resveratrol (Sigma-Aldrich; SRT501), 300μM Tempol (4-Hydroxy-TEMPO, MedChemExpress), or the combination of the three; instead, for CDK4/6 inhibitor (Palbociclib-PD0332991, Selleck Chemicals) administration, HSPCs were treated with 2μM CDK4/6i for 24h before washing out. For all treatments negative control was obtained treating cells with the same volume of DMSO or PBS vehicle.

Gene editing

HSPCs were edited according to a previously optimized protocol[60] after an overnight. or three days of *ex vivo* culture, cells were nucleofected with 2.5–1.25 μM of RNPs and electroporation enhancer (Integrated DNA Technologies) according to manufacturer's instructions using P3 Primary Cell 4D-Nucleofector X Kit and program EO-100 (Lonza). Ribonucleoproteins (RNPs) were assembled by incubating for 10 min at r.t at 1:1.5 M ratio S.p. Cas9 protein (Aldevron) with synthetic gRNAs (Integrated DNA Technologies) targeting *AAVS1* (high specificity) or *IL2RG* locus (low specificity).[12] Transduction with AAV6 was performed at a dose of 1 × 10^4 vg/cell 15 min after electroporation. AAV6 donor templates for HDR were generated from a construct containing AAV2 inverted terminal repeats, produced by the triple-transfection method, and purified by ultracentrifugation on a cesium chloride gradient as previously described.[61] The design of AAV6 donor templates with homologies for the *AAVS1* locus (encoding for a PGK.GFP reporter cassette) was previously reported.[12] BAR-coded AAV6 was provided by L. Naldini's group.[11]

Colony-forming unit cell assay

CFU-C assay was performed at the indicated timings, plating 800 cells in methylcellulose-based medium (MethoCult H4434, StemCell Technologies) supplemented with 100 IU/mL penicillin and 100 mg/mL streptomycin. Three technical replicates were performed for each sample, and the mean value was plotted and used for statistical analysis. Two weeks after plating, colonies were counted in a blinded fashion, and erythroid, myeloid, and mixed colonies were identified according to morphological criteria.

For the secondary CFU-C assay, one week after seeding primary CFU-C were washed in PBS and 2 × 10^4 cells were plated for secondary analysis as described above.

Artificial thymic organoid (ATO) system

The ATO platform was generated by A. Villa's group by aggregating 1.5 × 10^5 DLL4-expressing stromal cell line (MS5-hDLL4) with 7–10 × 10^3 CB-derived HSPCs. The resulting cellular suspension was seeded in 0.4 μm Millicell Transwell insert (Millipore) and placed on a 6-well plate containing 1mL of ATO complete medium as previously described.[21]

Single-cell differentiation assay

$CD34^+CD133^+CD45RA^-CD90^+$ population (negative to ZombieAqua viable dye) was sorted as single cells (1 cell/well) and seeded in U-bottom 96-well filled with 100 μL/well Myeloid-Erythroid-Megakaryocyte (MEM) cytokine medium: StemPro medium with nutrients supplement (Life Technologies) supplemented with cytokines (SCF 100 ng/mL, Flt3-L 20 ng/mL, TPO 100 ng/mL, IL-6 50 ng/mL, IL-3 10 ng/mL, all Peprotech; IL-11 50 ng/mL, GM-CSF 20 ng/mL, IL-2 10 ng/mL, IL-7 20 ng/mL; all Miltenyi Biotec), erythropoietin (EPO) 3 units/mL (Eprex, Janssen-Cilag), h-LDL 50 ng/mL (Stem Cell Technologies), 1% L-Glutamine (Life Technologies) and 1% Pen/Strep (Life Technologies). Cells were cultured for 3 weeks in a 5% CO_2 humidified atmosphere at 37°C. Cell sorting was performed on a BD FACSAria Fusion (BD Biosciences) using BDFACS Diva software and equipped with four lasers: blue (488 nm), yellow/green (561 nm), red (640 nm), and violet (405 nm). Cells were sorted with a 100 mm nozzle.

$CD34^+$ HSPC xenotransplantation studies in NSG mice

For primary transplantation, 1 to 2 × 10^5 CB- or 2 × 10^6 mPB-derived $CD34^+$ cells were injected 24h post-editing procedure intravenously into NSG mice after sub-lethal irradiation (150–180 cGy). The sample size was determined by the total number of available treated cells. For secondary transplants, $CD34^+$ cells purified from the BM of primary recipients were pooled according to the experimental group and transplanted in the same number of NSG recipient mice after sub-lethal irradiation (150–180 cGy). Mice were attributed to each experimental group randomly. Human $CD45^+$ cell engraftment and the presence of gene-edited cells were monitored by serial collection of blood from the mouse tail and, at the end of the experiment (15 weeks after transplantation), BM and spleen were harvested and analyzed. Immunophenotypic analyses were conducted as described below.

NHEJ analysis

For molecular analyses, genomic DNA was isolated with QIAamp DNA Micro Kit (QIAGEN). Nuclease activity (*AAVS1* intron 1) was measured by mismatch-sensitive endonuclease assay by PCR-based amplification of the targeted locus followed by digestion with T7 Endonuclease I (NEB) according to the manufacturer's instructions. Digested DNA fragments were resolved and quantified by capillary electrophoresis on LabChip GX Touch HT (PerkinElmer) according to the manufacturer's instructions.

Digital droplet PCR (ddPCR)

Genomic DNA was isolated with QIAamp DNA Micro Kit (QIAGEN). For digital droplet PCR analysis, 5–50 ng of genomic DNA was analyzed using the QX200 Droplet Digital PCR System (Biorad) according to the manufacturer's instructions. Primers and probes were designed between the HDR donor template sequence and the 3′ integration junction on the target AAVS1 locus (listed in Primers and DNA sequences). TTC5 gene was used as the control sequence and the respective primers and probes were purchased in the PrimePCR ddPCR Copy Number Assay: TTC5, Human. The different probes were conjugated with FAM (target) and HEX (TTC5 reference) fluorophores. Thermal conditions for annealing and extension were adjusted as follows: 95°C × 10 min; 94°C × 30 s, 55°C × 1 min, 72°C × 2 min (40 cycles); 98°C × 10 min.

Quantitative PCR (qPCR)

Total RNA was extracted using either miRNeasy Micro Kit (QIAGEN) or RNeasy Plus Micro Kit (QIAGEN), according to the manufacturer's instructions and DNase treatment was performed using RNase-free DNase Set (QIAGEN). For gene expression analyses, cDNA was synthesized with iScript cDNA Synthesis Kit (Bio-Rad), pre-amplified using TaqMan PreAmp Master Mix (ThermoFisher), and used for q-PCR in a Viia7 Real-time PCR thermal cycler using Fast SYBR Green Master Mix (Thermofisher), after standard curve method optimization to reach the 100% primer efficiency for each couple of primers listed in Table S1. Three technical replicates were performed for each sample, and the mean value was selected for further analysis. The relative expression of each target gene was first normalized to *GUSB* housekeeping gene expression and then represented as fold changes ($2^{-\Delta\Delta Ct}$) relative to the indicated control conditions. An RNP loaded with a gRNA with no reported target specificity against the human genome[12] was used as a control for Figure 1C.

Flow cytometry

Immunophenotypic and apoptosis analysis

For immunophenotypic analyses (performed on FACSCanto II; BD Pharmingen) of *ex vivo* cultured HSPCs, cellular suspension (approx. 3–5 × 10^4 cells) was incubated with anti-human FcR Blocking (1:100 dilution) (Miltenyi Biotec) to prevent unwanted binding of antibodies to human Fc receptor-expressing cells. Then, cells were stained with different fluorescent-labeled antibodies (1:100 dilution, each): anti-human CD34 PE (Miltenyi Biotec), anti-human CD133 PE-Vio 770 (Miltenyi Biotec), and anti-human CD90 APC (BD Biosciences). Where indicated immunophenotypic staining was combined with Annexin V (BioLegend) and 7-amino-actinomycin D (7-AAD) (BioLegend) viability staining according to the manufacturer's instructions (3 and 1μL *per* sample, respectively). Apoptosis analysis was performed as previously described.[12]

For immunophenotypic analyses (performed on FACSCanto II; BD Pharmingen) of cells retrieved from *in vivo* organs, we used anti-human and –mouse FcR Blocking (1:100 and 1:200 dilution, respectively) (BD Biosciences) and then cells were stained with different fluorescent-labeled antibodies (1:100 dilution, each).

(1) Peripheral blood: anti-human CD45 APC-eFluor 780, anti-human CD19 PE or BV510, anti-human CD13 BV421, anti-human CD3 APC or PE, anti-human CD33 PE-Cy7 (only at 6w) or anti-human CD8 PE-Cy7 (at 9,12, and 15w);
(2) Bone marrow: anti-human CD45 APC-eFluor 780, anti-human CD90 APC, anti-human CD34 PE-Cy7, anti-human CD19 BV510, anti-human CD13 BV421, and anti-human CD3 PE;
(3) Spleen: anti-human CD45 APC-eFluor 780, anti-human CD19 PE or BV510, anti-human CD13 BV421, anti-human CD3 APC or PE, anti-human CD8 PE-Cy7, anti-human CD71 BV421, anti-human CD235a (GlyA) APC, anti-human CD41 PE-Cy5, and anti-human CD61 PE-Cy7.

Single-stained and Fluorescence Minus One (FMO) stained cells were used as controls and SPHERO Rainbow Calibration Particles (Spherotech) were used to perform instrument calibration. Data were analyzed using the FlowJo software.

Phospho-p38 staining

Cellular suspension (approx. 3–5 × 10^4 cells) was washed with 3 mL of 2% FBS in PBS, eventually stained with surface markers, and fixed with 4% paraformaldehyde (Santa Cruz Biotechnology) at room temperature for 15 min. Cells were washed again with 3 mL of 2% FBS in PBS and permeabilized with 100 μL of 1X Click-iT saponin-based permeabilization at room temperature for 15 min. Then, cells were stained with phospho-p38 MAPK antibody (1:100 dilution) (pThr180/pTyr182; Cell Signaling) at 4°C overnight. After washing with 2% FBS in PBS, samples were stained with anti-rabbit secondary antibodies (1:1000 dilution) (Alexa Fluor 488 or Alexa Fluor 647, Thermo Fisher Scientific) for 45 min at room temperature. After washing with 2% FBS in PBS, sample acquisition was performed on FACSCanto II and the collected data were analyzed using the FlowJo software.

MEM single-cell differentiation assay analysis

All single-cell-derived colonies were harvested into 96 U-bottom plates. Cells were then stained with 50 μL/well of antibody mix (CD45-PECy7, CD11b-PE, CD41-PECy5, GlyA-APC, CD14-APCCy7, CD56-BV421, CD15-BV510, 1:300, 1:500, 1:200, 1:1000, 1:500, 1:200, 1:1000, respectively), incubated for 20 min in the dark at room temperature and then washed with 100 μL/well of 1xDPBS +2% FBS. The type (lineage composition) and the size of the colonies formed were assessed by high-throughput flow cytometry. A single cell was defined as giving rise to a colony if the sum of cells detected in the $CD45^+$ gates was ≥30 cells. Erythroid (Ery) colonies were identified as $CD45^-GlyA^+ \geq 30$ cells, Megakaryocytes (Meg) colonies as $CD45^+CD41^+ \geq 30$ cells, Myeloid (My) colonies as [Monocytes (Mono: $CD45^+CD14^+$) + Granulocytes (Gran: $CD45^+CD15^+$)] ≥ 30 cells, and NK colonies as $CD45^+CD56^+ \geq 30$ cells.

Artificial thymic organoid (ATO) analysis

After five weeks from seeding, ATOs were collected by adding MACS Buffer (Miltenyi Biotech) to each well and pipetting to dissociate the ATOs. Cells were then filtered with a 70 μm filter, counted, and stained with 100ul/tube of of T cell progenitor antibody mix (CD56-PE, CD45-PerCP-Cy5, CD1a-APC, CD7-APCH7, CD5-PECy7, CD34-VB, LiveDead-PO; 1:100 dilution, respectively) and mature T cell antibody mix (CD8a-APC-Vio770, TCRab-PerCP-Cy5.5, CD56-PE, CD3-APC, CD4-PE-Vio770, CD45-VB, LiveDead-PO; 1:100 dilution, respectively). Cells were incubated for 15 min at room temperature and then washed with 1mL/tube of 2% FBS in PBS. Absolute number of $TCRa/b^+$ cells was calculated from cell counts and percentage of positive cells from FACS analyses. Frequency of GFP^+ cells was gated on $CD56^-CD45^+$ cells. Sample acquisition was performed on FACSCanto II and the collected data were analyzed using the FlowJo software.

CM-H_2DCFDA and CellROX

CM-H_2DCFDA (Thermo Fisher Scientific) was dissolved in DMSO. This molecule passively diffuses into cells, subsequent oxidation yields a fluorescent adduct that is trapped inside the cell. Cells were resuspended in pre-warmed 1x DPBS and a 10 μM probe was added. After 30 min in the incubator at 37°C, cells were centrifuged and resuspended in pre-warmed 1xDPBS +2% FBS. Fluorescence was quickly acquired at FACSCanto II using excitation sources and filters appropriate for fluorescein (FITC) and the collected data were analyzed using the FlowJo software. Because the dye is susceptible to photo-oxidation, all the steps were performed in the dark.

When CM-H_2DCFDA was not compatible with the experimental conditions, ROS levels were analyzed using the CellROX Reagents (Thermo Fisher) according to the manufacturer's instructions. In detail, cells were incubated with 500nM CellROX Reagent for 60 min at 37°C protected from light.

MitoSOX red mitochondrial superoxide indicator

MitoSOX Red reagent (Thermo Fisher Scientific) permeates live cells and selectively targets mitochondria. It is rapidly oxidized by superoxide but not by other ROS and reactive nitrogen species (RNS). The oxidized product becomes highly fluorescent (Ex/Em 510/580) upon binding to nucleic acid. MitoSOX Red reagent was dissolved in DMSO and 5μM were directly added to the cell culture. Cells were incubated for 10 min at 37°C protected from light. After washing in 1xDPBS +2% FBS, fluorescence was quickly acquired at FACSCanto II and the collected data were analyzed using the FlowJo software.

8-Oxo-2′-deoxyguanosine staining

Cellular suspension (approx. 1.5×10^5 cells) was washed with 3 mL of 2% FBS in PBS and fixed with 4% paraformaldehyde (Santa Cruz Biotechnology) at room temperature for 15 min. Cells were washed again with 3 mL of 2% FBS in PBS and denatured with 100 μL of HCl (2N) at room temperature for 20 min. After washing with 2% FBS in PBS, cells were permeabilized with 800 μL of 1X Intracellular Staining Permeabilization Wash Buffer (BioLegend) at room temperature for 20 min. Then, cells were washed with 2% FBS in PBS and stained with 8-oxo-2′-deoxyguanosine Antibody (1:250 dilution) (Trevigen) at 4°C overnight. After washing

with 2% FBS in PBS, samples were stained with anti-mouse secondary antibody Alexa Fluor 488 (1:1000 dilution) (Thermo Fisher Scientific) for 45 min at room temperature. Cells were washed with 2% FBS in PBS and sample acquisition was performed on FACSCanto II and the collected data were analyzed using the FlowJo software.

Immunofluorescence analysis

Multitest slides (10 well, MP Biomedicals) were treated for 20 min with Poly-L-lysine solution (Sigma-Aldrich) at 1 mg/mL concentration. After two washes with DPBS solution, approximately 0.3/0.5 × 10^5 cells were seeded on covers for 20 min and fixed with 4% paraformaldehyde (Santa Cruz Biotechnology) for another 20 min. Cells were then permeabilized with 0.3% Triton X-100. After blocking with 0.5% BSA and 0.2% fish gelatin in DPBS, cells were probed with the indicated primary antibodies. After primary antibodies incubation (53BP1 Antibody, Bethyl Laboratories, 1:600 dilution; Anti-phospho Histone H2A.X (Ser139) Antibody, clone JBW301, Merk, 1:200 dilution; and phospho-RPA32 (S33) Antibody, Bethyl Laboratories, 1:200 dilution), cells were washed three times with DPBS and incubated with Alexa 488-, 568- and/or 647-labeled secondary antibodies (1:1000 dilution) (Thermo Fisher Scientific). Nuclear DNA was stained with DAPI (Sigma-Aldrich) and covers were mounted with Aqua-Poly/Mount solution (Polysciences. Inc.) on glass slides (Bio-Optica). Fluorescent images were acquired using Leica SP5 Confocal microscope and analyses of 53BP1 foci distribution, and γH2A.X and pRPA positive cells. Micronuclei quantifications were performed with ImageJ software on DAPI images.

Comet assay

HSPCs were suspended at 1 × 10^5 cells/mL in ice-cold 1xDPBS and mixed with molten Comet LMAgarose (Trevigen, MD) at a ratio of 1:10 (v/v) and immediately pipetted onto CometSlides (Trevigen, MD) and placed for 30 min at +4°C. Once solidified, the slides were immersed in pre-chilled Lysis Solution (Trevigen, MD) for 1 h at +4°C. Following lysis, slides were immersed in freshly prepared Alkaline Unwinding Solution pH > 13 (300 mM NaOH, 1mM EDTA) for 1 h at +4°C and then electrophoresed in Alkaline Electrophoresis Solution pH > 13 (300 mM NaOH, 1mM EDTA) at 300 mA for 40 min. Slides were washed twice in ddH2O and fixed in 70% ethanol for 5 min. Comets were stained with SYBR Safe (Invitrogen) at room temperature for 30 min. All steps were conducted in the dark to prevent additional DNA damage. Comets were analyzed using a Nikon Eclipse E600 microscope and a Nikon-DS-RI2 camera. At least 100 nuclei for each donor were analyzed with CaspLab software to determine the "Olive Tail Moments" of individual nuclei.

Seahorse metabolic flux analysis

Metabolic flux analyses were performed using the Seahorse XFe96 Analyzer according to the manufacturer's instructions. Briefly, an XF sensor cartridge was hydrated overnight in Seahorse XF Calibrant at 37°C in a non-CO_2 incubator. Then, a cell culture microplate was coated for 30 min with Cell-Tak diluted in sodium carbonate 0.1 M pH8 and washed twice with dH_2O. CB-derived HSPCs (about 10^5 cells) were resuspended in freshly made Seahorse XF RPMI medium (pH 7.4; supplemented according to the desired stress test to perform), seeded in a 96-well Seahorse cell culture microplate, centrifuged for 15 min at 1500 rpm, and incubated in the 37°C incubator in absence of CO_2 for 1 h. Six technical replicates were performed for each sample, and the mean value was selected for further analysis.

Oxygen Consumption Rate (OCR) was measured using the Seahorse XF Mito Stress Test Kit. Cells were sequentially treated with 1 μM oligomycin (port A), 4 μM carbonyl cyanide-4 (trifluoromethoxy) phenylhydrazone (FCCP) (port B) and 0.5 μM antimycin A/rotenone (port C). Measurements were conducted using the following settings: 5 min mix time and 9 min read time.

Extracellular Acidification Rate (ECAR) was measured using the Seahorse XF Glycolysis Stress Test Kit. Cells were sequentially treated with 10 mM Glucose (port A), 1 μM oligomycin (port B), and 50 mM 2-deoxy-glucose. Measurements were conducted using the following settings: 5 min mix time and 9 min read time.

Analyses were performed with the Agilent Seahorse Wave software (Agilent Technologies). OCR and ECAR values were normalized on the total number of cells per well; cell numbers were calculated using CyQuant Cell Proliferation Assay (Thermo Fisher Scientific).

Western blot

To prepare protein extracts for immunoblot analysis, cells were washed twice with cold PBS and lysed for 30 min on ice with RIPA buffer containing 50 mM Tris–HCl pH 8.0, 150 mM NaCl, 1% (v/v) NP-40, 0.5% (w/v) Sodium Deoxycholate, 1 mM EDTA, 0.1% (w/v) SDS, 0.01% (w/v) Sodium azide pH 7.4, and Pierce protease and phosphatase minitablets inhibitors (Thermo Fisher Scientific, A32961). Cells were centrifuged at 13,000 rpm at 4 °C for 10 min and the supernatants were quantified for protein content with Pierce's BCA protein assay kit (Thermo Fisher Scientific, 23227), according to manufacturer's instructions. Then, the extracted proteins were resolved by SDS–PAGE before transfer onto nitrocellulose membrane (Sigma-Aldrich, GEH10600003), followed by overnight incubation at 4°C with phospho-ATR (Ser428) (Cell Signaling, 2853, 1:250 dilution), phospho-CHK1 (Ser 345) (Cell Signaling, 2341, 1:500 dilution), phospho-CHK2 (Thr68) (Cell Signaling, 2661, 1:1000 dilution), phospho-MAPKAPK-2 (Thr334) (Cell Signaling, 3007, 1:500 dilution), MAPKAPK-2 (Cell Signaling, 3042, 1:1000 dilution) and Histone 3 (Abcam, AB1791, 1:1000 dilution) primary antibodies. Finally, membranes were incubated 1h at room temperature with an anti-rabbit or anti-mouse HRP-linked secondary antibodies (Thermo Fisher Scientific, 1:3000 and 1:2000 dilution, respectively) and signals were detected using ECL Western blotting substrate (Thermo Fisher Scientific, 32209) following the recommendations of the manufacturer's instructions. The images were acquired on a ChemiDoc imager (BioRad).

EdU incorporation and detection for flow cytometry

EdU (5-ethynyl-2′-deoxyuridine), supplied with Click-iT EdU Alexa Fluor 647 Imaging Kit (Thermo-Fisher Scientific), was diluted in DMSO to a final concentration of 10 mM and kept at −20°C. Cells were treated with 2μM EdU for 4 h in culture. Approximately 3–5 × 10^4 cells were washed with 3 mL of 1% BSA in PBS and fixed with 100 μL of Click-iT fixative for 15 min. Cells were washed again with 3 mL of 1% BSA in PBS and permeabilized with 100 μL of 1X Click-iT saponin-based permeabilization for 15 min. Detection of EdU-DNA was performed by incubating cells with 500 μL of Click-iT Plus reaction cocktail for 30 min at room temperature protected from light. Cells were subsequently washed with 3 mL of 1% BSA in PBS before staining DNA with 2μM Hoechst 33342 for o.n. at 4°C protected from light. After the incubation, sample acquisition was performed on FACSymphony A5 SORP (BD Biosciences), and the collected data were analyzed using the FlowJo software.

Live imaging analysis of confluency

IncuCyte (Essen Biosciences) was used to quantify confluency in live cells for 4 days 30.000 cells of each condition were plated in a 96-multiwell placed in an incubator to maintain the standard cell culture conditions (5% CO_2 humidified atmosphere at 37°C) and images were acquired each 15'. The confluence processing analysis tool (IncuCyte Software S3 v2018A) calculated confluency for each sample. Quantification of the cellular confluence of each condition was assessed by calculating fold change to the first time point.

Cell trace violet

Just after thawing, HSPCs were stained with Cell Trace Violet (Thermo Scientific, C34557) following the manufacturer's instructions. Cells were resuspended in 1xDPBS at a concentration of 10^6/mL and 1μL of Cell Trace solution was added per each mL of cell suspension for a final concentration of 5μM. Cells were incubated for 20 min at 37°C, protected from light, and then for 5 min with five times the original staining volume of 1xDPBS+2% FBS. After centrifugation, cells were resuspended in the appropriate culture medium volume and incubated for at least 30 min before the analysis. Samples acquisition was performed on FACSCanto II and the collected data were analyzed with the FlowJo software using the Proliferation Kinetics tool.

Cell cycle analyses with the Fucci2a system

Lentiviral Fucci2A expressing vector was generated as previously described.[62] The day after thawing, HSPCs were treated with DMSO, 2mM NAC, or 4μM p38 inhibitor and 12h later transduced at a multiplicity of infection (MOI) of 50 for 16h. On day 2, cells were treated with the second dose of NAC, p38 inhibitor, or DMSO, and the day after were counted and seeded at a density of 20.000 cells in a 96-well plate. Transduced cells were monitored with IncuCyte (Essen Biosciences) for 4 days and time-lapse imaging was acquired taking phase contrast, red and green fluorescent signal recording images each 30 min. Cell cycle kinetics of transduced HSPCs were analyzed by tracking single cells throughout animation and single measurements were made using analysis tools Pixel Inspection of ImageJ. The average red and green fluorescence intensity was recorded from every cell. Specifically, we took at least 5 completed cell cycle phases for the comparison between treatments. Cell cycle kinetics were determined by plotting the duration of red, green, or yellow fluorescence intensity over time using Prism software v5 (GraphPad Software Inc.).

BAR- and indels-based clonal tracking libraries

Library preparation was performed as previously described.[11] Briefly, for BAR-Seq library preparation: we analyzed only mice transplanted with HS + AAV6-edited HSPCs with detectable engraftment (>0.1%) of GFP^+ cells in the BM at 15 weeks. PCR amplicons for individual samples were generated by nested PCR using primers listed in Ferrari et al., 2020 and starting from >50 to 100 ng of purified gDNA. The first PCR step was performed with GoTaq G2 DNA Polymerase (Promega) according to the manufacturer's instructions using the following amplification protocol: 95°C for 5 min, (95°C for 0.5 min, 60°C for 0.5 min, 72°C for 0.5 min) × 20 cycles, 72°C for 5 min. Forward primer was designed to bind the donor template upstream of the BAR sequence, while the reverse primer annealed outside the homology arm, thus amplifying 328 bp of the on-target integrated cassette. For targeted deep sequencing of the plasmid and AAV libraries, the reverse primer was annealed to the homology arm. The second PCR step was performed with GoTaq G2 DNA Polymerase (Promega) according to the manufacturer's instructions using 5 μL of the first-step PCR product and the following amplification protocol: 95°C for 5 min, (95°C for 0.5 min, 60°C for 0.5 min, 72°C for 0.5 min) × 20 cycles, 72°C for 5 min. Second-step PCR primers were endowed with tails containing P5/P7 sequences, i5/i7 Illumina tags to allow multiplexed sequencing, and R1/R2 primer binding sites. PCR amplicons were separately purified using the MinElute PCR Purification kit (QIAGEN) and AmpPure XP beads (Beckman Coulter). Library quality was assessed by Agilent Tapestation (Agilent Technologies). Amplicons were multiplexed and run on MiSeq 2 × 75 bp or 2 × 150 bp paired-end (Illumina). Indels-based clonal tracking library preparation: PCR amplicons for individual samples were generated by nested PCR using primers listed in *Ferrari* et al*., 2020* and starting from >50 to 100 ng of purified gDNA. The first PCR stepwas performed with GoTaq G2 DNA Polymerase (Promega) according to the manufacturer's instructions using the following amplification protocol: 95°C for 5 min, (95°C for 0.5 min, 60°C for 0.5 min, 72°C for 0.25 min) × 20 cycles, 72°C for 5 min. The second PCR step was performed with GoTaq G2 DNA Polymerase (Promega) according to the manufacturer's instructions using 5 μL of the first-step PCR product and the following amplification protocol: 95°C for 5min; 95°C × 0.5 min, 60°C × 0.5 min, 72°C × 0.3 min, (20cycles); 72°Cx 5 min. Second-step PCR primers were endowed with tails containing P5/P7 sequences, i5/i7 Illumina tags to allow multiplexed sequencing, and R1/R2 primer binding sites. PCR amplicons were separately purified

performing double-side selection with AmpPure XP beads (Beckman Coulter). Library quality was assessed by LabChip GX Touch HT (PerkinElmer). Amplicons were multiplexed and sequenced by GeneWiz on MiSeq 2 × 300 bp paired-end sequencing (Illumina).

BAR-seq analysis

Barcoded samples were analyzed with the BAR-Seq2 pipeline (https://bitbucket.org/bereste/bar-seq2). In detail, input reads were pre-processed to get rid of low-quality bases and keep sequences having lengths ≥120bp (options: -m 120 -q 30) to ensure having the entire amplicon within each read. Barcodes (BARs) were then extracted using TagDust (by providing the amplicon structure) and corrected using a community-based strategy on a graph built on sequence similarity (edit distance ≤2). Resulting BARs were quantified based on their abundance (number of supporting reads) and filtered, keeping only those having a count greater than 2. Samples having a low number of extracted barcodes (<15000) were discarded from the analysis.

Indels-based clonal tracking analysis

Samples for indels-based clonal tracking were analyzed with CRISPResso2 (v2.2.8),[63] a suite of software developed to detect and quantify insertions, mutations, and deletions in reads from gene editing experiments. In details, input sequences were trimmed (CRISPResso2 options: –trim_sequences –trimmomatic_command trimmomatic –trimmomatic_options_string 'ILLUMINACLIP:TruSeq3-PE-2.fa:2:30:10 MINLEN:100′) to get rid of low-quality positions (score <30) and to remove Illumina adapters, keeping only trimmed reads having length greater than 100bp to ensure the full coverage of the region of interest. Then, the resulting sequences were mapped to the reference amplicon and a quantification window around the cut site (identified through the provided gRNA) was set to identify all the occurred events. The computed alleles were quantified by measuring the number of reads and their relative abundance based on total read counts. Finally, CRISPResso2 output alleles were post-processed by correcting all the mismatch positions outside the quantification window and re-quantifying the total read counts and consequently, the corresponding relative abundances, filtering out those having a relative abundance lower than the false positive threshold (set at 0.2%, based on untreated controls).

Single-cell RNA-sequencing and analysis

Droplet-based digital 3′-end scRNA-Seq was performed on a Chromium Single-Cell Controller (10X Genomics) using the Chromium Next GEM Single Cell 3′ Reagent Kit v3.1 according to the manufacturer's instructions. 24h after the editing treatment, viable $CD34^+$ cells (negative to ZombieAqua viable dye) were sorted according to surface expression of $CD34^+CD133^+CD45RA^-CD90^+GFP^+$ and $CD34^+CD133^+CD45RA^-CD90^+GFP^-$. Cell sorting was performed on a BD FACSAria Fusion (BD Biosciences) using BDFACS Diva software and equipped with four lasers: blue (488 nm), yellow/green (561 nm), red (640 nm), and violet (405 nm). Cells were sorted with a 100 mm nozzle. A highly pure sorting modality (two-way purity sorting) was chosen. Sorted cells were collected in 1.5 mL Eppendorf tubes containing 100 μL of 1xDPBS. The sorted populations were stained for 30′ at 4°C with Total Seq-B hashtag antibodies (Data S1F, H1 for $Zombie^-$ not edited DMSO and p38i, Hs Cas9 DMSO and p38i, and for $Zombie^-GFP^+$ HS + AAV6 DMSO and p38i; H2 for $Zombie^-$ not edited DMSO and p38i, Hs Cas9 DMSO and p38i, and for $Zombie^-GFP^-$ HS + AAV6 DMSO and p38i; H3 for $CD34^+CD133^+CD45RA^-CD90^+GFP^+$ HS + AAV6 DMSO and p38i; H4 for $CD34^+CD133^+CD45RA^-CD90^+GFP^-$ HS + AAV6 DMSO and H5 for $CD34^+CD133^+CD45RA^-CD90^+GFP^-$ HS + AAV6 p38i), and after pooling population from the same condition, viable cells were counted with Trypan Blue solution 0.4% (GIBCO) and 1,2–5 × 10^4 viable cells from each population were utilized for the subsequent procedure (estimated recovery: 3 × 10^4 cells/sample). Briefly, single cells were partitioned in Gel Beads in Emulsion (GEMs) and lysed, followed by RNA barcoding, reverse transcription, and PCR amplification (11 cycles). scRNA-Seq libraries were prepared according to the manufacturer's instructions, checked, and quantified on LabChip GX Touch HT (PerkinElmer) and Qubit 3.0 (Invitrogen) instruments. Sequencing was performed on a Nova Seq S2 (Illumina) using the NextSeq 500/550 High Output v2 kit (75 cycles).

Illumina sequencer's base call files (BCLs) were demultiplexed, for each flow cell directory, into FASTQ files using Cellranger mkfastq with default parameters (v. 6.1.1, https://github.com/10XGenomics/cellranger). FASTQ files of both genome expression (GEX) and hashtags (HTO) for each sample were then processed together using Cellranger count with default parameters, to obtain quantification of cells (in terms of UMI counts) on genes and hashtags. Internally, the software relies on STAR for aligning reads to the human reference genome (GRCh38) that was modified to include the insertion of the GFP gene in the AAVS1 locus. The output of CellRanger was analyzed in the R environment with the Seurat (v4.1.1) package, keeping cells having more than 200 and fewer than 6000 unique genes per cell, and genes expressed in more than 3 cells. Moreover, cells with more than 15% of features mapping to mitochondrial genes were excluded. HTO data of each sample were normalized with a centered log-ratio (CLR) transformation across features, and cell demultiplexing was performed for each sample with the HTODemux function from Seurat (positive.quantile = 0.9). Finally, only cells with a unique hashtag (singlet) identifying a sorted population were retained. Samples were merged together, obtaining a total of 102842 cells passing the quality check, with an average of ∼3826 genes per cell and ∼14973 UMIs/reads per cell. Counts were then normalized using the NormalizeData function with default parameters. Cell cycle scores were calculated using the CellCycleScoring function, providing as input a previously reported gene list.[64] Expression data were then scaled using the ScaleData function, also regressing on the cell cycle phases (S, G2M scores as calculated with the CellCycleScoring function), on the percentage of mitochondrial genes, and the total number of reads per cell.

After that, Principal Component Analysis (PCA) was performed using the RunPCA function, providing as input a list of the top 20% most variable genes (*vst* method in FindVariableFeatures function). To correct for the gender bias, that was extreme in the HSC compartment, a variable based on the XIST expression (XIST>0 for female, otherwise male) was created, and a batch correction based on this latter classification, as well as on the sample origin was performed with Harmony.[65] Cell clusters were defined by evaluating the first 50 principal components at a resolution of 2 and using the FindClusters function with standard parameters. Cells were visualized in 2 dimensions using UMAP (Uniform Manifold Approximation and Projection).[66] Genes enriched in cells within each cluster were identified by means of the Wilcoxon rank-sum test (FindAllMarkers function), selecting genes expressed in at least 20% of one of the two populations (min.pct = 0.2). For the cluster annotation, similarly to what has been published,[67] marker genes identified for each cluster were used to perform a pre-ranked GSEA[68] on signature lists from literature.[35–42,69] We annotated 15 cell clusters, including HSC/multi-potent progenitor (MPP), MPP, lympho-multi potent progenitors (LMPP), lymphoid progenitors (LyP), a small subset of pro-B progenitor cells, more committed progenitors as granulocyte-monocyte progenitors (GMP), monocyte-dendritic progenitors (MDP), megakaryocytes-erythroid progenitors (MEP), megakaryocyte erythroid mast cell and basophil progenitors (MEMBP), eosinophil baso-mast progenitors (EBMPs), megakaryocyte erythroid baso-mast progenitors (MEP_Baso_Mast) and Erythroid progenitor (EryP) (Data S1G). Once cluster annotation was defined, genes differentially expressed between different conditions/clusters were identified using the FindMarkers function, applying the Wilcoxon test and the default correction method (Bonferroni). For the functional annotation, differentially expressed genes were pre-ranked according to Log2FC values and GSEA was performed on MSigDB (http://www.gsea-msigdb.org/gsea/msigdb/collections.jsp), Gene Ontology biological processes (GO:BP), the Pathway Interaction Database, and literature available human and murine datasets. Specifically, the human signatures derived from García-Prat et al. 2021 and Cabezas-Wallscheid et al. 2014-17[29,45] identify HSC and dormant HSC (dHSC) signatures. Jacobs et al.[34] identify DNA replication stress signatures in HSCs. Lauridsen et al. 2018[46] dHSC signature is derived from the comparison of an HSC population with low expression of Retinoic Acid-CFP reported, which is a non-proliferative population displaying superior engraftment potential, vs. Retinoic Acid-CFP bright HSCs. Giladi et al. 2018[48] StemScore derived from a population of HSCs with high Hlf expression. Wilson et al. 2016[70] signatures derived from single-cell data of sorted LT-HSCs, expressing a gene program relative to a low cell cycle. Rodriguez-Fraticelli et al. 2020[47] identifies 4 different clusters of HSCs, 1–2 retaining a more stem signature, while clusters 3–4 are characterized by a more active cellular state and Mk priming respectively. Furthermore, Rodriguez-Fraticelli et al. 2020[47] characterizes HSC heterogeneity by low/high and lineage bias output of HSC clones detected by means of a barcoding strategy.

The AddModuleScore function was adopted to compute the average expression level of cell programs. Wilcoxon rank sum was adopted to test pairwise the differences across conditions, correcting the *p*-value with the Benjamini-Hochberg correction method.

QUANTIFICATION AND STATISTICAL ANALYSIS

Measurements were taken from distinct samples and sample size (n) is reported in the figure legends. Inferential techniques were carried out whenever an appropriate sample size was available; otherwise, descriptive statistics were reported. Mann-Whitney test was performed to compare two independent groups. In the presence of more than two independent groups, the Kruskal-Wallis test was performed, followed by post hoc pairwise comparisons. For paired observations, the Wilcoxon matched-pairs signed rank test was performed. For WB analysis, one-sample T-test was performed on normalized data. All tests were performed with two-tail statistics. Data were analyzed using Prism software v8 (GraphPad Software Inc.). Values are expressed as means ± SD or SEM as indicated. p values < 0.05 were considered significant (*, $p < 0.05$; **, $p < 0.01$; ***, $p < 0.001$; ****, $p < 0.0001$).

Manuscript 3:

Metabolic Control of Chromatin Accessibility Reverses Age Related Dysfunction in Human Hematopoietic Stem and Progenitor Cells

G. Farina[1,2], T. Tavella[2], E. Carsana[2], K. Giannetti[2], A. Santoro[2], F. Midena[2], R. Vacca[2], L. Cassina[3], A. Boletta[3], S. Cardaci[4], R. Di Micco[2]

[1]Università degli Studi di Milano Bicocca, School of Medicine and Surgery Milano, Italy.

[2]San Raffaele Telethon Institute for Gene Therapy, Via Olgettina, 60, 20132 Milano MI, Italy, Milan, Italy.

[3] Cystic Kidney Disorders, IRCCS San Raffaele Scientific Institute, Milan, Italy.

[4] Cancer Metabolism Unit, Division of Genetics and Cell Biology, IRCCS San Raffaele Scientific Institute, Milano, Italy

Abstract

Aging degrades human hematopoietic stem and progenitor cell (HSPC) function through coordinated epigenetic, transcriptional, and metabolic shifts. We hypothesized that a succinate/α-ketoglutarate (αKG) axis couples metabolism to chromatin state and energetics to drive age-associated dysfunction. We profiled young (18–25 y) and aged (>70 y) $CD34^+$ HSPCs by flow cytometry, CFU and MEM single-cell assays, RNA-seq, ATAC-seq, and untargeted LC-MS metabolomics, and applied short ex vivo exposures (72 h) to succinate or αKG before functional testing; energetic reliance was measured with SCENITH, HIF2α with immunoblotting, and in vivo activity by NSG xenotransplantation; HIF2α dependence was probed using PT2399. Aging increased primitive subsets yet reduced clonogenic efficiency and bi-lineage potential, with higher DNA damage. Transcriptome and chromatin profiling showed activation/accessibility of p53, inflammatory, Myc, glycolysis, hypoxia, and OXPHOS programs with globally increased accessibility, including TSS-proximal regions. Metabolomics revealed broad metabolite accumulation with age but relatively higher succinate in young HSPCs, nominating a succinate/αKG control point. Functionally, succinate (4 mM) increased H3K27me3, decreased H3K27ac, reduced chromatin accessibility, and improved CFU output and single-cell clonogenicity/bi-lineage potential; αKG produced opposite effects in young cells and little benefit in aged cells. In vivo, succinate-treated aged HSPCs restored peripheral-blood engraftment toward young controls without altering lineage composition at 12 weeks; αKG reduced engraftment of young cells. Energetically, succinate increased glycolytic reliance and HIF2α abundance; PT2399 partially blunted succinate's benefits, indicating mixed HIF2α-dependent and -independent mechanisms consistent with direct chromatin effects. These data position metabolite tuning along the succinate/αKG axis as a tractable strategy to realign chromatin and energetics, reduce DNA damage, and enhance early repopulating activity of aged human HSPCs.

Introduction

Adult hematopoietic stem and progenitor cells (HSPCs) maintain lifelong blood production. However, their function declines with age due to cell-intrinsic and niche-mediated mechanisms that, together, decrease regenerative capacity and alter lineage output.[32] Phenotypic HSC pools often expand in older marrow. Still, single-cell and functional assays show that a larger portion of these cells are biased or impaired, and multilineage stem cells become relatively less common.[32,36,37] Transplant studies further demonstrate that aged cells display impaired homing/engraftment and a progressive loss of self-renewal even in youthful environments, indicating an accumulated, cell-autonomous.[33,34] Clinically, these changes lead to delayed immune recovery, increased infections, and the emergence of clonal hematopoiesis in older adults.[38,39]

At the molecular level, aging in HSPCs is characterized by consistent transcriptional reprogramming: inflammatory and stress-response modules (such as interferon and NF-κB-linked networks) become more prominent, while lymphoid-priming and quiescence programs decrease.[32,40,41] Single-cell profiling reveals increased heterogeneity, with some subsets entering hyper-reactive states while others retain youthful features, and a weakened connection between cell-cycle control and long-term stemness.[42,43] Simultaneously, the regulatory framework is remodeled: enhancer and accessibility landscapes shift toward modules that favor myeloid output, and chronic niche inflammation stabilizes these states, reducing.[44,45,46] Aging also induces widespread, locus-specific changes in DNA methylation and chromatin marks linked to altered fate decisions, and, since these marks are potentially reversible, they remain promising targets for functional restoration.[44,47,48,49]

Metabolic organization is a key feature of stemness. Quiescent HSCs prefer glycolysis, maintain low mitochondrial membrane potential, and tightly control reactive oxygen species, a state actively maintained by pathways that limit pyruvate oxidation and support organelle quality control.[55,57,58,59] With age, baseline respiration and oxidative stress tend to increase, activation thresholds shift, and lineage output leans toward myeloid fates, reflecting a loss of metabolic flexibility and the ability to switch smoothly between quiescent and activated states.[55,57,61] Nutrient-sensing (PI3K–mTOR) and hypoxia-inducible pathways link these metabolic states to fate decisions: sustained mTOR activity reduces stemness. At the same time, hypoxia-driven programs push cells toward glycolysis and away from damaging mitochondrial stress.[62,63,64] Sirtuins and mitochondrial stress checkpoints further connect redox balance and proteostasis to chromatin regulation.65,66

Together, these observations suggest that metabolism and chromatin regulation are interconnected control layers in aging HSPCs. Many chromatin-modifying enzymes rely on cofactors and are sensitive to redox changes, creating pathways through which metabolic states and microenvironmental oxygen or inflammatory signals can leave lasting effects on regulatory programs.[46,49,50] Notably, age-related accessibility and enhancer remodeling are most prominent within stem-enriched compartments, positioning the metabolic–chromatin interface at the top of the hematopoietic hierarchy where small biochemical shifts can have significant impacts on stem cells.[44,45,48] These factors motivate a targeted investigation into whether brief, focused modulation of metabolite-sensitive chromatin pathways can shift aged human HSPC states toward better function, without forcing developmental fates or inducing proliferative stress.

RESULTS

Characterization of epigenetic, transcriptomic, and metabolomic profiles of young and aged human HSPCs

Human HSPCs (defined as CD34-positive cells) were isolated from the bone marrow of healthy young individuals (18-25 years old) and aged individuals (>70 years old). Since these cells are well known to lose functionality with aging in both mice and human[34,92,93], we initially assessed the cellular composition via flow cytometry and the functional differences via Colony Forming Unit (CFU) assay on bulk HSPCs after an overnight recovery in cytokine-enriched medium immediately after thawing (Fig. 1A). When analyzing early progenitors (CD34+CD133+90+), primitives (CD34+CD133+CD90-), and committed cells (CD34+CD133-CD90-), we observed a significant increase in aged HSPCs among early progenitors and a decrease in committed cells (Fig. 1B). Nonetheless, we noted compromised functionality, as evidenced by a reduction in the total number of colonies generated in a semisolid medium, especially erythroid colonies (Fig. 1C).

To further explore and gain insights into the most primitive subset of HSPCs, we expanded our functionality assessment with the Myeloid-Erythroid-Megakaryocyte (MEM) single-cell differentiation assay[94]. With MEM, we sorted single cells for the most primitive HSCs (CD45Ra-CD38-CD34+CD133+CD90+) in differentiation medium containing cytokines for erythroid, megakaryocytic, Natural Killer, and Myeloid lineages. After 21 days, we measured clonogenic efficiency, defined as the percentage of single cells that formed colonies, and potential, defined as lineage diversity at the single-cell level (whether they result in undifferentiated, uni-lineage, bi-lineage or multi-lineage outcomes) (Fig. 1D). As expected, we observed a decline in clonogenic efficiency with aging (Fig. 1E) and a decrease in bi-lineage potential (Fig. 1F). This supports the idea that the loss of functionality in aged HSPCs also impacts the most primitive human compartment, as previously reported in mice[32], and indicates that HSC functionality declines even if their percentage increases with age.

Since decreased functionality in the most primitive HSPC compartment of mice has been linked to DNA damage accumulation[79], we decided to measure DNA damage in our samples. Using the Alkaline Comet assay on bulk HSPCs, we observed increased DNA damage with age (Fig. 1G), consistent with previous studies in mice[95].

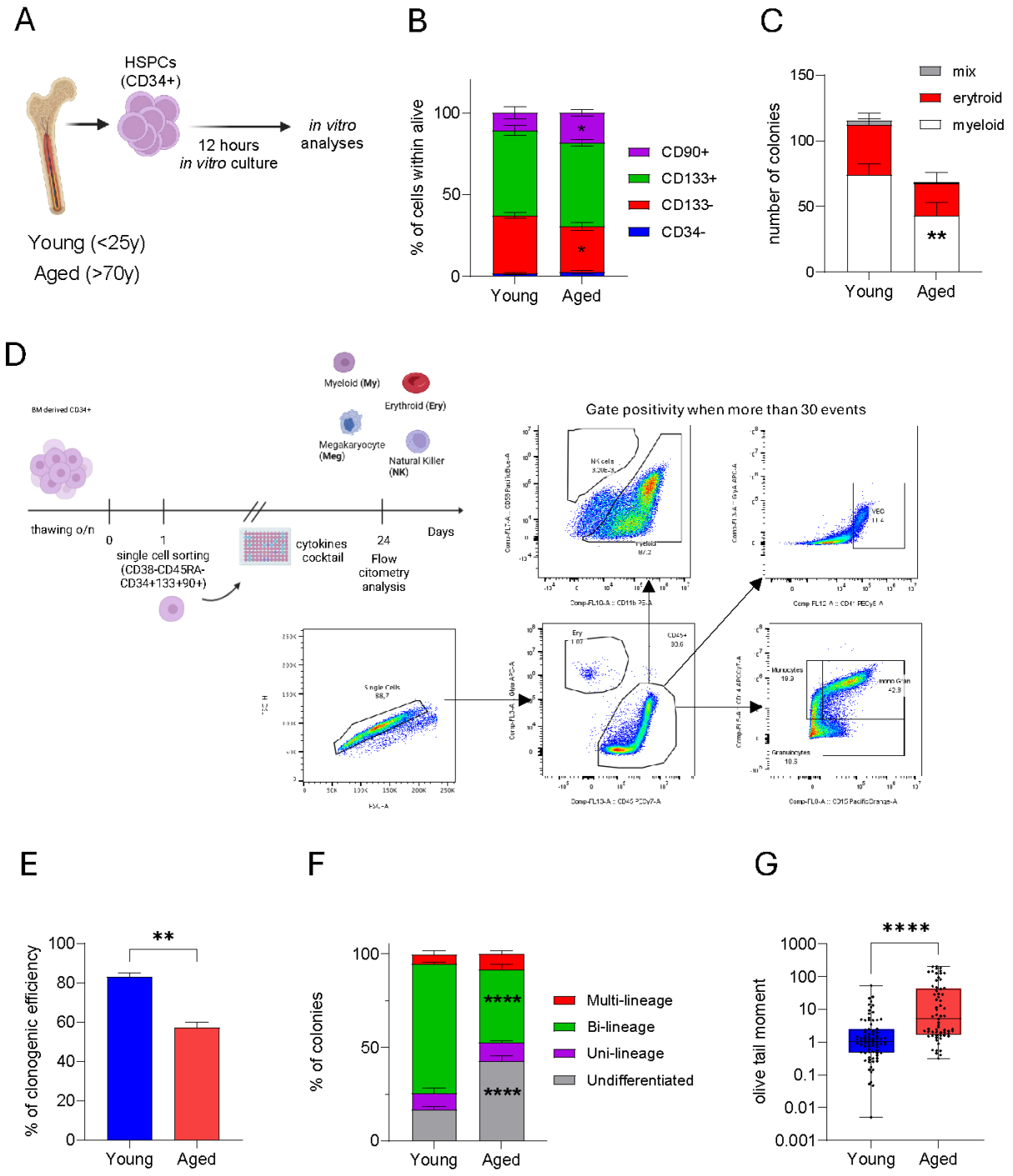

Figure 1: Functional decline of human HSPCs and HSCs associated with increased DNA damage burden
(A) Experimental workflow for studying functionality, transcriptomic, chromatin accessibility, and metabolomic features in BM-derived CD34+ cells from young donors (less than 25 years old) and aged donors (more than 70 years old). (B) Percentage of HSPC subpopulations (CD34-, $CD34^+CD133^-$, $CD34^+CD133^+$, and $CD34^+CD133^+CD90^+$ cells) (n = 6). Uncorrected Fisher's LSD test. (C) Number of colonies generated by BM-derived HSPCs plated in methylcellulose (n = 4). Uncorrected Fisher's LSD test. (D) Experimental workflow of the single-cell differentiation assay. BM-derived HSPCs were FACS-sorted for CD45RA-CD38-CD34+CD133+CD90+ and seeded as single cells in a cytokine-enriched medium. Colonies were harvested and analyzed after 24 days of culture, using the gating strategy described. (E) Clonogenic efficiency of single HSC/MPP pool from 3 independent BM. Welch's t-test. (F) Percentage of not differentiated uni-lineage, bi-lineage and multi-lineage colonies. Uncorrected Fisher's LSD test. (G) Quantification of SSBs and DSBs by comet assay BM-derived HSPCs; each point represents a single cell. Mann-Whitney test.

To understand the molecular basis of the observed phenotypes, we aimed to characterize the epigenetic, transcriptomic, and metabolomic profiles of HSPCs. For this, we created six

pools of aged HSPCs and three pools of young HSPCs, ensuring a balance of age and gender. This approach was necessary to obtain sufficient material for our analysis, as it was technically impossible to run all the desired tests on the most primitive cells.

When analyzing RNA-seq data using hallmark analysis, we highlighted the enrichment of signaling pathways related to DNA damage response (p53), inflammation (TNFα, IL-6, IL-2, and interferon gamma), proliferation (Myc targets), and metabolism (glycolysis, hypoxia and oxidative phosphorylation) (Fig. 2A). Notably, this data aligns with the increased proliferation and inflammation observed in HSPCs of aged mice and humans [43,93,96].

Regarding epigenetics, aged HSPCs exhibit an overall increase in chromatin-accessible regions (DARs) (Fig. 2B), including areas near transcription start sites (TSS) (Fig. 2C). Analyzing the pathways associated with the TSS, we observed an increase in accessibility related to pathways involved in DNA damage response (p53), inflammation (interferon gamma, IL-2), proliferation (Myc targets), and metabolism (glycolysis and oxidative phosphorylation) (Fig. 2D), which aligns with our transcriptomics data (Fig. 2A).

We then examined whether the differences in chromatin accessibility were regulated at the transcriptional level by analyzing our RNA-seq data for pathways involved in chromatin structure, including histone acetyltransferases, histone deacetylases, histone and DNA demethylases, and histone and DNA methylases. We observed no statistically significant differences in pathway activation between young and aged HSPCs that could explain the variation in chromatin accessibility. We then analyzed our dataset for transcripts of epigenetic modifiers and identified a few deregulated genes between young and aged samples (Fig. 2E). Specifically, with aging, we observed decreased expression of SMYD3 (a methyltransferase associated with activation-related chromatin and enhanced proliferation[93]) and KAT6B (an H3K9 acetyltransferase that promotes euchromatin[97]), along with increased expression of PRDM5 (which recruits repressive complexes to form heterochromatin [98]). Nonetheless, these gene-expression differences alone cannot explain the increased chromatin accessibility observed in our aging dataset.

Finally, we conducted metabolomic analyses given the well-established links between metabolites, epigenetic regulation, and the function of mouse HSPCs[99], as well as the enrichment of glycolysis and oxidative phosphorylation observed in our RNA-seq and ATAC-seq analyses. Consistently, using untargeted Liquid Chromatography-Mass Spectrometry (LC-MS), we observed a statistically significant accumulation of several metabolites involved in glycolysis (G-3P, G-6P), the TCA cycle (citrate, malate, alpha-ketoglutarate), the methionine cycle (SAM, SAH), and nucleotide synthesis in aged HSPCs (Fig. 2F). Conversely, only one metabolite was significantly more abundant in young HSPCs: succinate (Fig. 2F). Interestingly, this metabolite was shown to influence the activity of enzymes that remove methyl groups from histones, which belong to the JmjC family of demethylases[80]. This family of proteins uses alpha-ketoglutarate (αKG) to strip methyl groups from histones, producing succinate as a byproduct[81]. The accumulation of succinate has been linked to reduced enzyme efficiency in histone modification[82]. Therefore, we hypothesize that a decline in succinate with aging could lead to increased chromatin compaction, as it is not only a byproduct of demethylation but also a regulator of demethylation[83]. It remains unclear why aged HSPCs lose succinate, which is primarily produced in the TCA cycle [100].

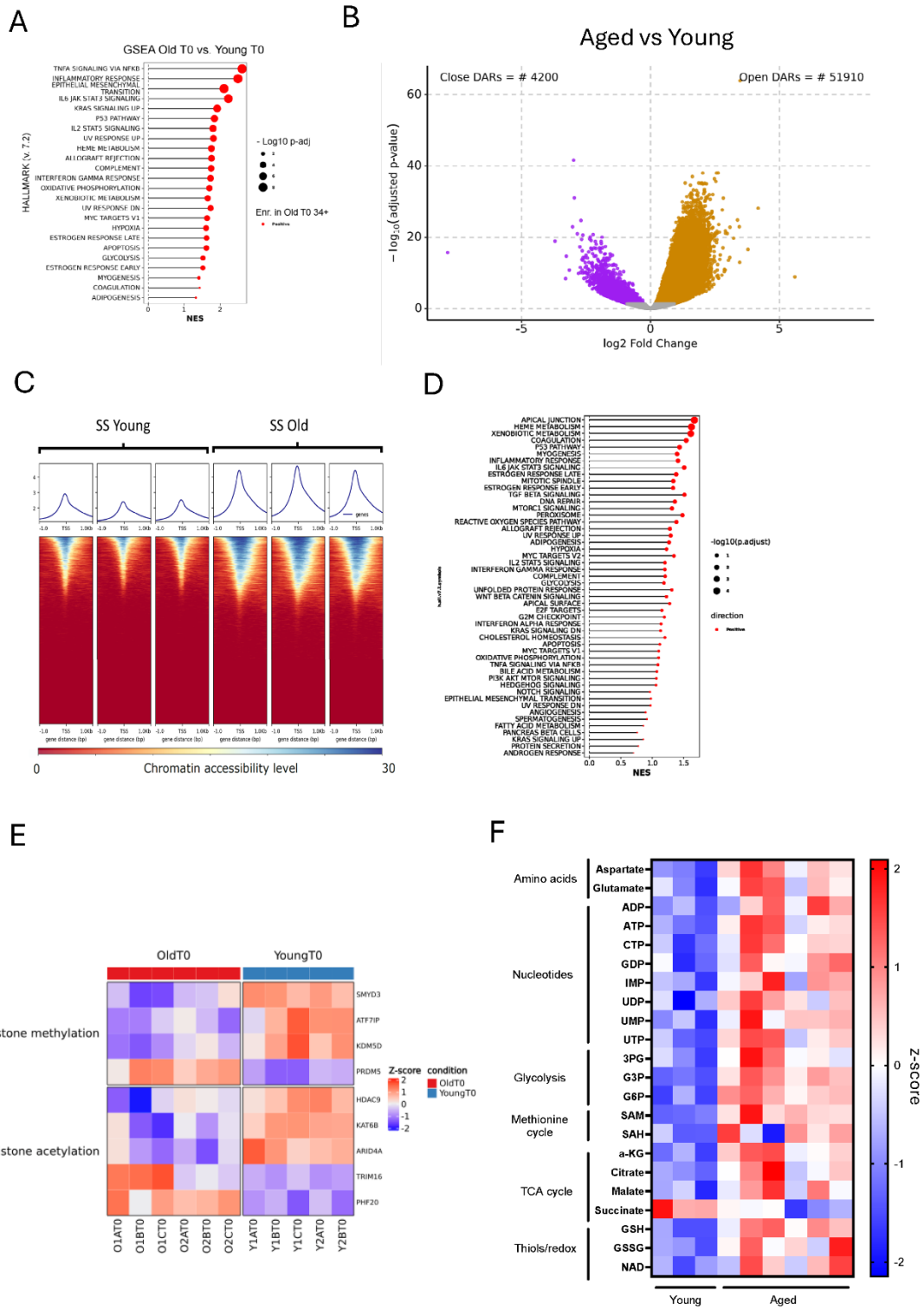

Figure 2: Increased chromatin accessibility in aged HSPCs and increased accumulation of succinate in young HSPCs (A)Enriched terms obtained by performing GSEA of intra-condition comparisons of RNAseq of aged vs young BM-derived CD34+ cells. Rows report terms enriched in at least one of the comparisons (columns) (false discovery rate < 0.1) from hallmark signatures (MSigDB). Colors indicate negative/positive normalized enrichment score (NES). (B) Volcano-plot of DARs identified by edgeR. X-axis indicates the log2 fold change of ATAC-seq signal difference between aged and young, Y-axis indicates the adjusted p-value. (C) Metaplot of ATAC-seq reads over the TSS of all protein-coding genes. (D) Enriched terms obtained by performing GSEA of intra-condition comparisons of ATAC-seq of aged vs young BM-derived CD34+. Rows report terms enriched in at least one of the comparisons (columns) (false discovery rate < 0.1) from hallmark signatures (MSigDB). Colors indicate negative/positive normalized enrichment score (NES). (E) HEATMAP showing the expression in Z-score of statistically differentially expressed genes from the RNAseq, involved in histone methylation and histone acetylation. Colors indicate negative/positive normalized enrichment score. (F) Metabolites detected via Untargeted intracellular metabolomic using liquid chromatography-mass spectrometry (LC-MS). Represented only metabolites whose abundance was statistically significant using the Mann-Whitney test. Colors indicate negative/positive normalized z-score.

Energetic Profiling Reveals OXPHOS Dependence and Succinate–αKG Tuning of Chromatin.

To test our hypothesis that the balance between succinate and αKG could be a key factor in regulating chromatin in HSPCs, we first performed a dose-response curve treating mPB CD34+ cells every 24 hours for 72 hours[101] with αKG or succinate at 1, 2, 4, or 8 mM (Fig. 3A). While 8 mM caused toxicity for succinate (Fig. 3B), a dose-dependent effect was observed for both metabolites on clonogenic output from 1 mM to 4 mM, with increasing colony-forming units for succinate and decreasing for αKG (Fig. 3C), along with no significant changes in viability (Fig. 3B) or cellular composition (Fig. 3D). We then continued our analyses on mPB HSPCs using the 4 mM dose for both metabolites, observing no changes in growth rate (Fig. 3E). WB analysis showed that the metabolic treatment affected histone modifications linked to chromatin changes, specifically H3K27me3 and H3K27ac: succinate administration increased H3K27me3 levels and decreased H3K27ac levels, while αKG had the opposite effect (Fig. 3F-G). This supports our hypothesis that CD34+ cells can use αKG and succinate to regulate their chromatin accessibility. Additionally, the effect of this treatment is consistent across different sources of CD34+, as we observed the same impact on clonogenic potential in both mPB and BM from middle age (Fig. 3H).

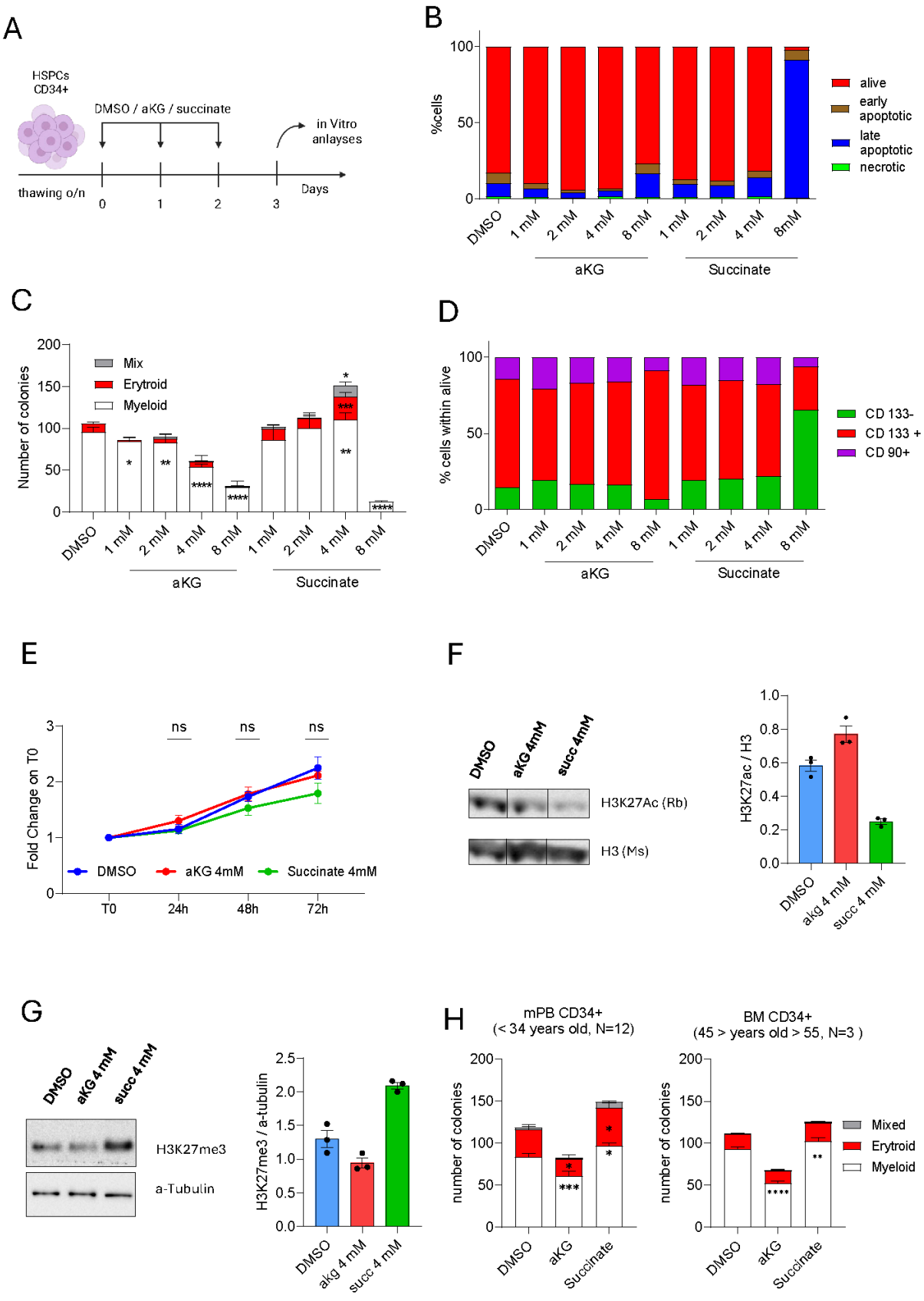
A
HSPCs CD34+
DMSO / aKG / succinate
in Vitro anlayses
thawing o/n
Days
0
1
2
3
B
%cells
alive
early apoptotic
late apoptotic
necrotic
DMSO
1 mM
2 mM
4 mM
8 mM
aKG
Succinate
C
Number of colonies
Mix
Erytroid
Myeloid
D
% cells within alive
CD 133-
CD 133 +
CD 90+
E
Fold Change on T0
ns
DMSO
aKG 4mM
Succinate 4mM
T0
24h
48h
72h
F
DMSO
aKG 4mM
succ 4mM
H3K27Ac (Rb)
H3 (Ms)
H3K27ac / H3
akg 4 mM
succ 4 mM
G
H3K27me3
a-Tubulin
H3K27me3 / a-tubulin
H
mPB CD34+
(< 34 years old, N=12)
BM CD34+
(45 > years old > 55, N=3)
number of colonies
Mixed
Erytroid
Myeloid

Figure 3: Effect of metabolite treatment upon cell culture in mPB
(A) Experimental workflow for studying the effect of the treatment of mPB CD34+ cells in cell culture with treatment every 24h with washout every day, cells were kept at 5*10^5/mL across all time points. (B) Apoptosis analysis performed within bulk mPB-derived CD34+ cells treated with DMSO, αKG, or succinate at the indicated concentration. Alive: 7AAD- /Annexin V-; Early apoptotic cells: 7AAD- /Annexin V+; late apoptotic cells: 7AAD+ /Annexin V+; necrotic cells: 7AAD+ /Annexin V-. (C) Number of colonies generated by mPB-derived CD34+ cells plated in methylcellulose (*n* = 3). Uncorrected Fisher's LSD test compared to DMSO. (D) Percentage of HSPC subpopulations ($CD34^+CD133^-$, $CD34^+CD133^+$, and $CD34^+CD133^+CD90^+$ cells) inside alive cells. (E) Proliferation rate of mPB CD34+ cultured for 72h (n=6). Dunnett's multiple comparisons test. (F) Western Blot analysis of H3K27Ac after the treatments for 72h of mPB CD34+ cells (n=3). H3 was used as a loading control, and the ratio between the target and the loading control is shown. Mann-Whitney test. (G) Western Blot analysis of H3K27Me3 after the treatments for 72h of mPB CD34+ cells (n=3). A-Tubulin was used as a loading control, and the ratio between the target and the loading control is shown. Mann-Whitney test. (H) Number of colonies generated by mPB-derived CD34+ cells (n=12) and BM-derived CD34+ from middle-aged (n=3), plated in methylcellulose. Uncorrected Fisher's LSD test compared to DMSO.

We then treated young and aged BM HSPCs with either DMSO, αKG, or Succinate, hypothesizing that αKG should “promote aging” in young HSPCs, while Succinate should “rejuvenate” aged HSPCs (Fig. 4A).

Using ATAC-seq, we observed that treating aged HSPCs with succinate decreased chromatin accessibility (Fig. 4B), while treating young HSPCs with αKG increased it (Fig. 4C), supporting our initial hypothesis that high levels of succinate in young HSPCs can induce heterochromatin and potentially explain the differences in chromatin accessibility between young and aged HSPCs.

At this stage, we wondered if metabolic treatments could influence the fitness of both aged and young HSPCs. First, we analyzed their clonogenic potential in bulk HSPCs, finding that succinate treatment increased clonogenic capacity in both age groups (Fig. 4D) without altering cellular composition (Fig. 4E). In contrast, αKG reduced the clonogenic potential in young HSPCs but had little to no effect on aged HSPCs (Fig. 4D). To explore the more primitive compartment further, we performed the MEM assay on sorted CD45RA-CD38-CD34+CD133+CD90+ cells that received metabolic treatments. Consistent with our bulk CFU differentiation assay (Fig. 4D), we observed that young DMSO still showed higher clonogenic efficiency (Fig. 4F) and bi-lineage colonies (Fig. 4G) than aged DMSO. Additionally, succinate treatment enhanced clonogenic efficiency in both young and aged cells (Fig. 4F) and increased bi-lineage colony numbers (Fig. 4G). Interestingly, young cells treated with αKG showed decreased clonogenic efficiency (Fig. 4F) and fewer bi-lineage colonies (Fig. 4G). Conversely, treatment with αKG in aged cells reduced both clonogenic efficiency and bi-lineage formation compared to aged DMSO (Fig. 4F-G).

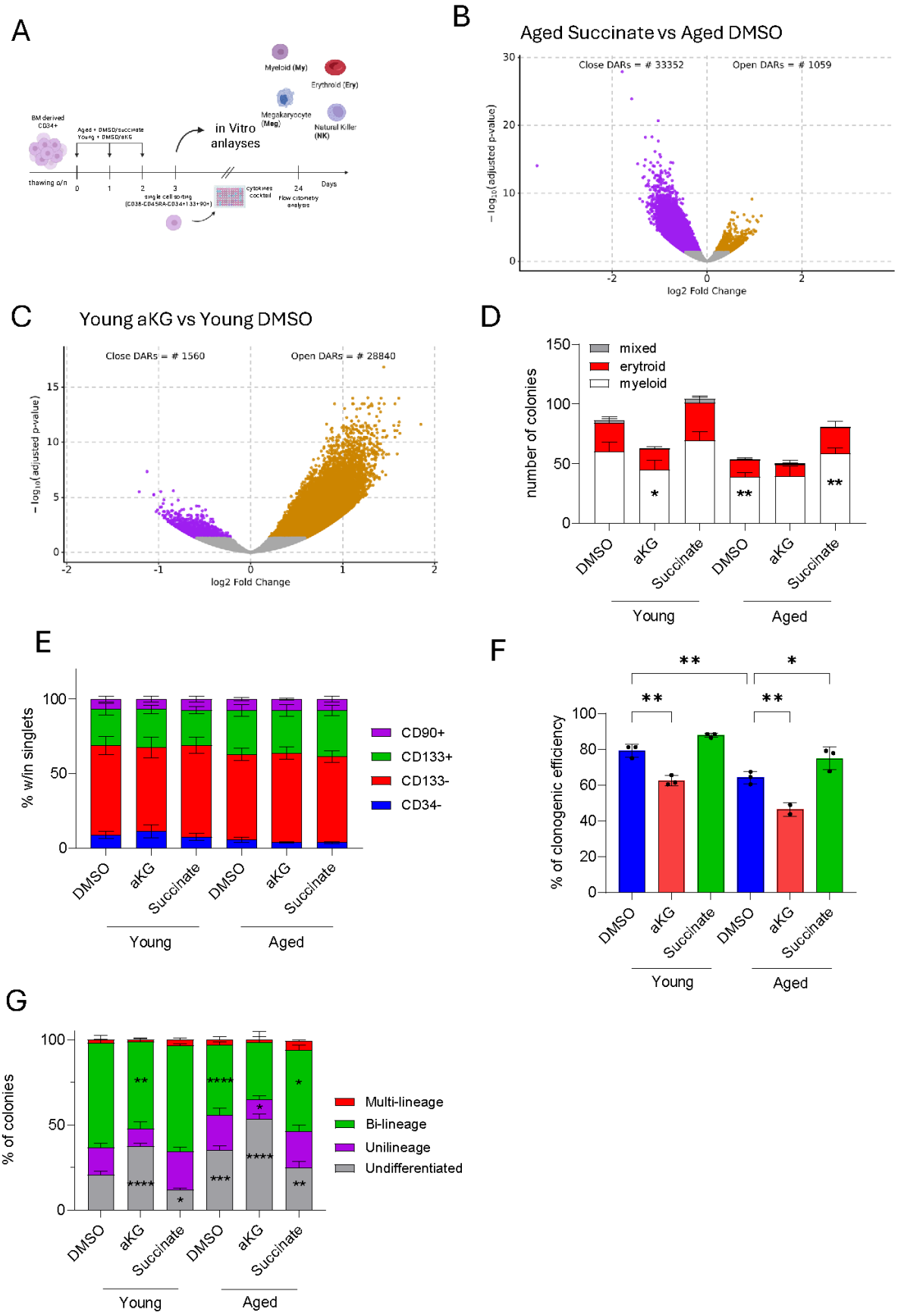

Figure 4: Effect of metabolite treatment on chromatin accessibility and functionality of young and aged HSCPs and HSCs

(A) Experimental workflow for studying the effect of the treatment of BM-derived CD34+ cells from young and aged donors in

cell culture with treatment respectively with DMSO or αKG and DMSO or succinate every 24h with washout every day, cells were kept at 5*10^5/mL across all time points. At 72h, cells were collected for in vitro analysis or FACS-sorted for CD45RA-CD38-CD34+CD133+CD90+ and seeded as single cells in a cytokine-enriched medium. Colonies were harvested and analyzed after 24 days of culture. (B) Volcano-plot of DARs identified by edgeR. X-axis indicates the log2 fold change of ATAC-seq signal difference between aged succinate and aged DMSO, Y-axis indicates the adjusted p-value. (C) Volcano-plot of DARs identified by edgeR. X-axis indicates the log2 fold change of ATAC-seq signal difference between young αKG and young DMSO, Y-axis indicates the adjusted p-value. (D) Number of colonies generated by BM-derived CD34+ cells plated in methylcellulose (*n* = 4). Uncorrected Fisher's LSD test compared to DMSO of each group, plus young DMSO vs aged DMSO. (E) Percentage of HSPC subpopulations ($CD34^+CD133^-$, $CD34^+CD133^+$, and $CD34^+CD133^+CD90^+$ cells) inside alive cells. (F) Clonogenic efficiency of single HSC/MPP pool from 3 independent BM. Tukey's multiple comparisons test. (G) Percentage of not differentiated uni-lineage, bi-lineage and multi-lineage colonies. Uncorrected Fisher's LSD test compared to DMSO of each group, plus young DMSO vs aged DMSO.

Metabolic treatment influences engraftment in NSG mice

Finally, we aimed to determine whether our 72-hour treatment could affect HSPC function in an in vivo setting, providing insights into their repopulating potential. After pre-treating *in vitro* young and aged HSPCs with metabolites, we transplanted $4*10^5$ CD34+ cells into immunodeficient non-obese diabetic (NOD)-severe combined immunodeficiency (SCID)-IL2Rg−/− (NSG) mice (Fig. 5A).

Concerning human cell engraftment in the peripheral blood (PB), measured as the percentage of human CD45+ (hCD45), despite an initial stage of no differences (week 6), the young outperformed the aged (both week 9 and 12), leading to a significantly higher engraftment (Fig. 5B), consistent with our results *in vitro*. On the same line, succinate pre-treatment of aged HSPCs increased the percentage of hCD45+ cells to levels comparable to those of the young DMSO-treated group. In contrast, pre-treatment with αKG of young HSPCs had the opposite effect, reducing engraftment to levels comparable to those of the aged DMSO-treated group (Fig. 5B).

Looking at the composition inside hCD45 in PB, only by week six did aged HSPCs DMSO show a higher percentage of CD33+ cells and a decrease in CD19+ cells comparing with young DMSO (Fig. 5C); this difference was not rescued by succinate treatment in aged cells, nor was it caused by αKG in young cells, indicating that the treatment did not alter differentiation patterns. Notably, at week twelve, there were no differences in PB composition among the groups (Fig. 5C).

Surprisingly, both BM (Fig. 5D) and spleen (Fig. 5E) showed no significant differences in the percentage of hCD45+ between young HSPCs DMSO and aged HSPCs DMSO. Treatment with succinate in aged HSPCs results in increased engraftment in both organs compared with young HSPCs treated with αKG (Fig. 5D-E). Nonetheless, in the spleen, aged succinate shows higher engraftment than aged DMSO (Fig. 5D). Accordingly to data gathered from PB, we observed no differences in the composition of young and aged HSPCs across any cell population (CD3, CD8, CD13, CD19, CD90, CD235a) in both the BM (Fig. 5F) and SP (Fig. 5G), regardless of the treatment.

Altogether, these data suggest that succinate treatment of aged HSPCs improves lineage potential and clonogenic efficiency while decreasing chromatin accessibility, thereby enhancing engraftment potential *in vivo*. As a proof of concept, we also observed that αKG can impair the function of young HSPCs in both *in vitro* and *in vivo* settings, strengthening the idea of an αKG/Succinate molecular axis with implications for HSPC status and fitness.

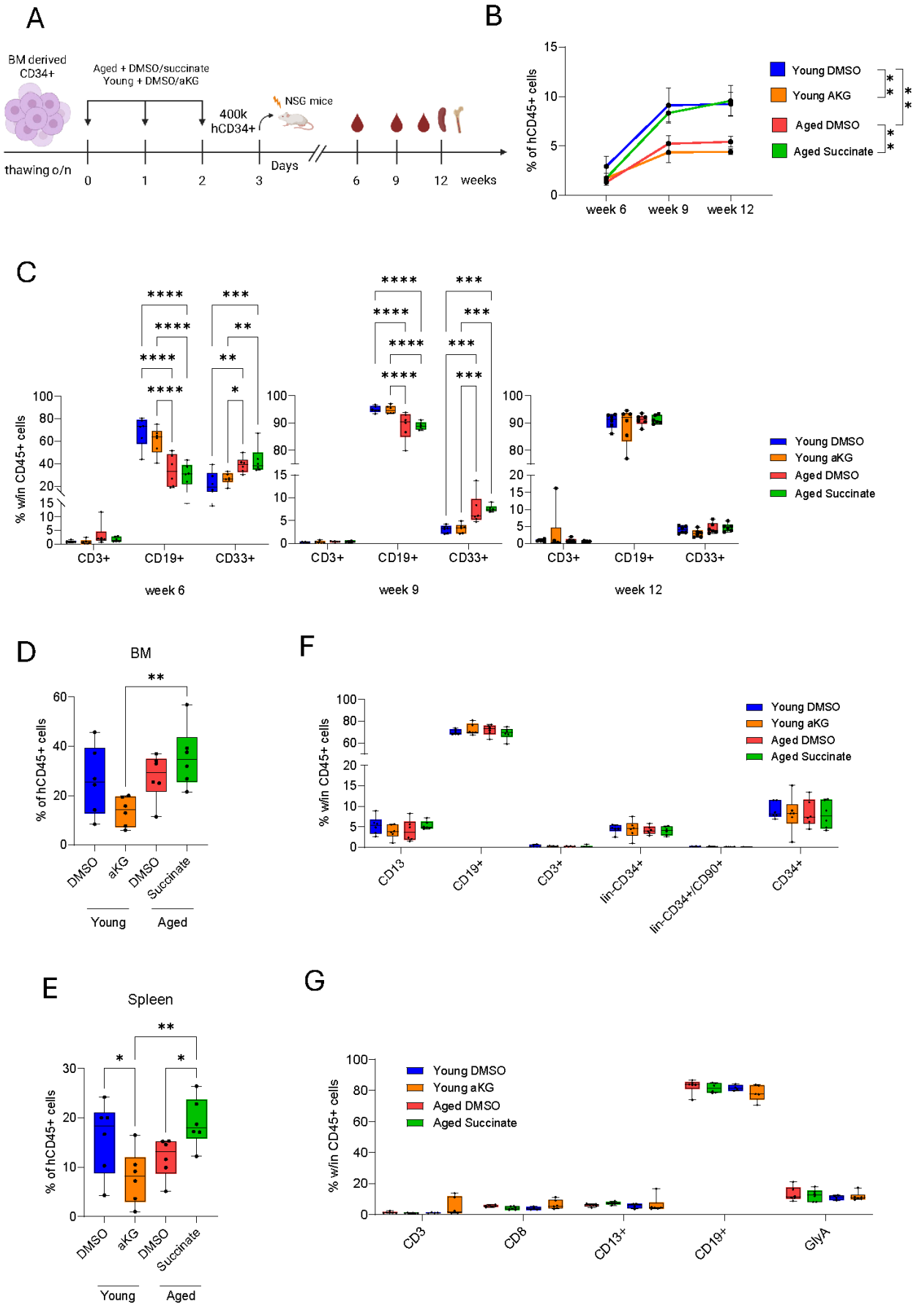

Figure 5: Ex-vivo metabolite treatment modulates young and aged HSPCs engraftment potential in PB
(A) Experimental workflow showing the time of *in vitro* treatments and *in vivo* injection of human BM-derived CD34+ cells from young and aged humans into NSG mice, followed by blood and organ analyses. (B) Percentage of human CD45$^+$ cells in

the PB (n=6). Uncorrected Fisher's LSD. (C) Percentage of CD3+, CD13+ and CD33+ cells within hCD45+ cells in the PB of mice in (B) (n = 6) at the referred time points. Uncorrected Fisher's LSD. (D) Percentage of human $CD45^+$ cells in the BM (n=6). Uncorrected Fisher's LSD. (E) Percentage of human $CD45^+$ cells in the spleen (n=6). Uncorrected Fisher's LSD. (F) Percentage of CD13+, CD19+, CD3+, CD34+, lin-CD34+, lin-CD34+CD90+ cells within $hCD45^+$ cells in the BM of mice in (B) (*n* = 6). Tukey's multiple comparisons test. (G)Percentage of CD3+, CD8+, CD13+, CD19+, GlyA cells within $hCD45^+$ cells in the spleen of mice in (B) (*n* = 6). Tukey's multiple comparisons test.

Succinate treatment is partially HIF2α-mediated and HIF2α-independent.

Since a correlation between DNA damage accumulation and HSPC functionality has already been established [68] and is evident in our results (Fig. 1C), we questioned whether the treatment affected DNA damage burden. Using the Comet Assay, we observed that even after cell culture, aged DMSO-treated cells showed higher levels of DNA damage compared to young DMSO-treated cells (Fig. 6A). Additionally, succinate was able to reduce DNA damage in both groups (Fig. 6A). Interestingly, αKG increased DNA damage in young HSPCs but, as with clonogenic potential, it did not impact aged HSPCs.

We then wondered how the succinate treatment could modulate the DNA damage burden in HSPCs. To this extent, we interrogate the literature to identify potential causes of differences in DNA damage burden with aging. We found that the DNA damage burden in HSPCs, especially during aging, is strongly correlated with an increase in mitochondrial respiration[55,69,70,71].

To evaluate if our treatment with succinate was altering the mitochondrial activity, we used Single Cell ENergetIc metabolism by profilIng Translation inHibition (Scenith)[72]. This enables us to detect mitochondrial and glycolytic dependence via flow cytometry in both bulk CD34+ cells and the most primitive compartment (CD34+CD133+CD90+) (Gating strategy, Fig. 6B). We found that succinate increased glycolytic reliance in aged cells, reaching levels not significantly different from those of young controls in both CD34+ cells (Fig. 6C) and the more primitive CD34+CD133+CD90+ subset (Fig. 6D). Conversely, young cells treated with αKG showed the opposite effect, with levels that did not significantly differ from those of the aged controls (Fig. 6C-D).

We then aimed to analyze how succinate altered energy dependency. It is, in fact, known that high levels of succinate can inhibit the degradation of HIFs, stabilizing them73,74. In turn, high levels of HIFs, especially HIF2α, can induce increased glycolytic dependence and decreased mitochondrial respiration[75]. Furthermore, HIF2α has been reported to regulate not only the response to chronic hypoxia but also to help maintain proper HSC function during differentiation and self-renewal[76].

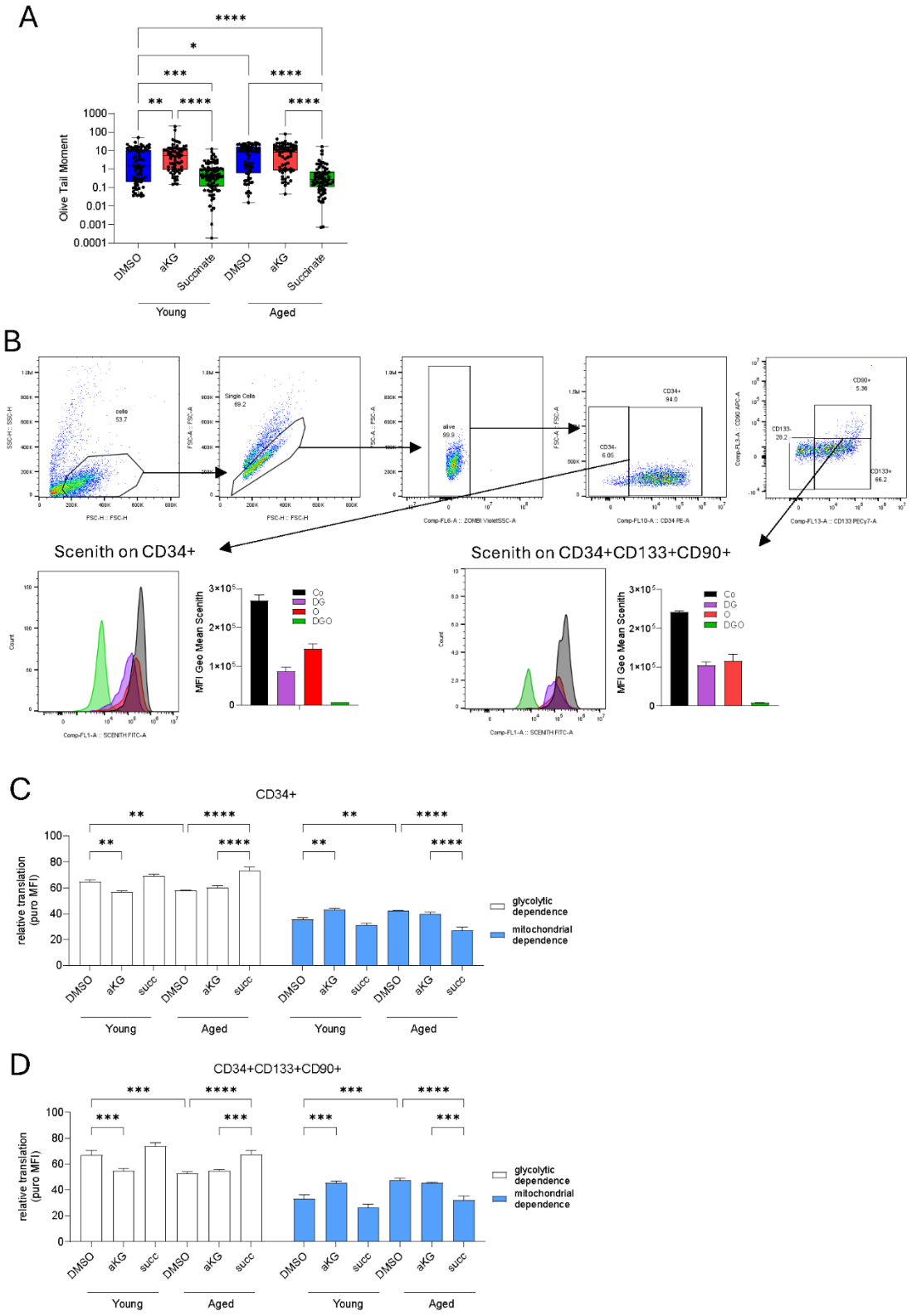

Figure 6: DNA damage burden in young and aged HSPCs upon treatment and metabolic shift in young and aged CD34+ and CD34+CD133+CD90+ cells

(A) Quantification of SSBs and DSBs by comet assay BM-derived CD34+ cells from young and aged after cell culture treatment with metabolites; each point represents a single cell. Kruskal-Wallis test. (B) Gating strategy for SCENITH analyses after 72h of treatment in cell culture via flow cytometry. Representation of MFI Geometrical Mean output after treatment with Co, DG, O, DGO to assess energetic dependency. (C) Relative translation (MFI geometric mean of anti-puromycin signal) in the CD34+ cell population showed glycolytic and mitochondrial dependence for each condition (n=3). Uncorrected Fisher's LSD. (D) Relative translation (MFI geometric mean of anti-puromycin signal) in the

CD34+CD133+CD90+ cell population showed glycolytic and mitochondrial dependence for each condition (n=3). Uncorrected Fisher's LSD.

Performing WB on both young and aged HSPCs, we found that young HSPCs had higher levels of HIF2α compared to aged HSPCs (Fig. 7A); nonetheless, both young and aged HSPCs with succinate showed increased HIF2α abundance, while with αKG it decreased (Fig. 7A), confirming the capacity of these two metabolites to regulate HIF levels.

To better understand how succinate affects the HIF2α pathway and its role in improving clonogenic capacity and reducing DNA damage, we combined our metabolite treatment with PT2399, a well-established HIF2α inhibitor, using a young HSPC source, mPB, to initiate this investigation. This inhibitor prevents HIF2α from binding to HIF1b in the nucleus, thereby blocking activation of the signaling cascade[77,78]. Notably, we found that PT2399 treatment decreased the clonogenic potential of CD34+ cells (Fig. 7B) and increased DNA damage burden (Fig. 7C). Unexpectedly, when combined with succinate, this inhibitor resulted in levels of clonogenic potential and DNA damage burden that fell between those seen with each treatment alone (Fig. 5E-F). This indicates that succinate's effect is partly dependent on HIF2α and partly independent, as the combination with the inhibitor did not completely negate succinate's influence.

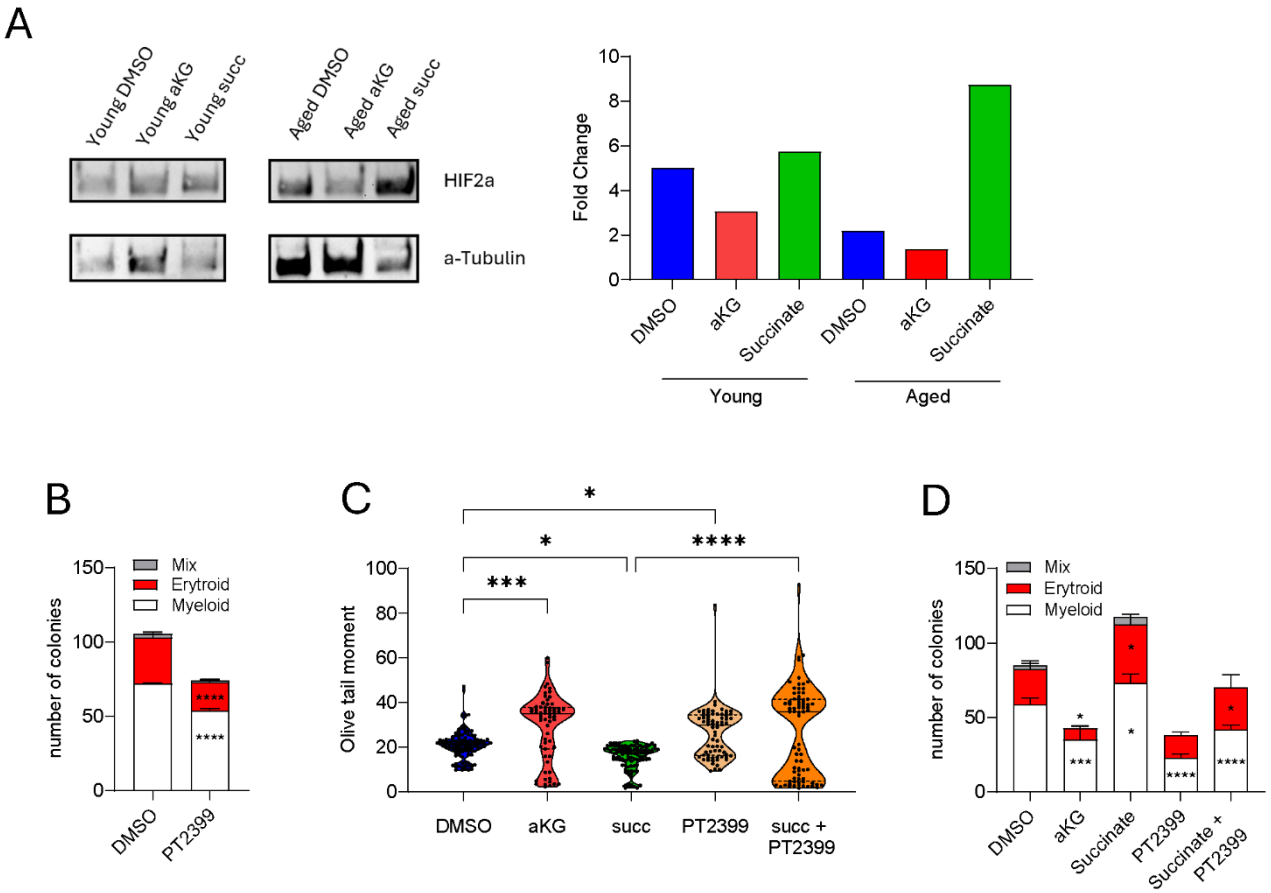

Figure 7: Metabolites treatment alters HIF2α abundance, suggesting succinate's effect on HIF2α pathway
(A) Western Blot analysis of HIF2α after the treatments for 72h of BM CD34+ cells. A-Tubulin was used as a loading control, and the ratio between the target and the loading control is shown. Mann-Whitney test. (B) Number of colonies generated by BM-derived CD34+ cells for young plated in methylcellulose after 72h treatment with DMSO or HIF2α inhibitor (PT2399) (*n* = 3). Uncorrected Fisher's LSD test compared to DMSO. (C) Quantification of SSBs and DSBs by comet assay mPB-derived CD34+ cells from after cell culture treatment with metabolites; each point represents a single cell. Kruskal-Wallis test. (D) Number of colonies generated by mPB-derived CD34+ cells from young plated in methylcellulose after 72h treatment with

DMSO, αKG, succinate, PT2399 or succinate plus PT2399 (*n* = 3). Uncorrected Fisher's LSD test compared to DMSO, PT2399 plus succinate instead was compared to succinate treatment.

Discussion

Aging of human HSPCs involves coordinated epigenetic, transcriptomic, and metabolic changes that collectively reduce their function. In bulk $CD34^+$ cells and in the most primitive $CD45RA^-CD38^-CD34^+CD133^+CD90^+$ HSCs, we observe increased DNA damage, reduced heterochromatin, and lower clonogenic efficiency with diminished bi-lineage potential. These findings align with reports indicating that aging enlarges phenotypically primitive subsets while compromising their quality.[32,79] At the transcriptional level, pathways related to DNA damage and inflammation (p53, TNFα/IL-6/IL-2, IFNγ) are activated alongside proliferative signals (Myc) and metabolic programs (glycolysis, hypoxia, OXPHOS). Consistently, ATAC-seq shows a global expansion of chromatin accessibility, including near TSSs of these pathways, reinforcing the connection between altered cellular states and impaired function in aged HSPCs.

To explore the causes of these molecular and functional changes, we focused our study on metabolomics, as it has been shown that metabolic alterations are particularly important for HSPC function during aging. Although there is a widespread accumulation of several glycolytic, TCA, and methyl-cycle intermediates in aged HSPCs, succinate seems to be relatively depleted with age. Since JmjC histone demethylases use αKG and are inhibited by succinate[80,81,82,83], we proposed that a succinate/αKG axis is a key regulator of chromatin accessibility in human HSPCs. We then disrupted this axis in vitro. Succinate decreased chromatin accessibility and increased H3K27me3 while reducing H3K27ac. Conversely, αKG had the opposite effects. Corresponding functional changes accompanied these chromatin modifications: succinate enhanced colony formation in bulk $CD34^+$ cells from various sources and improved single-cell clonogenic potential and bi-lineage output in sorted primitive HSCs. In contrast, αKG reduced these measures in young cells and did not improve them in aged cells. Overall, altering metabolite levels is sufficient to shift both chromatin state and clonogenic potential in opposite directions.

The interaction between metabolism, chromatin, and HSPCs is currently not well understood. However, it has been reported that αKG can be harmful in certain contexts, accelerating differentiation by disrupting the epigenetic profile in pluripotent stem cells.[84] Additionally, aging correlates with increased chromatin accessibility at specific modules, which can be detrimental.[45] Conversely, in other stem cells such as embryonic stem cells, αKG supports stemness by facilitating αKG-dependent demethylation and maintaining pluripotency, suggesting that increased chromatin accessibility could be beneficial.[85] On the other hand, restricting chromatin accessibility through succinate benefits HSC function in this study, aligning with evidence that reduced accessibility helps preserve stemness in hematopoiesis.[86,87] However, excess succinate elsewhere is associated with inflammatory signaling via SUCNR1 and epigenetic toxicity, indicating that tight regulation of metabolites is necessary to sustain proper cell function.[88,89] In summary, the role of chromatin remodeling varies across lineages and cell states, and our data suggest that modest chromatin compaction in aged human HSPCs is protective, decreasing DNA burden (alkaline comet assay) and increasing functionality (CFU, MEM, in vivo engraftment).

A second, mechanistically linked pathway involves cellular energetics. Prolyl hydroxylases that regulate HIF stability use the αKG/Fe(II)-dependent dioxygenase chemistry shared with JmjC demethylases. In short, increases in succinate can inhibit these enzymes, stabilizing.[73,74] In our system, succinate increased HIF2α levels, while αKG decreased it. Using SCENITH, we showed that succinate shifted dependence toward glycolysis in both bulk $CD34^+$ cells and the primitive $CD34^+CD133^+CD90^+$ subset, restoring aged cells to a more youthful energetic reliance. αKG produced the opposite effect in young cells. This aligns with the hypoxia-focused view of the HSC niche, in which HIF activity and glycolytic bias support stemness and limit mitochondrial stress.64,65 Notably, pharmacologic inhibition of HIF2α with PT2399 only partially reduced succinate's benefits on clonogenicity and DNA damage, indicating partial HIF2α dependence along with HIF-independent chromatin effects.
These in vitro benefits relate to in vivo effects. After 72 hours of treatment, young HSPCs engrafted into the PB of NSG mice more effectively than aged controls at both weeks 9 and 12. Succinate restored PB engraftment of aged HSPCs to levels seen in young DMSO controls. In contrast, αKG decreased PB engraftment of young HSPCs to levels similar to aged HSPCs. Differences in PB lineage composition observed at weeks 6 and 9 (with CD19+ higher in young and CD33+ higher in aged) were unaffected by metabolic treatment and became comparable by week 12. Lastly, engraftment in the BM and spleen showed a consistent increase in aged mice treated with succinate compared to young mice treated with αKG. We speculate that the similar engraftment in the BM and spleen seen with young and aged DMSO, along with the lack of differences in differentiation in both organs and PB at 12 weeks, might be a limitation of our model. NSG mice cannot support the full spectrum of human hematopoietic differentiation [90], which may limit our ability to detect differences in organ engraftment and differentiation. Supporting this, we have already observed differences in clonal efficiency and lineage potential between our groups in MEM in vitro. We hypothesize that a different mouse model, such as NOD.Cg-KitW-41JTyr+PrkdcscidIl2rgtm1Wjl/ThomJ (NBSGW), could better support human HSPCs and allow us to observe differences in differentiation and engraftment across organs.
By integrating all these elements, we propose a calibrated model. Succinate promotes, partly through HIF2α, an increased reliance on glycolysis and reduced mitochondrial activity, which in turn diminishes DNA damage. At the same time, it directly decreases chromatin accessibility by increasing H3K27me3 and decreasing H3K27ac through inhibition of αKG-dependent demethylases. These combined effects help maintain clonogenic capacity in the most primitive human HSPCs and enhance early PB engraftment. Conversely, αKG in young cells opens chromatin, shifts metabolism toward mitochondrial dependence, raises DNA damage, and reduces clonogenicity.
Despite clear gains after short ex vivo exposure to metabolites, our design limits definitive conclusions about deep stemness and lineage diversity. A 12-week xenograft period highlights early repopulating ability and, in standard NSG hosts, results from bone marrow and spleen underestimate human myeloid and lymphoid outputs, likely reducing the dynamic range and underestimating lasting effects. Molecularly, we infer chromatin changes from ATAC-seq and Western blot rather than detailed maps of H3K27me3/H3K27ac. Lastly, we have not examined the impact on 5-mC and 5-hmC, as the balance of succinate and αKG critically influences TET enzyme activity, leaving the cytosine chemistry aspect of the model untested.[91]
Within these limits, our data support the conclusion that modulating the succinate/αKG axis can realign chromatin and metabolism in aged human HSPCs, reducing DNA damage, restoring glycolytic dependence, and improving clonogenic potential, even in the most

primitive compartment, ultimately enhancing in vivo engraftment in peripheral blood. To finalize our analysis, we will extend the in vivo analysis with secondary transplants to quantify long-term repopulating capacity and reveal lineage-specific effects. Mechanistically, we will perform CUT&Tag for H3K27me3/H3K27ac in bulk $CD34^+$ and purified HSC-enriched fractions and implement base-resolved 5mC/5hmC profiling to connect metabolite exposure to promoter/enhancer remodeling at age-biased loci.

Conclusion

Our data show that a succinate/α-ketoglutarate (αKG) axis can influence chromatin accessibility and HIF2α levels in human HSPCs. Brief ex vivo re-balancing of this axis in aged cells improves short-term clonogenicity and early peripheral-blood engraftment in NSG mice. These findings emphasize metabolite tuning as a manageable, cell-intrinsic approach that links the metabolite–epigenome interface to hypoxia-related energy programs that support HSPC function. Next, locus-specific profiling (CUT&Tag for H3K27me3/H3K27ac and base-specific 5mC/5hmC) in purified HSPC subsets, combined with secondary transplants, will identify the genomic targets and distinguish HIF2α-dependent effects from αKG-demethylase–mediated effects. This will guide combination strategies that synchronize metabolic and hypoxia pathways for maximum therapeutic benefit.

Bibliography

1. Doulatov S, Notta F, Laurenti E, Dick JE. Hematopoiesis: a human perspective. Cell Stem Cell. 2012 Feb 3;10(2):120-36.
doi: 10.1016/j.stem.2012.01.006. PMID: 22305562.
2. Notta F, Zandi S, Takayama N, Dobson S, Gan OI, Wilson G, Kaufmann KB, McLeod J, Laurenti E, Dunant CF, McPherson JD, Stein LD, Dror Y, Dick JE. Distinct routes of lineage development reshape the human blood hierarchy across ontogeny. Science. 2016 Jan 8;351(6269):aab2116.
doi: 10.1126/science.aab2116
3. Watcham S, Kucinski I, Gottgens B. New insights into hematopoietic differentiation landscapes from single-cell RNA sequencing. Blood. 2019 Mar 28;133(13):1415-1426.
doi: 10.1182/blood-2018-08-835355
4. Velten L, Haas SF, Raffel S, Blaszkiewicz S, Islam S, Hennig BP, Hirche C, Lutz C, Buss EC, Nowak D, Boch T, Hofmann WK, Ho AD, Huber W, Trumpp A, Essers MA, Steinmetz LM. Human haematopoietic stem cell lineage commitment is a continuous process. Nat Cell Biol. 2017 Apr;19(4):271-281.
doi: 10.1038/ncb3493.
5. Buenrostro JD, Corces MR, Lareau CA, Wu B, Schep AN, Aryee MJ, Majeti R, Chang HY, Greenleaf WJ. Integrated Single-Cell Analysis Maps the Continuous Regulatory Landscape of Human Hematopoietic Differentiation. Cell. 2018 May 31;173(6):1535-1548.e16.
doi: 10.1016/j.cell.2018.03.074.
6. Pellin D, Loperfido M, Baricordi C, Wolock SL, Montepeloso A, Weinberg OK, Biffi A, Klein AM, Biasco L. A comprehensive single cell transcriptional landscape of human hematopoietic progenitors. Nat Commun. 2019 Jun 3;10(1):2395.
doi: 10.1038/s41467-019-10291-0.
7. Notta F, Doulatov S, Laurenti E, Poeppl A, Jurisica I, Dick JE. Isolation of single human hematopoietic stem cells capable of long-term multilineage engraftment. Science. 2011 Jul 8;333(6039):218-21.
doi: 10.1126/science.1201219.
8. Lee-Six H, Øbro NF, Shepherd MS, Grossmann S, Dawson K, Belmonte M, Osborne RJ, Huntly BJP, Martincorena I, Anderson E, O'Neill L, Stratton MR, Laurenti E, Green AR, Kent DG, Campbell PJ. Population dynamics of normal human blood inferred from somatic mutations. Nature. 2018 Sep;561(7724):473-478. doi: 10.1038/s41586-018-0497-0.
9. Morrison SJ, Scadden DT. The bone marrow niche for haematopoietic stem cells. Nature. 2014 Jan 16;505(7483):327-34.
doi: 10.1038/nature12984.
10. Qian H, Buza-Vidas N, Hyland CD, Jensen CT, Antonchuk J, Månsson R, Thoren LA, Ekblom M, Alexander WS, Jacobsen SE. Critical role of thrombopoietin in maintaining adult quiescent hematopoietic stem cells. Cell Stem Cell. 2007 Dec 13;1(6):671-84.
doi: 10.1016/j.stem.2007.10.008.
11. Butler JM, Nolan DJ, Vertes EL, Varnum-Finney B, Kobayashi H, Hooper AT, Seandel M, Shido K, White IA, Kobayashi M, Witte L, May C, Shawber C, Kimura Y, Kitajewski J, Rosenwaks Z, Bernstein ID, Rafii S. Endothelial cells are essential for the self-renewal and repopulation of Notch-dependent hematopoietic stem cells. Cell Stem Cell. 2010 Mar 5;6(3):251-64.
doi: 10.1016/j.stem.2010.02.001.
12. Poulos MG, Guo P, Kofler NM, Pinho S, Gutkin MC, Tikhonova A, Aifantis I, Frenette PS, Kitajewski J, Rafii S, Butler JM. Endothelial Jagged-1 is necessary for homeostatic and regenerative hematopoiesis. Cell Rep. 2013 Sep 12;4(5):1022-34.
doi: 10.1016/j.celrep.2013.07.048.
13. Xu C, Gao X, Wei Q, Nakahara F, Zimmerman SE, Mar J, Frenette PS. Stem cell factor is selectively secreted by arterial endothelial cells in bone marrow. Nat Commun. 2018 Jun 22;9(1):2449.
doi: 10.1038/s41467-018-04726-3.
14. Kunisaki Y, Bruns I, Scheiermann C, Ahmed J, Pinho S, Zhang D, Mizoguchi T, Wei Q, Lucas D, Ito K, Mar JC, Bergman A, Frenette PS. Arteriolar niches maintain haematopoietic stem cell quiescence. Nature.

2013 Oct 31;502(7473):637-43.
doi: 10.1038/nature12612.

15. PMID: 26416744 Acar M, Kocherlakota KS, Murphy MM, Peyer JG, Oguro H, Inra CN, Jaiyeola C, Zhao Z, Luby-Phelps K, Morrison SJ. Deep imaging of bone marrow shows non-dividing stem cells are mainly perisinusoidal. Nature. 2015 Oct 1;526(7571):126-30.
doi: 10.1038/nature15250.
16. Itkin T, Gur-Cohen S, Spencer JA, Schajnovitz A, Ramasamy SK, Kusumbe AP, Ledergor G, Jung Y, Milo I, Poulos MG, Kalinkovich A, Ludin A, Kollet O, Shakhar G, Butler JM, Rafii S, Adams RH, Scadden DT, Lin CP, Lapidot T. Distinct bone marrow blood vessels differentially regulate haematopoiesis. Nature. 2016 Apr 21;532(7599):323-8.
doi: 10.1038/nature17624. Epub 2016 Apr 13.
17. Bruns I, Lucas D, Pinho S, Ahmed J, Lambert MP, Kunisaki Y, Scheiermann C, Schiff L, Poncz M, Bergman A, Frenette PS. Megakaryocytes regulate hematopoietic stem cell quiescence through CXCL4 secretion. Nat Med. 2014 Nov;20(11):1315-20.
doi: 10.1038/nm.3707.
18. Zhao M, Perry JM, Marshall H, Venkatraman A, Qian P, He XC, Ahamed J, Li L. Megakaryocytes maintain homeostatic quiescence and promote post-injury regeneration of hematopoietic stem cells. Nat Med. 2014 Nov;20(11):1321-6.
doi: 10.1038/nm.3706.
19. Sugiyama T, Kohara H, Noda M, Nagasawa T. Maintenance of the hematopoietic stem cell pool by CXCL12-CXCR4 chemokine signaling in bone marrow stromal cell niches. Immunity. 2006 Dec;25(6):977-88.
doi: 10.1016/j.immuni.2006.10.016.
20. Chow A, Lucas D, Hidalgo A, Méndez-Ferrer S, Hashimoto D, Scheiermann C, Battista M, Leboeuf M, Prophete C, van Rooijen N, Tanaka M, Merad M, Frenette PS. Bone marrow CD169+ macrophages promote the retention of hematopoietic stem and progenitor cells in the mesenchymal stem cell niche. J Exp Med. 2011 Feb 14;208(2):261-71.
doi: 10.1084/jem.20101688.
21. Winkler IG, Sims NA, Pettit AR, Barbier V, Nowlan B, Helwani F, Poulton IJ, van Rooijen N, Alexander KA, Raggatt LJ, Lévesque JP. Bone marrow macrophages maintain hematopoietic stem cell (HSC) niches and their depletion mobilizes HSCs. Blood. 2010 Dec 2;116(23):4815-28.
doi: 10.1182/blood-2009-11-253534.
22. Méndez-Ferrer S, Lucas D, Battista M, Frenette PS. Haematopoietic stem cell release is regulated by circadian oscillations. Nature. 2008 Mar 27;452(7186):442-7.
doi: 10.1038/nature06685.
23. Casanova-Acebes M, Pitaval C, Weiss LA, Nombela-Arrieta C, Chèvre R, A-González N, Kunisaki Y, Zhang D, van Rooijen N, Silberstein LE, Weber C, Nagasawa T, Frenette PS, Castrillo A, Hidalgo A. Rhythmic modulation of the hematopoietic niche through neutrophil clearance. Cell. 2013 May 23;153(5):1025-35.
doi: 10.1016/j.cell.2013.04.040.
24. Chen Q, Liu Y, Jeong HW, Stehling M, Dinh VV, Zhou B, Adams RH. Apelin^{+} Endothelial Niche Cells Control Hematopoiesis and Mediate Vascular Regeneration after Myeloablative Injury. Cell Stem Cell. 2019 Dec 5;25(6):768-783.e6.
doi: 10.1016/j.stem.2019.10.006.
25. Maryanovich M, Zahalka AH, Pierce H, Pinho S, Nakahara F, Asada N, Wei Q, Wang X, Ciero P, Xu J, Leftin A, Frenette PS. Adrenergic nerve degeneration in bone marrow drives aging of the hematopoietic stem cell niche. Nat Med. 2018 Jun;24(6):782-791.
doi: 10.1038/s41591-018-0030-x.
26. Naveiras O, Nardi V, Wenzel PL, Hauschka PV, Fahey F, Daley GQ. Bone-marrow adipocytes as negative regulators of the haematopoietic microenvironment. Nature. 2009 Jul 9;460(7252):259-63.
doi: 10.1038/nature08099.
27. Ambrosi TH, Scialdone A, Graja A, Gohlke S, Jank AM, Bocian C, Woelk L, Fan H, Logan DW, Schürmann A, Saraiva LR, Schulz TJ. Adipocyte Accumulation in the Bone Marrow during Obesity and Aging Impairs

Stem Cell-Based Hematopoietic and Bone Regeneration. Cell Stem Cell. 2017 Jun 1;20(6):771-784.e6. doi: 10.1016/j.stem.2017.02.009.
28. Pinho S, Frenette PS. Haematopoietic stem cell activity and interactions with the niche. Nat Rev Mol Cell Biol. 2019 May;20(5):303-320. doi: 10.1038/s41580-019-0103-9.
29. Choi JS, Mahadik BP, Harley BA. Engineering the hematopoietic stem cell niche: Frontiers in biomaterial science. Biotechnol J. 2015 Oct;10(10):1529-45. doi: 10.1002/biot.201400758
30. Zhang P, Zhang C, Li J, Han J, Liu X, Yang H. The physical microenvironment of hematopoietic stem cells and its emerging roles in engineering applications. Stem Cell Res Ther. 2019 Nov 19;10(1):327. doi: 10.1186/s13287-019-1422-7.
31. Csaszar E, Kirouac DC, Yu M, Wang W, Qiao W, Cooke MP, Boitano AE, Ito C, Zandstra PW. Rapid expansion of human hematopoietic stem cells by automated control of inhibitory feedback signaling. Cell Stem Cell. 2012 Feb 3;10(2):218-29. doi: 10.1016/j.stem.2012.01.003.
32. Chambers SM, Shaw CA, Gatza C, Fisk CJ, Donehower LA, Goodell MA. Aging hematopoietic stem cells decline in function and exhibit epigenetic dysregulation. PLoS Biol. 2007 Aug;5(8):e201. doi: 10.1371/journal.pbio.0050201.
33. Liang Y, Van Zant G, Szilvassy SJ. Effects of aging on the homing and engraftment of murine hematopoietic stem and progenitor cells. Blood. 2005 Aug 15;106(4):1479-87. doi: 10.1182/blood-2004-11-4282.
34. Dykstra B, Olthof S, Schreuder J, Ritsema M, de Haan G. Clonal analysis reveals multiple functional defects of aged murine hematopoietic stem cells. J Exp Med. 2011 Dec 19;208(13):2691-703. doi: 10.1084/jem.20111490.
35. Geiger H, de Haan G, Florian MC. The ageing haematopoietic stem cell compartment. Nat Rev Immunol. 2013 May;13(5):376-89. doi: 10.1038/nri3433.
36. Sudo K, Ema H, Morita Y, Nakauchi H. Age-associated characteristics of murine hematopoietic stem cells. J Exp Med. 2000 Nov 6;192(9):1273-80. doi: 10.1084/jem.192.9.1273.
37. Verovskaya E, Broekhuis MJ, Zwart E, Ritsema M, van Os R, de Haan G, Bystrykh LV. Heterogeneity of young and aged murine hematopoietic stem cells revealed by quantitative clonal analysis using cellular barcoding. Blood. 2013 Jul 25;122(4):523-32. doi: 10.1182/blood-2013-01-481135.
38. Jaiswal S, Fontanillas P, Flannick J, Manning A, Grauman PV, Mar BG, Lindsley RC, Mermel CH, Burtt N, Chavez A, Higgins JM, Moltchanov V, Kuo FC, Kluk MJ, Henderson B, Kinnunen L, Koistinen HA, Ladenvall C, Getz G, Correa A, Banahan BF, Gabriel S, Kathiresan S, Stringham HM, McCarthy MI, Boehnke M, Tuomilehto J, Haiman C, Groop L, Atzmon G, Wilson JG, Neuberg D, Altshuler D, Ebert BL. Age-related clonal hematopoiesis associated with adverse outcomes. N Engl J Med. 2014 Dec 25;371(26):2488-98. doi: 10.1056/NEJMoa1408617.
39. Genovese G, Kähler AK, Handsaker RE, Lindberg J, Rose SA, Bakhoum SF, Chambert K, Mick E, Neale BM, Fromer M, Purcell SM, Svantesson O, Landén M, Höglund M, Lehmann S, Gabriel SB, Moran JL, Lander ES, Sullivan PF, Sklar P, Grönberg H, Hultman CM, McCarroll SA. Clonal hematopoiesis and blood-cancer risk inferred from blood DNA sequence. N Engl J Med. 2014 Dec 25;371(26):2477-87. doi: 10.1056/NEJMoa1409405.
40. Chen Z, Amro EM, Becker F, Hölzer M, Rasa SMM, Njeru SN, Han B, Di Sanzo S, Chen Y, Tang D, Tao S, Haenold R, Groth M, Romanov VS, Kirkpatrick JM, Kraus JM, Kestler HA, Marz M, Ori A, Neri F, Morita Y, Rudolph KL. Cohesin-mediated NF-κB signaling limits hematopoietic stem cell self-renewal in aging and inflammation. J Exp Med. 2019 Jan 7;216(1):152-175. doi: 10.1084/jem.20181505.
41. Rossi DJ, Bryder D, Zahn JM, Ahlenius H, Sonu R, Wagers AJ, Weissman IL. Cell intrinsic alterations underlie hematopoietic stem cell aging. Proc Natl Acad Sci U S A. 2005 Jun 28;102(26):9194-9. doi: 10.1073/pnas.0503280102.

42. PMID: 27009448 Grover A, Sanjuan-Pla A, Thongjuea S, Carrelha J, Giustacchini A, Gambardella A, Macaulay I, Mancini E, Luis TC, Mead A, Jacobsen SE, Nerlov C. Single-cell RNA sequencing reveals molecular and functional platelet bias of aged haematopoietic stem cells. Nat Commun. 2016 Mar 24;7:11075.
doi: 10.1038/ncomms11075.
43. Kowalczyk MS, Tirosh I, Heckl D, Rao TN, Dixit A, Haas BJ, Schneider RK, Wagers AJ, Ebert BL, Regev A. Single-cell RNA-seq reveals changes in cell cycle and differentiation programs upon aging of hematopoietic stem cells. Genome Res. 2015 Dec;25(12):1860-72.
doi: 10.1101/gr.192237.115.
44. Adelman ER, Huang HT, Roisman A, Olsson A, Colaprico A, Qin T, Lindsley RC, Bejar R, Salomonis N, Grimes HL, Figueroa ME. Aging Human Hematopoietic Stem Cells Manifest Profound Epigenetic Reprogramming of Enhancers That May Predispose to Leukemia. Cancer Discov. 2019 Aug;9(8):1080-1101.
doi: 10.1158/2159-8290.CD-18-1474.
45. Itokawa N, Oshima M, Koide S, Takayama N, Kuribayashi W, Nakajima-Takagi Y, Aoyama K, Yamazaki S, Yamaguchi K, Furukawa Y, Eto K, Iwama A. Epigenetic traits inscribed in chromatin accessibility in aged hematopoietic stem cells. Nat Commun. 2022 May 16;13(1):2691.
doi: 10.1038/s41467-022-30440-2.
46. Pietras EM, Mirantes-Barbeito C, Fong S, Loeffler D, Kovtonyuk LV, Zhang S, Lakshminarasimhan R, Chin CP, Techner JM, Will B, Nerlov C, Steidl U, Manz MG, Schroeder T, Passegué E. Chronic interleukin-1 exposure drives haematopoietic stem cells towards precocious myeloid differentiation at the expense of self-renewal. Nat Cell Biol. 2016 Jun;18(6):607-18.
doi: 10.1038/ncb3346.
47. Beerman I, Bock C, Garrison BS, Smith ZD, Gu H, Meissner A, Rossi DJ. Proliferation-dependent alterations of the DNA methylation landscape underlie hematopoietic stem cell aging. Cell Stem Cell. 2013 Apr 4;12(4):413-25.
doi: 10.1016/j.stem.2013.01.017.
48. Sun D, Luo M, Jeong M, Rodriguez B, Xia Z, Hannah R, Wang H, Le T, Faull KF, Chen R, Gu H, Bock C, Meissner A, Göttgens B, Darlington GJ, Li W, Goodell MA. Epigenomic profiling of young and aged HSCs reveals concerted changes during aging that reinforce self-renewal. Cell Stem Cell. 2014 May 1;14(5):673-88.
doi: 10.1016/j.stem.2014.03.002.
49. Djeghloul D, Kuranda K, Kuzniak I, Barbieri D, Naguibneva I, Choisy C, Bories JC, Dosquet C, Pla M, Vanneaux V, Socié G, Porteu F, Garrick D, Goodhardt M. Age-Associated Decrease of the Histone Methyltransferase SUV39H1 in HSC Perturbs Heterochromatin and B Lymphoid Differentiation. Stem Cell Reports. 2016 Jun 14;6(6):970-984.
doi: 10.1016/j.stemcr.2016.05.007.
50. Agathocleous M, Meacham CE, Burgess RJ, Piskounova E, Zhao Z, Crane GM, Cowin BL, Bruner E, Murphy MM, Chen W, Spangrude GJ, Hu Z, DeBerardinis RJ, Morrison SJ. Ascorbate regulates haematopoietic stem cell function and leukaemogenesis. Nature. 2017 Sep 28;549(7673):476-481.
doi: 10.1038/nature23876.
51. Moran-Crusio K, Reavie L, Shih A, Abdel-Wahab O, Ndiaye-Lobry D, Lobry C, Figueroa ME, Vasanthakumar A, Patel J, Zhao X, Perna F, Pandey S, Madzo J, Song C, Dai Q, He C, Ibrahim S, Beran M, Zavadil J, Nimer SD, Melnick A, Godley LA, Aifantis I, Levine RL. Tet2 loss leads to increased hematopoietic stem cell self-renewal and myeloid transformation. Cancer Cell. 2011 Jul 12;20(1):11-24.
doi: 10.1016/j.ccr.2011.06.001.
52. Challen GA, Sun D, Jeong M, Luo M, Jelinek J, Berg JS, Bock C, Vasanthakumar A, Gu H, Xi Y, Liang S, Lu Y, Darlington GJ, Meissner A, Issa JP, Godley LA, Li W, Goodell MA. Dnmt3a is essential for hematopoietic stem cell differentiation. Nat Genet. 2011 Dec 4;44(1):23-31.
doi: 10.1038/ng.1009.
53. Bloomfield GS, Mwangi A, Chege P, Simiyu CJ, Aswa DF, Odhiambo D, Obala AA, Ayuo P, Khwa-Otsyula BO. Multiple cardiovascular risk factors in Kenya: evidence from a health and demographic surveillance system using the WHO STEPwise approach to chronic disease risk factor surveillance. Heart. 2013

Sep;99(18):1323-9.
doi: 10.1136/heartjnl-2013-303913.

54. Florian MC, Dörr K, Niebel A, Daria D, Schrezenmeier H, Rojewski M, Filippi MD, Hasenberg A, Gunzer M, Scharffetter-Kochanek K, Zheng Y, Geiger H. Cdc42 activity regulates hematopoietic stem cell aging and rejuvenation. Cell Stem Cell. 2012 May 4;10(5):520-30.
doi: 10.1016/j.stem.2012.04.007.
55. Simsek T, Kocabas F, Zheng J, Deberardinis RJ, Mahmoud AI, Olson EN, Schneider JW, Zhang CC, Sadek HA. The distinct metabolic profile of hematopoietic stem cells reflects their location in a hypoxic niche. Cell Stem Cell. 2010 Sep 3;7(3):380-90.
doi: 10.1016/j.stem.2010.07.011.
56. Qiu J, Gjini J, Arif T, Moore K, Lin M, Ghaffari S. Using mitochondrial activity to select for potent human hematopoietic stem cells. Blood Adv. 2021 Mar 23;5(6):1605-1616.
doi: 10.1182/bloodadvances.2020003658.
57. Ito K, Hirao A, Arai F, Takubo K, Matsuoka S, Miyamoto K, Ohmura M, Naka K, Hosokawa K, Ikeda Y, Suda T. Reactive oxygen species act through p38 MAPK to limit the lifespan of hematopoietic stem cells. Nat Med. 2006 Apr;12(4):446-51.
doi: 10.1038/nm1388.
58. Takubo K, Nagamatsu G, Kobayashi CI, Nakamura-Ishizu A, Kobayashi H, Ikeda E, Goda N, Rahimi Y, Johnson RS, Soga T, Hirao A, Suematsu M, Suda T. Regulation of glycolysis by Pdk functions as a metabolic checkpoint for cell cycle quiescence in hematopoietic stem cells. Cell Stem Cell. 2013 Jan 3;12(1):49-61.
doi: 10.1016/j.stem.2012.10.011.
59. Mortensen M, Soilleux EJ, Djordjevic G, Tripp R, Lutteropp M, Sadighi-Akha E, Stranks AJ, Glanville J, Knight S, Jacobsen SE, Kranc KR, Simon AK. The autophagy protein Atg7 is essential for hematopoietic stem cell maintenance. J Exp Med. 2011 Mar 14;208(3):455-67.
doi: 10.1084/jem.20101145.
60. Nakamura-Ishizu A, Ito K, Suda T. Hematopoietic Stem Cell Metabolism during Development and Aging. Dev Cell. 2020 Jul 20;54(2):239-255.
doi: 10.1016/j.devcel.2020.06.029.
61. Morganti C, Cabezas-Wallscheid N, Ito K. Metabolic Regulation of Hematopoietic Stem Cells. Hemasphere. 2022 Jun 28;6(7):e740.
doi: 10.1097/HS9.0000000000000740.
62. Yilmaz OH, Valdez R, Theisen BK, Guo W, Ferguson DO, Wu H, Morrison SJ. Pten dependence distinguishes haematopoietic stem cells from leukaemia-initiating cells. Nature. 2006 May 25;441(7092):475-82.
doi: 10.1038/nature04703.
63. Chen C, Liu Y, Liu Y, Zheng P. mTOR regulation and therapeutic rejuvenation of aging hematopoietic stem cells. Sci Signal. 2009 Nov 24;2(98):ra75.
doi: 10.1126/scisignal.2000559.
64. Takubo K, Goda N, Yamada W, Iriuchishima H, Ikeda E, Kubota Y, Shima H, Johnson RS, Hirao A, Suematsu M, Suda T. Regulation of the HIF-1alpha level is essential for hematopoietic stem cells. Cell Stem Cell. 2010 Sep 3;7(3):391-402.
doi: 10.1016/j.stem.2010.06.020.
65. Mohrin M, Shin J, Liu Y, Brown K, Luo H, Xi Y, Haynes CM, Chen D. Stem cell aging. A mitochondrial UPR-mediated metabolic checkpoint regulates hematopoietic stem cell aging. Science. 2015 Mar 20;347(6228):1374-7.
doi: 10.1126/science.aaa2361.
66. Mohrin M, Widjaja A, Liu Y, Luo H, Chen D. The mitochondrial unfolded protein response is activated upon hematopoietic stem cell exit from quiescence. Aging Cell. 2018 Jun;17(3):e12756.
doi: 10.1111/acel.12756.
67. Martínez-Reyes I, Chandel NS. Mitochondrial TCA cycle metabolites control physiology and disease. Nat Commun. 2020 Jan 3;11(1):102.
doi: 10.1038/s41467-019-13668-3.

68. Rübe CE, Fricke A, Widmann TA, Fürst T, Madry H, Pfreundschuh M, Rübe C. Accumulation of DNA damage in hematopoietic stem and progenitor cells during human aging. PLoS One. 2011 Mar 7;6(3):e17487.
doi: 10.1371/journal.pone.0017487.
69. Sun X, Cao B, Naval-Sanchez M, Pham T, Sun YBY, Williams B, Heazlewood SY, Deshpande N, Li J, Kraus F, Rae J, Nguyen Q, Yari H, Schröder J, Heazlewood CK, Fulton M, Hatwell-Humble J, Das Gupta K, Kapetanovic R, Chen X, Sweet MJ, Parton RG, Ryan MT, Polo JM, Nefzger CM, Nilsson SK. Nicotinamide riboside attenuates age-associated metabolic and functional changes in hematopoietic stem cells. Nat Commun. 2021 May 11;12(1):2665.
doi: 10.1038/s41467-021-22863-0.
70. Wang N, Yin J, You N, Yang S, Guo D, Zhao Y, Ru Y, Liu X, Cheng H, Ren Q, Cheng T, Ma X. TWIST1 preserves hematopoietic stem cell function via the CACNA1B/Ca2+/mitochondria axis. Blood. 2021 May 27;137(21):2907-2919.
doi: 10.1182/blood.2020007489.
71. Maryanovich M, Zaltsman Y, Ruggiero A, Goldman A, Shachnai L, Zaidman SL, Porat Z, Golan K, Lapidot T, Gross A. An MTCH2 pathway repressing mitochondria metabolism regulates haematopoietic stem cell fate. Nat Commun. 2015 Jul 29;6:7901.
doi: 10.1038/ncomms8901.
72. Argüello RJ, Combes AJ, Char R, Gigan JP, Baaziz AI, Bousiquot E, Camosseto V, Samad B, Tsui J, Yan P, Boissonneau S, Figarella-Branger D, Gatti E, Tabouret E, Krummel MF, Pierre P. SCENITH: A Flow Cytometry-Based Method to Functionally Profile Energy Metabolism with Single-Cell Resolution. Cell Metab. 2020 Dec 1;32(6):1063-1075.e7.
doi: 10.1016/j.cmet.2020.11.007.
73. MacKenzie ED, Selak MA, Tennant DA, Payne LJ, Crosby S, Frederiksen CM, Watson DG, Gottlieb E. Cell-permeating alpha-ketoglutarate derivatives alleviate pseudohypoxia in succinate dehydrogenase-deficient cells. Mol Cell Biol. 2007 May;27(9):3282-9.
doi: 10.1128/MCB.01927-06.
74. Cho H, Du X, Rizzi JP, Liberzon E, Chakraborty AA, Gao W, Carvo I, Signoretti S, Bruick RK, Josey JA, Wallace EM, Kaelin WG. On-target efficacy of a HIF-2α antagonist in preclinical kidney cancer models. Nature. 2016 Nov 3;539(7627):107-111.
doi: 10.1038/nature19795.
75. Kong Y, Liu PK, Li Y, Nolan ND, Quinn PMJ, Hsu CW, Jenny LA, Zhao J, Cui X, Chang YJ, Wert KJ, Sparrow JR, Wang NK, Tsang SH. HIF2α activation and mitochondrial deficit due to iron chelation cause retinal atrophy. EMBO Mol Med. 2023 Feb 8;15(2):e16525.
doi: 10.15252/emmm.202216525.
76. Rouault-Pierre K, Lopez-Onieva L, Foster K, Anjos-Afonso F, Lamrissi-Garcia I, Serrano-Sanchez M, Mitter R, Ivanovic Z, de Verneuil H, Gribben J, Taussig D, Rezvani HR, Mazurier F, Bonnet D. HIF-2α protects human hematopoietic stem/progenitors and acute myeloid leukemic cells from apoptosis induced by endoplasmic reticulum stress. Cell Stem Cell. 2013 Nov 7;13(5):549-63.
doi: 10.1016/j.stem.2013.08.011.
77. Wang LL, Lu ZJ, Luo SK, Li Y, Yang Z, Lu HY. Unveiling the role of hypoxia-inducible factor 2alpha in osteoporosis: Implications for bone health. World J Stem Cells. 2024 Apr 26;16(4):389-409.
doi: 10.4252/wjsc.v16.i4.389.
78. Magliulo D, Simoni M, Caserta C, Fracassi C, Belluschi S, Giannetti K, Pini R, Zapparoli E, Beretta S, Uggè M, Draghi E, Rossari F, Coltella N, Tresoldi C, Morelli MJ, Di Micco R, Gentner B, Vago L, Bernardi R. The transcription factor HIF2α partakes in the differentiation block of acute myeloid leukemia. EMBO Mol Med. 2023 Nov 8;15(11):e17810.
doi: 10.15252/emmm.202317810.
79. Flach J, Bakker ST, Mohrin M, Conroy PC, Pietras EM, Reynaud D, Alvarez S, Diolaiti ME, Ugarte F, Forsberg EC, Le Beau MM, Stohr BA, Méndez J, Morrison CG, Passegué E. Replication stress is a potent driver of functional decline in ageing haematopoietic stem cells. Nature. 2014 Aug 14;512(7513):198-202.
doi: 10.1038/nature13619.

80. Tretter L, Patocs A, Chinopoulos C. Succinate, an intermediate in metabolism, signal transduction, ROS, hypoxia, and tumorigenesis. Biochim Biophys Acta. 2016 Aug;1857(8):1086-1101. doi: 10.1016/j.bbabio.2016.03.012.
81. Meng Y, Li H, Liu C, Zheng L, Shen B. Jumonji domain-containing protein family: the functions beyond lysine demethylation. J Mol Cell Biol. 2018 Aug 1;10(4):371-373. doi: 10.1093/jmcb/mjy010.
82. Xiao M, Yang H, Xu W, Ma S, Lin H, Zhu H, Liu L, Liu Y, Yang C, Xu Y, Zhao S, Ye D, Xiong Y, Guan KL. Corrigendum: inhibition of α-KG-dependent histone and DNA demethylases by fumarate and succinate that are accumulated in mutations of FH and SDH tumor suppressors. Genes Dev. 2015 Apr 15;29(8):887. Epub 2015 Apr 15. Erratum for: Genes Dev. 2012 Jun 15;26(12):1326-38. doi: 10.1101/gad.191056.112.
83. Cervera AM, Bayley JP, Devilee P, McCreath KJ. Inhibition of succinate dehydrogenase dysregulates histone modification in mammalian cells. Mol Cancer. 2009 Oct 22;8:89. doi: 10.1186/1476-4598-8-89.
84. TeSlaa T, Chaikovsky AC, Lipchina I, Escobar SL, Hochedlinger K, Huang J, Graeber TG, Braas D, Teitell MA. α-Ketoglutarate Accelerates the Initial Differentiation of Primed Human Pluripotent Stem Cells. Cell Metab. 2016 Sep 13;24(3):485-493. doi: 10.1016/j.cmet.2016.07.002.
85. Carey BW, Finley LW, Cross JR, Allis CD, Thompson CB. Intracellular α-ketoglutarate maintains the pluripotency of embryonic stem cells. Nature. 2015 Feb 19;518(7539):413-6. doi: 10.1038/nature13981.
86. Wendorff AA, Aidan Quinn S, Alvarez S, Brown JA, Biswas M, Gunning T, Palomero T, Ferrando AA. Epigenetic reversal of hematopoietic stem cell aging in Phf6-knockout mice. Nat Aging. 2022 Nov;2(11):1008-1023. doi: 10.1038/s43587-022-00304-x.
87. Wroblewski M, Scheller-Wendorff M, Udonta F, Bauer R, Schlichting J, Zhao L, Ben Batalla I, Gensch V, Päsler S, Wu L, Wanior M, Taipaleenmäki H, Bolamperti S, Najafova Z, Pantel K, Bokemeyer C, Qi J, Hesse E, Knapp S, Johnsen S, Loges S. BET-inhibition by JQ1 promotes proliferation and self-renewal capacity of hematopoietic stem cells. Haematologica. 2018 Jun;103(6):939-948. doi: 10.3324/haematol.2017.181354.
88. Rubic T, Lametschwandtner G, Jost S, Hinteregger S, Kund J, Carballido-Perrig N, Schwärzler C, Junt T, Voshol H, Meingassner JG, Mao X, Werner G, Rot A, Carballido JM. Triggering the succinate receptor GPR91 on dendritic cells enhances immunity. Nat Immunol. 2008 Nov;9(11):1261-9. doi: 10.1038/ni.1657.
89. van Diepen JA, Robben JH, Hooiveld GJ, Carmone C, Alsady M, Boutens L, Bekkenkamp-Grovenstein M, Hijmans A, Engelke UFH, Wevers RA, Netea MG, Tack CJ, Stienstra R, Deen PMT. SUCNR1-mediated chemotaxis of macrophages aggravates obesity-induced inflammation and diabetes. Diabetologia. 2017 Jul;60(7):1304-1313. doi: 10.1007/s00125-017-4261-z.
90. Choo S, Wolf CB, Mack HM, Egan MJ, Kiem HP, Radtke S. Choosing the right mouse model: comparison of humanized NSG and NBSGW mice for in vivo HSC gene therapy. Blood Adv. 2024 Feb 27;8(4):916-926. doi: 10.1182/bloodadvances.2023011371.
91. Xiao M, Yang H, Xu W, Ma S, Lin H, Zhu H, Liu L, Liu Y, Yang C, Xu Y, Zhao S, Ye D, Xiong Y, Guan KL. Inhibition of α-KG-dependent histone and DNA demethylases by fumarate and succinate that are accumulated in mutations of FH and SDH tumor suppressors. Genes Dev. 2012 Jun 15;26(12):1326-38. doi: 10.1101/gad.191056.112.
92. Su TY, Hauenstein J, Somuncular E, Dumral Ö, Leonard E, Gustafsson C, Tzortzis E, Forlani A, Johansson AS, Qian H, Månsson R, Luc S. Aging is associated with functional and molecular changes in distinct hematopoietic stem cell subsets. Nat Commun. 2024 Sep 11;15(1):7966. doi: 10.1038/s41467-024-52318-1.
93. Pang WW, Price EA, Sahoo D, Beerman I, Maloney WJ, Rossi DJ, Schrier SL, Weissman IL. Human bone marrow hematopoietic stem cells are increased in frequency and myeloid-biased with age. Proc Natl

Acad Sci U S A. 2011 Dec 13;108(50):20012-7.
doi: 10.1073/pnas.1116110108.

94. Belluschi S, Calderbank EF, Ciaurro V, Pijuan-Sala B, Santoro A, Mende N, Diamanti E, Sham KYC, Wang X, Lau WWY, Jawaid W, Göttgens B, Laurenti E. Myelo-lymphoid lineage restriction occurs in the human haematopoietic stem cell compartment before lymphoid-primed multipotent progenitors. Nat Commun. 2018 Oct 5;9(1):4100.
doi: 10.1038/s41467-018-06442-4.
95. Beerman I, Seita J, Inlay MA, Weissman IL, Rossi DJ. Quiescent hematopoietic stem cells accumulate DNA damage during aging that is repaired upon entry into cell cycle. Cell Stem Cell. 2014 Jul 3;15(1):37-50.
doi: 10.1016/j.stem.2014.04.016.
96. Bogeska R, Mikecin AM, Kaschutnig P, Fawaz M, Büchler-Schäff M, Le D, Ganuza M, Vollmer A, Paffenholz SV, Asada N, Rodriguez-Correa E, Frauhammer F, Buettner F, Ball M, Knoch J, Stäble S, Walter D, Petri A, Carreño-Gonzalez MJ, Wagner V, Brors B, Haas S, Lipka DB, Essers MAG, Weru V, Holland-Letz T, Mallm JP, Rippe K, Krämer S, Schlesner M, McKinney Freeman S, Florian MC, King KY, Frenette PS, Rieger MA, Milsom MD. Inflammatory exposure drives long-lived impairment of hematopoietic stem cell self-renewal activity and accelerated aging. Cell Stem Cell. 2022 Aug 4;29(8):1273-1284.e8.
doi: 10.1016/j.stem.2022.06.012.
97. Bergamasco MI, Ranathunga N, Abeysekera W, Li-Wai-Suen CSN, Garnham AL, Willis SN, McRae HM, Yang Y, D'Amico A, Di Rago L, Wilcox S, Nutt SL, Alexander WS, Smyth GK, Voss AK, Thomas T. The histone acetyltransferase KAT6B is required for hematopoietic stem cell development and function. Stem Cell Reports. 2024 Apr 9;19(4):469-485.
doi: 10.1016/j.stemcr.2024.02.005.
98. Zhou P, Chen X, Li M, Sun X, Tan J, Wang X, Chu Y, Zhang Y, Cheng T, Zhou J, Wang G, Yuan W. Overexpression of PRDM5 promotes acute myeloid leukemia cell proliferation and migration by activating the JNK pathway. Cancer Med. 2019 Jul;8(8):3905-3917.
doi: 10.1002/cam4.2261.
99. Zhang YW, Schönberger K, Cabezas-Wallscheid N. Bidirectional interplay between metabolism and epigenetics in hematopoietic stem cells and leukemia. EMBO J. 2023 Dec 11;42(24):e112348.
doi: 10.15252/embj.2022112348.
100. Grimolizzi F, Arranz L. Multiple faces of succinate beyond metabolism in blood. Haematologica. 2018 Oct;103(10):1586-1592. doi: 10.3324/haematol.2018.196097.
101. Hakak Y, Lehmann-Bruinsma K, Phillips S, Le T, Liaw C, Connolly DT, Behan DP. The role of the GPR91 ligand succinate in hematopoiesis. J Leukoc Biol. 2009 May;85(5):837-43.
doi: 10.1189/jlb.1008618.

Materials and Methods

Human hematopoietic samples.
We complied with all ethical regulations for the retrieval of biological materials from healthy donors. To characterize the hematopoietic compartment over aging, we collected BM samples from 43 young adults (18 to 28 years old) and 71 aged (>70 years old) healthy individuals. Aged BM samples were collected from subjects who underwent hip replacement surgery at San Raffaele Hospital, Milan, and IRCCS Galeazzi Orthopedic Institute, Milan, after obtaining written informed consent. BM CD34+ cells from young healthy donors for functional assays and mPB CD34+ cells were purchased from Lonza. For the phenotypic analyses, the sample size was determined by the number of individuals for whom excess material was available, after signing informed consent for research protocols approved by the San Raffaele Scientific Institute's Ethics Committee (according to protocol TIGET09). We excluded from our analyses all subjects with compromised immune functions and a previous history of cancer or cancer treatments. We also excluded subjects who were positive for HBV, HCV, and HIV infections. We included only subjects who scored as "no frail" upon the Edmonton Frailty Scale (EFS) evaluation.

Primary cell cultures
CD34+ HSPCs were either freshly purified from human BM after obtaining informed consent and upon approval by the San Raffaele Hospital ethical committee (TIGET09) or purchased frozen from Lonza. After thawing, HSPCs were seeded at a concentration of 5 × 10^5 cells/mL in serum-free StemSpan SFEM medium (StemCell Technologies) supplemented with 10 µM 16,16-dimethyl Prostaglandin E2 (added only at thawing) (Cayman), L-glutamine (2 mM) and Penicillin-Streptomycin (100 IU/mL penicillin, 100 µg/mL streptomycin), and human early-acting cytokines (SCF 100 ng/mL, Flt3-L 100 ng/mL, TPO 20 ng/mL, and IL-6 20 ng/mL; Peprotech). Cells were cultured at 37°C in a 5% CO2 humidified atmosphere.

ATAC-Seq library preparations and analyses
Library preparation for ATAC-Seq was performed on 1 x 10^5 CD34+ cells. The cells were lysed with digitonin (Promega; cat. #G944A) and tagmented with an engineered Tn5 transposase (Illumina; cat. #15027865) at 37°C for 30 minutes, following a protocol optimized for blood cells (PMID: 27526324). Tagmented DNA was purified and amplified using 10 PCR cycles. Before sequencing, fragments with a 1-5 kbp size range were removed by magnetic separation using AMPure XP beads (Beckman Coulter; cat. #A63881with Nextera DNA Sample Preparation kit (Illumina). 4 ATAC-seq libraries were sequenced per lane in HiSeq 2500 System (Illumina) to generate 40 × 106 paired-end reads per sample.
Reads were trimmed with Trim Galore, aligned with BWA-MEM (release 0.7.17-r1188), to the human genome (GRCh38 primary assembly). Bam files were filtered for mitochondrial, Y chromosome, and PCR duplicated reads with Picard (2.25.0-0). Blacklisted regions were filtered using the ENCODE blacklist (hg38 v2) as a reference. Peak calling was performed with macs2 (callpeak -t $bam -f BAMPE --nomodel --outdir $outdir -g hs --narrow --keep-dup all -n $sample_name --shift -100 --extsize 200 -B --SPMR -q 0.05). Data pre-processing and Differential accessible region (DARs) analysis were conducted with Diffbind (Ross-Innes CS, Stark R et al, 2012) package using the DESeq2 function. The peak-counts matrix was generated centering the peaks on the summit and a consensus peakset was created across sample conditions, requiring peaks to be present in more than 50% of samples within each

group (using the dba.count function). The function annotatePeak from Chipseeker package was used to annotate DARs.

Total RNA-seq library preparation and analysis

High-quality reads, obtained after trimming with Trim Galore (), were aligned to the human genome (GENCODE version hg38 primary assembly) with STAR release 2.7.6a (Dobin, Alexander, et al, 2013). The read count matrix was generated with featureCounts v2.0.1 (Liao, Yang et al 2014). Genes with zero count across all samples and immunoglobulin (Ig) genes were filtered out before downstream analysis. Differential gene expression analysis was performed using the DESeq2 package (Love et al., 2014) with a time-series model incorporating age, time, and their interaction term (~age + time + age:time). Adjusted P values for multiple hypothesis corrections were used to retain significant genes (FDR < 0.05). Gene Set Enrichment Analysis (GSEA) was conducted using the clusterProfiler package (Wu et al., 2021), with genes ranked by log2 fold change (Log2FC) (Subramanian et al., 2005). To identify specific gene changes due to the age effect, we categorized genes into distinct groups: those with the same effect (positive or negative) but of different magnitude in the two age groups, and those exhibiting opposite directions of change between age groups over time in culture. These gene sets were analyzed separately using Over-Representation Analysis (ORA) with the enrichGO function from the clusterProfiler package.

Untargeted intracellular metabolomic preparations and analyses

At the end of the treatments, monolayers were rapidly washed three times with ice-cold PBS and extracted with 600 µL of ice-cold extraction solution, composed of methanol, acetonitrile, and water (5:3:2) for intracellular metabolite determination. Media derived from wells lacking cells but incubated in the same conditions were used as a reference to quantify the exchange rate (consumption/secretion). Culture media and cells were then centrifuged at 16,000g for 30 min at 4 °C and the supernatants were analyzed by liquid chromatography-mass spectrometry (LC-MS). Intracellular metabolites were normalized to the protein content in each well, determined at the end of the experiment, using the Lowry assay. Log-transformed metabolic intensities were analyzed in R using the Limma package, which implements the moderated t-statistic with empirical Bayes correction and Benjamini-Hochberg-adjusted P-values. The final metabolite value was converted to a z-score.

Colony forming unit assay

CFU-C assay was performed by plating 800 cells (in vitro experiments, three technical replicates performed for each condition) in methylcellulose-based medium (MethoCult H4434, StemCell Technologies) supplemented with 100 IU/ml penicillin and 100 mg/ml streptomycin. After 14 days of incubation in a 5% CO2 humidified atmosphere at 37°C, colonies were counted in a blind fashion and erythroid, myeloid, and mixed colonies were identified according to morphological criteria.

Myeloid-Erythoid-Megakaryocyte (MEM) single-cell differentiation assay

Before cell culture (T0) and after 72 hours of ex vivo culture, HSC/MPP cells were sorted based on the expression of surface markers of CD34+CD133+CD45RA−CD38−CD90+ (negative to ZombieAqua viable dye) as single cells (1 cell/well) and seeded in U-bottom 96-well filled with 100 µL/well Myeloid-Erythroid-Megakaryocyte (MEM) cytokine medium: StemPro medium with nutrients supplement (Life Technologies) supplemented with cytokines (SCF 100 ng/mL, Flt3-L 20 ng/mL, TPO 100 ng/mL, IL-6 50 ng/mL, IL-3 10 ng/mL, all

Peprotech; IL-11 50 ng/mL, GM-CSF 20 ng/mL, IL-2 10 ng/mL, IL-7 20 ng/mL; all Miltenyi Biotec), erythropoietin (EPO) 3 units/mL (Eprex, Janssen-Cilag), h-LDL 50 ng/mL (Stem Cell Technologies), 1% L-Glutamine (Life Technologies) and 1% Pen/Strep (Life Technologies). Cells were cultured for 3 weeks in a 5% CO2 humidified atmosphere at 37°C. Cell sorting was performed on a BD FACSAria Fusion (BD Biosciences) using BDFACS Diva software and equipped with five lasers: blue (488 nm), yellow/green (561 nm), red (640 nm), and violet (405 nm). Cells were sorted with a 100 µm nozzle.
All single-cell-derived colonies were harvested into 96 U-bottom plates. Cells were then stained with 50 µL/well of antibody mix (CD45-PECy7, CD11b-PE, CD41-PECy5, GlyA-APC, CD14-APCCy7, CD56-BV421, CD15-BV510, 1:300, 1:500, 1:200, 1:1000, 1:500, 1:200, 1:1000, respectively), incubated for 20 min in the dark at room temperature and then washed with 100 µL/well of DPBS (1×) +2% FBS. The type (lineage composition) and the size of the colonies formed were assessed by high-throughput flow cytometry. A single cell was defined as giving rise to a colony if the sum of cells detected in the CD45+ gates was ≥30 cells (clonogenic efficiency). Erythroid (Ery) colonies were identified as CD45−GlyA+ ≥ 30 cells, Megakaryocytes (Meg) colonies as CD45+CD41+ ≥ 30 cells, Myeloid (My) colonies as [Monocytes (Mono: CD45+CD14+) + Granulocytes (Gran: CD45+CD15+)] ≥ 30 cells, and NK colonies as CD45+CD56+ ≥ 30 cells. Undifferentiated colonies were defined as those with a sum of cells detected in the CD45+ gates being ≥30 cells, but these cells did not express any other markers as previously described. The presence of Ery, Meg, My, or NK positivity indicates the development of unilineages, bilineages, or multilineages.

In vitro treatments
HSPCs were seeded at 5 × 10^5 cells at mL and kept at the same cellular concentration for all the time course. Cells were treated with 4 mM diethyl succinate (#112402 Sigma-Aldrich), 4 mM dimethyl-αKG (#349631 Sigma-Aldrich), or 8 µM PT2399 (HY-108697), with a washout every 24 h for the duration of the treatment. For all treatments, negative control was obtained by treating cells with the same volume of DMSO. pH was measured after administration of both metabolites and DMSO to ensure pH stability.

Alkaline Comet Assay
HSPCs were suspended at 2 × 10^4 cells/ml in ice-cold DPBS (1×) and mixed with molten Comet LMAgarose (Trevigen, MD) at a ratio of 1:10 (v/v) and immediately pipetted onto CometSlides (Trevigen, MD) and placed at 4°C. Once solidified, the slides were immersed in pre-chilled Lysis Solution (Trevigen, MD) for 1 hour or overnight at 4°C. Following lysis, slides were immersed in freshly prepared Alkaline Unwinding Solution pH > 13 (300 mM NaOH, 1mM EDTA) for 1 hour at 4°C and then electrophoresed in Alkaline Electrophoresis Solution pH > 13 (300 mM NaOH, 1mM EDTA) at 21V/cm for 30 min. Slides were washed twice in ddH2O and fixed in 70% ethanol for 5 min. Comets were dried at 37°C and then stained with SYBR Safe (Invitrogen) for 30 min at room temperature. All steps were conducted in the dark to prevent additional DNA damage. Comets were analyzed using a Nikon Eclipse E600 microscope and a Nikon-DS-RI2 camera. At least 50 nuclei for each individual donor were analyzed with CASP software to determine “Olive Tail Moments” of individual nuclei.

Scenith
5*10^4 HSPCs were seeded in 100 microliters in 96 well plates for studying HSPCs metabolism. SCENITH reagents kit (inhibitors, puromycin, and antibodies) were obtained from www.scenith.com/try-it and used according to the provided protocol. Experimental

triplicates were performed in all conditions. Wells were treated for 30 minutes with Control, 2-Deoxy-D-Glucose (DG, final concentration 100 mM), Oligomycin (Oligo, final concentration 1 µM), or a sequential combination of the drugs at the final concentrations mentioned before. As a negative control, the translation initiation inhibitor Harringtonine was added 15 minutes before the addition of puromycin (Harringtonine, 2 µg/ml). Puro (final concentration 10 µg/ml) is added during the last 45 minutes of the metabolic inhibitors treatment. After puromycin treatment, cells were washed in cold PBS and stained with a combination of a fluorescent cell viability marker and primary antibodies conjugated to surface markers for 25 minutes at 4°C in PBS containing 1× 5% FCS and 2 mM EDTA (FACS wash buffer). After washing, cells were fixed and permeabilized using FOXP3 fixation and permeabilization buffer (Thermofisher eBioscience™) following manufacturer instructions. Intracellular staining of puromycin using then stained with anti-Puromycin Alexa Fluor 488 for 1h at 4°C

Western blot

To prepare protein extracts for immunoblot analysis, cells were washed twice with cold PBS and lysed for 30 min on ice with RIPA buffer containing 50 mM Tris–HCl pH 8.0, 150 mM NaCl, 1% (v/v) NP-40, 0.5% (w/v) Sodium Deoxycholate, 1 mM EDTA, 0.1% (w/v) SDS, 0.01% (w/v) Sodium azide pH 7.4, and Pierce protease and phosphatase minitablets inhibitors (Thermo Fisher Scientific, A32961). Cells were centrifuged at 13,000 rpm at 4 °C for 10 min and the supernatants were quantified for protein content with Pierce's BCA protein assay kit (Thermo Fisher Scientific, 23227), according to manufacturer's instructions. Then, the extracted proteins were resolved by SDS–PAGE before transfer onto nitrocellulose membrane (Sigma-Aldrich, GEH10600003),

Xenotransplantation in immunocompromised mice of activated human HSPC across aging

NOD-SCID-IL2Rg−/− (NSG) mice were purchased from Charles River Laboratories and maintained in specific-pathogen-free (SPF) conditions. Specifically, in order to ensure higher transplantation success, engraftment, and better reproducibility, only female mice (8 weeks of age) were used. The procedures involving animals were designed and performed with the approval of the Animal Care and Use Committee of the San Raffaele Hospital and communicated to the Ministry of Health and local authorities according to Italian law (IACUC 1385). For transplantation, BM-derived CD34+ cells (4 × 10 ^5 cells) were injected intravenously into immunocompromised mice after sublethal irradiation (180 cGy). Mice were randomly distributed to experimental groups. Human CD45+ cell engraftment was monitored by serial collection of blood from the mouse tail vein, and the BM and spleen were retrieved and analyzed at the end of the experiment. Immunophenotypic analyzes were conducted as described below.

Flow cytometry

For immunophenotypic analyses (performed on FACSCanto II; BD Biosciences) of ex vivo cultured HSPCs, cellular suspension (approx. 3–5 × 104 cells) was incubated with anti-human FcR Blocking (1:100 dilution) (Miltenyi Biotec) to prevent unwanted binding of antibodies to human Fc receptor-expressing cells. Then, cells were stained with different fluorescent-labeled antibodies (1:100 dilution, each): anti-human CD34 PE (Miltenyi Biotec), anti-human CD133 PE-Vio 770 (Miltenyi Biotec), and anti-human CD90 APC (BD Biosciences). Where indicated immunophenotypic staining was combined with Annexin V (BioLegend) and 7-amino-actinomycin D (7-AAD) (BioLegend) viability staining according to the

manufacturer's instructions (3 and 1µL per sample, respectively). Apoptosis analysis was performed using 7-AAD staining in combination with Annexin V (BioLegend), according to the manufacturer's instructions. For immunophenotypic analyses (performed on FACSCanto II; BD Biosciences) of cells retrieved from in vivo organs, we used anti-human and –mouse FcR Blocking (1:100 and 1:200 dilution, respectively) (BD Biosciences) and then cells were stained with different fluorescent-labeled antibodies (1:100 dilution, each).
(1) Peripheral blood: anti-human CD45 APC-eFluor 780, anti-human CD19 PE or BV510, anti-human CD3 APC or PE, anti-human CD33 PE-Cy7 (at 6,9 and 12);
(2) Bone marrow: anti-human CD45 APC-eFluor 780, anti-human CD90 APC, anti-human CD34 PE-Cy7, anti-human CD19 BV510, anti-human CD13 BV421, and anti-human CD3 PE;
(3) Spleen: anti-human CD45 APC-eFluor 780, anti-human CD19 PE or BV510, anti-human CD13 BV421, anti-human CD3 APC or PE, anti-human CD8 PE-Cy7, anti-human CD71 BV421, anti-human CD235a (GlyA) APC, anti-human CD41 PE-Cy5, and anti-human CD61 PE-Cy7.
Single-stained and Fluorescence Minus One (FMO) stained cells were used as controls and SPHERO Rainbow Calibration Particles (Spherotech) were used to perform instrument calibration. Data was analyzed using the FlowJo software.

Statistical analysis
Data are presented as means ± SEM or as dot plots with median values indicated by a line. Analyses were conducted using GraphPad Prism software. Differences were considered statistically significant at *$p < 0.05$, **$p < 0.01$, ***$p < 0.001$, ****$p < 0.0001$. The specific statistical tests used are indicated in each figure.

Antibodies

Category	Target/Reagent	Clone	Conjugate	Vendor	Catalog #	RRID
Antibody	CD133/1	AC133	PE-Vio770	Miltenyi Biotec	130-113-110	AB_2725939
Antibody	CD34	AC136	PE	Miltenyi Biotec	130-113-179	AB_2726006
Antibody	CD90	5.00E+10	APC	BD Biosciences	559869	AB_398677
Antibody	CD45	HI30	APC-eFluor 780	Invitrogen	47-0459-42	AB_1944368
Antibody	CD19	SJ25C1	PE	BD Biosciences	345789	AB_2868815
Antibody	CD13	WM15	BV421	BD Biosciences	562596	AB_2737672
Antibody	CD3	UCHT1	APC	BD Biosciences	555335	AB_398591
Antibody	CD33	P67.6	PE-Cy7	BD Biosciences	333952	AB_2713932
Antibody	CD33	WM53	BV421	BD Biosciences	562854	AB_2737405
Antibody	CD11b	M1/70	PE	BioLegend	101207	AB_312790
Antibody	CD41	HIP8	PE-Cy5	BioLegend	303708	AB_314378
Antibody	CD45	HI30	PE-Cy7	BioLegend	304016	AB_314404
Antibody	CD235a (GlyA)	GA-R2 (HIR2)	APC	BD Biosciences	551336	AB_398499
Antibody	CD14	M5E2	APC-Cy7	BioLegend	301820	AB_493695
Antibody	CD56	MEM-188	Pacific Blue	BioLegend	304629	AB_2282499
Antibody	CD45RA	HI100	Alexa Fluor 700	BioLegend	304120	AB_493763
Antibody	CD15	W6D3	BV510	BioLegend	323028	AB_2563400
Antibody	CD3	OKT3	PE	BioLegend	317308	AB_571913
Antibody	CD19	HIB19	BV510	BioLegend	302242	AB_2561668
Antibody	CD56	AF12-7H3	PE	Miltenyi Biotec	130-113-312	AB_2726090
Antibody	CD45	2D1	PerCP-Cy5.5	BioLegend	368504	AB_2566352
Antibody	CD3	REA613	APC	Miltenyi Biotec	130-113-135	AB_2725963
Antibody	CD45	REA747	VioBlue	Miltenyi Biotec	130-110-637	AB_2658243
Reagent	FcR Blocking (human)			Miltenyi Biotec	130-059-901	AB_2892112
Antibody	Histone H3 (rabbit)			Abcam	ab1791	AB_302613
Antibody	Goat anti-rabbit IgG (H+L)		HRP	Thermo Fisher Scientific	31460	AB_228341
Antibody	Goat anti-mouse IgG (H+L)		HRP	Thermo Fisher Scientific	31430	AB_228307
Dye	7-AAD viability			BioLegend	420403	
Dye	Annexin V		Pacific Blue	BioLegend	640918	
Probe	CellROX Deep Red			Thermo Fisher	C10422	
Buffer	Intracellular Staining Perm Wash			BioLegend	421002	
Kit/Reagent	CometAssay Lysis Solution			R&D Systems	4250-050-01	
Reagent	CometAssay LMAgarose			R&D Systems	4250-050-02	
Reagent	Poly-L-lysine solution			Sigma-Aldrich	P8920	
Fixative	Paraformaldehyde 4% in PBS			Santa Cruz Biotechnology	SC-281692	
Stain	DAPI			Sigma-Aldrich	D9542	
Inhibitor mix	Pierce Protease/Phosphatase Inhibitor Mini Tablets			Thermo Scientific	A32961	